Western Australia School of Mines: Minerals, Energy and Chemical Engineering

Fuels and Energy Technology Institute

Investigation of Cathode/Electrolyte Interfaces in Solid Oxide Fuel Cells by using FIB-STEM Techniques

Shuai He

This thesis is presented for the Degree of

Doctor of Philosophy

of

Curtin University

January 2019

Declaration

To the best of my knowledge and belief this thesis contains no material previously published by any other person except where due acknowledgment has been made.

This thesis contains no material which has been accepted for the award of any other degree or diploma in any university.

Signature: ……Shuai He……

Date: ……15/01/2019……

Acknowledgement

Over the past three years' PhD study at Curtin University, I have been through one of the most important and memorable periods in my life. It is such a significant milestone that dramatically changes my future in a fantastic and unforgettable way. I have to admit that my successful completion of the PhD project is a result of the help and kindness received from countless great people. Here, I would like to express my greatest acknowledgement to the people that accompanying me during this tough but rewarding journey.

First of all, I want to thank to my supervisor, Prof. San Ping Jiang for giving me this invaluable opportunity to further my postgraduate study under his continuous guidance. His great patience, exceptional knowledge and expertise constantly inspired me throughout my study, which helped me to get through some of the toughest moments that I struggled with. Being strict in research, humble and kind in person, professor has shown himself as a great role model to me, greatly influencing me both academically and personally. His constructive ideas and supervision have made the completion of my PhD project possible. Without his continuous help and guidance, I would never be able to complete the PhD project and to reach the stage as today.

Also, I would like to express my sincere gratitude to Prof. Martin Saunders from The University of Western Australia, who has been continuously providing constructive and inspirational advice to my research in terms of the electron microscope. His selfless and professional assistance significantly helped me to tackle a number of academic and technical difficulties over the past three years. The advanced FIB workshop organised by him transformed my research, enabling me to advance my study to a much higher level. Besides, he has been constantly encouraging and motivating me without any condition, and also giving me great support and recommendation to my academic career. I truly believe he is the person who deserves my great respect.

Furthermore, my sincere thanks also go to Dr Kongfa Chen, Dr Na Li, Dr Meng Li and Dr Na Ai for teaching me the fundamental knowledge as well as the basic experimental skills throughout my study. Their patience and kindness made my PhD journey a pleasant and easier one. I am also grateful to the previous and current

members in my group for their encouragement and insightful discussions, including but not limited to (in no particular order): Dr Yi Cheng, Dr Cheng Cheng Wang, Dr Jin Zhang, Yiming Zhong, Haohua Kuang, Shiyong Zhao, Xiao Zhang, Qi Zhang, Dr Chunbo Jiang, Dr Shikui Yao, Dr Jian Pan and Yi Sun. I also want to show my appreciation to Dr Shao Xin, Huu Dang, Dr Yu Liu and Dechao Chen for their help and suggestions.

In addition, I want to thank to Ms Veronica Avery, Dr William Rickard, Ms Elaine Miller from John de Laeter Centre, Curtin University, and to Dr Alexandra Suvorova from Centre for Microscopy, Characterisation and Analysis, The University of Western Australia for their scientific and technical assistance.

Last but not the least, I would like to give my greatest gratitude to my parents, who have been believing in me, supporting me, encouraging me and loving me since the very first day. Their unconditional understanding and trust in me are the driving force that motivates me to go further and beyond.

Abstract

Solid oxide fuel cells (SOFCs) are considered one of the most promising energy conversion devices, directly converting chemical energy of a wide range of fuels, like H_2, natural gas and hydrocarbons to electricity with significantly less greenhouse gas emission. A typical SOFC device is often operated at high temperature, e.g. 800^{o}C-1000^{o}C, thus capable of using non-precious metal catalysts with high efficiency. For SOFCs, the durability and degradation issues are some of the most important concerns for commercialisation, and the degradation of cell performance closely relates to its electrochemical reactions that occur at the three-phase boundary (TPB), where fuel or oxygen, electrode and electrolyte meet. Therefore, the evolution of electrode/electrolyte interface during operation is an important indicator for evaluating the overall performance of a cell. Despite its significance in both scientific and practical points of view for the development of SOFC technology, there appears to be a lack of systematic and thorough investigation over the last decade on the evolution of electrode/electrolyte interface, particularly in relation to its composition, microstructure and crystallography.

In this thesis, the most important and typical cathode/electrolyte interfaces were studied in great details under a wide range of SOFC operation conditions. In addition, by using the direct assembly method developed in our group, the *in situ* and instantaneous formation and change of cathode/electrolyte interface as a function of cathodic or anodic polarisation were conveniently investigated without requiring the conventional high temperature pre-sintering process, and thus avoiding the issues of interfacial chemical reactions associated with pre-sintering steps. To be specific, the $La_{0.8}Sr_{0.2}MnO_3$ (LSM)/Y_2O_3-ZrO_2 (YSZ), LSM/Gd_2O_3-CeO_2 (GDC), $La_{0.6}Sr_{0.4}Co_{0.2}Fe_{0.8}O_3$ (LSCF)/YSZ and $La_{0.6}Sr_{0.4}Co_{0.2}Fe_{0.8}Nb_{0.1}O_3$-$Er_{0.4}Bi_{1.6}O_3$ (LSCFNb-ESB)/YSZ interfaces with and without pre-sintering were studied in terms of their composition, morphology and crystallography, crystalline phase orientation, defect, and interfacial reaction, using focus ion beam and scanning transmission electron microscopy (FIB-STEM). The details are summarised as follows:

Firstly, for pre-sintered LSM/YSZ and LSM/GDC system, the electrode/electrolyte interfaces were characterised by the formation of convex contact rings, and the atomic geometry of the interface was identified by the lattice plane matching of the cathode

and electrolyte, without forming voids or a third phase. Cations diffusion such as Mn^{2+} and La^{3+} were found in the case of pre-sintered LSM/YSZ cells, while no cation migration was detected for pre-sintered LSM/GDC cells. As a comparison, the directly assembled LSM/YSZ and LSM/GDC interfaces under the influence of cathodic polarisation were investigated. Secondly, for directly assembled LSM/YSZ interface, it appears that cathodic current promoted the disintegration of LSM cathode particles at the interface, forming a large number of tiny particles in contact with the electrolyte. The disintegration of LSM particle became more obvious with prolonged polarisation. Whereas in the case of directly assembled LSM/GDC interface, the cathodic polarisation clearly induced the formation of clean and sharp electrode/electrolyte interface, and the interface was much more stable with increasing polarisation time as compared to the LSM/YSZ interface. However, the electrochemical performance of both cells was greatly improved after polarisation. Thirdly, the evolution of directly assembled $La_{0.6}Sr_{0.4}Co_{0.2}Fe_{0.8}O_{3-\delta}$ (LSCF)/YSZ interfaces was examined as a function of cathodic polarisation time. It was found that initial polarisation can promote the formation of intimate LSFC/YSZ interface, but further polarising the cell induced the Sr segregation from the cathode, forming a thin SrO layer at the interface. The segregated SrO subsequently reacted with YSZ electrolyte under the influence of polarisation, and an insulating $SrZrO_3$ layer was formed between LSCF cathode and YSZ electrolyte. The morphology of YSZ electrolyte was also characterised by the formation of a large amount of contact craters after polarisation. Lastly, the direct assembly method was further adopted to an anode-supported YSZ electrolyte cell with the $Er_{0.4}Bi_{1.6}O_3$ (ESB) decorated $La_{0.6}Sr_{0.4}Co_{0.2}Fe_{0.7}Nb_{0.1}O_{3-\delta}$ (LSCFNb) cathode, and their interface was studied before and after cathodic polarisation as well. The results indicated that the ESB decoration significantly enhanced the electrochemical performance as well as the interface stability of the cell. It was also revealed that ESB tends to migrate towards the electrode/electrolyte interface under the influence of cathodic polarisation, forming an ESB layer between LSCFNb and YSZ. Such ESB layer was found to suppress the Sr segregation from the cathode, preventing the direct contact and reaction between SrO and YSZ.

This thesis provides an insight in the fundamental understanding of electrode/electrolyte interface formation and has significant implications in the development of active and stable cathodes of SOFCs in general. The crystallography,

microstructure and composition of electrode/electrolyte interface as a function of polarisation have been presented and discussed for the first time in detail using combined FIB-STEM techniques. The information obtained from the directly assembled electrode on barrier-layer-free YSZ or GDC electrolytes reveals the fundamental mechanism of the interface evolution and cation segregation in SOFCs under polarisation conditions. Also, the *in situ* formation of highly active and functional bismuth oxide interlayer under cathodic polarisation was discovered and it indicates the promising potential of the approach for the development in intermediate temperature SOFCs. This thesis clearly demonstrates the dynamic relationship between interface, segregation, and performance of directly assembled cathode materials for fuel cells.

List of Publications

1. **S. He**, K. Chen, M. Saunders, J. Li, C.Q. Cui, S.P. Jiang, A FIB-STEM Study of $La_{0.8}Sr_{0.2}MnO_3$ Cathode and Y_2O_3-ZrO_2/Gd_2O_3-CeO_2 Electrolyte Interfaces of Solid Oxide Fuel Cells, Journal of The Electrochemical Society, 164 (2017) F1437-F1447.
2. **S. He**, M. Saunders, K. Chen, H. Gao, A. Suvorova, W.D.A. Rickard, Z. Quadir, C.Q. Cui, S.P. Jiang, A FIB-STEM Study of Strontium Segregation and Interface Formation of Directly Assembled $La_{0.6}Sr_{0.4}Co_{0.2}Fe_{0.8}O_{3-\delta}$Cathode on Y_2O_3-ZrO_2 Electrolyte of Solid Oxide Fuel Cells, Journal of The Electrochemical Society, 165 (2018) F417-F429.
3. **S. He**, K. Chen, M. Saunders, Z. Quadir, S. Tao, J.T.S. Irvine, C.Q. Cui, S.P. Jiang, Interface formation and Mn segregation of directly assembled $La_{0.8}Sr_{0.2}MnO_3$ cathode on Y_2O_3-ZrO_2 and Gd_2O_3-CeO_2 electrolytes of solid oxide fuel cells, Solid State Ionics, 325 (2018) 176-188.
4. **S. He**, Q. Zhang, G. Maurizio, L. Catellani, K. Chen, Q. Chang, M. Santarellic and S.P. Jiang, In situ formation of $Er_{0.4}Bi_{1.6}O_3$ protective layer at cobaltite cathode/Y_2O_3-ZrO_2 electrolyte interface under solid oxide fuel cells operation conditions, ACS Applied Materials & Interfaces, accepted. DOI: 10.1021/acsami.8b14026
5. N. Li, N. Ai, K. Chen, Y. Cheng, **S. He**, M. Saunders, A. Dodd, A. Suvorova, S.P. Jiang, In situ assembled $La_{0.8}Sr_{0.2}MnO_3$ cathodes on a Y_2O_3–ZrO_2 electrolyte of solid oxide fuel cells – interface and electrochemical activity, RSC Advances, 6 (2016) 99211-99219.
6. M.R. Rowles, C.C. Wang, K. Chen, N. Li, **S. He**, S.-P. Jiang, Temperature-dependent structural behaviour of samarium cobalt oxide, Powder Diffraction, (2017) 1-5.
7. C.C. Wang, **S. He**, K. Chen, M.R. Rowles, S. Darvish, Y. Zhong, S.P. Jiang, Effect of SO_2 Poisoning on the Electrochemical Activity of $La_{0.6}Sr_{0.4}Co_{0.2}Fe_{0.8}O_{3-\delta}$ Cathodes of Solid Oxide Fuel Cells, Journal of The Electrochemical Society, 164 (2017) F514-F524.
8. N. Ai, N. Li, **S. He**, Y. Cheng, M. Saunders, K. Chen, T. Zhang, S.P. Jiang, Highly active and stable $Er_{0.4}Bi_{1.6}O_3$ decorated $La_{0.76}Sr_{0.19}MnO_{3+\delta}$

nanostructured oxygen electrodes for reversible solid oxide cells, Journal of Materials Chemistry A, 5 (2017) 12149-12157.

9. N. Ai, M. Chen, **S. He**, K. Chen, T. Zhang, S.P. Jiang, High performance nanostructured bismuth oxide–cobaltite as a durable oxygen electrode for reversible solid oxide cells, Journal of Materials Chemistry A, 6 (2018) 6510-6520.
10. N. Ai, **S. He**, N. Li, Q. Zhang, W.D.A. Rickard, K. Chen, T. Zhang, S.P. Jiang, Suppressed Sr segregation and performance of directly assembled $La_{0.6}Sr_{0.4}Co_{0.2}Fe_{0.8}O_{3-\delta}$ oxygen electrode on Y_2O_3 -ZrO_2 electrolyte of solid oxide electrolysis cells, Journal of Power Sources, 384 (2018) 125-135.
11. K. Chen, **S. He**, N. Li, Y. Cheng, N. Ai, M. Chen, W.D.A. Rickard, T. Zhang, S.P. Jiang, Nb and Pd co-doped $La_{0.57}Sr_{0.38}Co_{0.19}Fe_{0.665}Nb_{0.095}Pd_{0.05}O_{3-\delta}$ as a stable, high performance electrode for barrier-layer-free Y_2O_3-ZrO_2 electrolyte of solid oxide fuel cells, Journal of Power Sources, 378 (2018) 433-442.
12. N. Li, N. Ai, **S. He**, Y. Cheng, W.D.A. Rickard, K. Chen, T. Zhang, S.P. Jiang, Effect of Pd doping on the activity and stability of directly assembled $La_{0.95}Co_{0.19}Fe_{0.76}Pd_{0.05}O_{3-\delta}$ cathodes of solid oxide fuel cells, Solid State Ionics, 316 (2018) 38-46.
13. M. Chen, Y. Cheng, **S. He**, N. Ai, J.-P. Veder, W.D.A. Rickard, M. Saunders, K. Chen, T. Zhang, S.P. Jiang, Active, durable bismuth oxide-manganite composite oxygen electrodes: Interface formation induced by cathodic polarization, Journal of Power Sources, 397 (2018) 16-24.
14. Z. He, L. Zhang, **S. He**, N. Ai, K. Chen, Y. Shao, S.P. Jiang, Cyclic polarization enhances the operating stability of $La_{0.57}Sr_{0.38}Co_{0.18}Fe_{0.72}Nb_{0.1}O_{3-\delta}$ oxygen electrode of reversible solid oxide cells, Journal of Power Sources, 404 (2018) 73-80.

Contents

Declaration I
Acknowledgement II
Abstract IV
List of Publications VII
Contents IX
Chapter 1: Introduction 1
1.1 Background 1
1.2 Research objectives 3
1.3 Thesis outline 4
1.4 References 6
Chapter 2: Literature Review 10
2.1 Introduction 10
2.2 Oxygen electrode/electrolyte interface 12
2.2.1 Effects of high temperature sintering 12
2.2.2 Effects of polarization 14
2.2.3 Interfacial reactions and micropore formation 26
2.2.4 Element segregation and diffusion 30
2.3 Hydrogen electrode/electrolyte interfaces 36
2.3.1 High temperature sintering effect 36
2.3.2 Polarization effect 38
2.3.3 Interface modification 41
2.4 Interface characterization Techniques 43
2.4.1 Focused Ion Beam 43
2.4.2 Raman spectroscopy 50
2.4.3 X-ray photoelectron spectroscopy 51
2.4.4 X-ray nano-computed tomography 52
2.4.5 Atomic force microscopy 52
2.5 Conclusions 53
2.6 References 54

Chapter 3: Experimental 71
3.1 Powder synthesis 71
3.1.1 $La_{0.8}Sr_{0.2}MnO_3$ 71
3.1.2 $La_{0.6}Sr_{0.4}Co_{0.2}Fe_{0.8}O_{3-\delta}$ 71
3.1.3 $Er_{0.4}Bi_{1.6}O_3$ decorated $La_{0.6}Sr_{0.4}Co_{0.2}Fe_{0.7}Nb_{0.1}O_{3-\delta}$ 71
3.2 Fuel cell fabrication 73
3.2.1 Electrolyte supported cell 73
3.2.2 Anode supported cell 74
3.3 Characterisation 75
3.3.1 Electrochemical characterisation 75
3.3.2 X-ray diffraction (XRD) 76
3.3.3 Scanning electron microscopy (SEM) 77
3.3.4 Atomic force microscopy (AFM) 78
3.3.5 Transmission electron microscopy (TEM) 79
3.3.6 Focused ion beam (FIB) 80
Chapter 4: A FIB-STEM Study of $La_{0.8}Sr_{0.2}MnO_3$ Cathode and Y_2O_3-ZrO_2/Gd_2O_3-CeO_2 Electrolyte Interfaces of Solid Oxide Fuel Cells 82
Abstract 82
4.1 Introduction 82
4.2 Experimental 84
4.3 Results and Discussion 86
4.3.1. Thermal compatibility between LSM and YSZ and GDC electrolytes 86
4.3.2 Electrochemical performance of LSM/YSZ and LSM/GDC 87
4.3.3 Microstructure of contact rings 88
4.3.4 LSM/YSZ interface 90
4.3.5 LSM/GDC interface 96
4.4 Conclusion 100
4.5 References 101
Chapter 5: A FIB-STEM Study of Strontium Segregation and Interface Formation of Directly Assembled $La_{0.6}Sr_{0.4}Co_{0.2}Fe_{0.8}O_{3-\delta}$ Cathode on Y_2O_3-ZrO_2 Electrolyte of Solid Oxide Fuel Cells 107

Abstract 108
5.1 Introduction 108
5.2 Experimental 110
5.2.1 Fabrication of electrolyte supported cells and directly assembled electrode 110
5.2.2 Characterization 111
5.3 Results and Discussion 112
5.3.1 Thermal compatibility and electrochemical performance 112
5.3.2 Microstructure of directly assembled LSCF/YSZ interfaces 113
5.3.3 LSCF/YSZ interfaces after polarization for 1 h 116
5.3.4 LSCF/YSZ interfaces after polarization for 12 h 119
5.3.5 LSCF/YSZ interfaces polarised for 100 h 124
5.3.6 Effect of polarization on Sr segregation and LSCF/YSZ interface formation 129
5.4 Conclusion 132
5.5 References 132
Chapter 6: Interface Formation and Mn Segregation of Directly Assembled $La_{0.8}Sr_{0.2}MnO_3$ Cathode on Y_2O_3-ZrO_2 and Gd_2O_3-CeO_2 Electrolytes of Solid Oxide Fuel Cells 142
Abstract 142
6.1 Introduction 142
6.2 Experimental 144
6.2.1. Fabrication of direct assembled LSM electrode on YSZ or GDC electrolyte 144
6.2.2. Characterization 145
6.3 Results and Discussion 146
6.3.1 Electrochemical performance of directly assembled LSM/YSZ and LSM/GDC electrodes 146
6.3.2 Microstructure of the polarization induced interface 147
6.3.3 LSM/YSZ interface 151
6.3.4 LSM/GDC interface 154
6.3.5 Effect of polarization on the interface formation and Mn segregation 157

6.4 Conclusion 162

6.5 References 163

Chapter 7: In situ Formation of $Er_{0.4}Bi_{1.6}O_3$ Protective Layer at Cobaltite Cathode/Y_2O_3-ZrO_2 Electrolyte Interface under Solid Oxide Fuel Cells Operation Conditions 170

Abstract 170

7.1 Introduction 171

7.2 Experimental 174

7.2.1 Synthesis and fabrication of ESB decorated LSCFNb cathode and anode-supported cell 174

7.2.2 Characterization 175

7.3 Results and Discussion 176

7.3.1. Thermal compatibility and microstructure of cathode powder and cell 176

7.3.2. Electrochemical performance and microstructure of electrode/electrolyte interface 177

7.3.3. LSCFNb/YSZ interface 181

7.3.4. ESB-LSCFNb/YSZ interface 183

7.3.5. Effects of polarization on Sr segregation and ESB-LSCFNb/YSZ interface formation 186

7.4 Conclusions 188

7.5 References 189

Chapter 8: Conclusions and Recommendations 196

8.1 Conclusions 196

8.2 Recommendations 199

Appendix: Permission of Reproduction from the Copyright Owner 201

Chapter 1: Introduction

1.1 Background

Energy and environment issues are currently the most important matters in the world [1-3]. At the moment, the fossil fuels are still considered the primary energy sources that meet the increased energy consumption of the human society. However, as the human civilisation keeps advancing rapidly, the limited fossil fuel reserves will be soon failing to cope with the increasing demand of human society. The sustainable development of the human civilisation will be critically challenged if the energy crisis cannot be addressed properly. On the other hand, the mass combustion of fossil fuels brings serious issues that greatly pollute the environment. It is widely accepted that burning fossil fuels inevitably contributes to the increase of the carbon dioxide level in the atmosphere, which would cause greenhouse effect, i.e. global warming crisis. The pollutant produced by combusting the fossil fuels also includes hazardous gases such as nitric oxide (e.g. NO, NO_2), sulphur oxide (e.g. SO_2, SO_3), etc., which are the main contributors to the low air quality, ozone layer depletion, large scale of acid rain and the destruction of natural ecosystem. Therefore, the development of clean energy technology as well as utilising the conventional fossil fuels with significantly higher efficiency are becoming essential strategic issues that attract extensive attention in almost every country [4-7].

Fuel cells are considered one of the most promising clean energy technologies that directly convert the chemical energy of fuels like hydrogen, natural gas and other carbohydrates into electricity with high efficiency, low pollution and good fuel flexibility as compared to the conventional internal combustion engine [8-10]. Theoretically, fuel cells can continuously generate electricity and heat if sufficient fuel and oxygen are constantly supplied. Depending on the type of electrolyte materials, fuel cells can be divided into five different categories: (1) polymer exchange membrane fuel cell (PEMFC), (2) alkaline fuel cell, (3) solid oxide fuel cell (SOFC), (4) phosphorous acid fuel cell and (5) molten carbonate fuel cell (MCFC) [11-14]. Among all kinds of fuel cells, SOFCs show distinctive advantages over the other fuel cells. SOFCs use ionic conducting materials (oxygen ion or proton conductors) as electrolyte and are all ceramic components devices. The typical operating temperature

for SOFCs is in the range of 500-1000 ^{o}C, and such high temperature greatly decreases the energy barrier for the electrode reactions, enabling the utilisation of non-precious metal catalysts. Most importantly, due to the high operating temperature and using ionic conducting electrolyte, all types of fuels can be electrochemically oxidised in the anode of a SOFC device, theoretically[15]. Figure 1.1 shows the schematic diagram of a typical SOFC device. A SOFC device consists of anode, electrolyte and cathode, and oxygen reduction reaction occurs at the cathode side, forming O^{2-}, which then transports through the dense oxygen ion conducting electrolyte to the anode side, and reacts with the fuels such as hydrogen or hydrocarbons, producing water, carbon dioxide, heat and electricity. The chemical to electrical conversion efficiency of a SOFC device can reach 60-70% when combined with heat and power applications, and also it can be used in large-scale stationary power generation industry [16, 17].

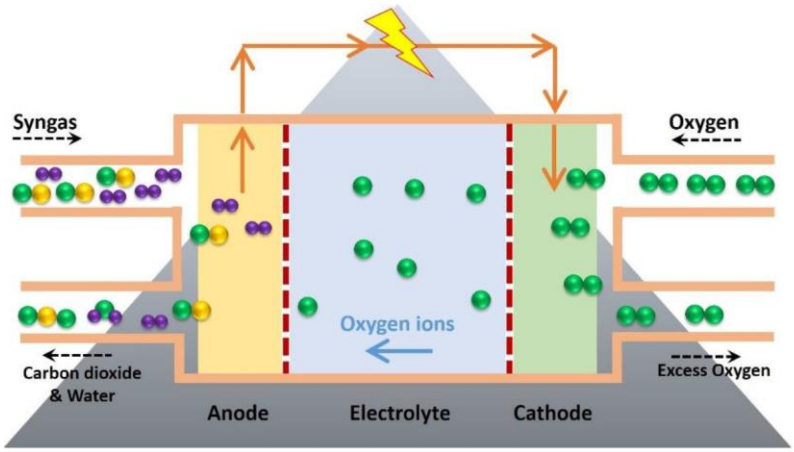

Figure 1.1 Schematic diagram showing the operating principle of a typical SOFC

The performance of a SOFC device strongly relies on the activity of the electrochemical reactions occurred at the electrode/electrolyte interface, and therefore the electrode/electrolyte interface plays a critical role in determining the overall performance and durability of SOFCs [18-20]. The electrode/electrolyte interface of SOFCs is generally formed by high temperature sintering, e.g. ~1150 ^{o}C for $La_{0.8}Sr_{0.2}MnO_3$ (LSM) cathode and yttrium stabilised zirconia (YSZ) electrolyte. In the case of LSM/YSZ cell, the electrolyte surface morphology is significantly changed after high temperature pre-sintering, forming a large amount of convex contact rings. These rings act as three phase boundary (TPB), where cathode, electrolyte and O_2 meet. In addition, the polarization also greatly impacts the electrode/electrolyte interface under the normal fuel cell operation conditions, causing the microstructure change of

the interface [21-24]. However, although tremendous amount of efforts have been made to examine and modify the electrode/electrolyte interface, there appears no systematic investigations on the fundamental mechanism of the interface evolution at various conditions, particularly in the aspects of composition, microstructure and crystallography. Moreover, our group has recently developed a novel cathode direct assembly method, which means the cathode can be directly applied onto the electrolyte without further high temperature sintering, and the electrode/electrolyte interface is formed by electrochemical polarisation [25-27]. Initial studies show that the electrochemical performance of the directly assembled cell is comparable to that of high temperature pre-sintered cell, and the electrolyte surface is characterised by the formation of contact clusters after polarisation, as compared to the convex rings formed after high temperature pre-sintering. The direct assembly method opens a new platform for the investigation of the fundamental mechanism governing the surface segregation, electrode/electrolyte interface formation, and interfacial reaction of cathode under SOFC polarisation conditions. The fundamental understanding of the electrode/electrolyte interface formation under the influence of polarisation has significant implications for the future design and development of SOFC technologies.

1.2 Research objectives

The main objective of this thesis is to understand the fundamental mechanism underneath the evolution of electrode/electrolyte and the intrinsic relationship between the segregation, interface formation, and interfacial reactions under the influence of cathodic polarization in solid oxide fuel cells, using both pre-sintering and directly assembled electrodes. The detailed aims of this study are summarised as follows.

1. Establishing an effective characterisation system using combined FIB-STEM techniques to study the electrode/electrolyte interfaces.
2. Investigating the most common and typical cathode/electrolyte interface induced by high temperature sintering regarding its microstructural, compositional and crystallographic changes, including $La_{0.8}Sr_{0.2}MnO_3$ (LSM)/Y_2O_3-ZrO_2 (YSZ), LSM/Gd_2O_3-CeO_2 (GDC), $La_{0.6}Sr_{0.4}Co_{0.2}Fe_{0.8}O_3$ (LSCF)/YSZ and $La_{0.6}Sr_{0.4}Co_{0.2}Fe_{0.8}Nb_{0.1}O_3$-$Er_{0.4}Bi_{1.6}O_3$ (LSCFNb-ESB) /YSZ interfaces.

3. Examining the most common and typical cathode/electrolyte interface induced by polarisation via directly assembled technique, and identifying the effects of polarization on the interface formation, surface segregation and chemical reaction.
4. Applying the directly assembled cathode onto anode-supported YSZ electrolyte cells and investigating the influence of cathodic polarization on its power output, stability and impedance.
5. Investigating the phase change and distribution of the bismuth oxide decorated cobaltite cathode on YSZ electrolyte, and examining its effect on the performance and stability of the interface under the influence of polarization.

1.3 Thesis outline

This thesis contains eight chapters. The first chapter gives an introduction on the background of the study as well as the outline of the thesis. Chapter 2 summarises the relevant recent literature and the research progress in relation to the main topic of this study. Chapter 3 presents detailed experimental methods adopted in this thesis, including the cell fabrication and characterisation. Chapter 4-7 are the results and discussion sections, showing the detailed research findings. In Chapter 8, conclusions of this thesis are drawn and perspectives for the future studies are proposed as well.

Chapter 1: Introduction

This chapter explains the research background, significance and challenges remained to understand the evolution of electrode/electrolyte interfaces. It justifies the adoption of direct assembly method in fuel cell fabrication and presents the significance of this concept. The research objectives and thesis outlines are also presented in this chapter.

Chapter 2: Literature Review

A comprehensive review of recent research progress on the electrode/electrolyte interfaces is summarised. The studies in element segregation, interfacial reaction, cation diffusion and interface modification at cathode/electrolyte and anode/electrolyte interfaces are thoroughly reviewed, and the commonly used techniques for interface examination are summarised.

Chapter 3: Experimental

This chapter presents the details of the experimental methods adopted in the thesis, including the synthesis of electrode and electrolyte materials, fabrication of fuel cells, electrochemical characterisation, combined FIB-STEM techniques and other characterisation methods.

Chapter 4: A FIB-STEM Study of $La_{0.8}Sr_{0.2}MnO_3$ Cathode and Y_2O_3-ZrO_2/Gd_2O_3-CeO_2 Electrolyte Interfaces of Solid Oxide Fuel Cells

The high temperature pre-sintered cathode/electrolyte interfaces are discussed in this chapter. The electrolyte surface microstructure is characterised by the formation of considerable number of convex rings after sintering. The cation diffusion (Mn^{2+}, La^{3+}) is observed in the rings as well as along the grain boundary of YSZ electrolyte, however, there is no element deposition detected in GDC electrolyte. The intimate cathode/electrolyte interfaces are identified by the lattice plane matching without forming cracks or amorphous phases. The lattice distortion is observed in the vicinity of the interface, as a result of accommodating lattice mismatch of the cathode and electrolyte.

Chapter 5: A FIB-STEM Study of Strontium Segregation and Interface Formation of Directly Assembled $La_{0.6}Sr_{0.4}Co_{0.2}Fe_{0.8}O_{3-\delta}$ Cathode on Y_2O_3-ZrO_2 Electrolyte of Solid Oxide Fuel Cells

The evolution of LSCF/YSZ interfaces under the influence of cathodic polarization is thoroughly investigated. The LSCF cathode is directly assembled onto the YSZ electrolyte, free of barrier layer and high temperature pre-sintering. The effects of cathodic polarization on the LSCF/YSZ interfaces are studied at different stages. At the initial stage of cathodic polarization, the intimate LSCF/YSZ interface is formed, clean and free of voids, accompanied by the improvement of electrochemical performance. It is found that prolonged polarisation induces the Sr segregation and its subsequent reaction with YSZ electrolyte, forming $SrZrO_3$ layer at low temperature. The electrochemical performance of the cell then experiences a gradual decrease.

Chapter 6: Interface Formation and Mn Segregation of Directly Assembled $La_{0.8}Sr_{0.2}MnO_3$ Cathode on Y_2O_3-ZrO_2 and Gd_2O_3-CeO_2 Electrolytes of Solid Oxide Fuel Cells

This chapter continues to use the FIB-STEM techniques to study the effect of polarization on the interface formation of directly assembled LSM/YSZ and LSM/GDC. The initial polarization also induces the formation of intimate cathode/electrolyte interfaces, and the disintegration of LSM cathode particles at the interface is observed for LSM/YSZ after long term polarization, whereas the LSM/GDC cell is more stable. The YSZ electrolyte surface morphology is changed largely after the polarization, forming a great number of contact craters, while the change of GDC surface is significantly smaller. In addition, the Mn segregation is observed after cathodic polarization regardless of the electrolyte material, and Mn does not preferentially segregate towards the electrode/electrolyte interface.

Chapter 7: In Situ Formation of $Er_{0.4}Bi_{1.6}O_3$ Protective Layer at Cobaltite Cathode/Y_2O_3-ZrO_2 Electrolyte Interface under Solid Oxide Fuel Cells Operation Conditions

In this chapter, the cathode direct assembly method is applied to anode-supported YSZ electrolyte cells, and the cathode is decorated by erbium stabilised bismuth oxide (ESB, $Er_{0.4}Bi_{1.6}O_3$). The electrochemical performance is significantly improved after ESB decoration, and the activation energy of the pristine cobaltite is reduced by half. In addition, the cathode/electrolyte interface stability is greatly enhanced by the ESB decoration. Further microstructural analysis reveals that ESB migrates to the interface under the influence of cathodic polarization, forming a protective layer. Such ESB layer effectively suppresses the Sr segregation and its subsequent reaction with YSZ electrolyte, thus greatly improving the cathode/electrolyte interface stability.

Chapter 8: Conclusions and Recommendations

The main achievements of this thesis are highlighted in this chapter and recommendations are proposed for future studies in this research area.

1.4 References

[1] A.M. Omer, Energy, environment and sustainable development, Renewable and Sustainable Energy Reviews, 12 (2008) 2265-2300.
[2] L. Shi, M.Y.L. Chew, A review on sustainable design of renewable energy systems, Renewable and Sustainable Energy Reviews, 16 (2012) 192-207.

[3] T.A. Faunce, W. Lubitz, A.W. Rutherford, D. MacFarlane, G.F. Moore, P. Yang, D.G. Nocera, T.A. Moore, D.H. Gregory, S. Fukuzumi, K.B. Yoon, F.A. Armstrong, M.R. Wasielewski, S. Styring, Energy and environment policy case for a global project on artificial photosynthesis, Energy & Environmental Science, 6 (2013).

[4] Z.L. Wang, Triboelectric nanogenerators as new energy technology for self-powered systems and as active mechanical and chemical sensors, ACS Nano, 7 (2013) 9533-9557.

[5] A. Cheon, J. Urpelainen, Oil prices and energy technology innovation: An empirical analysis, Global Environmental Change, 22 (2012) 407-417.

[6] Q. Cui, H.-b. Kuang, C.-y. Wu, Y. Li, The changing trend and influencing factors of energy efficiency: The case of nine countries, Energy, 64 (2014) 1026-1034.

[7] S. Hossain, A.M. Abdalla, S.N.B. Jamain, J.H. Zaini, A.K. Azad, A review on proton conducting electrolytes for clean energy and intermediate temperature-solid oxide fuel cells, Renewable and Sustainable Energy Reviews, 79 (2017) 750-764.

[8] N. Mahato, A. Banerjee, A. Gupta, S. Omar, K. Balani, Progress in material selection for solid oxide fuel cell technology: A review, Progress in Materials Science, 72 (2015) 141-337.

[9] S. Wang, S.P. Jiang, Prospects of Fuel Cell Technologies, National Science Review, 4 (2017) 163-166.

[10] N. Mohammad, A.B. Mohamad, A.A.H. Kadhum, K.S. Loh, A review on synthesis and characterization of solid acid materials for fuel cell applications, Journal of Power Sources, 322 (2016) 77-92.

[11] Y.J. Wang, D.P. Wilkinson, J. Zhang, Noncarbon support materials for polymer electrolyte membrane fuel cell electrocatalysts, Chem Rev, 111 (2011) 7625-7651.

[12] T.M. Gur, Critical review of carbon conversion in "carbon fuel cells", Chem Rev, 113 (2013) 6179-6206.

[13] BCH Steele, A. Heinzel, Materials for fuel-cell technologies, Nature, 414 (2001) 345-352.

[14] M. Winter, R.J. Brodd, What Are Batteries, Fuel Cells, and Supercapacitors?, Chemical Reviews, 104 (2004) 4245-4270.

[15] T.M. Gür, Comprehensive review of methane conversion in solid oxide fuel cells: Prospects for efficient electricity generation from natural gas, Progress in Energy and Combustion Science, 54 (2016) 1-64.

[16] S.C. Singhal, Solid oxide fuel cells for power generation, Wiley Interdisciplinary Reviews: Energy and Environment, 3 (2014) 179-194.
[17] T. Elmer, M. Worall, S. Wu, S. Riffat, Assessment of a novel solid oxide fuel cell tri-generation system for building applications, Energy Conversion and Management, 124 (2016) 29-41.
[18] M.J. Jørgensen, P. Holtappels, C.C. Appel, Durability test of SOFC cathodes, Journal of Applied Electrochemistry, 30 (2000) 411-418.
[19] H. Fukunaga, The relationship between overpotential and the three phase boundary length, Solid State Ionics, 86-88 (1996) 1179-1185.
[20] Y.L. Liu, A. Hagen, R. Barfod, M. Chen, H.J. Wang, F.W. Poulsen, P.V. Hendriksen, Microstructural studies on degradation of interface between LSM–YSZ cathode and YSZ electrolyte in SOFCs, Solid State Ionics, 180 (2009) 1298-1304.
[21] S.P. Jiang, W. Wang, Effect of Polarization on the Interface Between (La,Sr)MnO3 Electrode and Y2O3-ZrO2 Electrolyte, Electrochemical and Solid-State Letters, 8 (2005) A115.
[22] T. Matsui, M. Komoto, H. Muroyama, K. Eguchi, Interfacial Stability between Air Electrode and Ceria-Based Electrolyte under Cathodic Polarization in Solid Oxide Fuel Cells, Fuel Cells, 14 (2014) 1022-1027.
[23] F. Wang, M.E. Brito, K. Yamaji, D.-H. Cho, M. Nishi, H. Kishimoto, T. Horita, H. Yokokawa, Effect of polarization on Sr and Zr diffusion behavior in LSCF/GDC/YSZ system, Solid State Ionics, 262 (2014) 454-459.
[24] Y.L. Liu, K. Thydén, M. Chen, A. Hagen, Microstructure degradation of LSM-YSZ cathode in SOFCs operated at various conditions, Solid State Ionics, 206 (2012) 97-103.
[25] K. Chen, N. Li, N. Ai, M. Li, Y. Cheng, W.D.A. Rickard, J. Li, S.P. Jiang, Direct application of cobaltite-based perovskite cathodes on the yttria-stabilized zirconia electrolyte for intermediate temperature solid oxide fuel cells, J. Mater. Chem. A, 4 (2016) 17678-17685.
[26] S.P. Jiang, Thermally and Electrochemically Induced Electrode/Electrolyte Interfaces in Solid Oxide Fuel Cells: An AFM and EIS Study, Journal of The Electrochemical Society, 162 (2015) F1119-F1128.
[27] N. Li, N. Ai, K. Chen, Y. Cheng, S. He, M. Saunders, A. Dodd, A. Suvorova, S.P. Jiang, In situ assembled La0.8Sr0.2MnO3 cathodes on a Y2O3–ZrO2 electrolyte of

solid oxide fuel cells – interface and electrochemical activity, RSC Adv., 6 (2016) 99211-99219.

Chapter 2: Literature Review

2.1 Introduction

Solid oxide fuel cells (SOFCs) are regarded as one of the most promising energy-conversion devices for sustainable and green energy development [1-6]. SOFCs consist of all-ceramic components and do not require precious-metal catalysts as a result of their high operating temperatures (typically 800~1000 ^{o}C). SOFCs are an efficient alternative to the conventional combustion technology for electricity generation, and one of the biggest advantages is their good fuel flexibility, including H_2, methanol, ethanol, natural gas and hydrocarbons [7-10]. SOFCs are particularly suitable for distributed power-supply and stationary applications with their good scalability, which is realised by assembling individual SOFCs into stacks, with the power ranging from a few kilowatts up to several megawatts [11-13]. The major challenges in SOFCs include the high operation temperature related issues, stack durability and thermal cycle capability [14-17]. For a given electrode/ electrolyte material system (e.g. LSM/YSZ), its performance is greatly determined by the electrode processes, such as charge transfer and mass transport. The mass transport process is strongly influenced by the micro- and macrostructural features of the entire electrode, while the charge transfer process, often the rate-determining step at reduced operating temperature, largely depends on the electrocatalytic activity and microstructure of the electrode/electrolyte interface. The electrochemically active interface region often extends a few micrometers from the electrolyte to the electrode, and plays essential role in terms of the performance and durability of SOFCs. Despite the significance of the electrode/electrolyte interface, there appears to be no comprehensive review on its fundamental issues and current development. In this chapter, studies relating to the failure mechanism and the evolving microstructure of the interface as well as the commonly adopted characterisation techniques are thoroughly reviewed.

The evolution of the interface upon ageing or regeneration often presents a dynamic and intricate structure [18], and though conventionally the changing electrode/electrolyte interface is considered to be detrimental in terms of the cell durability, it has recently been reported that the evolving interface can also be

beneficial to the enhancement of cell stability and performance. The typical change in interface, particularly its microstructure, can be contributed to interfacial reaction [19, 20], micropore formation [21, 22], element segregation and diffusion [23, 24], delamination [25, 26], impurity contamination [27, 28] and intimate interface establishment. These phenomena occurred at the electrode/electrolyte interface noticeable impacts the electrochemical performance of the cell. For example, the interfacial reaction between LSCF cathode and YSZ electrolyte increases the interfacial resistance, as a result of forming insulating layers like $SrZrO_3$ and $La_2Zr_2O_7$ [29-32]. On the other hand, it was also reported that the interfacial reaction between Ni-BZCY anode and ceria electrolyte promotes the formation of a $BaCeO_3$ layer at the interface, preventing the electronic current leakage across the ceria electrolyte and thus improving the performance of the cell [33]. In addition, the element segregation at the interface like Sr segregation from LSCF electrode due to cation size mismatch is often considered to be one of the main reasons for cell degradation [34, 35], but in the case of Mn^{2+} diffusion and migration at the LSM/YSZ interface, it was suggested to be beneficial to the charge transfer process [36]. Moreover, the micropore formation at the interface during long term operation, the delamination of bilayered electrolyte structure and impurity contamination like SiO_2 accumulation and Cr poisoning at the interface are regarded as the most problematic issues that cause the performance deterioration of SOFC devices.

This review is outlined into three sections. The first part reviews the cathode/electrolyte interfaces. For example, the influence of high temperature and polarisation on the interface microstructure and the correlation between interface morphology and cell performance were discussed with respect to the current research progress. The second part summarises the studies focusing on the evolution of anode/electrolyte interface in recent years. The last section discusses the common techniques employed to investigate the electrode/electrolyte interface behaviour under different test environment, such as focused ion beam (FIB), scanning transmission electron microscopy (STEM), atomic force microscopy (AFM) and secondary ion mass spectroscopy (SIMS) etc.

2.2 Oxygen electrode/electrolyte interface

2.2.1 Effects of high temperature sintering

SOFCs are all ceramic components devices and typically, a SOFC cell consists of yittria-stabilized zirconia (YSZ) electrolyte and perovskite cathode, e.g. $La_{0.8}Sr_{0.2}MnO_3$ (LSM). Due to the nature of ceramic components in SOFCs, the high temperature pre-sintering process is generally considered necessary in order to form intimate electrode/electrolyte interface, e.g. ~1150^{o}C in the case of LSM/YSZ cell or ~900^{o}C for LSCF/GDC cell [37-39]. The cathode/electrolyte interface formed during high temperature sintering is generally identified by the formation of a large number of convex contact rings on the electrolyte surface[21, 22, 40-42]. In the case of LSM cathode, since it is predominantly an electronic conductor with negligible oxygen ionic conductivity, the oxygen reduction reaction primarily occurs at the three phase boundary (TPB), where O_2, LSM and electrolyte meet. The formation of TPB provides a direct pathway for oxygen ions migration, and thus is critical in determining the overall cell performance and durability [43, 44]. The correlation between TPB and the electrochemical performance of the cell has been extensively studied in recent years due to its unique positions in the fundamental understanding of oxygen reduction reaction kinetics and mechanism.

Fukunaga et al [43] investigated the relationship between the cell overpotential and the TPB length by model construction. The pure LSM and LSM-YSZ composite cathode materials were adopted, since the TPB of pure LSM only exists at the LSM/YSZ interface, while the TPB of the composite exists not only on the interface but also in the electrode itself. The TPB length was measured by multiplying the average length of the cathode particle at the interface with the number of particles per unit area. The results suggested a three-dimensional distribution of TPB in LSM-YSZ composite cathode, which contributes to the significant reduction of cell overpotential. Horita et al [45] studied the influence of heat treatment on microstructure and the oxygen diffusion at $LaMnO_3$ film/YSZ interface using ^{18}O. After the heat treatment, the TPB region was characterized by the formation of convex parts of the YSZ surface, and the manganese concentration was found to be higher in these convex parts, while at the $LaMnO_3$/YSZ two phase boundary, the interface is very clear without any defects (Figure 2.1). The height difference of the electrolyte surface is about 50 nm after the

heat treatment, and the authors proposed that the change in microstructure is caused by the cation inter-diffusion. Moreover, the concentration of ^{18}O was found the highest at the convex part of the YSZ surface, indicating that the oxygen incorporation mainly occurs at the convex parts, i.e. the TPB region.

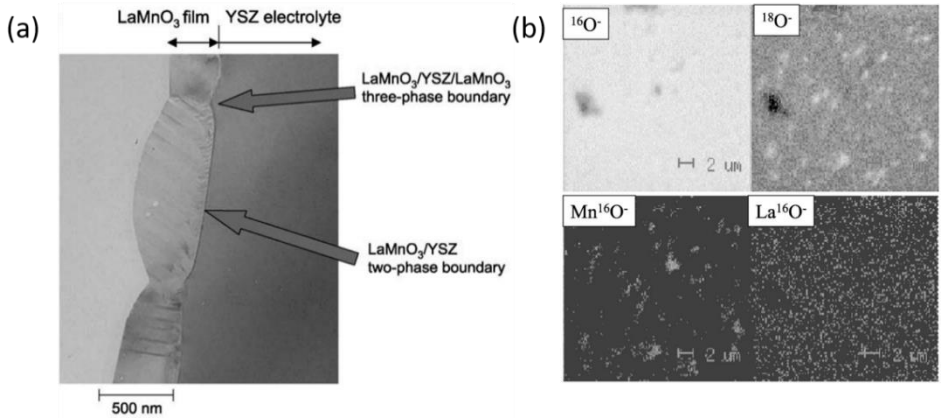

Figure 2.1 (a) TEM image of the cross-section at the $LaMnO_3$ film interface after heat-treated at 1473 K for 5 h. (b) SIMS images of YSZ surface after removing the covered $LaMnO_3$ film [45].

The high temperature sintering process also further complicates the interface between cathode and electrolyte as a result of the reactivity and cation inter-diffusion between electrode and electrolyte. A. Mitterdorfer [46] studied the $La_2Zr_2O_7$ (LZO) formation at the LSM/YSZ interface as a function of manganese concentration in the perovskite at 1373 K. The surface topography was found dominated by evenly distributed rings, and the thickness as well as the height of the ring increase quickly with increasing sintering time. After prolonged sintering time (>4 h), cube-shaped LZO islands were observed on top of the zirconia rings (Figure 2.2). The presence of LZO drastically influences the oxygen reduction properties of the electrochemical interfaces, and the polarization resistance (Rp) increases markedly after the sintering process at 1373 K in air. The authors also reported that the TPB length of LSM/YSZ interfaces reaches its maximum value (~$5*10^6$ m/m^2) after 30 min of sintering, and with increasing sintering time, the TPB length decreases.

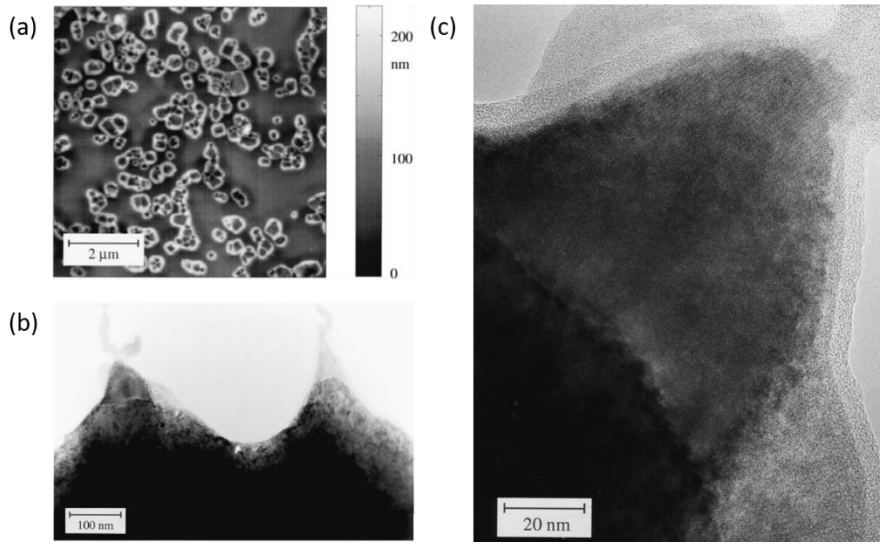

Figure 2.2 (a) AFM image of YSZ surface after sintering with LSM cathode. (b) Bright-field TEM of cross section of ring-shaped island. (c) HRTEM of the left tip shown in (b) [46].

2.2.2 Effects of polarization

2.2.2.1 Cathodic polarization

In SOFC, cathodic polarization is a phenomenon that the cathode potential shifts in the "negative" direction when the oxygen reduction reaction starts on the cathode side. Generally, oxygen diffusion and dissociative adsorption, oxygen ion migration at the interface and charge transfer processes will occur during the cathodic polarization. It has been well known that cathodic polarization has a significant effect on the interface microstructure and composition, e.g. interface formation, degradation, element diffusion and reaction [47-51]. Jiang et al [52] reported that the polarization has a significant effect on the morphology and topography of the TPB at the interface between LSM electrode and YSZ electrolyte. In this study, cathodic polarization was applied to pre-sintered LSM/YSZ cells at 200 mA cm^{-2} and 900^{o}C, and the sharp edge of the convex contact rings formed on the electrolyte during the high temperature sintering became broadened and flattened (Figure 2.3). The broadening and flattening of the convex rings reduce the surface energy and thus stabilizes the reaction sites at the interface. The significant topography change of the convex rings after cathodic polarization was proposed to be a result of the incorporation of oxygen and manganese and interdiffusion processes between LSM electrode and YSZ electrolyte, and the convex ring areas are most likely the reaction sites for ORR. Backhaus-Ricoult et al [36] adopted XPS technique to study the surface chemistry of LSM/YSZ interface after

the large cathodic polarization treatment. The Mn in LSM was found reduced to an oxidation state of 2^+ and enriched at the YSZ electrolyte surface. The high concentration of Mn was detected first at the TPB region, but then rapidly spread from the TPB over the entire YSZ electrolyte surface. The electronic conductivity in the Mn-rich surface region is found effectively high, and the electrochemical activation of LSM cathode under polarization was related to the extension of the active area for ORR from TPB to the entire activated electrolyte surface. Matsui et al [21] also investigated and compared the interfacial stability between LSM electrode/SDC electrolyte and LSCF electrode/SDC electrolyte under the influence of cathodic polarization. In the case of LSM cathode, the TPB length at the interface was increased after polarization, while for the LSCF/SDC cell, no appreciable change in interface structure was found regardless of polarization conditions. It was suggested that under the influence of cathodic current passage, the oxide ion conductivity of the cathode is responsible for the microstructural change at the interface. The polarization can also induce the chemical reaction between the electrode and electrolyte. Yung et al [53] studied the chemical compatibility of $Ba_{0.5}Sr_{0.5}Co_{0.8}Fe_{0.2}O_{3-\delta}$ (BSCF) with ceria based electrolytes under cathodic polarization conditions. It was found that Ba-containing particles, most likely barium cerate, were formed at the electrode/electrolyte interface under cathodic current passage at a temperature as low as 700^{o}C (Figure 2.4), and it was pointed out that such reaction only occurs at 900^{o}C without cathodic polarization. The accelerated reaction between BSCF and ceria was proposed to be related to Ba species segregation to the electrode/electrolyte interface and subsequently reacting with electrolyte under the influence of polarization.

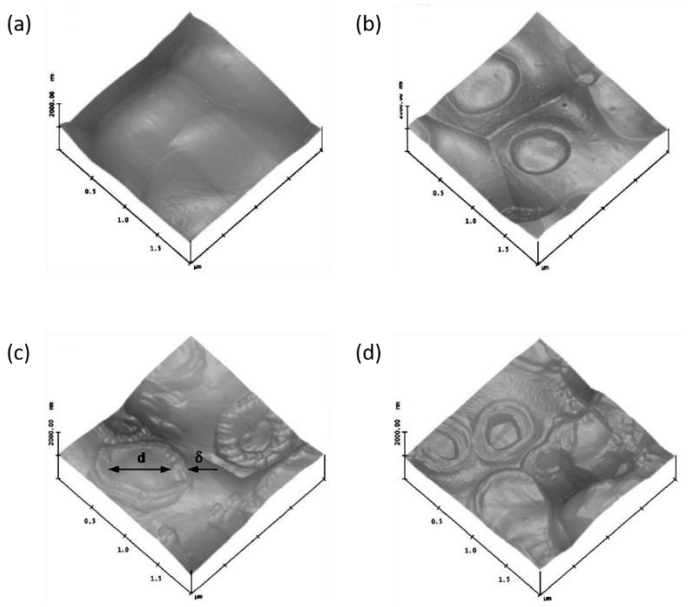

Figure 2.3 AFM images of (a) pure YSZ electrolyte surface and (b) YSZ electrolyte surface in contact with LSM coating before polarization treatment. YSZ surface in contact with LSM coating after (c) cathodic current treatment or (d) anodic current treatment for 3 h at 200 mA cm^{-2} and 800 ºC in air [52].

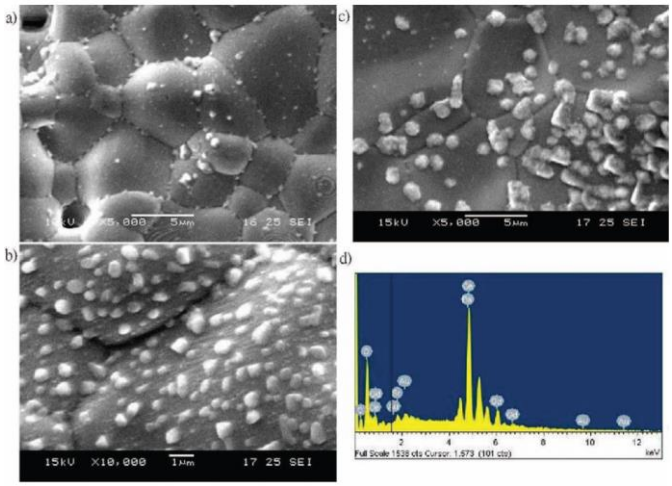

Figure 2.4 SEM images of the GDC electrolyte surface in contact with BSCF cathode. (a) as-prepared before polarization; (b) polarized at 200 mA cm^{-2} and 700 ºC for 20 h; (c) polarized at 400 mA cm^{-2} at 700 ºC for 20 h and, (d) EDX of the surface shown in (c) [53].

Moreover, it has been reported that cathodic polarization has a promotion effect on the element diffusion from the current collector to the electrode/electrolyte interface, noticeably changing the microstructure of the interface [54-63]. Simner et al [55] investigated the performance degradation of La(Sr)FeO_3 (LSF) cathode with three

kinds of current collectors, i.e. Pt, Ag and Au. For the cell with Pt and Ag current collectors, a noticeable migration/deposition of the respective noble metal after polarization was observed at the cathode/electrolyte interface, while no Au deposition was found when using Au as current collector (Figure 2.5). The use of Pt and Ag current collectors is accompanied by the improved cell performance and durability, and in the case of Au current collector, severe degradation was observed. It was proposed that the deposition of noble metal at the electrode/electrolyte interface can potentially catalyze the ORR as well as suppress the intrinsic degradation phenomenon of LSF electrode. Xiong et al [58] also reported the Pt deposition at TPB region of a LSM/ScSZ cell after cathodic polarization at 1073K. A considerable amount of Pt particles were observed only in the vicinity of TPB after a power generation test, and a rapid activation of the cathode performance was ascribed to the Pt deposition (Figure 2.6). Such activation behavior did not appear to the cell using Au current collector, as no Au particles were found at TPB. Yamaji et al [60] investigated the effect of polarization on Pt deposition at LSM/YSZ interface. In this study, fixed polarization voltage of -0.1 V or -0.3 V was applied to the cell at 1073 K. In the case of large polarization of -0.3 V, an abnormal rapid increment of cell performance was achieved, and Pt particles were found at the TPB regions around the LSM/YSZ interface. On the other hand, a normal slow increment of cell performance was observed at the small polarization of -0.1 V, and no Pt particles were deposited at the interface.

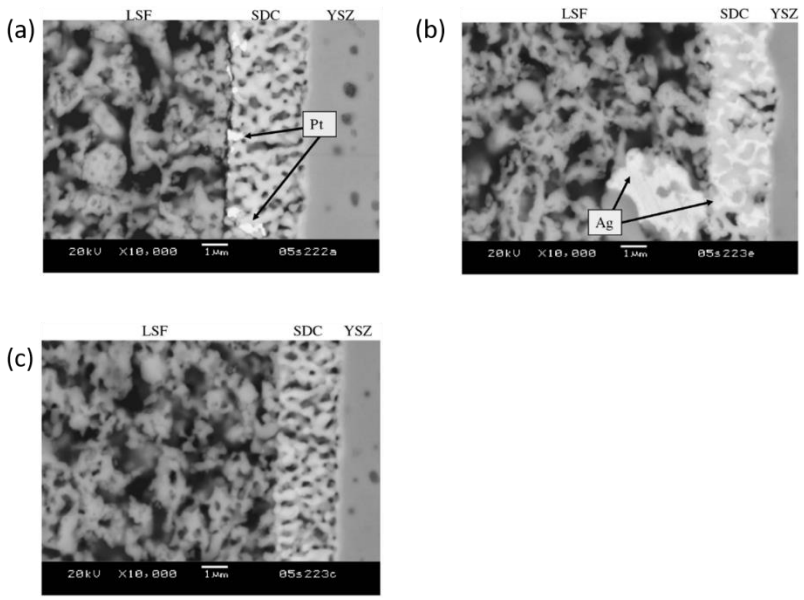

Figure 2.5 Backscattered SEM images of LSF/SDC/YSZ cell after test using (a) Pt, (b) Ag or (c) Au current collectors [55].

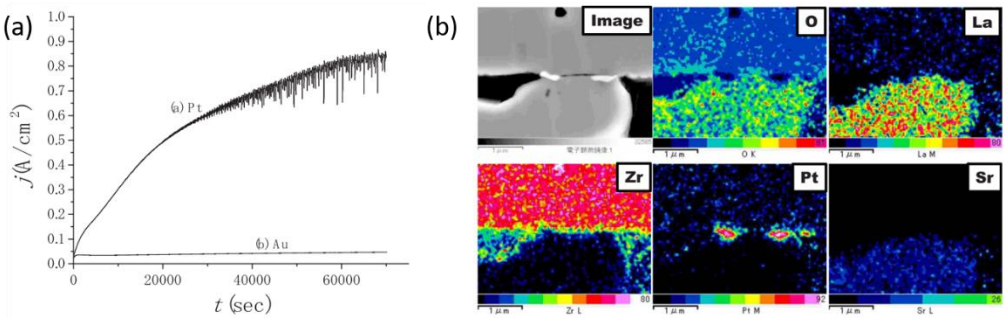

Figure 2.6 (a) Long-term current data on LSM cathodes using a platinum current collector or a gold current collector at a fixed potential of -0.5 V vs the air reference electrode at 1073 K. (b) Element mapping of the cross-section of LSM/ScSZ interface after the cell test using platinum current collector [58].

Most recently, we showed that cathodic polarization can induce the interface formation between the directly assembled electrode and electrolyte without requiring high temperature sintering [64]. Early study [51] shows that comparable electrode/electrolyte interfaces, e.g. LSM/YSZ or LSCF/GDC, were formed by high temperature sintering and cathodic polarization. The thermally induced interface was characterized by convex contact rings, while the electrochemically induced interface was identified by particle-shaped contact marks or clusters and their number and distribution greatly depend on the current density as well as the electrode/electrolyte materials (Figure 2.7). The electrocatalytic activities of the thermally and electrochemically induced interfaces for ORR are comparable and similar. It was suggested that the electrochemically induced interface is most likely due to the incorporation of oxygen species and cation inter-diffusion under the influence of polarization. The direct assembly method not only significantly reduces the fabrication steps for SOFCs but also make the utilization of cobaltite perovskite electrodes on YSZ electrolyte possible, as the elimination of high temperature sintering step avoids the chemical reaction between cobaltite electrodes and YSZ electrolyte. We have shown the feasibility of directly assembling LSCF, $(La_{0.6}Sr_{0.4})_{0.95}Co_{0.2}Fe_{0.7}Nb_{0.1}O_{3-\delta}$ (LSCFN), $(La_{0.6}Sr_{0.4})_{0.95}(Co_{0.2}Fe_{0.7}Nb_{0.1})_{0.95}Pd_{0.05}O_{3-\delta}$ (LSCFNPd), $La_{0.95}(Co_{0.2}Fe_{0.8})_{0.95}Pd_{0.05}O_{3-\delta}$ (LCFPd), $Sm_{0.95}Co_{0.95}Pd_{0.05}O_{3-\delta}$ (SmCPd), $PrBa_{0.5}Sr_{0.5}Co_{1.5}Fe_{0.5}O_{5+d}$ (PBSCF) electrodes on YSZ electrolyte with excellent performance [64-66]. For example, a cell with SmCPd-GDC composite cathode shows a high power output of 1.4 W cm^{-2} at 750 ^{o}C and is very stable at 500 mA cm^{-2} for 240 h. For LSCFN, LSCFNPd, LCFPd-GDC and SmCPd-GDC cathodes, contact marks in

the size range of 60-260 nm were observed on the YSZ electrolyte surface, and an initial decrease in ohmic resistance of the cell during polarization was observed for all electrode materials, which in turn implies the establishment of electrode/electrolyte interface under the cathodic current passage.

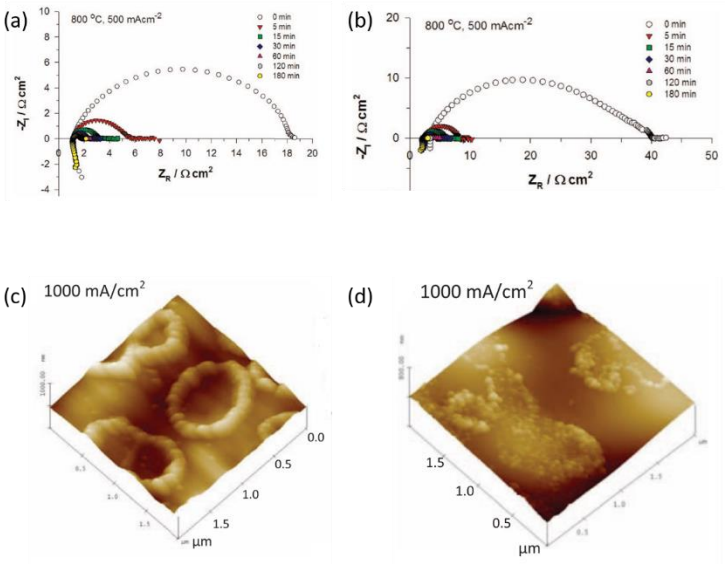

Figure 2.7 Impedance curves of (a) pre-sintered LSM cathode or (b) directly assembled LSM cathode on YSZ electrolyte as a function of cathodic polarization currents of 500 mA cm^{-2} at 800 ^{o}C. AFM micrographs of YSZ electrolyte surface morphology in contact with (c) pre-sintered or (d) directly assembled LSM cathode after polarization at 1000 mA cm^{-2} and 800 ^{o}C are also given [51].

2.2.2.2 Anodic polarization

When a SOC device is operated as an electrolysis cell, an anodic current passage will be applied to the oxygen electrode, and oxygen evolution reaction would occur at the anode/electrolyte interface [67-73]. Knibbe et al [74] examined degradation behavior of an electrolysis cell with LSM-YSZ composite oxygen electrode at high current density of 1, 1.5 and 2 A cm^{-2} and 850 ^{o}C. An ohmic resistance degradation was observed, and it became more pronounced with higher anodic current density. The degradation of the cell was attributed to the oxygen formation in the YSZ grain boundaries close to the oxygen electrode/electrolyte interface. A systematic study of the failure mechanism of LSM oxygen electrode in SOEC was reported by Chen et al [75]. The delamination behavior of LSM oxygen electrode was observed under anodic current passage of 500 mA cm^{-2} and 800 ^{o}C for 48 h, and this is accompanied by the significant increase in the electrode polarization and ohmic resistance. The

polarization behavior of the oxygen electrode was characterized by three stages, i.e. activation stage (~10 h), steady stage (~32 h) and degradation stage (~48 h). Before the anodic polarization, the LSM electrode was in intimate contact with the YSZ electrolyte, as indicated by the formation of convex contact rings on the electrolyte surface. After the polarization at 500 mA cm^{-2} for 48 h, a clear gap was observed at the interface between the LSM oxygen electrode and YSZ electrolyte, indicating the delamination of the LSM oxygen electrode. Moreover, a considerable amount of nanoparticle clusters was formed in the convex rings on the electrolyte. The formation of such nanoparticles was ascribed to the disintegration of LSM electrode under the influence of anodic polarization (Figure 2.8). The fundamental mechanism for the evident interface microstructure change and disintegration of the LSM particles was proposed as the nature of LSM electrode being a predominantly electronic conductor with negligible oxygen ionic conductivity, therefore the oxygen formed during OER must be evolved at the oxygen electrode/electrolyte interface via oxygen incorporation into LSM lattice. This in turn results in the cation vacancy formation and shrinkage of the LSM lattice, causing the local tensile strain in the LSM particles and eventually the disintegration of LSM. It was suggested that by adding highly oxygen ionic conductors, e.g. YSZ [76, 77], GDC [78-80] or Pd [81] nanoparticles, to the LSM oxygen electrode, the stability of the electrode/electrolyte interface under anodic polarization will be significantly enhanced.

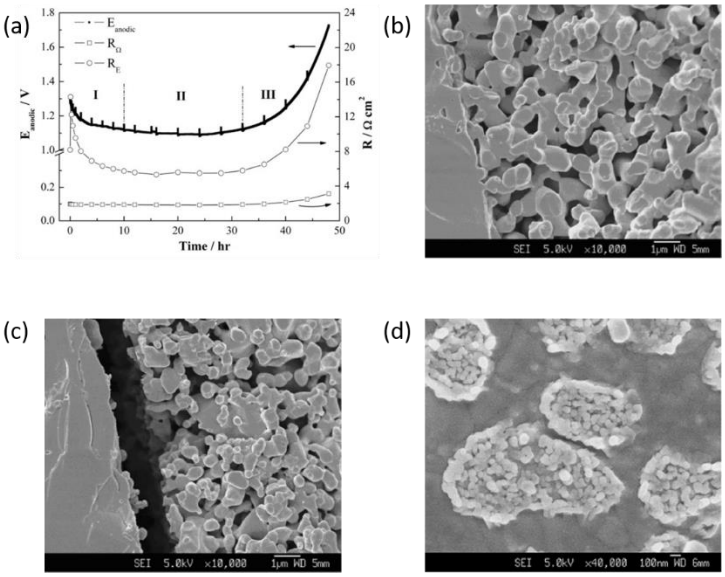

Figure 2.8 (a) Polarization curves for the oxygen evolution reaction on a freshly-prepared LSM oxygen electrode as a function of anodic current passage time at 500

mA cm^{-2} and 800 ^{o}C in air for 48 h. SEM images of (b) the cross-section of LSM/YSZ interface before polarization and (c) after anodic polarization at 500 mA cm^{-2} and 800 ^{o}C for 48 h. The YSZ electrolyte surface in contact with the LSM oxygen electrode after anodic polarization is also shown in (d) [75].

Kim et al [82] investigated the electrode/electrolyte durability of an LSCF oxygen electrode on YSZ electrolyte with or without a GDC interface under the influence of anodic polarization. The cell was tested at 800 ^{o}C with an anodic current density of 800 mA cm^{-2}. The LSCF/YSZ cell without an interlayer showed a large increase in ohmic resistance, from 0.09 Ω cm^2 to 0.16 Ω cm^2 after anodic polarization for 50 h, and the delamination between LSCF and YSZ was observed. In the case of the LSCF/YSZ cell with a GDC interlayer, the change in the ohmic resistance is negligible and the GDC/YSZ interface appeared to be very stable after the anodic polarization for 100 h. Moreover, the influence of anodic polarization on the Sr segregation as well as the LSCF oxygen electrode/YSZ electrolyte interface formation as a comparison to cathodic polarization was studied by Ai et al [83]. The LSCF oxygen electrode was directly assembled to the YSZ electrolyte without high temperature sintering, and it was found that anodic polarization effectively induces the formation of intimate electrode/electrolyte interface at 750 ^{o}C and 0.5 A cm^{-2}. The electrolysis cell showed an excellent stability under the anodic polarization for 300 h, as compared to the significant performance decay of the cell under the cathodic polarization. Further microstructural analysis revealed that although Sr segregation is inevitable for LSCF oxygen electrode, the anodic polarization significantly suppressed Sr segregation and migration to the electrode/electrolyte interface (Figure 2.9), leading to the formation of stable and efficient electrode/electrolyte interface for steam and CO_2 electrolysis under SOEC operation conditions.

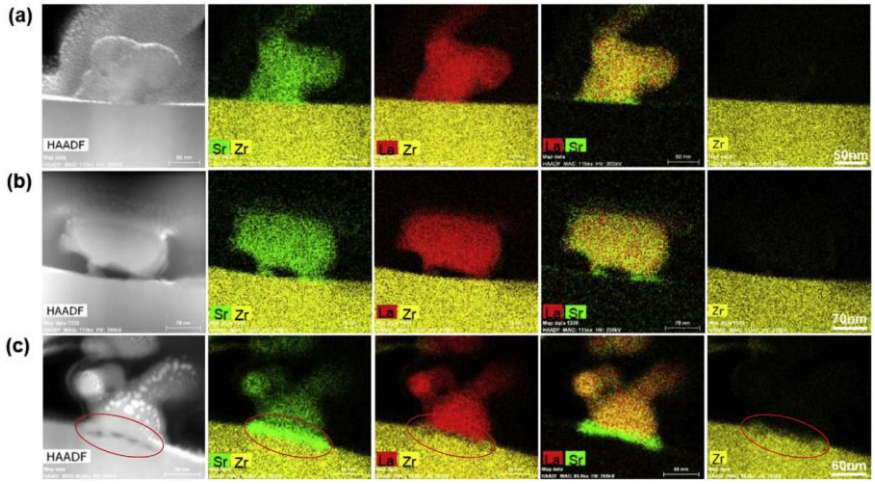

Figure 2.9 STEM-EDS element mapping of electrode/electrolyte interface of directly assembled LSCF electrode after polarization at 0.5 A cm^{-2} and 750 ^{o}C under (a) anodic current for 12 h, (b) anodic current for 40 h, and (c) cathodic current for 40 h [83].

Several models have been developed to better understand the main causes for the origin of the delamination at the oxygen electrode/electrolyte interface. The model proposed by Virkar et al [84] and Jacobsen et al [85] predicted that the oxygen electrode delamination occurs as a result of the accumulated high internal oxygen partial pressure, near the oxygen electrode/electrolyte interface. It was proposed that the detrimental oxygen pressure inside the closed pores and cavities in the electrolyte is a result of the different profile of electromotive and Galvani potentials in the case of anodic polarization. Under anodic polarization, the oxygen electrode is forced towards more positive potentials while the hydrogen electrode is driven towards more negative potentials, and as a consequence, the gradient in the electromotive potential between the anode and cathode is increased and more oxygen would be accumulated around the defects at the solid/solid interface [85]. In addition, Rashkeev et al [86] used a combination of first-principles, density-functional-theory (DFT) calculations and thermodynamic modeling to elucidate the main processes that contribute to the oxygen electrode/electrolyte interface delamination in typical SOEC device, e.g. LSM/YSZ cell. In order to estimate the oxygen gas pressure in a pre-existing interfacial void, a simple thermodynamic equation for the change of the pressure- and temperature-dependent Gibbs potential at the free YSZ electrolyte surface was given:

$$\Delta G(p,T) = E^{surface-2O^{2-}} - E^{O_2}_{mol} - E^{surface} + \mu^{(0)}_{O_2} + kT \cdot ln\frac{p_{O_2}}{p^{(0)}_{O_2}}, \quad (1)$$

where in the right hand side of the equation, the first three terms correspond to the O_2 formation energy at the surface, i.e. $E^{surface}$, $E^{surface-2O^{2-}}$ and $E_{mol}^{O_2}$ are calculated total energies for electrolyte surface without defects, surface with two oxygen vacancies and for a single oxygen molecule in vacuum, respectively; $\mu_{O_2}^{(0)}$ and $p_{O_2}^{(0)}$ are oxygen chemical potential and pressure at normal conditions, i.e. 1 atm; p_{O_2} is the partial pressure of the O_2 gas that is in an equilibrium condition with the YSZ electrolyte surface. It was found that the delamination processes at the electrode/electrolyte interface under anodic polarization should be significantly accelerated by high temperature metal cation inter-diffusion across the LSM/YSZ interface, i.e. La, Sr and Mn from LSM to YSZ, and Zr from YSZ to LSM. For instance, the La and Sr substitutional defects positioned in ZrO_2 oxide and near the LSM/YSZ interface significantly change oxygen transport, which could contribute to the pressure buildup in the interface region and ultimately develop delamination process under the influence of anodic polarization.

2.2.2.3 Cyclic anodic/cathodic polarization

The utilization of reversible solid oxide cell (SOC) system for energy storage and electricity regeneration is attracting increasing attention nowadays [87-92]. The SOCs is capable of operating in solid oxide electrolysis cell (SOEC) mode to store electricity generated by solar or wind power in the form of fuels like hydrogen, and then regenerate electricity using the stored fuels in solid oxide fuel cell (SOFC) mode. Therefore, the investigation on the influence of the cyclic anodic/cathodic polarization on oxygen electrode/electrolyte interface is critical and has been studied by many research groups.

However, the deterioration of the performance of the oxygen electrode as well as the electrode/electrolyte interface under SOEC operating mode, i.e. anodic polarization, is the most critical issue that greatly influences the stability of the SOCs and thus essential in the development of high performance and durable SOCs. Chen et al [50] studied the directly assembled LSM oxygen electrode with YSZ electrolyte, and demonstrated the feasibility of operating the solid oxide cells reversibly. It was found that the electrocatalytic activity of the LSM oxygen electrode and the contact at the electrode/electrolyte interface were deteriorated under the anodic polarization for the OER in SOEC mode, as indicated by the significant increase in ohmic resistance and

polarization resistance. Nevertheless, the deteriorated LSM/YSZ interface can be partially or completely reversed and recovered in the subsequent cathodic polarization for the ORR in SOFC mode, as indicated by the significant decrease in both ohmic resistance and polarization resistance (Figure 2.10a). It was proposed that fundamentally, the remarkable reversibility of the LSM based SOCs is a result of the self-healing and regeneration of the deteriorated LSM/YSZ interface under cathodic polarization (Figure 2.10b). The incorporation of oxygen species and/or cation inter-diffusion between LSM/YSZ by cathodic polarization was attributed to the formation of the electrode/electrolyte interface. Graves et al [93] also reported that solid oxide cell degradation can be eliminated by reversible operation, i.e. cyclic anodic/cathodic polarization. A cell configuration of Ni-YSZ/YSZ/LSM-YSZ was used and operated at 800 ^{o}C with a reversible cycling current density of 1 A cm^{-2} for 4000 h. The cell operated only in electrolysis mode experienced rapid degradation, and the cell operated with reversible cycling under anodic/cathodic polarization did not show noticeable degradation. Similarly, the delamination at the electrode/electrolyte interface and the formation of nanosized cavities were observed after anodic polarization. The deterioration is proposed by the high anodic overpotential (η) of the oxygen electrode during high electrolysis polarization, yielding a high internal oxygen pressure (>100 bar) at the oxygen electrode/electrolyte interface, $p_{O_{2,int}}$:

$$p_{O_{2,int}} = p_{O_{2,gas}} \exp(-\eta \frac{4F}{RT}) \quad (2)$$

where $p_{O_{2,gas}}$ is the gas phase oxygen partial pressure in the porous electrode, F is Faraday's constant, R is the universal gas constant and T is the temperature. The high internal oxygen pressure results in the precipitation of O_2 bubbles, leading to the formation of nanosized pores at the electrode/electrolyte interface. On the other hand, the reversible operation, i.e. anodic/cathodic cycling, was found very effective in mitigating the delamination of the electrode/electrolyte interface. It was suggested that the reversible operation either avoids the formation of O_2 bubbles or enables reversal of their growth. The nanosized pore formation might be prevented if there is an incubation period in polarization electrolysis mode during which the critical level of the high internal pressure is not reached. The driving force for the pressure release was assumed to be the very low $p_{O_{2,int}}$ due to the cathodic overpotential. In addition, recent study shows that cyclic polarization can enhance the operating stability of

$La_{0.57}Sr_{0.38}Co_{0.18}Fe_{0.72}Nb_{0.1}O_{3-\delta}$ (LSCFN) oxygen electrode of reversible SOCs [94]. The electrocatalytic activity of LSCFN electrode is greatly degraded under cathodic polarization, but its performance loss is largely recovered under anodic polarization. It is found that the surface segregation of Sr and deposition at the electrode/electrolyte interface induced by cathodic polarization can be significantly mitigated by anodic polarization.

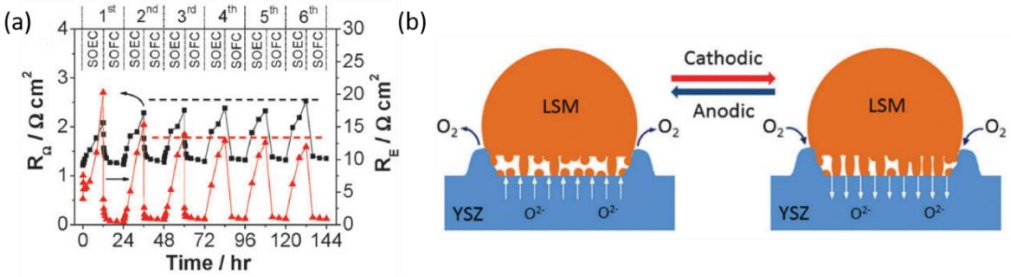

Figure 2.10 (a) R_Ω and R_E plots of LSM oxygen electrodes as a function of polarization time during cyclic 12 h-anodic/12 h-cathodic polarization at 800 °C and 500 mA cm^{-2}. (b) Schematic diagram showing the reversibility of the LSM-YSZ interface of a solid oxide cell under cyclic cathodic and anodic polarization conditions [50].

By introducing an interlayer, e.g. ceria based oxides, at the oxygen electrode/electrolyte interface has been proved to be an effective way to improve the cell stability under cyclic anodic/cathodic polarization in reversible SOCs. Shimura et al [95] applied a samaria-doped ceria (SDC) interlayer at the LSCF-SDC composite oxygen electrode/YSZ electrolyte interface, and the cell was operated at 900 °C and 0.5 Acm^{-2} for 5500 h. It was found that an increase in the ohmic resistance was observed under cathodic polarization, while under anodic polarization, the ohmic resistance was nearly constant. Nevertheless, a good adhesion between electrode/SDC interlayer was observed under both polarization conditions. Besides, the changes in the distribution of Sr component was found dependent to the polarization. For instance, the Sr segregation was effectively suppressed at the SDC interlayer under anodic polarization, whereas an appreciable concentration of Sr was detected at the SDC/YSZ interface under the influence of cathodic polarization. Fan et al [96] also studied the effects of GDC interlayer on the electrochemical performance and the durability of the LSCF oxygen electrode/YSZ electrolyte interface operated as reversible SOC. Repeated fuel cell/steam electrolysis cycles (1 h of steam electrolysis and 1 h of fuel

cell per cycle) were performed at 300 mA cm^{-2} and 800 ^{o}C, and it showed that the cell has higher degradation rate (5.9%) under electrolysis mode that under fuel cell mode (2.7%) after 13 repeated cycles. The microstructural analysis revealed that the GDC barrier layer was delaminated from the YSZ electrolyte, causing the cell performance to deteriorate.

2.2.3 Interfacial reactions and micropore formation

2.2.3.1 Interfacial reactions

Solid oxide fuel cell devices are regarded as an attractive power generation system in the future, and in principle, it should have high durability in a long-term operation. However, there are many factors that contribute to the degradation of the SOFCs, e.g. interfacial reactions between the electrode and electrolyte. The study of the interactions between the electrode and electrolyte has been widely investigated [19, 20, 22, 41, 47, 82, 97-100]. Many reactions occur during the essential high-temperature sintering process, which gives rise to mutual reactions and inter-diffusion of the cell component materials. Nevertheless, it has also been reported that the chemical reactions can also occur at lower temperature under the influence of polarization.

Kawada et al [101] investigated the reactivity of $LaMnO_3$ and YSZ, and it was estimated by thermodynamic calculations. It was found that the nonstoichiometry at the A-site, i.e. La site, plays a crucial role on the reaction. The diffusion of Mn into YSZ under high temperature leads to the increase of La activity at the electrode/electrolyte interface and then promotes the reaction, forming insulating layer $La_2Zr_2O_7$ (LZO). Excess amount of Mn was suggested for improving the stability of the cell in a long term operation. Kharton et al [102] investigated the reaction mechanism between cobaltite electrodes and bismuth oxide electrolyte. The formation of solid solutions $La_{1-x-y}Sr_xBi_yCoO_{3-\delta}$ (x=0-0.5; y=0-0.1) as well as $(Bi_{1-x}Co_x)_{1-y}Y_yO_{1.5}$ (x=0-0.4; y=0-0.25) was found in the diffusion layer between the cobaltite electrodes and the bismuth oxide electrolytes. The substitution of lanthanum and strontium with bismuth results in a decrease in the electrical conductivity and oxygen permeability of cobaltite electrodes, e.g. the oxygen permeability of the cobaltites decreases 8 to 10 times with the replacement of 10% of lanthanum by bismuth. The drop in oxygen ion transfer parameter with increasing bismuth content was explained by the strengthening of interaction of anions with the ions of A-site sublattice, as a result of the decrease in the mean radius of the cations of this sublattice. Lee et al [98] studied the electrical

and ionic properties of the reaction products at the LSM/YSZ interface and its influence on the cathode performance degradation at 900 ^{o}C. The interfacial product was identified as LZO, and the resistance resulted from the formation of LZO was found kept increasing with time to reach up to 40% if the total resistance after 500 h operation. The electrical conductivity of LZO was 2.4×10^{-5} S cm^{-1} at 1000 ^{o}C, 4 to 7 orders of magnitude smaller that of LSM electrode (100 S cm^{-1} at 1000 ^{o}C) or YSZ electrolyte (0.1 S cm^{-1} at 1000^{o}C). It was concluded that the cathode degradation was mainly attributed to the growth of the interfacial LZO layer and its contribution to the cell ohmic resistance. The reactivity between LSM and YSZ also depends greatly on the Sr content in LSM. Kleveland et al [103] investigated the formation of secondary phases between YSZ electrolyte and LSM electrode substituted with 0 to 60 mol% strontium. The reaction layer was observed after 1 h heat treatment at 1350 ^{o}C, and its composition vary from LZO to $SrZrO_3$ (SZO) at increasing contend in $La_xSr_{1-x}MnO_3$. The reaction layer was most pronounced for the diffusion couple $La_{0.4}Sr_{0.6}MnO_3$/YSZ, where a ~10 μm thick layer of SZO was formed at the electrode/electrolyte interface (Figure 2.11). The thickness of the SZO layer was greatly decreased to ~2 μm when the Sr content was reduced to 40 mol%. It was proposed that LSM and YSZ are not coexistent phases independent of the Sr content, and the rate of interfacial layer formation strongly depends on the Sr content and shows a minimum near 30 mol% Sr in LSM. It was found that the formation of SZO, LZO and manganese oxide is primarily due to the cations diffusion from LSM into YSZ. Moreover, Zhang et al [104] investigated the interfacial reactions between $(Pr_{0.8}Sr_{0.2})_yMnO_3$ (PSM) with different A-site stoichiometry, and YSZ electrolyte at 1200 ^{o}C and 1400 ^{o}C. A diffusion layer of Pr and Mn in zirconia was formed regardless of the A-site stoichiometry and the heat treatment temperature. A pyrochlore layer was formed at the interface of PSM and Pr- and Mn-dissolved zirconia at 1200 ^{o}C, and this layer grew much thicker at 1400 ^{o}C. It has been found that at the initial stage of heat treatment, both Pr and Mn ions diffused into YSZ forming a cubic zirconia solid solution, and when the solubility of Pr ions in the cubic YSZ was reached, a pyrochlore phase was formed. The solubility limit of Pr in YSZ for $(Pr_{0.8}Sr_{0.2})MnO_3$/YSZ and $(Pr_{0.8}Sr_{0.2})_{0.9}MnO_3$/YSZ were reached after much longer time compared with $(Pr_{0.8}Sr_{0.2})_{1.05}MnO_3$/YSZ, and thus the formation of the pyrochlore phase was delayed. It was proposed that the amount of pyrochlore phase formed at the interface was determined by the A-site stoichiometry of PSM.

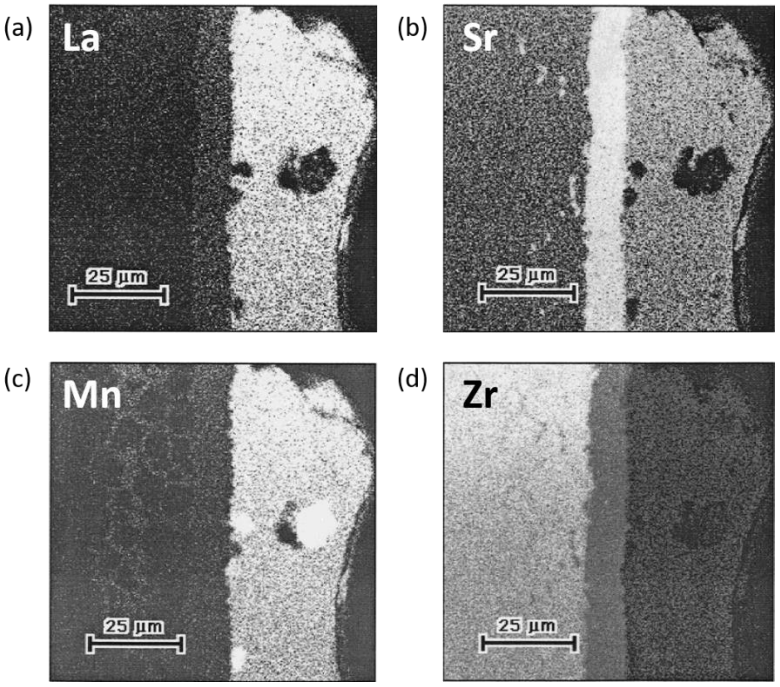

Figure 2.11 Elemental analysis (X-ray maps) of the diffusion couple of YSZ and $La_{0.4}Sr_{0.6}MnO_3$ fired at 1350 ^oC for 1 h [103].

However, the interfacial reaction can be beneficial for the cell overall performance in some cases. Su et al [33] fabricated a Ni-$BaZr_{0.4}Ce_{0.4}Y_{0.2}O_3$ (BZCY) anode-supported cell with SDC electrolyte and $Ba_{0.5}Sr_{0.5}Co_{0.8}Fe_{0.2}O_{3-\delta}$ (BSCF) cathode, and proposed an intriguing cell concept that taking advantage of beneficial interfacial reaction between anode and electrolyte to achieve both high open circuit voltage (OCV) and power output. The anode-supported cells were prepared by dry-pressing the anode-electrolyte into a dual layer disk, followed by high temperature sintering at 1450 ^oC for 5 h in air. A very thin and dense interfacial layer (2-3 µm) with compositional gradient was created by *in situ* reaction between anode and electrolyte. The cell with a configuration of Ni-BZCY/SDC/BSCF has an OCV as high as 1.02 V and delivered a power density of 462 mW cm^{-2} at 0.7 V at 600 ^oC. It was found that the diffusion of Ba^{2+} from the anode into the SDC electrolyte can increase the cell OCV, with the formation of $BaCe_{0.8}Sm_{0.2}O_3$ perovskite, which is a proton conductor with much lower electronic conductivity than SDC.

2.2.3.2 Micropore formation

The formation of micropore at the electrode/electrolyte interface during the cell operation has been widely reported, and is generally considered to be one of the reasons that contribute to the degradation of the overall cell performance. Kuznecov

et al [22] studied the ageing issue at the LSM/YSZ interface under cathodic overpotential, and it was found that the LSM grain showed partial disintegration and the formation of nanopores near the LSM/YSZ interface. The formation of such micropores was attributed to the generation of additional oxygen vacancies in the LSM as a result of the overpotential at the electrode/electrolyte interface. Matsui et al [21] also observed small closed pores formation at the LSM/SDC interface after cathodic current passage, and such microstructural change became obvious with increasing current density or the reduction in partial pressure of oxygen. It was found that the pore formation region extended to the center of the contact domain between LSM and SDC by increasing current density or lowering the oxygen partial pressure. However, the pore formation was not observed at the LSCF/SDC interface, and it appeared that this interfacial structure was stable regardless of the polarization conditions. It was proposed that since the oxide ion conductivity of LSCF is 4 orders of magnitude higher than that of LSM at 1000 ^{o}C (~10^{-2} S cm^{-1} for LSCF and 10^{-6} S cm^{-1} for LSM), the oxide ion can migrate through the two phase boundary of LSCF/SDC even at low overpotential. This leads to the much lower oxygen potential gradient in the vicinity of TPB under cathodic polarization as compared to the case of LSM/SDC cell, thus resulting in the more stable electrode/electrolyte interface. Jørgensen et al [47] carried out a durability test with LSM-YSZ composite cathode and YSZ electrolyte, and the cell was tested at 1000 ^{o}C with a current density of 300 mA cm^{-2} for 2000 h. An increase in the overvoltage exceeding 100 % of the initial value was observed after the durability test. Further microstructural analysis showed that a considerable number of less than 1 μm pores were formed close to the composite cathode/electrolyte interface after the current loading. The morphology change due to pore formation was assumed to be the main reason for the cell performance degradation, and the current load was proposed to create an oxygen potential difference across the composite cathodes, leading to the observed pore formation and pore movement. On the other hand, Haider et al [48] proposed that the activation behavior of LSM cathode can be partly attributed to the formation of pores at the LSM/YSZ interface. The LSM/YSZ cell was tested at 973 K with a cathodic current density of 200 mA cm^{-2} for 16 h, and it showed a significant reduction in the polarization resistance after the cathodic polarization with the formation of pores observed at the electrode/electrolyte interface. It was suggested that the pore formation significantly increases the active electrode area and creates the TPB points for oxygen ion incorporation, leading to the observed large decrease in R_P.

2.2.4 Element segregation and diffusion

2.2.4.1 Element segregation

Cation segregation at the interfaces of electrode/electrolyte greatly impacts the oxygen reduction reactions that are critical to the overall performance of a SOFC device, and it has direct relations to the electrode activity and stability during the cell operation [35, 105-110]. An example is the Sr segregation at the LSM- or LSCF-based electrode/electrolyte interface. It was suggested by Lee et al [111] that such segregation is driven by cation size mismatch at the A-site of the perovskite as well as by the charged defect interactions, i.e. a strong association of dopant cations with oxygen vacancies.

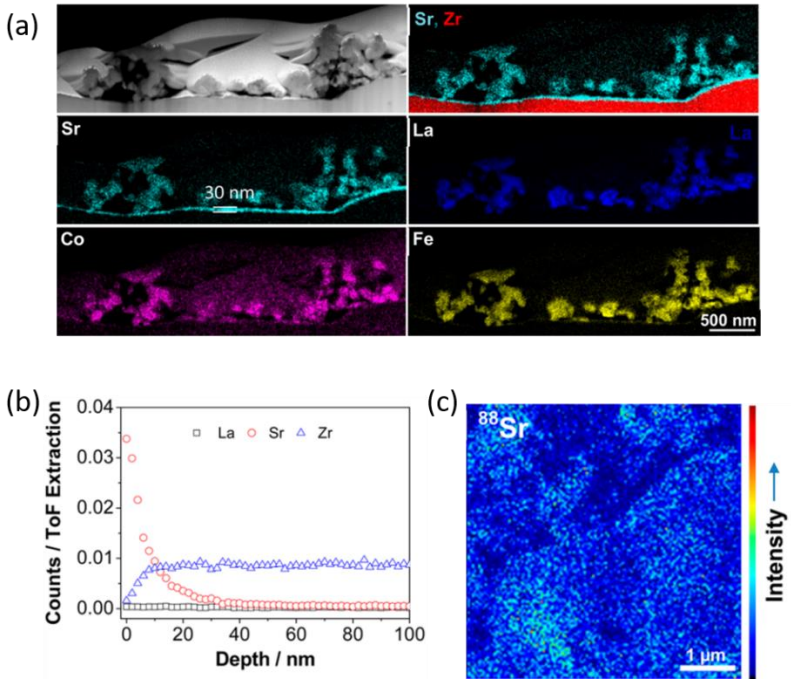

Figure 2.12 (a) STEM-EDS element mapping at the LSCF/YSZ interface after polarization at 700 ^{o}C and 500 mAcm^{-2} for 100 h. (b) SIMS depth profiles for La, Sr and Zr. (c) Near surface ^{88}Sr SIMS map (top ~10 nm) [112].

Chen et al [112] investigated the polarization-induced LSCF/YSZ interface at 750^{o}C with a cathodic current density of 500 mA cm^{-2} and observed a deposition of Sr-rich layer (~30 nm) at the electrode/electrolyte interface (Figure 2.12). It was found that the Sr layer initially starts to deposit at the LSCF/YSZ contact regions and then propagates to the entire YSZ electrolyte surface under the influence of cathodic polarization. The Sr surface segregation and its migration to the LSCF/YSZ interface are proposed to be the main reason for the performance degradation of the cell. The

segregated Sr species are highly mobile and reactive with the YSZ electrolyte under cathodic polarization conditions, forming insulating $SrZrO_3$ layer. Matsuda et al [113] observed the $SrZrO_3$ formation at the LSCF/GDC/YSZ interfaces. It was found that after sintering the LSCF/GDC/YSZ cell at 1100 ^oC for 1 h, a Sr-Zr-O reaction phase formed at the GDC/YSZ interface, and grew along the interface and into the YSZ electrolyte. Huber et al[114] suggested that the SrO segregation at the electrode surface as well as the electrode/electrolyte interface was closely correlated to the activation/deactivation process of a $La_{0.75}Sr_{0.25}Cr_{0.5}Mn_{0.5}O_{3\pm\delta}$ (LSCrM) electrode. It was found that under the cathodic polarization, the concentration of the segregated Sr species was significantly reduced, while the anodic polarization increased the Sr accumulation. It was proposed that under cathodic polarization, the segregated Sr species are incorporated back into the LSCrM lattice with concomitant reduction of manganese ions. The removal of the passivating Sr species at the electrode surface as well as the electrode/electrolyte interface facilitates the oxygen surface exchange reaction. While the anodic polarization induces the Sr segregation at the interface and electrode surface, leading to the decreased electrochemical activation. Chen et al [115] also found that the segregated SrO can promote the significant Cr deposition and poisoning at the electrode/electrolyte interface. The LSM/YSZ electrolysis cell was studied at 800 ^oC with the presence of an Fe-Cr alloy metallic interconnect, and a high intensity of Cr deposition was found on the LSM electrode inner surface as well as the YSZ electrolyte surface after the operation for 20 h with an anodic current density of 500 mA cm^{-2}. The formation of chromium oxide and $SrCrO_4$ were observed on the YSZ electrolyte surface, and it is thus suggested that under SOEC operating conditions, the nucleation agent for Cr deposition at the electrode/electrolyte interface is the segregated Sr species. The accelerated migration and segregation of SrO from the electrode bulk to the free surface under the influence of anodic polarization and its subsequent reaction with gaseous Cr species can be summarized as follow:

Sr segregation: $La_{0.8}Sr_{0.2}MnO_{3+\delta} \rightarrow La_{0.8}Sr_{0.2-x}MnO_{3+\delta} + xSrO$ (3)

Cr deposition via nucleation and grain growth route:

$$SrO + CrO_3 \rightarrow Cr\text{-}Sr\text{-}O_x \text{ (nuclei)} \quad (4)$$

$$Cr\text{-}Sr\text{-}O + CrO_3 \rightarrow CrO_y + Cr_2O_3 \quad (5)$$

$$Cr\text{-}Sr\text{-}O + SrO + CrO_3 \rightarrow SrCrO_4 \quad (6)$$

2.2.4.2 Element diffusion

Element diffusion is a widely observed phenomenon between SOFC components during cell operation, and it is driven by a gradient in chemical potential of the diffusion species, favored thermodynamically. The behavior of element diffusion between electrode/electrolyte is directly related to the element segregation, interfacial reaction and performance degradation of a cell, and thus the investigations on element inter-diffusion is of great importance in SOFCs [23, 99, 103, 106, 116-125].

Grosjean et al [126] examined the LSM/YSZ interfaces using TEM analysis, and observed a significant amount of manganese (~2 at.%) in YSZ grains after co-sintering LSM cathode and YSZ electrolyte at 1350 ^{o}C for 4 h. The diffusion of Mn toward YSZ was proposed to be associated with the YSZ structural changes and properties variation; instability and decomposition of LSM; higher reactivity between YSZ and LSM. It was suggested that the manganese diffusion irrevocably resulted in the decomposition of LSM into lanthanum and strontium oxides, which in turn reacted with YSZ to form SZO and LZO. Li [127] also observed the Mn diffusion on the YSZ electrolyte surface as well as along its grain boundary after co-sintering the LSM electrode on the YSZ electrolyte at 1150 ^{o}C for 2h. A clear accumulation of Mn cation and in a lesser extent, La cation was detected within the edge of the convex contact ring on the YSZ electrolyte surface, extending as far as 70-90 nm into the YSZ. The diffusion of Mn and La into YSZ was attributed to their limited solubility in YSZ, forming MnO-La_2O_3-Y_2O_3-ZrO_2 solid solution. However, at the center region of the convex contact ring on the YSZ electrolyte, the intensity of Mn accumulation was found qualitatively smaller than that within the rim region of the convex rings. The formation of convex contact rings at LSM/YSZ electrolyte interface after high temperature sintering was correlated to such cation inter-diffusion. Izuki et al [123] investigated the cation diffusion behavior across the LSCF/GDC interface, and the diffusion couple was prepared by depositing LSCF thick film onto the GDC substrate using Pulse Laser Deposition (PLD) technique. The diffusion couple was then treated at 1000-1200 ^{o}C for up to 672 h, and a significant diffusion of La into GDC as well as the diffusion of Ce into LSCF were detected. It was found that the grain boundary diffusion of La into GDC is at least five orders of magnitude faster than bulk diffusion.

The temperature dependence of the diffusion coefficients in the bulk GDC were described:

La in GDC: $D_{bulk}/m^2s^{-1} = 4.2 \times 10^{-5} \exp\left(\frac{-390\ kJ\ mol^{-1}}{RT}\right)$ (1273-1473 K) (7)

Sr in GDC: $D_{bulk}/m^2s^{-1} = 1.1 \times 10^{-7} \exp\left(\frac{-320\ kJ\ mol^{-1}}{RT}\right)$ (1373-1473 K) (8)

Wang et al [128] also studied the Sr and Zr diffusion in LSCF/GDC/YSZ diffusion triplets, and the triplets were annealed at 1100 ^oC and 1200 ^oC for one week. The formation of SZO was observed at the LSCF/GDC and the GDC/YSZ interfaces, and two diffusion paths were identified: grain boundary diffusion and surface diffusion. The Sr species were found diffused through GDC layer toward YSZ and form SZO at the GDC/YSZ interface, while Zr diffusion was also found across the GDC interlayer to the LSCF/GDC interface, forming SZO (Figure 2.13). The chemical potential gradient inside the GDC interlayer was proposed to be the reason for these cation diffusions.

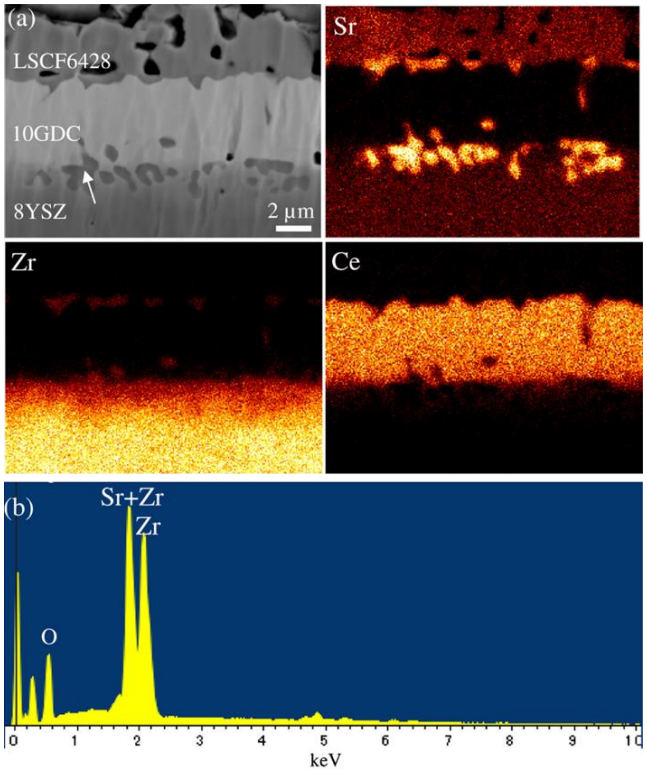

Figure 2.13 (a) EDX mapping of the cross-section of LSCF6428/10GDC/8YSZ annealed at 1200 ^oC for 168 h, and (b) EDS spectrum of the point analysis indicated by the arrow in (a) [128].

The polarization has also been reported to influence the cation inter-diffusion behavior in many cell configurations. Wang et al [24] studied the effect of cathodic polarization on Sr and Zr diffusion behavior in a LSCF/GDC/YSZ cell system, and the cells were evaluated under open circuit and cathodic polarization conditions. The cell was treated at 900 ^{o}C for 400 h, and only a few fine particles, i.e. SZO, were observed at the LSCF/GDC interface under open circuit condition, while under cathodic polarization of -0.3 V, a large amount of SZO particles were found at the LSCF/GDC and GDC/YSZ interfaces. On the other hand, after the cell was treated at 1000 ^{o}C, there was no obvious difference between open circuit and cathodic polarization conditions in terms of the amount of formed SZO particles. It was proposed that at 900 ^{o}C, the formation of SZO is still in the early stage, and the electrochemically enhanced Zr diffusion resulted in a significant difference between the two conditions. While at 1000 ^{o}C, the sufficient amount of SZO is already formed under the thermal effect at the LSCF/GDC interface, GDC grain boundaries and GDC/YSZ interface. Therefore, the effect of the cathodic polarization on the Sr and Zr diffusion is not very significant as compared to that of at 900 ^{o}C. Nevertheless, it was considered that under cathodic polarization, the steep Sr and Zr chemical potential gradient resulted in the rapid Sr and Zr diffusion across the GDC interlayer.

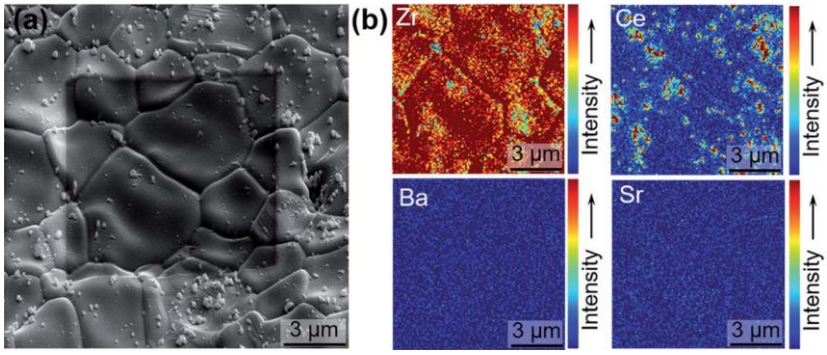

Figure 2.14 (a) SEM image of the YSZ electrolyte surface in contact with PBSCF-GDC composite cathode after the cell stability test. (b) ToF-SIMS element mapping from a 10 × 10 μm scan area as indicated in (a) at the depth of 50 nm [129].

Li et al [129] studied the influence of cathodic polarization on the interface formation between the directly assembled $PrBa_{0.5}Sr_{0.5}Co_{1.5}Fe_{0.5}O_{5+\delta}$ (PBSCF) – GDC composite cathode and YSZ electrolyte at 750 ^{o}C and a cathodic current passage of 500 mA cm^{-2} for 100 h, and found a mass diffusion of GDC particles at the electrode/electrolyte interface. It was shown that after the polarization, the ohmic resistance as well as the

polarization resistance of the cell decreased noticeably, and an increase of 23.4% in the power output was observed as well. The improvement of the electrochemical performance was considered to be the better physical contact between the cathode and YSZ electrolyte. Further microstructural analysis revealed that a large number of GDC particles with a dimension ranging from 0.1 to 1 μm were deposited on the YSZ electrolyte surface (Figure 2.14). Such mass diffusion of GDC under the influence of polarization was also reported by Li et al [65], in which the $La_{0.95}Co_{0.2}Fe_{0.8}O_{3-\delta}$ (LCF) – GDC composite cathode was directly assembled on the YSZ electrolyte. After the cathodic polarization at 750 ºC and 500 mA cm^{-2} for 130 h, a thin layer of GDC was found deposited at the electrode/electrolyte interface. Moreover, the diffusion of erbium stabilized bismuth oxide (ESB) toward the electrode/electrolyte interface was also reported under the influence of polarization and heat treatment. Ai et al [130] and Chen et al [131] studied the interface structure of a ESB-LSM composite cathode/YSZ electrolyte cell, and observed a dense interfacial layer formed after cathodic polarization at 750 ºC and 500 mA cm^{-2}. The interfacial layer consists of a well distributed ESB network with a couple of LSM particles. It was found that under the influence of cathodic polarization, Er migrated from the ESB phase and then reacted with the segregated Mn cations from the LSM particles, forming $Er_{0.63}Bi_{0.15}Mn_{0.22}O_x$ phase. The loss of Er in the ESB was suggested to lower the melting point of ESB and thus forming a dense interfacial layer (Figure 2.15).

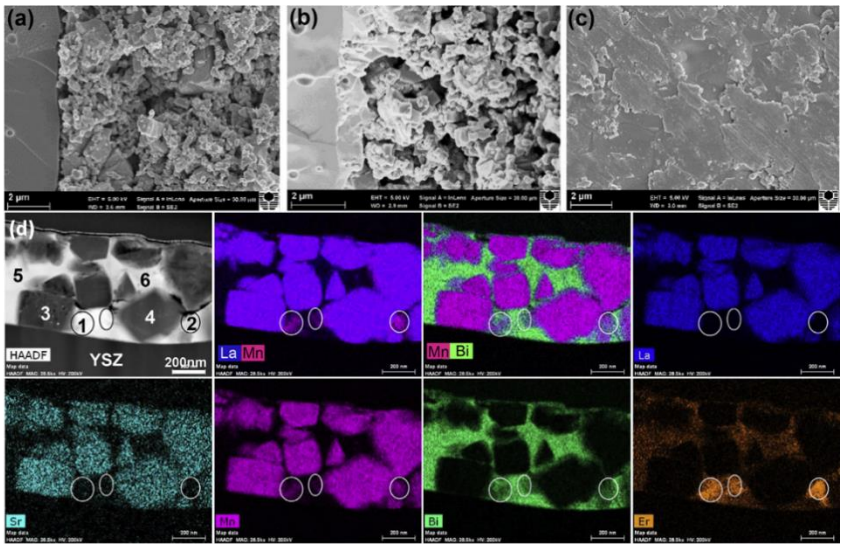

Figure 2.15 SEM micrographs of (a) cross-section of as prepared LSMPt-ESB composite electrode, (b) cross section of electrode/electrolyte interface and (c) exposed YSZ electrolyte surface after the removal of the LSMPt-ESB electrode after

the stability test at 0.5 A cm^{-2} and 750 ^{o}C for 20 h and at 0.25 A cm^{-2} and 600 ^{o}C for 350 h. (d) STEM-EDS mapping of the dense layer on the electrolyte surface shown in (c).

2.3 Hydrogen electrode/electrolyte interfaces

2.3.1 High temperature sintering effect

Solid oxide fuel cells (SOFCs) are all ceramic components devices, and typical SOFC consists of YSZ electrolyte and Ni-YSZ anode cermet. Generally, in order to establish an intimate electrode/electrolyte interface, pre-sintering the YSZ electrolyte and Ni-YSZ anode at high temperature, e.g. ~1400 ^{o}C, is considered necessary.

2.3.1.1 High temperature induced triple phase boundary

High temperature treatment of the anode/electrolyte is one of the most important steps in the preparation of high performance and stable cells. As a large volume of coarse anode particles could incur weak contact at the anode/electrolyte interface, the particle size and distribution of the anode particles are an important factor in determining the Ni-YSZ/YSZ cell performance, and thus the high temperature treatment is an effective way to control the their particle size distribution. Fukui et al [38] studied the sintering temperature effect on the electrochemical performance of a Ni-YSZ anode prepared by spray pyrolysis with YSZ electrolyte cell. The Ni-YSZ anodes were pre-sintered at 1200, 1300, 1350, 1400 and 1500 ^{o}C on the YSZ electrolyte, and the cell pre-sintered at 1350 ^{o}C shows the best electrochemical performance. It was proposed that after higher temperature sintering (1350 ^{o}C), the increased TPB length at the anode/electrolyte interface and the good connections between the anode particles contributed to the electrochemical performance improvement. Further increasing the sintering temperature will result in the larger polarization resistance, and it was suggested to be caused by the decrease of TPB length due to the growth of YSZ grains and Ni grains in the cermet anode. On the other hand, the formation of Ni-to-Ni electronic contact and YSZ-to-YSZ ionic contact networks are closely related to the sintering temperatures of the anode/electrolyte, and the high temperature sintering is essential to create a good bonding between the YSZ phase in the anode cermet and the YSZ electrolyte, leading to the formation of a rigid YSZ structure to support the Ni phase. Primdahl et al [132] also investigated the sintering temperature effect on the

electrochemical performance and mechanical strength of Ni-YSZ/YSZ cells. A NiO-YSZ layer was sintered at temperatures between 1100 and 1500 ^{o}C onto dense YSZ electrolyte, and a minimum polarization of 0.09 Ω cm^2 at 1000 ^{o}C was obtained for sintering temperatures of 1300 - 1400 ^{o}C. It was also found the fracture strength of the electrolyte-supported cells decreased with the increased sintering temperature, as a result of the formation of channel cracks due to the thermal expansion coefficient mismatch between the anode and the electrolyte.

2.3.1.2 High temperature induced element diffusion

During high temperature sintering process, element diffusion and segregation can also occur at the anode/electrolyte interface, resulting in microstructural change in cell components. Ou et al [133] prepared a NiO-SDC anode supported SDC electrolyte cell pre-sintered at 1400 ^{o}C, and observed the diffusion of Ni from the cermet anode to the electrolyte film with a depth of about 1μm. The concentration of Ni in the electrolyte was found to be up to 18-22 at.% near the anode/electrolyte interfaces, and there was no considerable compositional difference between the grains and the grain boundaries. It was proposed that the diffusion of Ni into SDC can lead to a degradation of the ionic conductivity of the electrolyte as Ni cations can act as a dopant and contribute to the increased concentration and ordering of oxygen vacancies. In addition, the reduction in Ce in the electrolyte film near the anode/electrolyte interface was observed. These microstructural characteristics were suggested to have negative impacts on the conductivity of the electrolyte films. Moreover, Ye et al [122] also studied the effect of Ni diffusion on the microstructure of the Ni-GDC/GDC interface, and the anode supported cell was pre-sintered at 1400 ^{o}C. The Ni diffusion into GDC electrolyte was observed, and its concentration was estimated to be 17-19 at.% after high temperature sintering. The Ni concentration decreases rapidly with increasing distance (*d*) to the anode/electrolyte interface, and Ni was not detected when *d* is larger than 0.5 μm. It was found that the Ni diffusion contributed to the formation of inhomogeneous microstructures and high ordering level of oxygen vacancies near the Ni-GDC/GDC interface. The diffusion and segregation of Ni along grain boundary at the Ni-GDC/GDC interface was also investigated by Li et al [106], in which the Ni segregation at the GDC grain boundary was observed after high temperature sintering at 1400 ^{o}C. The grain boundary was believed to provide pathway for Ni to diffuse from anode to electrolyte, and the diffusion enhances the microstructural inhomogeneity of

the grain boundary, leading to the superstructure formation. It was suggested that the oxygen diffusion across the grain boundary may be significantly hindered due to the formation of superstructure, strongly increasing the grain boundary resistance.

2.3.2 Polarization effect

2.3.2.1 Anodic polarization

On the anode side of a SOFC device, H_2 is oxidized at the anode/electrolyte interface, and anodic polarization would occur concomitantly. The anodic polarization has been reported to facilitate the chemical reactions at the anode/electrolyte interface. Marina et al [134] studied the influence of anodic polarization on the interfacial reactions between Ni and H_2Se at the Ni-YSZ/YSZ interface. The Ni-YSZ supported YSZ electrolyte cell was tested at a temperature range of 600-800 ^oC with a current load of 0.1-0.5 A cm^{-2}. It was found that the cell exposed to H_2Se resulted in a rapid decrease in cell performance, and the extent of performance degradation was relatively insensitive to the concentration of H_2Se in the range of 0.5-2 ppm at low anodic polarization. However, under high anodic polarization, rapid and irreversible cell failure was observed, even at H_2Se concentrations as low as 0.5 ppm. Further microstructural analysis revealed significant changes in morphology at the active anode/electrolyte interface, e.g. a large number of fine particles (< 100 nm) were formed at the interface and adversely affected the anode bonding to the YSZ electrolyte, and anode delamination was observed directly at the active interface region. The fine particles formed were characterized to be a mixture of Ni, NiO and $Ni_{1-x}Se$ phases. It was suggested that the cell failure was favoured by low temperature, high H_2Se concentration and high anodic polarization, and the local chemical conditions at the active interface under the influence of anodic polarization were proposed to be of overriding importance to the extent of Ni interactions with H_2Se. The accumulation of impurities at the anode/electrolyte interface has also been found induced by anodic current. For example, the microstructural degradation of the anode/electrolyte interface under the anodic polarization was studied by Liu et al [135], in which a Ni-YSZ anode/YSZ electrolyte cell was tested at 850 ^oC for 1800 h with an anodic current load of 300 mA cm^{-2}. It was found that after the long-term operation, the segregation and accumulation of a very low SiO_2 content (~100 ppm) introduced by the raw materials degraded the anode/electrolyte interface by forming nanometer-thin silicate glass films (Figure 2.16). Jensen et al [136] also discovered a significant

microstructural changes at the Ni/YSZ interface under anodic polarization as a result of impurity segregation (e.g. Si, Mn, Al and Mg) from the bulk of the Ni material and accumulation along the three phase boundary, forming a rim ridge of impurities. The initially flat contact area on the YSZ electrolyte developed a hill and valley structure with an amplitude of 100 nm.

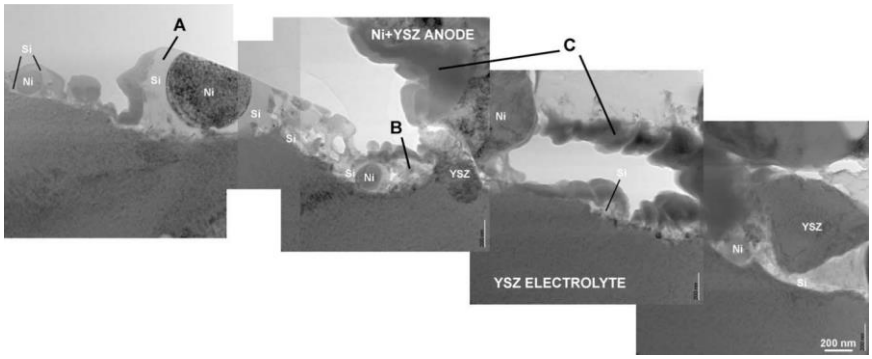

Figure 2.16 TEM micrographs showing the entire length of the Ni-YSZ anode/YSZ electrolyte interface [135].

On the other hand, Aaberg et al [137] found that the anodic polarization can induce a self-catalytic effect on the anode. It was observed that under anodic polarization, the Ni migrated to the electrolyte surface, forming a "necklace" of Ni particles around the anode/electrolyte interface, leading to an increase of TPB length and thus improved anode activity.

2.3.2.2 Cathodic polarization

When the solid oxide cells are operated as SOEC devices, cathodic current flow can be observed on the hydrogen electrode side. The influence of cathodic polarization on the hydrogen electrode/electrolyte interface has also been reported. Klotz et al [138] discovered that by applying a short-time cathodic current load of 2 Acm^{-2} to the Ni-YSZ electrode/YSZ electrolyte cell at 700 ^{o}C, a progressive decrease of the overall area specific resistance was obtained. After the current treatment, a nanostructured Ni-YSZ interlayer was observed at the electrode/electrolyte interface with sizes of a few 10 nm and a porosity of 20-30% (Figure 2.17). The formation of such nanostructured interlayer was considered to contribute to a remarkable increase of TPB length, resulting in a distinctive performance enhancement after the short-term cathodic polarization. Moreover, the impact of short-term strong cathodic polarization on Ni-YSZ interface was further investigated by Kreka et al [139]. One to three orders of magnitude decrease in the high frequency resistance and four to five orders of

magnitude decrease in the low frequency resistance were observed upon increasing cathodic polarization from 0 V to -2 V, suggesting the introduction of electronic conductivity and the increase of the reaction zone from the TPB to the YSZ surface. Also, the accumulation of impurities (Si, Na and Ca) around the Ni/YSZ interface was found after the cathodic current treatment.

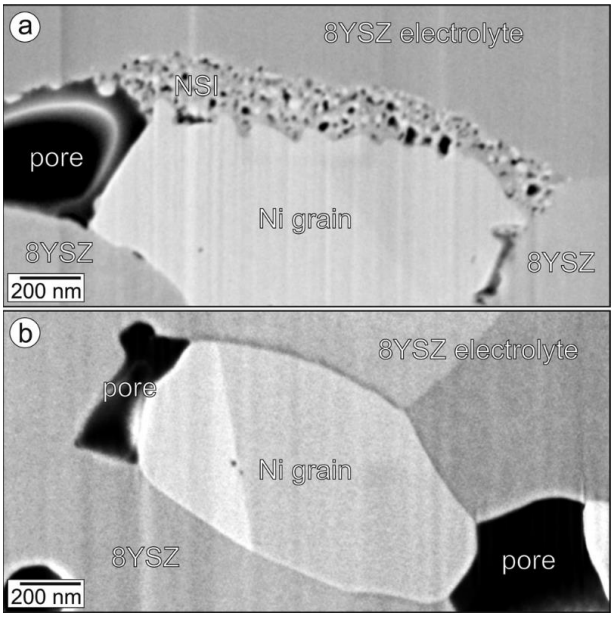

Figure 2.17 SEM images of the interface between Ni-YSZ and YSZ electrolyte: (a) under the influence of strong cathodic polarization, (b) without the influence of strong cathodic polarization (NSI: nanostructured interlayer) [138].

The influence of long-term cathodic polarization on the hydrogen electrode/electrolyte interface structure has also been reported. For example, the microstructure degradation of the Ni-YSZ electrode/YSZ electrolyte cell under SOEC mode was studied by Hauch et al [140]. The cell was tested at 850 ^{o}C for more than 1500 h with a cathodic current load of 0.5 A cm^{-2}, and a cell voltage degradation of 2%/1000 h was obtained. The degradation was attributed to the Si-containing impurities accumulation at the electrode/electrode interface under the influence of cathodic polarization. Under a much higher cathodic current density (2 A cm^{-2}), a significant microstructural change was observed at the interface as a result of Ni particles relocation, and a 2-4 μm thick dense layer of Ni-YSZ was formed. Chen et al [141] reported that after the Ni-YSZ electrode/YSZ electrolyte cell was exposed to 1.5 A cm^{-2} at 850 ^{o}C, formation of ZrO_2 nano-particles on Ni surfaces close to the interface was observed. It was suggested that

the formation of such nano-particles greatly lowered the electrode performance due to the loss of Ni percolation.

2.3.3 Interface modification

2.3.3.1 Anode functional layer

During the fabrication of anode-supported solid oxide cells, the porosity and the pore structure of the anode is critical and closely related to the cell overall performance. Generally, the gas pores are produced by adding the pore formers, i.e. starch, and reducing the NiO to Ni. However, the pores formed at the anode/electrolyte interface would result in the disconnection between the two layers as well as the triple phase boundary length. Therefore, an introduction of the dense anode functional layer (AFL) with fine microstructure at the anode/electrolyte interface has been proposed to increase the three-phase boundary length and to restrain the activation polarization for hydrogen oxidation. Chen et al [142] studied the effect of AFL thickness on gas impermeability and electrochemical performance of an anode-supported cell, in which different number of AFL layers were fabricated on the anode support using slurry spin coating method. It was found that the open circuit voltage and the ohmic resistance of the cells were generally increased as the AFL thickness increase, and the cell with a single-layer AFL (~5 μm) exhibited the best electrode performance. The authors proposed that although more potential reactions are produced as the AFL thickness increases, the low porosity of AFL and the increased gas diffusion path associated with the increased AFL thickness limit the diffusion of gases across the AFL layer. Therefore, developing an optimum thickness of AFL is critical to achieve a trade-off between the enhancement of electrochemical performance due to the increasing TPB and the decrease of performance due to the increased gas diffusion resistance. Similarly, Zhang et al [143] studied the effects of anode functional layer on proton-conducting electrolyte based cells. The addition of the AFL was demonstrated to significantly reduce the electrode resistance as a result of the optimized TPB length at anode/electrode interface and excellent electrocatalytic activity of the AFL. A peak power density of 489 mW cm^{-2} and a low electrode polarization resistance of 0.37 Ω cm^2 were obtained at 650 ^oC.

2.3.3.2 Other approaches

In order to increase the power density of a SOFC device, various methods have been investigated to modify the anode/electrolyte interface structure. Konno et al [144]

proposed a mesoscale-structure modification (10-100 μm) by introducing grooves or fins at the electrode/electrolyte interface to increase the electrochemically active area (Figure 2.18a, b). It was suggested the mesoscale-structure control will reduce not only the reaction resistance related to the activation loss but also the electrolyte ohmic resistance (Figure 2.18c, d). The mesoscale-grooved structure at the anode/electrolyte interface was proved to be effective for enhancing the power generation performance, if the groove scale is sufficiently larger than the effective thickness of the electrode. The impedance of the grooved cell was also found smaller than that of the flat cell. From the simulation results of the mesoscale-grooved cell, it was found that the hydrogen oxidation reaction actively occurs at the groove bottom, as a result of the similar activation overpotentials and the higher vapour potential pressure compared with those at the top of a convexity. Rednyk et al [145] developed a novel design of active sites on anode by depositing trace amount of platinum oxides at the anode/electrolyte interface. PtO_x thin films were deposited on the anode using radio frequency magnetron sputtering technique, and the amount of deposited Pt was estimated to be 9 to 91 ppm. The IR free current density value of 185 mA cm^{-2} at 0.8 V observed for the cell with an anode sputtered with a trace amount of PtO_x at 973 K was dramatically higher than 85 mA cm^{-2} obtained for the cell without platinum sputtering. Further microstructural analysis revealed that the defect structure was formed on Ni surface by active Pt species, and such formation creates new active sites for hydrogen oxidation, facilitating the anode electrocatalytic activity with improved electrochemical performance of the SOFC cell at 973 K.

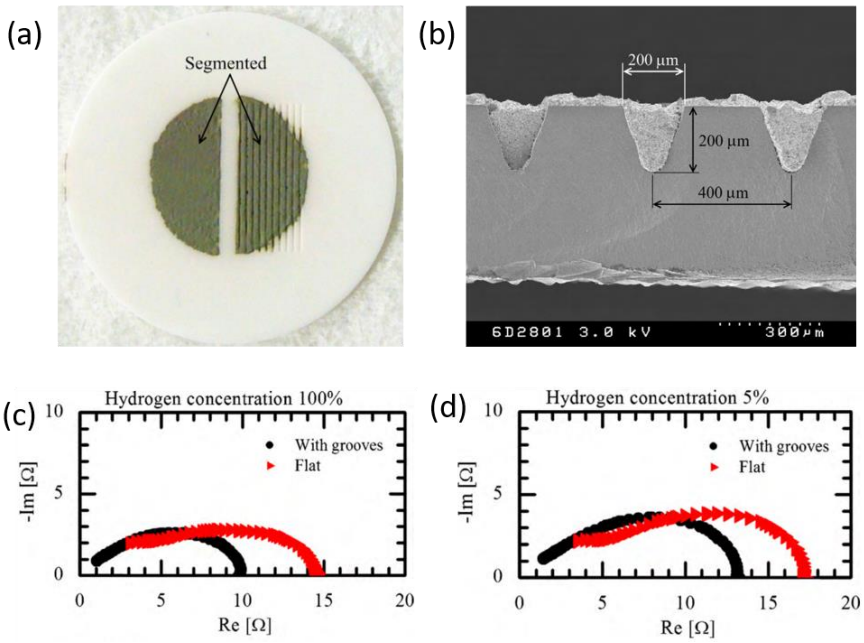

Figure 2.18 (a) Anode-side surface of an electrolyte with grooves. (b) SEM image of the cross-section of the grooved area of a cell filled with Ni-YSZ anode. Impedance spectra measured between anode and electrolyte at 800 ^{o}C with hydrogen concentration of (c) 100% and (b) 5% [144].

2.4 Interface characterization Techniques

2.4.1 Focused Ion Beam

2.4.1.1 Combined FIB-STEM technique

The focused ion beam (FIB) instrument has been gaining increasing attention in recent years as an important and effective way to prepare thin lamella for TEM characterization in solid oxide fuel cells [126, 146-151]. The application of combined FIB-STEM technique offers opportunities of more precise analysis of the electrode/electrolyte interface microstructure on a nanoscale. The FIB technique not only allows a TEM lamella to be prepared from a specific area of interest with submicron precision, but also can uniformly mill heterogeneous microstructures that consist of compositionally and structurally distinct regions.

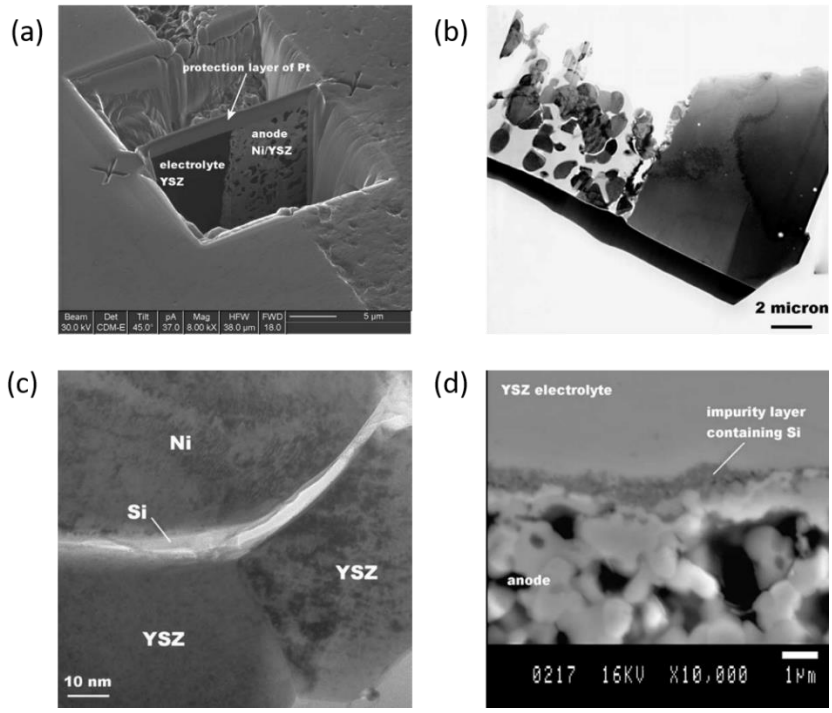

Figure 2.19 (a) FIB ion image showing the sample preparation. TEM micrograph of (b) the overview of the foil and (c) the Ni/YSZ grain boundary in the anode bulk. (d) SEM image showing the segregation of impurities at the anode/electrolyte interface after long-term test [135].

Liu et al [135] conducted one of the first attempts that use FIB lift-out technique to prepare TEM specimens for examining electrode/electrolyte interfaces in solid oxide fuel cells. The authors investigated the anode/electrolyte interface microstructure degradation after a long-term stability test at 850 ^{o}C over 1800 h with an anodic current load of 300 mA cm^{-2}. An interface region of interest was prepared using FIB milling, with a dimension of 15 μm in width, 8 μm in depth and 100 nm in thickness for the final lamella. It was proposed that although the quality of an FIB lamella is sufficient to meet the conditions for TEM imaging and EDS analysis for a wide range of materials such as Si, binary alloy, ceramics and polymer; the FIB specimens tend to exhibit some artefacts such as re-deposition of sputtered materials, deposition of the ion source and amorphisation of specimen surface during the milling process. Nevertheless, the authors suggested that the FIB lift-out techniques were successfully applied to prepare TEM specimen, allowing the interfacial microstructure to be analysed on a nano-scale, and it was shown that the TEM specimen represented the material of the bulk sufficiently well. The microstructural degradation of the anode/electrolyte interface was found through segregation and accumulation of a very

low SiO_2 content (~100 ppm), among other impurities introduced by the raw materials, forming nanometer-thin silicate glass films at the anode/electrolyte interface and the Ni/YSZ grain boundary (Figure 2.19). Grosjean et al [126] also adopted the combined FIB-TEM technique to examine the reactivity and diffusion behaviour between LSM and YSZ at the interfaces. A cell with LSM cathode, YSZ electrolyte and Ni-YSZ anode was tested at 850 ^oC, and it was found that the electrical performance was one order of magnitude less than expected and the cell deteriorated quickly at 0.7 V. In order to obtain precisely located chemical and structural information, the FIB technique was employed to extract a thin lamella (5×10×0.1 μm) at LSM/YSZ interface for high resolution TEM characterization. It was found that the manganese diffused toward the electrode/electrolyte interface and the electrolyte grains under the influence of high temperature sintering (~1350 ^oC), leading to the rise of a significant electronic conduction and to a drop of the ionic conductivity. The manganese diffusion caused the irreversible decomposition of LSM into lanthanum and strontium oxides, which in turn reacted with the YSZ electrolyte to form insulating strontium zirconate and lanthanum zirconate. Knibbe et al [152] studied the $(La_{0.6}Sr_{0.4})_{0.99}CoO_{3-\delta}$ cathode/GDC barrier layer/YSZ electrolyte interfaces using the combined FIB-TEM techniques. The cell was tested for 1500 h at 650 ^oC with a current load of 0.75 A cm^{-2}, and it was found that periodic $SrZrO_3$ asperities were formed at the YSZ electrolyte/GDC barrier layer interface, spreading along the interface region and growing into the adjacent GDC grain boundary. Moreover, the HRTEM observation on the FIB lamella further revealed epitaxy growth of GDC layer on the polycrystalline YSZ electrolyte. The deposited GDC layer matched well with the YSZ grain boundary with a low mismatch factor of 5.1%. Soldati et al [147] conducted a site-specific investigations on the LSCF/GDC interface long-term operation stability using FIB lift-out technique. A number of FIB lamellae were prepared at the electrode/electrolyte interface before and after heat treatment at 500 ^oC for 1000 h. Further HRTEM, EDS and electron diffraction characterization revealed a semi-coherent growth of a polycrystalline LSCF cathode on GDC electrolyte, and no differences were found comparing the composition and microstructure at the interface before and after the thermal treatment. FIB technique was also adopted by Wang et al [153] to study the microstructure degradation of the LSM/YSZ interface in the presence of Cr-containing interconnect, in which the cell was operated at 800 ^oC with a current load of 440 mA cm^{-2} for 500 h and a number of lamellae were milled at different locations of the

electrode/electrolyte interface followed by TEM observation. Distinct microstructural changes were observed as a result of the interactions between the chromium and the LSM-YSZ cathode, and the degradation was not uniform in the entire cell and the most degradation occurred in the regions of high electrochemical activity, i.e. near the cathode/electrolyte interface. Nanosized particles of $(Cr, Mn)_3O_4$ and Cr_2O_3 were observed on the surface of the YSZ electrolyte. It was proposed that Mn species facilitated the formation of a stable Cr-Mn-O nuclei on the electrolyte, and under high overpotentials the LSM was found decomposing into complex oxides, likely driven by the MnO formation and its subsequent reaction with Cr-vapor species. Liu et al [148] used the combined FIB-TEM technique to observe the atomic structure of boundaries and phase contrast of a Ni-YSZ anode, e.g. the Ni/YSZ interface as well as the Ni/YSZ/pore triple-phase boundary were examined. The Ni (111) lattice planes were identified at the Ni/YSZ interface, and the contact surface of YSZ was found to be a high-index step surface with facet $(3\bar{1}1)$ acting as the main contact surface while (020) is the step. The HRTEM observation on the TPB region further revealed that the Ni and YSZ are in the zone axis of $[2\bar{1}1]$ and the Ni/YSZ interface is very close to cubic-on-cubic orientation relationship. The authors also conducted a detailed research on the crystallographic orientation relationship and the contact surfaces between Ni and YSZ with FIB milled samples [154]. The orientation relationships of the three examined areas are identified: Ni[001]//YSZ[013], Ni(220)//YSZ(200), Ni(200)//YSZ(331) and Ni[112]//YSZ[110], Ni(220)//YSZ(113), Ni(311)//YSZ(111). The misfits of the lattice planes at the interface were found small in both *x* and *y* directions (Figure 2.20). It was proposed that different interfaces could correspond to different energy states of interfacial bonding between Ni and YSZ.

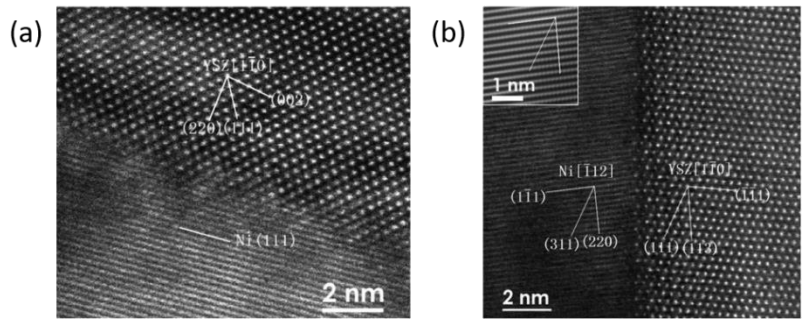

Figure 2.20 HRTEM images showing two different regions of the Ni/YSZ interface [154].

2.4.1.2 FIB 3D modelling

A number of quantitative models have been developed in recent years to understand the correlation between electrode/electrolyte microstructure and performance in solid oxide fuel cells. Conventional methods of microstructural analysis such as SEM only provide two dimensional information of the microstructure. However, understanding the macrohomogeneous properties such as surface area, three-phase boundary (TPB) length, volume fraction of the different phases, ionic and electronic transport paths, requires a detailed three-dimensional analysis. Wilson et al [155] demonstrated the use of a dual-beam FIB-SEM instrument to make a complete three-dimensional reconstruction of a Ni-YSZ composite anode. The fuel cell was first cut and polished with the cross-section of the anode/electrolyte interface exposed on the surface. The FIB was then used to mill a rectangular trench into this surface, and thin (50 nm) sections were removed from the exposed surface, followed by SEM imaging of the surface, and this entire process was repeated to obtain a series of consecutive 2D SEM images. A 3D reconstruction of the anode was acquired by stacking the 2D SEM images in 3D space. With the 3D microstructural information, the authors reconstructed the anode microstructure, and a 3D map of the three phase boundaries in the anode as well as the tortuosity of specific subphases were obtained (Figure 2.21). It was found that 63% of TPB were interconnected and 19% were short unconnected segments where the three phases have poor connectivity with the rest of the microstructure. The FIB 3D reconstruction technique was also adopted by Matsui et al [42] to quantitative analyse the microstructural change at the LSM cathode/YSZ electrolyte interface under the influence of cathodic polarization. The LSM/YSZ cell was operated at 1000 ^{o}C with a current passage of 200 mA cm^{-2} for 20 h, and an obvious increase in performance was observed. The FIB 3D reconstruction of the LSM/YSZ interface before and after discharge operation revealed that the interface structure changed depending on the time duration of discharge, and the roughness of the YSZ electrolyte surface increased with time. The TPB length of the as-prepared sample was calculated to be 1.26 μm $μm^{-2}$, and it increased to 1.72 μm $μm^{-2}$ after 300 min discharge operation. However, the active TPB length after cathodic polarization was 1.35 μm $μm^{-2}$, only 7% larger than that of the as-prepared cell. It was concluded that the increase in TPB length is one of the factors that contribute to the enhancement of cathode performance, but not the major factor. Similar study was conducted by Yang et al [156] to investigated the influence of large cathodic current on the

microstructure of A-site deficient LSM/YSZ interface. The microstructural change at the interface was quantitatively investigated, and it was found that after discharge at 1.2 A cm^{-2} for 60 h, the YSZ electrolyte surface was covered by a dense layer of LSM, accompanied with the formation of closed nanopores at the LSM/YSZ interface. The 3D reconstructed results indicate that the total TPB length of the as-prepared cell was 1.08 μm $μm^{-2}$, equal with the active TPB length. Whereas after the cathodic polarization for 5 h and 40 h, the active TPB length was reduced to 0.49 μm $μm^{-2}$ and 0.26 μm $μm^{-2}$, respectively. It was proposed that the newly formed dense LSM layer at the LSM/YSZ interface reduced the TPB length, and formation of nanopores at the interface gave rise to many fragmented but inactive TPB lines.

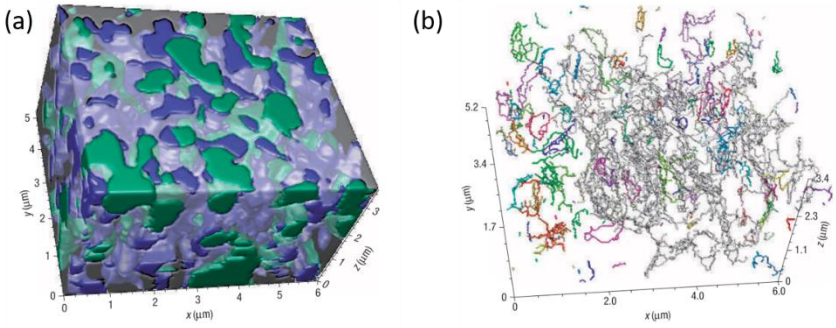

Figure 2.21 (a) 3D anode reconstruction showing the Ni (green), YSZ (grey) and pore (blue) and, (b) 3D map of the three-phase boundaries in the anode showing connected TPB length (63% with grey colour) and disconnected TPB sements (other colours) [155].

2.4.1.3 FIB-SIMS

Focused ion beam – secondary ion mass spectrometry (FIB-SIMS) is a material identification technique that combines the high spatial resolution of FIB with the high elemental sensitivity of SIMS. It is a technique used to analyse the composition of solid surfaces by sputtering and ionizing the surface of a specimen with a focused primary ion beam (usually Ga^{+}) and collecting and analysing ejected secondary ions. SIMS is a very sensitive analytical technique that can provide parts per million (ppm) to parts per billion (ppb) sensitivity for most elements when relatively large areas of analysis are available.

Souza [157] et al used the SIMS technique to study the oxygen tracer diffusion and surface exchange behaviour in LSM perovskite oxide material at temperatures between 700 ^{o}C and 1000 ^{o}C with $^{18}O/^{16}O$ isotope. The ^{18}O penetration profiles in the LSM

samples were determined by sputter depth profiling, and the analysis was carried out by recording the intensities of $^{16}O^-$ and $^{18}O^-$ as a function of sputtering time. The activation enthalpy for oxygen tracer diffusion in the bulk was found to be 270 ± 13 kJ mol^{-1}, while it was 128 ± 21 kJ mol^{-1} for oxygen tracer surface exchange. It was suggested that the bulk oxygen diffusion in the LSM perovskite oxide involves the migration of oxygen vacancies, and the diffusion of oxygen along grain boundaries is much faster than through the bulk. Horita et al [158] also used SIMS technique to examine the oxygen reduction sites and diffusion paths at LSM/YSZ interface under different cathodic polarization conditions. The $^{18}O/^{16}O$ isotope exchange under cathodic polarization was examined by SIMS to visualize the oxygen incorporation/reduction active sites. The oxygen reduction active sites were determined at the O_2/LSM/YSZ interface region under cathodic polarization conditions, and high concentrations of ^{18}O was observed as spots in the shape of LSM cathode. It was found that at high overvoltage, the diffusion paths of ^{18}O are parallel to the depth direction with peaks of ^{18}O concentration at the TPB, while under lower cathodic polarization, the diffusion paths of ^{18}O are observed in a broad band with the width of about 2 μm. With the SIMS imaging technique, Horita et al [159] investigated the influence of anodic polarization on the electrocatalytic activities at the Ni-YSZ interfaces for CH_4 decomposition and elimination of carbon deposition. Labelled gases such as D_2O and $^{18}O_2$ were used to identify the movements of hydrogen and oxygen. It was suggested that a significant carbon deposition was observed on the Ni electrode under open circuit condition at 1073 K, and the anodic polarization was found to be effective in eliminating the deposited carbon, suggesting that the oxygen supplied to the Ni electrode effectively oxidizes the deposited carbon. The SIMS imaging technique has been used by many researchers to examine the surface element distribution. For example, Kreka et al [139] used SIMS to image the contact area between Ni electrode and YSZ under the impact of strong cathodic polarization. Ai et al [160] performed SIMS imaging technique to analyse the directly assembled electrode/electrolyte interface under the influence of polarization. Chen et al [161] also adopted this technique to examine the boron deposition at the electrode/electrolyte interface after anodic polarization.

2.4.2 Raman spectroscopy

Raman spectroscopy is a technique that used to investigate molecule vibration, rotation and other low-frequency modes, and it relies on inelastic scattering of a laser beam in the visible, near infrared or near ultraviolet range. The laser light interacts with the molecular vibrations in the sample, resulting in the energy of the laser being shifted, and the shift in energy gives information about the vibrational modes in the sample. Due to the nature of the Raman technique, it is widely adopted in SOFCs [162-165].

Agarkov et al [164] performed *in-situ* Raman spectroscopy to analyse the interfaces between Ni-based anodes and YSZ electrolyte, and the kinetics of NiO reduction at the anode/electrolyte interface under open circuit conditions was assessed at 400-600 ^{o}C. The novel experimental approach for *in-situ* analysis of the inner interfaces in SOFCs under operating conditions was validated, and the behaviour of the cermet anodes during reduction was found capable of being described by the classical Avrami model. The authors used this technique to further investigate the anode/electrolyte interface under current load and found the area of 460 cm^{-1} Raman peak of ceria exhibits detectable variation in terms of oxygen nonstoichiometry with the anodic current and hydrogen partial pressure. Meng et al [166] also used the Raman spectroscopy to study the carbon resistance of Metal-$BaZr_{0.1}Ce_{0.7}Y_{0.1}Yb_{0.1}O_{3-\delta}$ (M-BZCYYb) anode that close to the anode/electrolyte interface. The peaks at 1350 cm^{-1} (D: disordered carbon) and 1580 cm^{-1} (G: graphitic carbon) were observed for Pd- and Ni-BZCYYb anodes after 12 h exposure in dry CH_4, indicating carbon deposition (Figure 2.22). Zhao et al [163] and Wang et al [167] carried out a Raman spectroscopy study of chromium and sulphur deposition and poisoning on LSCF electrode, and the Raman mapping results clearly indicated the formation of $SrCrO_4$ (at wavelength of 860 cm^{-1}) and $SrSO_4$ (at wavelength of 1000 cm^{-1}). It was proposed that the SrO surface segregation from the electrode plays an important role in the nucleation and grain growth for the Cr deposition process.

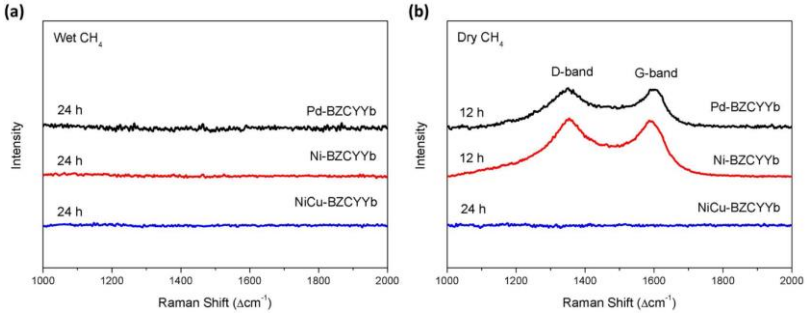

Figure 2.22 Raman spectra of M-BZCYYb anodes exposed to (a) wet CH_4 and (b) dry CH_4 at 750 ^oC for various durations of time [166].

2.4.3 X-ray photoelectron spectroscopy

X-ray photoelectron spectroscopy (XPS) is a technique for analysing the surface chemistry of a material, and can measure the elemental composition, empirical formula, chemical state and electronic state of the elements within a material. XPS spectra are obtained by irradiating a solid surface with a beam of X-rays while simultaneously measuring the kinetic energy and electrons that are emitted from the top 1-10 nm of the material being analysed. This technique has been widely used to study the surface element composition and chemistry of the electrode/electrolyte interface in solid oxide fuel cells [36, 49, 168-176].

Backhaus-Ricoult et al [36] conducted an *in-situ* study using XPS to investigate the LSM electrode/YSZ electrolyte interface chemistry after cathodic polarization. Under increasingly negative bias, Mn was found to exhibit a continuous reduction in its average surface oxidation state. Under anodic polarization or open circuit condition, Mn adopted an oxidation state of 4^+ at the LSM surface, and a mixed oxidation state of 3^+ - 4^+ was found under low cathodic polarization. Under strong cathodic polarization Mn reached an average surface oxidation state close to 2^+. Manganese was observed to spread in response to an increase in cathodic bias from the TPB over the electrolyte surface and was also found to retreat slowly when the bias was released or faster when an anodic bias applied (Figure 2.23). The authors then proposed that the electrochemical activation of LSM cathode under cathodic polarization was strongly related to the rapid spread of the partially reduced manganese oxide species from the three phase boundary over the electrolyte surface, thus providing high electronic conductivity in the electrolyte surface and promoting the direct incorporation of oxygen into the electrolyte. Chen et al [115, 161] also adopted XPS technique to examine the boron and chromium deposition and poisoning of LSM oxygen electrodes under the influence of anodic polarization. For instance, after anodic polarization at 500 mA cm^{-2} for 20 h in the presence of the Fe-Cr interconnect, three distinctive $Cr2p_{3/2}$ peaks were observed at LSM/YSZ interface, which can be ascribed to the formation of Cr_2O_3, Cr_2O_5 and $SrCrO_4$.

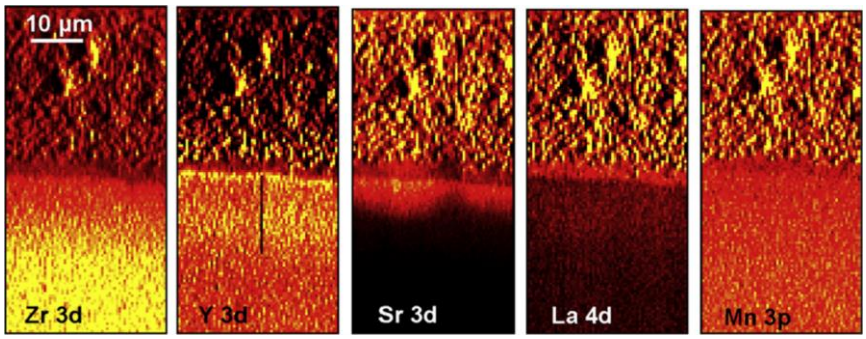

Figure 2.23 XPS spectro-images of Zr 3d, Y 3d, Sr 3d, La 4d and Mn 3p peaks in the TPB region at bias of -0.6 V. The upper portion of the image is LSM particles, while the bottom is the YSZ electrolyte. The yellow contrast corresponds to high concentration [36].

2.4.4 X-ray nano-computed tomography

As a comparison to the destructive nature of FIB tomography, X-ray nano-computed tomography (X-ray nano-CT) has a significant benefit of being non-destructive to the sample, allowing direct comparison of a microstructure before and after treatment, providing a valuable method for characterization of materials at submicrometer length scale.

Izzo et al [177] adopted the nano-CT technique to image the 3D microstructure of a SOFC anode (Ni/YSZ) at a spatial resolution of 42.7 nm without physically removing the material. The reconstructed volume data was visualized as 3D images to calculate the porosity and tortuosity of the material, which showed good agreement with other direct-measurement techniques. Guan et al [178] used X-ray nano-CT technique to visualize the 3D microstructure of Ni/YSZ, and the model was utilized to characterize and quantify the Ni/YSZ interface and volume specific TPB length. Shearing et al [150] provided a comparison study of FIB and X-ray nano-CT techniques regarding the prediction of pore and solid volume fraction of a composite electrode. The comparison of the porosity data acquired from the two reconstruction volumes provided good agreement, suggesting that a sacrifice in resolution could be couple with an increased reconstruction volume without compromising key microstructural information.

2.4.5 Atomic force microscopy

Atomic force microscopy (AFM) works by scanning a probe over a sample surface, building up a map of the height or topography of the surface as it goes along, and it demonstrates a resolution on the order of a nanometer. The AFM has been widely

utilized to acquire the topographic information of the electrode/electrolyte interface in solid oxide fuel cells [49, 110, 136, 167, 174, 179].

Wang et al [180] used AFM to investigate the active reaction sites for ORR at LSM/YSZ interface under strong cathodic polarization conditions. The LSM cathode was directly painted on the YSZ electrolyte without high temperature sintering, and cathodic polarization as high as 2000 mA cm^{-2} was applied to the LSM/YSZ cell at 800^{o}C. Under the influence of polarization, the polarization resistance of the cell decreased significantly, and the AFM study at the LSM/YSZ interface revealed obvious topographical changes. A large number of clusters were formed on the YSZ electrolyte surface, serving as TPB contact points for oxygen incorporation. Such morphological changes at the electrode/electrolyte interface were proposed to be a result of oxygen incorporation process under large cathodic current passage. Jiang et al [51, 52] also used AFM to study and compare the electrode/electrolyte interface under the influence of high temperature and cathodic polarization. Mitterdorfer et al [46] adopted AFM technique to investigate the $La_2Zr_2O_7$ formation at LSM/YSZ interface at a function of Mn non-stoichiometry. The LZO phase was characterized to be cube-like islands, growing in between the cathode grains and the YSZ surface.

2.5 Conclusions

In summary, this chapter has reviewed recent progress in studying the electrode/electrolyte interfaces under the influence of various conditions in SOFCs. The correlation between the cell performance and interface phenomena such as element segregation, impurity contamination, micropore formation and interfacial reaction, are discussed with respect to the current research advances. Moreover, the commonly adopted characterisation techniques for examining the interface are evaluated and summarised.

It has been shown that the evolution of electrode/electrolyte interface critically relates to the ageing and performance of a SOFC device, and therefore understanding the fundamental mechanism and reasons for its change can provide valuable insights to control the interface evolution and to develop the next generations of SOFCs. We have presented that the interface can be affected and developed by heat treatment, polarisation, impregnation and addition of bi-layered electrolyte structure, and many

of these methods have demonstrated great potential to effectively improve the electrochemical performance of SOFCs. Nevertheless, limited by the cost and scale of manufacturing, these modification methods need to be further investigated to meet the requirement of commercialisation. In addition, the development and application of state-of-the-art characterisation techniques, which are essential and powerful tools, will largely allow us to better understand the evolution of interface and to optimise future SOFC devices. Combined with electrochemical characterisation, techniques such as scanning transmission electron microscopy, focused ion beam, nano-SIMS, *in situ* Raman and XPS, provide detailed information with respect to the composition, microstructure and crystallography of the evolving interface. However, there is still much work to do to further develop the *in situ* and *in operando* techniques, which are capable of examining the real-time chemistry and structure on the nanoscale in three dimensions. Considering the significant role of electrode/electrolyte interface in SOFCs, it is worth paying great effort to understand its evolving mechanism and to design intricate interface nanostructure.

2.6 References

[1] S. Singhal, Advances in solid oxide fuel cell technology, Solid State Ionics, 135 (2000) 305-313.

[2] E. Fabbri, L. Bi, D. Pergolesi, E. Traversa, Towards the next generation of solid oxide fuel cells operating below 600 degrees c with chemically stable proton-conducting electrolytes, Adv Mater, 24 (2012) 195-208.

[3] M.A. Laguna-Bercero, Recent advances in high temperature electrolysis using solid oxide fuel cells: A review, Journal of Power Sources, 203 (2012) 4-16.

[4] K.T. Lee, H.S. Yoon, E.D. Wachsman, The evolution of low temperature solid oxide fuel cells, Journal of Materials Research, 27 (2012) 2063-2078.

[5] S. Hossain, A.M. Abdalla, S.N.B. Jamain, J.H. Zaini, A.K. Azad, A review on proton conducting electrolytes for clean energy and intermediate temperature-solid oxide fuel cells, Renewable and Sustainable Energy Reviews, 79 (2017) 750-764.

[6] N. Mahato, A. Banerjee, A. Gupta, S. Omar, K. Balani, Progress in material selection for solid oxide fuel cell technology: A review, Progress in Materials Science, 72 (2015) 141-337.

[7] W. Wang, C. Su, Y. Wu, R. Ran, Z. Shao, Progress in solid oxide fuel cells with nickel-based anodes operating on methane and related fuels, Chem Rev, 113 (2013) 8104-8151.

[8] J. Jeong, S.-W. Baek, J. Bae, A diesel-driven, metal-based solid oxide fuel cell, Journal of Power Sources, 250 (2014) 98-104.

[9] T.M. Gür, Comprehensive review of methane conversion in solid oxide fuel cells: Prospects for efficient electricity generation from natural gas, Progress in Energy and Combustion Science, 54 (2016) 1-64.

[10] D. Papurello, R. Borchiellini, P. Bareschino, V. Chiodo, S. Freni, A. Lanzini, F. Pepe, G.A. Ortigoza, M. Santarelli, Performance of a Solid Oxide Fuel Cell short-stack with biogas feeding, Applied Energy, 125 (2014) 254-263.

[11] A. Choudhury, H. Chandra, A. Arora, Application of solid oxide fuel cell technology for power generation—A review, Renewable and Sustainable Energy Reviews, 20 (2013) 430-442.

[12] A.B. Stambouli, E. Traversa, Solid oxide fuel cells (SOFCs): a review of an environmentally clean and efficient source of energy, Renewable and Sustainable Energy Reviews, 6 (2002) 433-455.

[13] R.M. Ormerod, Solid oxide fuel cells, Chemical Society Reviews, 32 (2003) 17-28.

[14] S. Wang, S.P. Jiang, Prospects of Fuel Cell Technologies, National Science Review, 4 (2017) 163-166.

[15] B. Singh, S. Ghosh, S. Aich, B. Roy, Low temperature solid oxide electrolytes (LT-SOE): A review, Journal of Power Sources, 339 (2017) 103-135.

[16] E. Bucher, W. Sitte, Long-term stability of the oxygen exchange properties of (La,Sr)1−z(Co,Fe)O3−δ in dry and wet atmospheres, Solid State Ionics, 192 (2011) 480-482.

[17] H. Tu, U. Stimming, Advances, aging mechanisms and lifetime in solid-oxide fuel cells, Journal of Power Sources, 127 (2004) 284-293.

[18] J.T.S. Irvine, D. Neagu, M.C. Verbraeken, C. Chatzichristodoulou, C. Graves, M.B. Mogensen, Evolution of the electrochemical interface in high-temperature fuel cells and electrolysers, Nature Energy, 1 (2016) 15014.

[19] F. Figueiredo, Reactions between a zirconia-based electrolyte and LaCoO3-based electrode materials, Solid State Ionics, 101-103 (1997) 343-349.

[20] M. Chen, Y.L. Liu, A. Hagen, P.V. Hendriksen, F.W. Poulsen, LSM-YSZ Reactions in Different Atmospheres, Fuel Cells, 9 (2009) 833-840.

[21] T. Matsui, M. Komoto, H. Muroyama, K. Eguchi, Interfacial Stability between Air Electrode and Ceria-Based Electrolyte under Cathodic Polarization in Solid Oxide Fuel Cells, Fuel Cells, 14 (2014) 1022-1027.

[22] M. Kuznecov, Diffusion controlled oxygen transport and stability at the perovskite/electrolyte interface, Solid State Ionics, 157 (2003) 371-378.

[23] T. Daio, S. R. Bishop, B. Yildiz, H. L. Tuller, S. M. Lyth J. Hyodo K. Kaneko, N.H. Perry, Specific Cation Diffusion across the (La,Sr)MnO3 (Ce,Gd)O2 interface in SOFCs, (2017).

[24] F. Wang, M.E. Brito, K. Yamaji, D.-H. Cho, M. Nishi, H. Kishimoto, T. Horita, H. Yokokawa, Effect of polarization on Sr and Zr diffusion behavior in LSCF/GDC/YSZ system, Solid State Ionics, 262 (2014) 454-459.

[25] S.P. Simner, M.D. Anderson, M.H. Engelhard, J.W. Stevenson, Degradation Mechanisms of La–Sr–Co–Fe–O[sub 3] SOFC Cathodes, Electrochemical and Solid-State Letters, 9 (2006) A478.

[26] Y.-M. Kim, P. Kim-Lohsoontorn, J. Bae, Effect of unsintered gadolinium-doped ceria buffer layer on performance of metal-supported solid oxide fuel cells using unsintered barium strontium cobalt ferrite cathode, Journal of Power Sources, 195 (2010) 6420-6427.

[27] J.Y. Kim, V.L. Sprenkle, N.L. Canfield, K.D. Meinhardt, L.A. Chick, Effects of Chrome Contamination on the Performance of La[sub 0.6]Sr[sub 0.4]Co[sub 0.2]Fe[sub 0.8]O[sub 3] Cathode Used in Solid Oxide Fuel Cells, Journal of The Electrochemical Society, 153 (2006).

[28] K. Chen, S.-S. Liu, P. Guagliardo, M.R. Kilburn, M. Koyama, S.P. Jiang, A Fundamental Study of Boron Deposition and Poisoning of La0.8Sr0.2MnO3Cathode of Solid Oxide Fuel Cells under Accelerated Conditions, Journal of The Electrochemical Society, 162 (2015) F1282-F1291.

[29] A. Mai, M. Becker, W. Assenmacher, F. Tietz, D. Hathiramani, E. Iverstiffee, D. Stover, W. Mader, Time-dependent performance of mixed-conducting SOFC cathodes, Solid State Ionics, 177 (2006) 1965-1968.

[30] H. Yokokawa, Understanding Materials Compatibility, Annual Review of Materials Research, 33 (2003) 581-610.

[31] H. Yokokawa, Thermodynamic Analysis of Reaction Profiles Between LaMO[sub 3] (M=Ni,Co,Mn) and ZrO[sub 2], Journal of The Electrochemical Society, 138 (1991).

[32] A. Petric, Evaluation of La–Sr–Co–Fe–O perovskites for solid oxide fuel cells and gas separation membranes, Solid State Ionics, 135 (2000) 719-725.

[33] C. Su, Z. Shao, Y. Lin, Y. Wu, H. Wang, Solid oxide fuel cells with both high voltage and power output by utilizing beneficial interfacial reaction, Phys Chem Chem Phys, 14 (2012) 12173-12181.

[34] D. Oh, D. Gostovic, E.D. Wachsman, Mechanism of La0.6Sr0.4Co0.2Fe0.8O3 cathode degradation, Journal of Materials Research, 27 (2012) 1992-1999.

[35] H. Ding, A.V. Virkar, M. Liu, F. Liu, Suppression of Sr surface segregation in La(1-x)Sr(x)Co(1-y)Fe(y)O(3-delta): a first principles study, Phys Chem Chem Phys, 15 (2013) 489-496.

[36] M. Backhaus-Ricoult, K. Adib, T. St.Clair, B. Luerssen, L. Gregoratti, A. Barinov, In-situ study of operating SOFC LSM/YSZ cathodes under polarization by photoelectron microscopy, Solid State Ionics, 179 (2008) 891-895.

[37] H. Moon, S. Kim, S. Hyun, H. Kim, Development of IT-SOFC unit cells with anode-supported thin electrolytes via tape casting and co-firing, International Journal of Hydrogen Energy, 33 (2008) 1758-1768.

[38] T. Fukui, S. Ohara, M. Naito, K. Nogi, Performance and stability of SOFC anode fabricated from NiO–YSZ composite particles, Journal of Power Sources, 110 (2002) 91-95.

[39] S.P. Jiang, Development of lanthanum strontium manganite perovskite cathode materials of solid oxide fuel cells: a review, Journal of Materials Science, 43 (2008) 6799-6833.

[40] T. Matsui, Y. Mikami, H. Muroyama, K. Eguchi, Influence of (La,Sr)MnO3+δ cathode composition on cathode/electrolyte interfacial structure during long-term operation of solid oxide fuel cells, Journal of Power Sources, 242 (2013) 790-796.

[41] Y.L. Liu, A. Hagen, R. Barfod, M. Chen, H.J. Wang, F.W. Poulsen, P.V. Hendriksen, Microstructural studies on degradation of interface between LSM–YSZ cathode and YSZ electrolyte in SOFCs, Solid State Ionics, 180 (2009) 1298-1304.

[42] T. Matsui, Y. Mikami, H. Muroyama, K. Eguchi, Quantitative Analysis of Microstructural Change at the Interface Between (La,Sr)MnO[sub 3] Cathode and YSZ

Electrolyte upon Discharge Operation, Journal of The Electrochemical Society, 157 (2010) B1790.

[43] H. Fukunaga, The relationship between overpotential and the three phase boundary length, Solid State Ionics, 86-88 (1996) 1179-1185.

[44] M. Mukhopadhyay, J. Mukhopadhyay, A.D. Sharma, R.N. Basu, In-situ patterned intra-anode triple phase boundary in SOFC electroless anode: An enhancement of electrochemical performance, International Journal of Hydrogen Energy, 36 (2011) 7677-7682.

[45] T. Horita, T. Tsunoda, K. Yamaji, N. Sakai, T. Kato, a.H. Yokokawa, Microstructures and oxygen diffusion at the LaMnO3 film/yttria-stabilized zirconia interface, Solid State Ionics, 152-153 (2002) 439–446.

[46] A. Mitterdorfer, L.J. Gauckler, La2Zr2O7 formation and oxygen reduction kinetics of the La0.85Sr0.15MnyO3, O2(g)|YSZ system, Solid State Ionics, 111 (1998) 185-218.

[47] M.J. Jørgensen, P. Holtappels, C.C. Appel, Durability test of SOFC cathodes, Journal of Applied Electrochemistry, 30 (2000) 411-418.

[48] M.A. Haider, S. McIntosh, Evidence for Two Activation Mechanisms in LSM SOFC Cathodes, Journal of The Electrochemical Society, 156 (2009).

[49] G.J. la O', R.F. Savinell, Y. Shao-Horn, Activity Enhancement of Dense Strontium-Doped Lanthanum Manganite Thin Films under Cathodic Polarization: A Combined AES and XPS Study, Journal of The Electrochemical Society, 156 (2009) B771-B781.

[50] K. Chen, S.S. Liu, N. Ai, M. Koyama, S.P. Jiang, Why solid oxide cells can be reversibly operated in solid oxide electrolysis cell and fuel cell modes?, Phys Chem Chem Phys, 17 (2015) 31308-31315.

[51] S.P. Jiang, Thermally and Electrochemically Induced Electrode/Electrolyte Interfaces in Solid Oxide Fuel Cells: An AFM and EIS Study, Journal of The Electrochemical Society, 162 (2015) F1119-F1128.

[52] S.P. Jiang, W. Wang, Effect of Polarization on the Interface Between (La,Sr)MnO3 Electrode and Y2O3-ZrO2 Electrolyte, Electrochemical and Solid-State Letters, 8 (2005) A115.

[53] H. Yung, L. Jian, S.P. Jiang, Polarization Promoted Chemical Reaction between Ba0.5Sr0.5Co0.8Fe0.2O3- Cathode and Ceria Based Electrolytes of Solid Oxide Fuel Cells, Journal of the Electrochemical Society, 159 (2012) F794-F798.

[54] M. Watanabe, High Performance Catalyzed-Reaction Layer for Medium Temperature Operating Solid Oxide Fuel Cells, Journal of The Electrochemical Society, 141 (1994) 342.

[55] S.P. Simner, M.D. Anderson, L.R. Pederson, J.W. Stevenson, Performance Variability of La(Sr)FeO[sub 3] SOFC Cathode with Pt, Ag, and Au Current Collectors, Journal of The Electrochemical Society, 152 (2005) A1851.

[56] J. Nielsen, T. Jacobsen, Three-phase-boundary dynamics at Pt/YSZ microelectrodes, Solid State Ionics, 178 (2007) 1001-1009.

[57] J. Nielsen, T. Jacobsen, Three-Phase-Boundary dynamics at metal/YSZ microelectrodes, Solid State Ionics, 178 (2008) 1769-1776.

[58] Y. Xiong, K. Yamaji, H. Kishimoto, M.E. Brito, T. Horita, H. Yokokawa, Deposition of Platinum Particles at LSM/ScSZ/Air Three-Phase Boundaries Using a Platinum Current Collector, Electrochemical and Solid-State Letters, 12 (2009) B31.

[59] Y. Guo, Y. Zhou, D. Chen, H. Shi, R. Ran, Z. Shao, Significant impact of the current collection material and method on the performance of Ba0.5Sr0.5Co0.8Fe0.2O3−δ electrodes in solid oxide fuel cells, Journal of Power Sources, 196 (2011) 5511-5519.

[60] K. Yamaji, T. Shimonosono, H. Kishimoto, M.E. Brito, T. Horita, D.-H. Cho, M. Izuki, F. Wang, H. Yokokawa, Effect of Polarization on Platinum Deposition at LSM/YSZ Interfaces, ECS Transactions, 35 (2011) 2213-2216.

[61] Y. Gong, C. Qin, K. Huang, Can Silver Be a Reliable Current Collector for Electrochemical Tests?, ECS Electrochemistry Letters, 2 (2012) F4-F7.

[62] Y. Guo, Y. Liu, R. Cai, D. Chen, R. Ran, Z. Shao, Electrochemical contribution of silver current collector to oxygen reduction reaction over Ba0.5Sr0.5Co0.8Fe0.2O3−δ electrode on oxygen-ionic conducting electrolyte, International Journal of Hydrogen Energy, 37 (2012) 14492-14500.

[63] S.M. Shin, B.Y. Yoon, J.H. Kim, J.M. Bae, Performance improvement by metal deposition at the cathode active site in solid oxide fuel cells, International Journal of Hydrogen Energy, 38 (2013) 8954-8964.

[64] K. Chen, N. Li, N. Ai, M. Li, Y. Cheng, W.D.A. Rickard, J. Li, S.P. Jiang, Direct application of cobaltite-based perovskite cathodes on the yttria-stabilized zirconia electrolyte for intermediate temperature solid oxide fuel cells, J. Mater. Chem. A, 4 (2016) 17678-17685.

[65] N. Li, N. Ai, S. He, Y. Cheng, W.D.A. Rickard, K. Chen, T. Zhang, S.P. Jiang, Effect of Pd doping on the activity and stability of directly assembled La 0.95 Co 0.19 Fe 0.76 Pd 0.05 O 3-δ cathodes of solid oxide fuel cells, Solid State Ionics, 316 (2018) 38-46.

[66] K. Chen, S. He, N. Li, Y. Cheng, N. Ai, M. Chen, W.D.A. Rickard, T. Zhang, S.P. Jiang, Nb and Pd co-doped La 0.57 Sr 0.38 Co 0.19 Fe 0.665 Nb 0.095 Pd 0.05 O 3-δ as a stable, high performance electrode for barrier-layer-free Y 2 O 3 -ZrO 2 electrolyte of solid oxide fuel cells, Journal of Power Sources, 378 (2018) 433-442.

[67] A. Brisse, J. Schefold, M. Zahid, High temperature water electrolysis in solid oxide cells, International Journal of Hydrogen Energy, 33 (2008) 5375-5382.

[68] M. Ni, M. Leung, D. Leung, Technological development of hydrogen production by solid oxide electrolyzer cell (SOEC), International Journal of Hydrogen Energy, 33 (2008) 2337-2354.

[69] P. Moçoteguy, A. Brisse, A review and comprehensive analysis of degradation mechanisms of solid oxide electrolysis cells, International Journal of Hydrogen Energy, 38 (2013) 15887-15902.

[70] S. Häfele, M. Hauck, J. Dailly, Life cycle assessment of the manufacture and operation of solid oxide electrolyser components and stacks, International Journal of Hydrogen Energy, (2016).

[71] J.H. Myung, D. Neagu, D.N. Miller, J.T. Irvine, Switching on electrocatalytic activity in solid oxide cells, Nature, 537 (2016) 528-531.

[72] Y. Wang, T. Liu, L. Lei, F. Chen, High temperature solid oxide H 2 O/CO 2 co-electrolysis for syngas production, Fuel Processing Technology, 161 (2017) 248-258.

[73] L. Ye, M. Zhang, P. Huang, G. Guo, M. Hong, C. Li, J.T. Irvine, K. Xie, Enhancing CO2 electrolysis through synergistic control of non-stoichiometry and doping to tune cathode surface structures, Nat Commun, 8 (2017) 14785.

[74] R. Knibbe, M.L. Traulsen, A. Hauch, S.D. Ebbesen, M. Mogensen, Solid Oxide Electrolysis Cells: Degradation at High Current Densities, Journal of The Electrochemical Society, 157 (2010) B1209.

[75] K. Chen, S.P. Jiang, Failure mechanism of (La,Sr)MnO3 oxygen electrodes of solid oxide electrolysis cells, International Journal of Hydrogen Energy, 36 (2011) 10541-10549.

[76] K. Chen, N. Ai, S.P. Jiang, Performance and stability of (La,Sr)MnO3–Y2O3–ZrO2 composite oxygen electrodes under solid oxide electrolysis cell operation conditions, International Journal of Hydrogen Energy, 37 (2012) 10517-10525.

[77] K. Chen, N. Ai, S.P. Jiang, Reasons for the high stability of nano-structured (La,Sr)MnO3 infiltrated Y2O3–ZrO2 composite oxygen electrodes of solid oxide electrolysis cells, Electrochemistry Communications, 19 (2012) 119-122.

[78] K. Chen, N. Ai, S.P. Jiang, Development of (Gd,Ce)O[sub 2]-Impregnated (La,Sr)MnO[sub 3] Anodes of High Temperature Solid Oxide Electrolysis Cells, Journal of The Electrochemical Society, 157 (2010) P89.

[79] N. Ai, K. Chen, S.P. Jiang, A fundamental study of infiltrated CeO2 and (Gd,Ce)O2 nanoparticles on the electrocatalytic activity of Pt cathodes of solid oxide fuel cells, Solid State Ionics, 233 (2013) 87-94.

[80] K. Chen, N. Ai, S.P. Jiang, Performance and structural stability of Gd0.2Ce0.8O1.9 infiltrated La0.8Sr0.2MnO3 nano-structured oxygen electrodes of solid oxide electrolysis cells, International Journal of Hydrogen Energy, 39 (2014) 10349-10358.

[81] K. Chen, N. Ai, S.P. Jiang, Enhanced electrochemical performance and stability of (La,Sr)MnO3–(Gd,Ce)O2 oxygen electrodes of solid oxide electrolysis cells by palladium infiltration, International Journal of Hydrogen Energy, 37 (2012) 1301-1310.

[82] S.J. Kim, G.M. Choi, Stability of LSCF electrode with GDC interlayer in YSZ-based solid oxide electrolysis cell, Solid State Ionics, 262 (2014) 303-306.

[83] N. Ai, S. He, N. Li, Q. Zhang, W.D.A. Rickard, K. Chen, T. Zhang, S.P. Jiang, Suppressed Sr segregation and performance of directly assembled La 0.6 Sr 0.4 Co 0.2 Fe 0.8 O 3-δ oxygen electrode on Y 2 O 3 -ZrO 2 electrolyte of solid oxide electrolysis cells, Journal of Power Sources, 384 (2018) 125-135.

[84] A.V. Virkar, Mechanism of oxygen electrode delamination in solid oxide electrolyzer cells, International Journal of Hydrogen Energy, 35 (2010) 9527-9543.

[85] T. Jacobsen, M. Mogensen, The Course of Oxygen Partial Pressure and Electric Potentials across an Oxide Electrolyte Cell, ECS Transactions, 13 (2008) 259-273.

[86] S.N. Rashkeev, M.V. Glazoff, Atomic-scale mechanisms of oxygen electrode delamination in solid oxide electrolyzer cells, International Journal of Hydrogen Energy, 37 (2012) 1280-1291.

[87] K. Eguchi, Power generation and steam electrolysis characteristics of an electrochemical cell with a zirconia- or ceria-based electrolyte, Solid State Ionics, 86-88 (1996) 1245-1249.

[88] A. Aguadero, D. Pérez-Coll, J.A. Alonso, S.J. Skinner, J. Kilner, A New Family of Mo-Doped SrCoO3−δ Perovskites for Application in Reversible Solid State Electrochemical Cells, Chemistry of Materials, 24 (2012) 2655-2663.

[89] C. Graves, Reversing and Repairing Microstructure Degradation in Solid Oxide Cells during Operation, ECS Transactions, 57 (2013) 3127-3136.

[90] G.A. Hughes, K. Yakal-Kremski, S.A. Barnett, Life testing of LSM-YSZ composite electrodes under reversing-current operation, Phys Chem Chem Phys, 15 (2013) 17257-17262.

[91] P. Puengjinda, H. Nishino, K. Kakinuma, M.E. Brito, H. Uchida, Effect of Microstructure on Performance of Double-Layer Hydrogen Electrodes for Reversible SOEC/SOFC, Journal of The Electrochemical Society, 164 (2017) F889-F894.

[92] J. Wang, T. Yang, L. Lei, K. Huang, Ta-Doped SrCoO3−δ as a promising bifunctional oxygen electrode for reversible solid oxide fuel cells: a focused study on stability, J. Mater. Chem. A, 5 (2017) 8989-9002.

[93] C. Graves, S.D. Ebbesen, S.H. Jensen, S.B. Simonsen, M.B. Mogensen, Eliminating degradation in solid oxide electrochemical cells by reversible operation, Nat Mater, 14 (2015) 239-244.

[94] Z. He, L. Zhang, S. He, N. Ai, K. Chen, Y. Shao, S.P. Jiang, Cyclic polarization enhances the operating stability of La0.57Sr0.38Co0.18Fe0.72Nb0.1O3-δ oxygen electrode of reversible solid oxide cells, Journal of Power Sources, 404 (2018) 73-80.

[95] K. Shimura, H. Nishino, K. Kakinuma, M.E. Brito, H. Uchida, High durability of La0.6Sr0.4Co0.2Fe0.8O3/samaria-doped ceria (SDC) composite oxygen electrode with SDC interlayer for reversible solid oxide fuel cell/solid oxide electrolysis cell, Journal of the Ceramic Society of Japan, 125 (2017) 218-222.

[96] H. Fan, M. Keane, P. Singh, M. Han, Electrochemical performance and stability of lanthanum strontium cobalt ferrite oxygen electrode with gadolinia doped ceria barrier layer for reversible solid oxide fuel cell, Journal of Power Sources, 268 (2014) 634-639.

[97] C. Brugnoni, SOFC cathode/electrolyte interface. Part I: Reactivity between La0.85Sr0.15MnO3 and ZrO2-Y2O3, Solid State Ionics, 76 (1995) 177-182.

[98] H. Lee, Origin of Cathodic degradation and new phase formation at the La0.9Sr0.1MnO3/YSZ interface, Solid State Ionics, 90 (1996) 133-140.

[99] J. Mizusaki, A Chemical Diffusion-Controlled Electrode Reaction at the Compact La1_SrMnO3/Stabilized Zirconia Interface in Oxygen Atmospheres, Journal of The Electrochemical Society, 143 (1996) 3065-3073.

[100] Y.L. Liu, K. Thydén, M. Chen, A. Hagen, Microstructure degradation of LSM-YSZ cathode in SOFCs operated at various conditions, Solid State Ionics, 206 (2012) 97-103.

[101] Tatsuya Kawada, Natsuko Sakai, Harumi Yokokawa, M. Dokiya, Reaction between solid oxide fuel cell materials, Solid State Ionics, 50 (1992) 189-196.

[102] V. Kharton, E. Naumovich, V. Samokhval, Formation and properties of reaction layers of cobaltite electrodes on bismuth oxide electrolytes, Solid State Ionics, 99 (1997) 269-280.

[103] K. Kleveland, M.-A. Einarsrud, C.R. Schmidt, S. Shamsili, S. Faaland, K. Wiik, T. Grande, Reactions between Strontium-Substituted Lanthanum Manganite and Yttria-Stabilized Zirconia: II, Diffusion Couples, Journal of the American Ceramic Society, 82 (2004) 729-734.

[104] Jin-Ping Zhang, San-Ping Jiang, Jonathan G. Love, K.F. and, S.P.S. Badwal, Chemical interactions between strontium-doped praseodymium manganite and 3 mol% yttria-zirconia, Journal of Materials Chemistry, 8 (1998) 2787–2794.

[105] H. Dulli, P.A. Dowben, S.H. Liou, E.W. Plummer, Surface segregation and restructuring of colossal-magnetoresistant manganese perovskites La0.65Sr0.35MnO3, Physical Review B, 62 (2000) 14629-14632.

[106] Z.-P. Li, T. Mori, G.J. Aucheterlonie, J. Zou, J. Drennan, M. Miyayama, Diffusion and segregation along grain boundary at the electrolyte–anode interface in IT-SOFC, Solid State Ionics, 191 (2011) 55-60.

[107] W. Jung, H.L. Tuller, Investigation of surface Sr segregation in model thin film solid oxidefuel cell perovskite electrodes, Energy Environ. Sci., 5 (2012) 5370-5378.

[108] L. Zhao, J. Drennan, C. Kong, S. Amarasinghe, S.P. Jiang, Insight into surface segregation and chromium deposition on La0.6Sr0.4Co0.2Fe0.8O3−δ cathodes of solid oxide fuel cells, Journal of Materials Chemistry A, 2 (2014) 11114.

[109] Z. Pan, Q. Liu, L. Zhang, X. Zhang, S.H. Chan, Effect of Sr Surface Segregation of La0.6Sr0.4Co0.2Fe0.8O3 − δElectrode on Its Electrochemical Performance in SOC, Journal of The Electrochemical Society, 162 (2015) F1316-F1323.

[110] Y. Yu, K.F. Ludwig, J.C. Woicik, S. Gopalan, U.B. Pal, T.C. Kaspar, S.N. Basu, Effect of Sr Content and Strain on Sr Surface Segregation of La1-xSrxCo0.2Fe0.8O3-delta as Cathode Material for Solid Oxide Fuel Cells, ACS Appl Mater Interfaces, 8 (2016) 26704-26711.

[111] W. Lee, J.W. Han, Y. Chen, Z. Cai, B. Yildiz, Cation size mismatch and charge interactions drive dopant segregation at the surfaces of manganite perovskites, J Am Chem Soc, 135 (2013) 7909-7925.

[112] K. Chen, N. Li, N. Ai, Y. Cheng, W.D. Rickard, S.P. Jiang, Polarization-Induced Interface and Sr Segregation of in Situ Assembled La0.6Sr0.4Co0.2Fe0.8O3-delta Electrodes on Y2O3-ZrO2 Electrolyte of Solid Oxide Fuel Cells, ACS Appl Mater Interfaces, 8 (2016) 31729-31737.

[113] J. Matsuda, S. Kanae, T. Kawabata, J.T. Chou, Y. Inoue, S. Taniguchi, K. Sasaki, TEM and ETEM Study on SrZrO3Formation at the LSCF/GDC/YSZ Interfaces, ECS Transactions, 78 (2017) 993-1001.

[114] A.K. Huber, M. Falk, M. Rohnke, B. Luerssen, L. Gregoratti, M. Amati, J. Janek, In situ study of electrochemical activation and surface segregation of the SOFC electrode material La0.75Sr0.25Cr0.5Mn0.5O(3+/-delta), Phys Chem Chem Phys, 14 (2012) 751-758.

[115] K. Chen, J. Hyodo, A. Dodd, N. Ai, T. Ishihara, L. Jian, S.P. Jiang, Chromium deposition and poisoning of La0.8Sr0.2MnO3 oxygen electrodes of solid oxide electrolysis cells, Faraday Discuss, 182 (2015) 457-476.

[116] J. van Roosmalen, Chemical reactivity and interdiffusion of (La, Sr)MnO3 and (Zr, Y)O2, solid oxide fuel cell cathode and electrolyte materials, Solid State Ionics, 52 (1992) 303-312.

[117] D. Waller, J.D. Sirman, J.A. Kilner, Manganese diffusion in single crystal and polycrystalline yttria stabilised zirconia, 1997.

[118] T. Kawashima, M. Hishinuma, Phase Transformation of Yttria-Stabilized Zirconia (3 mol% Y2O3) in Fuel Cell Caused by Manganese Diffusion, Materials Transactions, JIM, 39 (1998) 617-620.

[119] C. Argirusis, M. Kilo, A. Müller, A. Weber, G. Borchardt, E. Ivers-Tiffée, Interdiffusion between electrode and electrolyte materials for cathode supported SOFCs with thin film electrolytes, 10th International IUPAC conference on high temperature materials chemistry (Jülich, Germany), 2000.

[120] S.P.S. Badwal, S.P. Jiang, J. Love, J. Nowotny, M. Rekas, E.R. Vance, Chemical diffusion in perovskite cathodes of solid oxide fuel cells: the Sr doped LaMn1−xMxO3 (M Co, Fe) systems, Ceramics International, 27 (2001) 419-429.

[121] M. Katsuki, S. Wang, M. Dokiya, a.T. Hashimoto, High temperature properties of La0.6Sr0.4Co0.8Fe0.2O3-d oxygen nonstoichiometry and chemical diffusion constant, Solid State Ionics, 156 (2003) 453–461.

[122] F. Ye, T. Mori, D.R. Ou, J. Zou, J. Drennan, S. Nakayama, M. Miyayama, Effect of nickel diffusion on the microstructure of Gd-doped ceria (GDC) electrolyte film supported by Ni–GDC cermet anode, Solid State Ionics, 181 (2010) 646-652.

[123] M. Izuki, M.E. Brito, K. Yamaji, H. Kishimoto, D.-H. Cho, T. Shimonosono, T. Horita, H. Yokokawa, Interfacial stability and cation diffusion across the LSCF/GDC interface, Journal of Power Sources, 196 (2011) 7232-7236.

[124] Z.-P. Li, T. Mori, G.J. Auchterlonie, Y. Guo, J. Zou, J. Drennan, M. Miyayama, Mutual Diffusion and Microstructure Evolution at the Electrolyte−Anode Interface in Intermediate Temperature Solid Oxide Fuel Cell, The Journal of Physical Chemistry C, 115 (2011) 6877-6885.

[125] L.M. Ushkalov, E.M. Brodnikovs'kyi, N.O. Lysunenko, M.M. Brychevs'kyi, B.D. Vasyliv, O.D. Vasyl'ev, Diffusion Processes Between the Barrier Cathodic Layer and the Electrolyte of a Solid-Oxide Fuel Cell, Materials Science, 51 (2016) 555-562.

[126] A. Grosjean, O. Sanseau, V. Radmilovic, A. Thorel, Reactivity and diffusion between La0.8Sr0.2MnO3 and ZrO2 at interfaces in SOFC cores by TEM analyses on FIB samples, Solid State Ionics, 177 (2006) 1977-1980.

[127] N. Li, N. Ai, K. Chen, Y. Cheng, S. He, M. Saunders, A. Dodd, A. Suvorova, S.P. Jiang, In situ assembled La0.8Sr0.2MnO3 cathodes on a Y2O3–ZrO2 electrolyte of solid oxide fuel cells – interface and electrochemical activity, RSC Adv., 6 (2016) 99211-99219.

[128] F. Wang, M. Nishi, M.E. Brito, H. Kishimoto, K. Yamaji, H. Yokokawa, T. Horita, Sr and Zr diffusion in LSCF/10GDC/8YSZ triplets for solid oxide fuel cells (SOFCs), Journal of Power Sources, 258 (2014) 281-289.

[129] M. Li, K. Chen, B. Hua, J.-l. Luo, W.D.A. Rickard, J. Li, J.T.S. Irvine, S.P. Jiang, Smart utilization of cobaltite-based double perovskite cathodes on barrier-layer-free zirconia electrolyte of solid oxide fuel cells, Journal of Materials Chemistry A, 4 (2016) 19019-19025.

[130] N. Ai, N. Li, S. He, Y. Cheng, M. Saunders, K. Chen, T. Zhang, S.P. Jiang, Highly active and stable Er0.4Bi1.6O3 decorated La0.76Sr0.19MnO3+δ nanostructured oxygen electrodes for reversible solid oxide cells, J. Mater. Chem. A, 5 (2017) 12149-12157.

[131] M. Chen, Y. Cheng, S. He, N. Ai, J.-P. Veder, W.D.A. Rickard, M. Saunders, K. Chen, T. Zhang, S.P. Jiang, Active, durable bismuth oxide-manganite composite oxygen electrodes: Interface formation induced by cathodic polarization, Journal of Power Sources, 397 (2018) 16-24.

[132] S. Primdahl, B.F. Sørensen, M. Mogensen, Effect of Nickel Oxide/Yttria-Stabilized Zirconia Anode Precursor Sintering Temperature on the Properties of Solid Oxide Fuel Cells, Journal of the American Ceramic Society, 83 (2004) 489-494.

[133] D.R. Ou, T. Mori, F. Ye, M. Miyayama, S. Nakayama, J. Zou, G.J. Auchterlonie, J. Drennan, Microstructural Characteristics of SDC Electrolyte Film Supported by Ni–SDC Cermet Anode, Journal of The Electrochemical Society, 156 (2009).

[134] O.A. Marina, L.R. Pederson, C.A. Coyle, E.C. Thomsen, D.J. Edwards, Polarization-Induced Interfacial Reactions Between Nickel and Selenium in Ni/Zirconia SOFC Anodes and Comparison with Sulfur Poisoning, Journal of The Electrochemical Society, 158 (2011).

[135] Y. Liu, C. Jiao, Microstructure degradation of an anode/electrolyte interface in SOFC studied by transmission electron microscopy, Solid State Ionics, 176 (2005) 435-442.

[136] K. Vels Jensen, Microstructural and chemical changes at the Ni/YSZ interface, Solid State Ionics, 144 (2001) 197-209.

[137] R.J. Aaberg, Morphological Changes at the Interface of the Nickel-Yttria Stabilized Zirconia Point Electrode, Journal of The Electrochemical Society, 145 (1998).

[138] D. Klotz, B. Butz, A. Leonide, J. Hayd, D. Gerthsen, E. Ivers-Tiffée, Performance Enhancement of SOFC Anode Through Electrochemically Induced Ni/YSZ Nanostructures, Journal of The Electrochemical Society, 158 (2011) B587-B595.

[139] K. Kreka, K.V. Hansen, M.B. Mogensen, K. Norrman, C. Chatzichristodoulou, T. Jacobsen, The Impact of Strong Cathodic Polarization on Ni|YSZ Microelectrodes, Journal of The Electrochemical Society, 165 (2018) F253-F263.

[140] A. Hauch, S.D. Ebbesen, S.H. Jensen, M. Mogensen, Solid Oxide Electrolysis Cells: Microstructure and Degradation of the Ni/Yttria-Stabilized Zirconia Electrode, Journal of The Electrochemical Society, 155 (2008) B1184.

[141] M. Chen, Y.L. Liu, J.J. Bentzen, W. Zhang, X. Sun, A. Hauch, Y. Tao, J.R. Bowen, P.V. Hendriksen, Microstructural Degradation of Ni/YSZ Electrodes in Solid Oxide Electrolysis Cells under High Current, Journal of the Electrochemical Society, 160 (2013) F883-F891.

[142] K. Chen, X. Chen, Z. Lü, N. Ai, X. Huang, W. Su, Performance of an anode-supported SOFC with anode functional layers, Electrochimica Acta, 53 (2008) 7825-7830.

[143] X. Zhang, Y.e. Qiu, F. Jin, F. Guo, Y. Song, B. Zhu, A highly active anode functional layer for solid oxide fuel cells based on proton-conducting electrolyte BaZr0.1Ce0.7Y0.2O3−δ, Journal of Power Sources, 241 (2013) 654-659.

[144] A. Konno, H. Iwai, K. Inuyama, A. Kuroyanagi, M. Saito, H. Yoshida, K. Kodani, K. Yoshikata, Mesoscale-structure control at anode/electrolyte interface in solid oxide fuel cell, Journal of Power Sources, 196 (2011) 98-109.

[145] A. Rednyk, T. Mori, S. Yamamoto, A. Suzuki, Y. Yamamoto, T. Tanji, N. Isaka, P. Kúš, S. Ito, F. Ye, Design of Active Sites on Nickel in the Anode of Intermediate-Temperature Solid Oxide Fuel Cells using Trace Amount of Platinum Oxides, ChemPlusChem, (2018).

[146] M. Baram, W.D. Kaplan, Quantitative HRTEM analysis of FIB prepared specimens, J Microsc, 232 (2008) 395-405.

[147] A.L. Soldati, L. Baqué, H. Troiani, C. Cotaro, A. Schreiber, A. Caneiro, A. Serquis, High resolution FIB-TEM and FIB-SEM characterization of electrode/electrolyte interfaces in solid oxide fuel cells materials, International Journal of Hydrogen Energy, 36 (2011) 9180-9188.

[148] S.S. Liu, S. Matsumura, M. Koyama, Boundary Observation and Contrast Tuning of Ni/YSZ Anode by TEM and FIB-SEM, ECS Transactions, 68 (2015) 1275-1279.

[149] S.S. Liu, A. Takayama, S. Matsumura, M. Koyama, Image contrast enhancement of Ni/YSZ anode during the slice-and-view process in FIB-SEM, J Microsc, 261 (2016) 326-332.

[150] P.R. Shearing, J. Gelb, N.P. Brandon, X-ray nano computerised tomography of SOFC electrodes using a focused ion beam sample-preparation technique, Journal of the European Ceramic Society, 30 (2010) 1809-1814.

[151] M. Jublot, M. Texier, Sample preparation by focused ion beam micromachining for transmission electron microscopy imaging in front-view, Micron, 56 (2014) 63-67.

[152] R. Knibbe, J. Hjelm, M. Menon, N. Pryds, M. Søgaard, H.J. Wang, K. Neufeld, Cathode-Electrolyte Interfaces with CGO Barrier Layers in SOFC, Journal of the American Ceramic Society, 93 (2010) 2877-2883.

[153] S. Wang, T.A. Cruse, M. Krumpelt, B.J. Ingram, P.A. Salvador, Microstructural Degradation of (La,Sr)MnO[sub 3]/YSZ Cathodes in Solid Oxide Fuel Cells with Uncoated E-Brite Interconnects, Journal of The Electrochemical Society, 158 (2011).

[154] S.S. Liu, Z. Jiao, N. Shikazono, S. Matsumura, M. Koyama, Observation of the Ni/YSZ Interface in a Conventional SOFC, Journal of the Electrochemical Society, 162 (2015) F750-F754.

[155] J.R. Wilson, W. Kobsiriphat, R. Mendoza, H.Y. Chen, J.M. Hiller, D.J. Miller, K. Thornton, P.W. Voorhees, S.B. Adler, S.A. Barnett, Three-dimensional reconstruction of a solid-oxide fuel-cell anode, Nat Mater, 5 (2006) 541-544.

[156] J. Yang, H. Muroyama, T. Matsui, K. Eguchi, The influence of discharge operation on the microstructure of strontium-doped lanthanum manganite cathode for solid oxide fuel cells, Journal of Power Sources, 204 (2012) 25-33.

[157] R.A. De Souza, J.A. Kilner, J.F. Walker, A SIMS study of oxygen tracer diffusion and surface exchange in La0.8Sr0.2MnO3+δ, Materials Letters, 43 (2000) 43-52.

[158] T. Horita, Oxygen reduction sites and diffusion paths at La0.9Sr0.1MnO3-x/yttria-stabilized zirconia interface for different cathodic overvoltages by secondary-ion mass spectrometry, Solid State Ionics, 127 (2000) 55-65.

[159] T. Horita, K. Yamaji, T. Kato, H. Kishimoto, Y. Xiong, N. Sakai, M.E. Brito, H. Yokokawa, Imaging of CH4 decomposition around the Ni/YSZ interfaces under anodic polarization, Journal of Power Sources, 145 (2005) 133-138.

[160] N. Ai, N. Li, W.D. Rickard, Y. Cheng, K. Chen, S.P. Jiang, Highly Stable Sr-Free Cobaltite-Based Perovskite Cathodes Directly Assembled on a Barrier-Layer-Free Y2 O3 - ZrO2 Electrolyte of Solid Oxide Fuel Cells, ChemSusChem, 10 (2017) 993-1003.

[161] K. Chen, J. Hyodo, N. Ai, T. Ishihara, S.P. Jiang, Boron deposition and poisoning of La0.8Sr0.2MnO3 oxygen electrodes of solid oxide electrolysis cells under accelerated operation conditions, International Journal of Hydrogen Energy, (2015).

[162] L. Zhao, J. Hyodo, T. Ishihara, K. Sasaki, S.R. Bishop, XRD and Raman Spectroscopy Study of Mn Solubility in Cerium Oxide, ECS Transactions, 57 (2013) 1607-1612.

[163] L. Zhao, J. Zhang, T. Becker, S.P. Jiang, Raman Spectroscopy Study of Chromium Deposition on La0.6Sr0.4Co0.2Fe0.8O3- Cathode of Solid Oxide Fuel Cells, Journal of the Electrochemical Society, 161 (2014) F687-F693.

[164] D.A. Agarkov, I.N. Burmistrov, F.M. Tsybrov, I.I. Tartakovskii, V.V. Kharton, S.I. Bredikhin, In-situ Raman spectroscopy analysis of the interfaces between Ni-based SOFC anodes and stabilized zirconia electrolyte, Solid State Ionics, 302 (2017) 133-137.

[165] D.A. Agarkov, I.N. Burmistrov, F.M. Tsybrov, I.I. Tartakovskii, V.V. Kharton, S.I. Bredikhin, In-situ Raman spectroscopy analysis of the interface between ceria-containing SOFC anode and stabilized zirconia electrolyte, Solid State Ionics, 319 (2018) 125-129.

[166] M. Li, B. Hua, J. Pu, B. Chi, L. Jian, Electrochemical performance and carbon deposition resistance of M-BaZr(0).(1)Ce(0).(7)Y(0).(1)Yb(0).(1)O(3)(-)delta (M = Pd, Cu, Ni or NiCu) anodes for solid oxide fuel cells, Sci Rep, 5 (2015) 7667.

[167] C.C. Wang, K. Chen, S.P. Jiang, Sulfur Deposition and Poisoning of La0.6Sr0.4Co0.2Fe0.8O3- Cathode Materials of Solid Oxide Fuel Cells, Journal of the Electrochemical Society, 161 (2014) F1133-F1139.

[168] G. Vovk, X. Chen, C.A. Mims, In situ XPS studies of perovskite oxide surfaces under electrochemical polarization, J Phys Chem B, 109 (2005) 2445-2454.

[169] F.S. Baumann, J.r. Fleig, M. Konuma, U. Starke, H.-U. Habermeier, J. Maier, Strong Performance Improvement of La[sub 0.6]Sr[sub 0.4]Co[sub 0.8]Fe[sub 0.2]O[sub 3−δ] SOFC Cathodes by Electrochemical Activation, Journal of The Electrochemical Society, 152 (2005) A2074.

[170] Q.-H. Wu, M. Liu, W. Jaegermann, X-ray photoelectron spectroscopy of La0.5Sr0.5MnO3, Materials Letters, 59 (2005) 1980-1983.

[171] H. Jalili, J.W. Han, Y. Kuru, Z. Cai, B. Yildiz, New Insights into the Strain Coupling to Surface Chemistry, Electronic Structure, and Reactivity of La0.7Sr0.3MnO3, The Journal of Physical Chemistry Letters, 2 (2011) 801-807.

[172] Z. Cai, M. Kubicek, J. Fleig, B. Yildiz, Chemical Heterogeneities on La0.6Sr0.4CoO3−δThin Films—Correlations to Cathode Surface Activity and Stability, Chemistry of Materials, 24 (2012) 1116-1127.

[173] T. Wei, Q. Zhang, Y.-H. Huang, J.B. Goodenough, Cobalt-based double-perovskite symmetrical electrodes with low thermal expansion for solid oxidefuel cells, J. Mater. Chem., 22 (2012) 225-231.

[174] K. Chen, J. Hyodo, K.M. O'Donnell, W. Rickard, T. Ishihara, S.P. Jiang, Effect of Volatile Boron Species on the Electrocatalytic Activity of Cathodes of Solid Oxide Fuel Cells: III. Ba0.5Sr0.5Co0.8Fe0.2O3- Electrodes, Journal of the Electrochemical Society, 161 (2014) F1163-F1170.

[175] C.C. Wang, K. Chen, S.P. Jiang, Mechanism and Kinetics of SO2Poisoning on the Electrochemical Activity of La0.8Sr0.2MnO3Cathodes of Solid Oxide Fuel Cells, Journal of The Electrochemical Society, 163 (2016) F771-F780.

[176] T. Götsch, C. Praty, M. Grünbacher, L. Schlicker, M.F. Bekheet, A. Doran, A. Gurlo, M. Tada, H. Matsui, N. Ishiguro, B. Kloetzer, S. Penner, Iron Exsolution Phenomena in Lanthanum Strontium Ferrite SOFC Anodes, ECS Transactions, 78 (2017) 1327-1341.

[177] J.R. Izzo, A.S. Joshi, K.N. Grew, W.K.S. Chiu, A. Tkachuk, S.H. Wang, W. Yun, Nondestructive Reconstruction and Analysis of SOFC Anodes Using X-ray Computed Tomography at Sub-50 nm Resolution, Journal of The Electrochemical Society, 155 (2008).

[178] Y. Guan, W. Li, Y. Gong, G. Liu, X. Zhang, J. Chen, J. Gelb, W. Yun, Y. Xiong, Y. Tian, H. Wang, Analysis of the three-dimensional microstructure of a solid-oxide fuel cell anode using nano X-ray tomography, Journal of Power Sources, 196 (2011) 1915-1919.

[179] N. Tsvetkov, Q. Lu, L. Sun, E.J. Crumlin, B. Yildiz, Improved chemical and electrochemical stability of perovskite oxides with less reducible cations at the surface, Nat Mater, (2016).

[180] Wei Wang, S.P. JIANG, In-situ Observation on the Active Reaction Sites for the Oxygen Reduction in Solid Oxide Fuel Cells, ECS Transactions, 7 (2007) 875-880.

Chapter 3: Experimental

3.1 Powder synthesis

3.1.1 $La_{0.8}Sr_{0.2}MnO_3$

$La_{0.8}Sr_{0.2}MnO_3$ (LSM) powder was synthesized via sol-gel method, using $La(NO_3)_3{\cdot}6H_2O$ (99.9%, A.R., Alfa Aesar, UK), $Sr(NO_3)_2$ (99%, A.R., Sigma-Aldrich, US), $Mn(NO_3)_2$ (50 wt% solution, A.R., Alfa Aesar, UK) as starting materials, and anhydrous citric acid (99.5%, A.R., Chem Supply, Australia), ethylenediaminetetraacetic acid (EDTA, 99%, Acros Organics, Australia) and ammonia solution (28%w.w., SigmaAldrich, US) as complexing agents with a molar ratio of 1:1.5:1 (metal ions/citric acid/EDTA). Stoichiometric metal nitrates were blended with deionized water, and the calculated amounts of citric acid, EDTA and ammonia solution were subsequently added. The pH of the solution was adjusted to 7 and the solution was stirred on a hot plate until the dry gel was formed. The resultant gel powder was calcined at 1000 °C for 2 h to obtain LSM powder.

3.1.2 $La_{0.6}Sr_{0.4}Co_{0.2}Fe_{0.8}O_{3-\delta}$

$La_{0.6}Sr_{0.4}Co_{0.2}Fe_{0.8}O_{3-\delta}$ (LSCF) powder was synthesized using a sol-gel method, using $La(NO_3)_3 \cdot 6H_2O$ (99.9%, AlfaAesar, UK), $Sr(NO_3)_2$ (99%, Sigma-Aldrich, US), $Co(NO_3)_2 \cdot 6H_2O$ (98.0−102.0%, Alfa-Aesar, UK), $Fe(NO_3)_3 \cdot 9H_2O$ (98%, Chem Supply, Australia), citric acid (99.5%, Chem Supply, Australia), ethylenediaminetetraacetic acid (EDTA, 99%, Acros Organics, Australia), and ammonia solution (28%, Ajax Finechem, Australia). In this method, citric acid and EDTA act as complexing agents with the molar ratio of metal ions:citric acid:EDTA = 1:1.5:1. Stoichiometric metal nitrates were blended with deionized water, and the calculated amounts of citric acid and EDTA ammonia solution were subsequently added. The pH of the solution was adjusted to 7 and the solution was stirred on a hot plate until the dry gel was formed. The resultant dried gel powder was calcined at 900^{o}C for 2 h, forming LSCF powder.

3.1.3 $Er_{0.4}Bi_{1.6}O_3$ decorated $La_{0.6}Sr_{0.4}Co_{0.2}Fe_{0.7}Nb_{0.1}O_{3-\delta}$

$La_{0.6}Sr_{0.4}Co_{0.2}Fe_{0.7}Nb_{0.1}O_{3-\delta}$ (LSCFNb) powder was synthesized using a modified Pechini method. The starting chemicals were $La(NO_3)_3{\cdot}6H_2O$ (99.9%, Alfa-Aesar), $Sr(NO_3)_2$ (99%, Sigma-Aldrich), $Co(NO_3)_2{\cdot}6H_2O$ (98.0–102.0%, Alfa-Aesar),

$Fe(NO_3)_3 \cdot 9H_2O$ (98%, Chem Supply), ammonium niobate oxalate hydrate ($C_4H_4NNbO_9 \cdot xH_2O$, 99.99%, Sigma-Aldrich), citric acid (99.5%, Chem Supply), ethylenediaminetetraacetic acid (EDTA, 99%, Acros Organics), and ammonia (28%, Ajax Finechem). Metal ions/citric acid/EDTA molar ratio was fixed as 1:1.5:1. The resultant powders were calcined at 900 °C in air for 2 h. $Er_{0.4}Bi_{1.6}O_3$ (ESB) decorated LSCFNb powder with 40 wt.% ESB and 60 wt.% LSCFNb was synthesized by a gelation process, see Figure 2.1. In this process, ESB aqueous precursor solution consisting of $Er(NO_3)_3 \cdot 5H_2O$ (99.9%, Sigma-Aldrich), $Bi(NO_3)_3 \cdot 5H_2O$ (98%, Sigma-Aldrich), citric acid, EDTA and ammonia solution was constantly stirred on a heating stage. Then the LSCFNb powder was added to the solution and stirred until the gelation starts. The resultant gel was further dried in an oven at 150^{o}C overnight and then calcined at 600^{o}C in air for 2h, forming ESB decorated LSCFNb powder (ESB-LSCFNb).

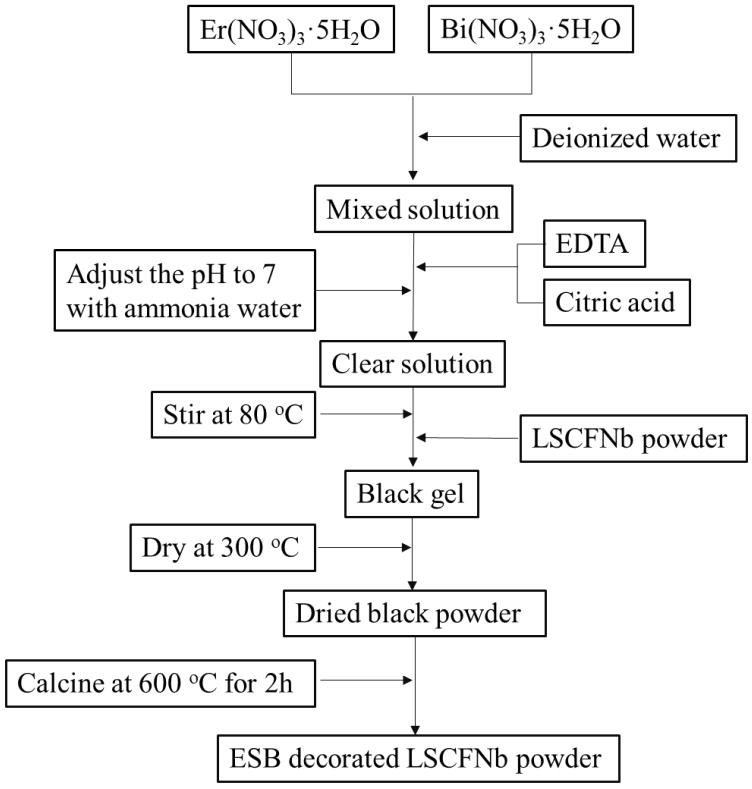

Figure 3.1 Flowchart of synthesis route of ESB decorated LSCFNb powder by sol-gel method

3.2 Fuel cell fabrication

3.2.1 Electrolyte supported cell

The electrolyte supported half-cells used in this thesis are all fabricated by die pressing and high temperature sintering for the electrolyte. The die pressing is one of the simplest method for powder moulding, and the basic procedures consist of (a) adding powder into the mould; (b) applying pressure (e.g. 4 MPa) to make the powder compact and (c) releasing the pressure to obtain the pellet. Figure 3.2 shows the diagram of die pressing process. The raw electrolyte powders used in this thesis are 8 mol% Y_2O_3 doped ZrO_2 (YSZ, Tosoh, Japan) and $Gd_{0.1}Ce_{0.9}O_{1.95}$ (GDC, Seimi Chemical Co Ltd).

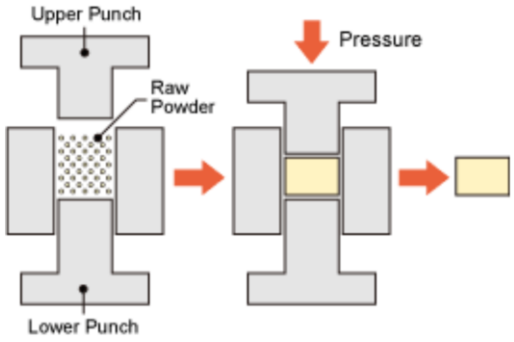

Figure 3.2 Scheme of the die pressing method

The raw electrolyte pellet is then subject to high temperature sintering at 1450 ^oC for 5 hrs. The YSZ pellets before and after sintering are shown in Figure 3.3. The electrolyte pellets are approximately 1 mm in thickness and 18 mm in diameter.

Figure 3.3 YSZ electrolyte pellets before (left) and after (right) high temperature sintering

On the one side of the sintered electrolyte pellet, Pt paste (Gwent Electronic Materials Ltd, UK) is painted at the centre as well as along the edge of the pellets, followed by sintering at 1100 ^oC for 2 hrs, serving as counter and reference electrodes. For the working electrode, the cathode powder is thoroughly mixed with an ink vehicle (Fuel

Cell Materials, US) at a weight ratio of 5:5 in an agate mortar to form a uniform electrode paste, and the paste is subsequently printed on the other side of the electrolyte pellet symmetrically opposite to the Pt counter electrode and then dried at 100 ^{o}C for 2 hrs to form directly assembled electrodes without further high temperature pre-sintering step. The three-electrode method is particularly important for studying a sole electrode without the influence of other cell components. The positioning of the electrodes needs to ensure the even distribution of the current in working electrode, and the distance between counter electrode and reference electrode should be more than three times of the thickness of the electrolyte. The typical setup of the cell is shown in Figure 3.4.

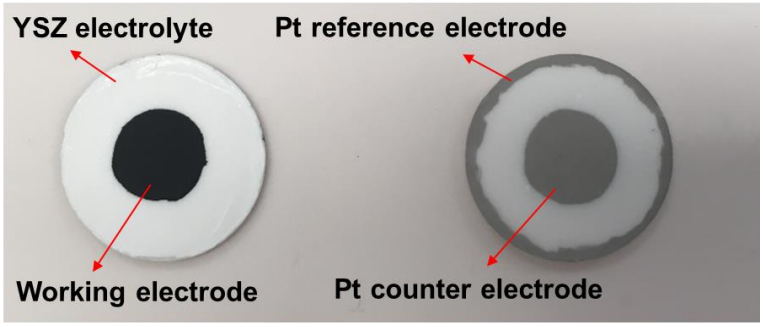

Figure 3.4 Typical setup for electrolyte supported three-electrode cell.

3.2.2 Anode supported cell

The anode supported cells fabricated in this thesis have a structure of NiO-YSZ/YSZ/cathode. For the NiO-YSZ anode support, NiO (J.T. Baker), YSZ and tapioca (pore former) with a weight ratio of 5:5:2.5 are ball milled for 24 hrs using ethanol as solvent. The resultant slurry is further dried in an oven at 120 ^{o}C and then grinded to obtain the fine anode powder. The anode powder (typically 0.6 grams) is die pressed under the pressure of 7 MPa, and the pellet is then pre-sintered at 1000 ^{o}C for 2 hrs to burn the pore former. The anode functional layer (AFL) slurry is also prepared by mixing the NiO and YSZ powders with ink vehicle in mortar at a weight ratio of 2.5:2.5:5, and the AFL slurry is spin-coated onto the anode pellet, followed by sintering at 600 ^{o}C for 2 hrs. YSZ electrolyte slurry is prepared by mixing the YSZ powder and ink vehicle with a weight ratio of 3:7, and the electrolyte slurry is then spin-coated on top of the AFL layer, followed by sintering at 600 ^{o}C for 2 hrs. This process (YSZ electrolyte) is repeated once. The as-prepared pellet is further subject to high temperature sintering at 1450 ^{o}C for 5 hrs. The thickness of the final anode

support, AFL and YSZ electrolyte film are 800, 9 and 11 μm, respectively. The cathode paste is prepared by mixing the cathode powder with ink vehicle at a weight ratio of 7:3, and the paste is painted on the electrode side of the anode supported cell, dried at 120 ^{o}C for 2 hrs. Gold ink (Gwent Electronic Materials Ltd, UK) is then applied on top of the cathode surface as well as the anode surface symmetrically opposite to the cathode, serving as current collectors. The ink is then dried at 120 ^{o}C for 2 hrs.

3.3 Characterisation

3.3.1 Electrochemical characterisation

Electrochemical impedance spectroscopy (EIS) is an experimental method for measuring the impedance of a cell at different frequencies by applying a small amplitude sinusoidal voltage disturbance to the cell under equilibrium or steady state conditions. It is noticeable that the frequency for the EIS test ranges from a few millihertz to several kilohertz, thus obtaining information over a wide range of time scales. A typical EIS data for a cell tested at 800 ^{o}C under open circuit condition using YSZ electrolyte as support, LSM as cathode is shown in Figure 3.6. The electrode ohmic resistance (R_{Ω}) is obtained from the high frequency intercept, and the total electrode resistance (R_T) is obtained from the low frequency intercept. The polarization resistance (R_P) is calculated by the difference between R_T and R_{Ω}. R_P is mainly composed of activation polarization resistance and concentration polarization resistance. The concentration polarization is closely associated with the gas transport process in the porous electrode, thus its impedance depends on the microstructure of the electrode, especially the size and porosity of the electrode pores and the tortuosity factor of the electrode. The activation polarization is related to the charge transport process, so its impedance is affected by the electrode/electrolyte/gas three-phase reaction area and the catalytic activity of the electrode itself. It can be seen that the ionic conductivity of the cathode not only affects the overall ohmic impedance of the cell, but also contributes to the polarization impedance of the electrode. In this thesis, electrochemical impedance is measured under open circuit conditions in a frequency range of 0.1 Hz to 100 kHz with a signal amplitude of 20 mV. Air is supplied to the cathode side at a flow rate of 100 mL min^{-1}, while hydrogen is supplied to the anode side with a flow rate of 50 mL min^{-1}.

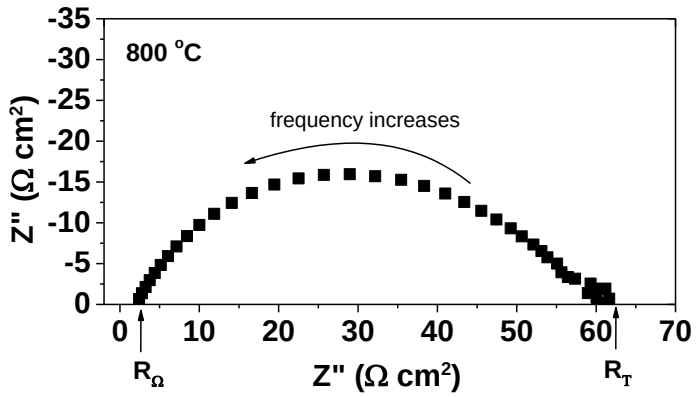

Figure 3.6 Typical electrochemical impedance spectra of an YSZ electrolyte supported cell with LSM cathode tested at 800 °C under open circuit.

Moreover, the kinetic study of electrode process usually includes a current-voltage curve, and it can be divided into transient method and constant current or potentiostatic method according to different test conditions. Transient method measures the change of the corresponding current (or voltage) by continuously (or intermittently) changing the voltage (or current) of the studied electrode. Transient method is a rapid measurement method that is able to minimize the interference to the electrode during the measuring. In this thesis, the current density (I) –voltage (V) curve is obtained by continuously changing the current and then measuring the corresponding voltage. In full cell test, to evaluate its output performance, the corresponding power density can be calculated according to the I-V curve. In addition, the constant current (galvanostatic) method is also used to measure the change of cell potential with time by controlling the current constant. This method is adopted in this thesis to characterise the long-term operation stability of the cell. The electrochemical workstations used in this thesis are Zahner Electrochemical Workstation and Gamry Reference 3000 Potentiostat.

3.3.2 X-ray diffraction (XRD)

Theoretically, any wave will be diffracted when it is incident on a regularly arranged array of scatterers, but only when the spacing of the scatterers is close to the wavelength of the incident wave, a sufficiently strong diffraction pattern can be obtained. A crystal is a lattice structure composed of atoms, which can be regarded as a regularly arranged array of scatterers, while X-rays can be regarded as

electromagnetic diffraction waves. The wavelength (λ) of the X-ray is on the same order of magnitude (1~100 Å) as the interplanar spacing (d) of the crystal, thus producing a strong diffraction pattern. When an X-ray enters a crystal at a specific angle, the incident ray is reflected by the crystal to form a series of peaks (Bragg peaks), which can be expressed by Bragg's law:

$$2d\sin\theta = n\lambda \tag{3.1}$$

where d is the interplanar spacing of the lattice planes, θ is the angle between the incident wave and the scattering plane, while λ is the wavelength of the incident wave, n is the positive integer. Each crystal produces a unique diffraction pattern due to its particular crystal lattice and lattice parameters, therefore by comparing the XRD spectrum of the synthesised powder with the standard XRD diffraction data of the target product, the phase formation of the synthesised powder can be analysed and determined. The X-ray diffractometer used in this study is Bruker AXS D8 Advance, equipped with a Cu Kα X-ray source (λ=1.54056Å). The tube voltage and current are 40kV×40mA with a scan rate of 3 °/min.

3.3.3 Scanning electron microscopy (SEM)

Scanning electron microscopy is an electron microscopy technique that scans a sample through a focused electron beam to obtain an image. The signal generated by the interaction of the electron beam with the atoms in the sample contains information on the surface topography and composition of the sample. The position of the electron beam and the detected signal can be used to obtain information on the surface of the sample. The resolution of SEM can reach 1 nm. Samples can be probed in high vacuum, low vacuum, humid environment (environmental SEM) and low or high temperature conditions. The signals generated by SEM include secondary electrons (SE), backscattered electrons (BSE), characteristic X-rays and cathodoluminescence (CL), which are the result of the interaction of the electron beam with atoms of different depths in the sample. The most common mode of SEM is to detect the secondary electrons generated by the electron beam exciting the atoms in the sample. The secondary electrons escape from a region very close to the surface of the sample. The number of secondary electrons that can be detected depends on the angle between the incident electron beam and the surface of the sample, that is, on the morphology of the sample surface. Therefore, the morphology of the sample surface can be obtained by

scanning the surface of the sample through focusing the electron beam and detecting the escaped secondary electrons. Backscattered electrons are electrons that interact with atoms in a sample and are reflected by elastic scattering. Backscattered electrons escape from deeper areas of the sample, so the resolution of the BSE image is lower than the secondary electron image. Since the BSE signal is highly dependent on the atomic number of the atoms in the sample, the BSE image can show the distribution of different elements in the sample. Characteristic X-ray means that the inner electrons of the atoms in the sample are bombarded by the incident electron beam to leave an electron hole in the inner layer, and then the higher-energy electron of the outer layer falls into the inner layer to fill the hole, releasing X-rays with a certain energy. Characteristic X-rays are commonly used to analyse the composition of elements in a sample.

Usually, in order to prevent the static charge from accumulating on the surface of the sample to cause charging effect, the sample for SEM test should be conductive, or at least the surface of the sample is conductive. The materials studied in this thesis are mostly ceramics without electronic conductivity, therefore it is necessary to prepare an ultra-thin conductive film on the surface of the sample by magnetron sputtering before SEM characterization. The conductive films used here are platinum and carbon, and since the particle size of these materials are very small, they will not be observed by SEM imaging. The SEM instrument used in this thesis is Neon 40ESB FIB-SEM, at a typical working voltage of 5 kV for imaging.

3.3.4 Atomic force microscopy (AFM)

AFM is a scanning microscopy technique with a resolution of nanometers, which is 1000 times better than the optical diffraction limit. AFM information is obtained by “feeling” and “touching” the surface of a sample with a cantilever that controls the probe for small and precise movements to obtain highly accurate scan results on the sample surface. The AFM mainly has three functions: force measurement, manipulation and imaging. In the force measurement mode, AFM can be used to measure the force and mutual distance between the probe and the sample to obtain the corresponding force spectrum. In manipulative mode, the force between the probe and the sample can be used to alter the characteristics of the sample, such as atomic manipulation, scanning probe etching, and in situ stimulation of cells. In the imaging mode, the force applied by the sample surface to the probe can be used to generate a

high resolution image of the three dimensional topography of the sample surface. AFM's imaging modes are mainly static and dynamic. In the static mode, the cantilever is swept from the surface of the sample, and the height map of the surface can be directly known from the deflection of the cantilever. In dynamic mode, the cantilever vibrates near its fundamental frequency or harmonics, and its amplitude, phase, and resonance are related to the force between the probe and the sample. These changes in parameters reflect the nature of the sample surface. The mode used in this thesis is the dynamic tapping mode. In the tapping mode, the probe vibrates up and down around its resonant frequency with amplitudes ranging from a few nanometers to 200 nanometers. The frequency and magnitude of the drive signal remain the same, so the amplitude of the probe remains constant if it is not interacting with the sample surface. When the probe is close to the surface of the sample, it interacts with the sample, such as van der Waals force, polar intermolecular forces, electrostatic forces, etc., resulting in a change (usually a decrease) in the amplitude of the probe. The electronic servo system that controls the height of the probe takes these changes in amplitude as a parameter, constantly adjusting the amplitude of the drive signal so that the probe sweeps across the entire sample surface with a constant amplitude value. An AFM tapping mode image can be obtained by imaging the interaction force between the probe and the surface of the sample.

AFM has a number of advantages over SEM. While electron microscopy can only have two dimensional image of a sample, AFM is capable of providing three dimensional topography of a sample's surface. In addition, AFM test does not require the sample to be conductive, thus avoiding the damage caused by Pt or C coating. Electron microscopy imaging needs to be performed in a high vacuum environment, and most AFM imaging can be performed in air or even liquid phase environments. In this thesis, the AFM is used to analyse the electrolyte surface topography before and after polarisation treatment. The instrument employed for AFM test is Alpha 300 SAR, WITec GmbH, Ulm Germany.

3.3.5 Transmission electron microscopy (TEM)

Transmission electron microscopy is a microscopic technique that uses an electron beam to pass through an ultrathin sample and interact with the sample during its penetration. The electrons collide with atoms in the sample to change direction, resulting in solid angle scattering. The magnitude of the scattering angle is related to

the density and thickness of the sample, so that images with different brightness and darkness can be formed, and the image will be displayed on the imaging device (such as fluorescent screen, film, and photosensitive coupling component) after being enlarged and focused. Since the de Broglie wavelength of electrons is very short, TEM can obtain a particularly high resolution image. The resolution of the TEM is way higher than that of the optical microscope, reaching 0.1 to 0.2 nm. The fine structure of the sample can be observed using TEM and can even be used to observe structures with only one column of atoms. The instrument employed in this thesis is a high angle annular dark field scanning transmission electron microscopy (HAADF-STEM, FEI Titan G2 60-300 TEM/STEM with ChemiSTEM Technology, FEI company, US) at 200 kV.

The sample preparation for TEM is much more complicated as compared to other microscopic techniques. The thickness of a TEM sample should be less than a few hundred nanometers, and the thickness of a high-quality sample is comparable to the mean free path of electrons passing through the sample, possibly only a few tens of nanometers. The way of preparing TEM samples needs to be determined based on the material and the information required for the test, thus there are many common preparation techniques available. Some materials are themselves small enough to pass electrons, such as powders and nanotubes, which can be simply diluted and deposited on a TEM sample grid for examination. Other thicker samples require filming, or etching a portion of the sample to allow electrons to pass through. Common techniques include tissue slicing, mechanical polishing, chemical etching, ion etching, and replication. The TEM samples containing electrode/electrolyte interface information in this study are all prepared by focused ion beam, i.e. ion etching.

3.3.6 Focused ion beam (FIB)

In recent years, focused ion beam (FIB) has been used to prepare TEM lamella for large-sized samples, which is a relatively new technology. Unlike inert gas ion sputtering, FIB ionizes Ga into Ga^+, and then uses electric field acceleration and electrostatic lens aggregation to drive high-energy, high-speed Ga^+ ions to a specified position. The application of combined FIB-TEM technique offers opportunities of more precise analysis of the electrode/electrolyte interface microstructure on a nanoscale. The FIB technique not only allows a TEM lamella to be prepared from a specific area of interest with submicron precision, but also can uniformly mill

heterogeneous microstructures that consist of compositionally and structurally distinct regions. Figure 3.7 shows the typical FIB milling process.

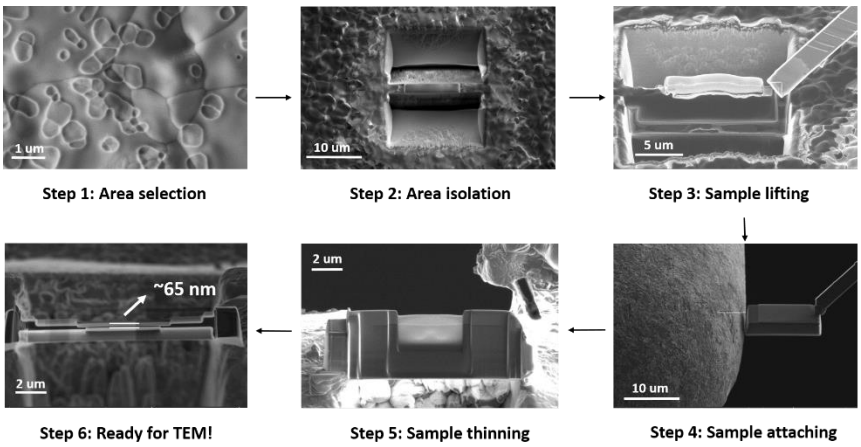

Figure 3.7 Flowchart of FIB lamella milling procedures

First of all, a Pt or C protection layer is deposited on the area of interest, in order to prevent the damage caused during ion milling (Step 1); and trenches on both sides of the protection strip are milled to obtain a thick sample sheet (Step 2); the sample sheet is then attached onto a needle using Pt and lifted out from the bulk sample after a 'U-cut' (Step 3); the thick sample sheet is welded onto a FIB sample grid (Step 4); since the sample is still quite thick (~1 μm), further thinning process is performed by ion milling until the thickness of the lamella is less than 100 nm (Step 5). After final low voltage ion beam cleaning, the lamella is ready for TEM examination. The FIB instrument adopted in this thesis is Dual Beam Focused Ion Beam – Scanning Electron Microscope (FIB-SEM, Helio Nanolab G3 CX, FEI company, US) with Ga^+ source at 30 kV for the ion beam.

Chapter 4: A FIB-STEM Study of $La_{0.8}Sr_{0.2}MnO_3$ Cathode and Y_2O_3-ZrO_2/Gd_2O_3-CeO_2 Electrolyte Interfaces of Solid Oxide Fuel Cells

Abstract

The interfaces between cathode and electrolyte in solid oxide fuel cells (SOFCs) play a critical role in the overall performance and durability, and are generally formed by pre-sintering at high temperatures, e.g., ~1150 ◦C in the case of $La_{0.8}Sr_{0.2}MnO_3$ (LSM) cathodes. Here the interface between LSM and yttria-stabilized zirconia (YSZ) or Gd-doped ceria (GDC) electrolytes formed under high temperature sintering is studied using Focused Ion Beam and Scanning Transmission Electron Microscope (FIB-STEM) techniques. In the case of LSM/YSZ interface, there is a significant cation interdiffusion, particularly Mn^{2+} into YSZ electrolyte in the convex contact ring region and Mn, La and Y cation diffusion along the grain boundary of YSZ electrolyte also occurs. For LSM/GDC interface, no cation interdiffusion was observed. The results indicate the formation of semi-coherent interface, i.e., an atom-by-atom matching only exists locally in regions along the interface, but orientation relationship and lattice mismatch factor between electrode and electrolyte crystallographic planes at the LSM/YSZ and LSM/GDC interfaces vary significantly. Lattice disorientation and misfit of the crystallographic planes occur within a narrow region of 0.10–0.5 nm wide with no amorphous or solid solution formation. The results demonstrate that cation interdiffusion is not an essential requirement for the formation of heterointerfaces for LSM electrode, and disorientation and dislocation of the crystallographic planes at the interface does not impede the oxygen diffusion and incorporation process for the O_2 reduction reaction.

4.1 Introduction

Solid Oxide Fuel Cells (SOFCs) have been regarded as the most efficient energy-conversion technologies to electrochemically convert chemical energy of fuels like hydrogen, natural gas to generate electricity [1-5]. SOFCs are all ceramic components devices and typical SOFC cells consist of Y_2O_3-stablized zirconia (YSZ) electrolyte,

lanthanum strontium manganite ($La_{0.8}Sr_{0.2}MnO_3$, LSM) perovskite cathode and Ni/YSZ cermet anodes. Due to the nature of ceramic components of SOFCs, it is generally considered that in order to form an intimate electrode/electrolyte interface in SOFCs, pre-sintering of the electrode/electrolyte at high temperatures is necessary, e.g., ~1400 ^oC in the case of Ni/YSZ cermet anodes and ~1150 ^oC for LSM cathodes[6-8].

Similar to other electrochemical devices, the performance of a SOFC depends strongly on the activity of the electrochemical reactions at the electrolyte/electrode interface and thus the electrode/electrolyte interfaces play a crucial role in terms of determining the performance and durability of the SOFCs [9-12]. The formation of triple phase boundary (TPB) at the interface provides a direct pathway for oxygen ion migration, facilitating the electrochemical processes significantly [13, 14]. The cathode and electrolyte interface formed during the high temperature sintering is generally characterized by the formation of convex ring-shaped contact features [10, 15-22]. Mitterdorfer and Gaucker investigated the inter-relation between interface formation and manganese stoichiometry in LSM/YSZ system during the high temperature sintering process and observed formation of contact rings and presence of manganese at the interface, most likely due to the zirconium and manganese cation diffusion towards the three phase area to reduce the free surface energy of the interface [23]. Matsui et al.[20] quantitatively studied the relationship between the change of TPB length and the electrochemical performance by combined FIB-SEM technique and proposed that the increase in TPB length is one of the factors contributing to the enhancement of the electrochemical performance of LSM electrode. Horita et al.[24] analyzed the effect of the heat treatment on ^{18}O diffusion and the microstructure at $LaMnO_3$ film/YSZ interface. The results indicate that the main oxygen incorporation points are at the TPB region and the presence of manganese in the convex contact rings on the YSZ electrolyte surface. Based on the observation, cation inter-diffusion has been considered to cause the microstructural change of YSZ at the interface [24]. Backhaus-Ricoult[25] studied the interface chemistry in LSM-YSZ composite SOFC cathodes using an interface point defect modeling and proposed that the high Mn^{2+} concentration level at the interface would increase the local oxygen vacancy concentration at the interface and thus facilitate the electron transfer for the oxygen incorporation process. The inter-diffusion behavior between LSM and YSZ and the

bulk diffusivities of La, Mn and Sr in YSZ were studied by Argirusis et al[26]. However, despite a substantial amount of work on the high-temperature sintered interface between LSM and electrolyte, there is lack of detailed studies on the compositional change and crystallographic nature of the interface.

In this work, the interface formed between LSM/YSZ and LSM/GDC during high temperature sintering is investigated in detail using combined focus ion beam and scanning transmission electron microscopy (FIB-STEM) techniques. The results indicate that Mn and in less extent La can accumulate inside the convex contact rings at the YSZ interface, while cation inter-diffusion was not observed at the LSM/GDC interface. The high resolution TEM reveals the presence of lattice disorientation and misfit dislocations in the interface regions of both LSM/YSZ and LSM/GDC. However, electrochemical performance of LSM electrode indicates that the presence of such disorientation at the interface region does not impede the oxygen diffusion and incorporation steps of the O_2 reduction reaction.

4.2 Experimental

Electrolyte pellets were fabricated by die-pressing powders of 8mol% Y_2O_3 doped ZrO_2 (YSZ, Tosoh) and $Gd_{0.1}Ce_{0.9}O_{1.95}$ (GDC, AGC Seimi Chemical Co Ltd), followed by sintering at 1450^{o}C for 5h. The pellets were approximately 1 mm in thickness and 18 mm in diameter. $La_{0.8}Sr_{0.2}MnO_3$ (LSM) powder was synthesized by sol-gel solution, using $La(NO_3)_3{\cdot}6H_2O$ (99.9%, A.R., Alfa Aesar), $Sr(NO_3)_2$ (99%, A.R., Sigma-Aldrich), $Mn(NO_3)_2$ (50 wt.% solution, A.R., Alfa Aesar) as raw materials, and anhydrous citric acid (99.5%, A.R., Chem Supply), EDTA (99%, Acros Organics) and ammonia solution (28%w.w., Sigma–Aldrich) as complexing agents. The powder was calcined at 1000^{o}C for 2h. The phase formation of the powder was examined by X-ray diffractometry (XRD, Bruker D8 Advance).

Cathode powder was mixed with organic binder (Fuel Cell Materials, USA) to form a paste and subsequently slurry-coated onto the electrolyte pellet to form LSM electrode. The electrode/electrolyte pellets were then sintered at 1150^{o}C for 2h. Pt paste was applied at the center and edge of the opposite side of the electrolyte to make counter and reference electrodes, respectively, and then calcined at 1100^{o}C for 2h. Electrochemical tests were carried out on a Zahner Electrochemical Workstation using

a three-electrode configuration. The cell was polarized at 800 ^{o}C and 500 mA cm^{-2} for 20 h, and the polarization was interrupted from time to time to measure the electrochemical impedance under open-circuit conditions in a frequency range of 0.1 Hz to 100 kHz with a signal amplitude of 20 mV. Electrode ohmic resistance (R_{Ω}) was obtained from the high frequency intercept, and electrode polarization resistance (R_p) was obtained from the differences between the low and high frequency intercepts of the impedance curves. In order to investigate the compatibility between LSM cathode, YSZ and GDC electrolyte, oxide couples of LSM/YSZ and LSM/GDC with weight ratio of 1:1 was prepared and calcined at 800, 1150 and 1300^{o}C for 2 hours in air.

Microstructure of electrolyte surfaces in contact with LSM was characterized by scanning electron microscopy (SEM, Zeiss Neon 40EsB) and atomic force microscopy (AFM, Alpha 300 SAR, WITec GmbH, Ulm Germany) at intermittent contact mode. LSM electrode coating was completely removed by treatment in 32wt% hydrochloric acid solution to examine the microstructure and cation inter-diffusion along the contact rings on clean electrolyte surface. In order to examine the LSM/electrolyte interface, LSM electrode coating was also removed by adhesive tape. The electrolyte lamella with distinct contact marks and LSM/electrolyte contact were lifted out and milled to around 100 nm in thickness using FEI Helios Nanolab G3 CX DualBeam Focused Ion Beam-SEM with 30kV for the ion beam and 2kV for the electron beam. Focused ion beam (FIB) was adopted to cut a thin lamella across the contact ring to further analyze the crystallographic and compositional change within this area. Figure 4.1 shows detailed procedures of preparing the lamella samples. Elemental mapping, electron energy loss spectroscopy (EELS) and microstructure analysis were performed using a high angle annular dark field scanning transmission electron microscopy (STEM, Titan G2 60-300) at 200kV on the FIB milled lamella. The fast Fourier transform (FFT) images were extracted using TEM Imaging & Analysis software (TIA, FEI Company) to examine the diffraction behavior of selected area, while inverse FFT (IFFT) simulations were performed on Gatan Digital Micrograph (Gatan Digital Microscopy Suite, Gatan Inc.) to reconstruct the selected lattice planes using FFT images.

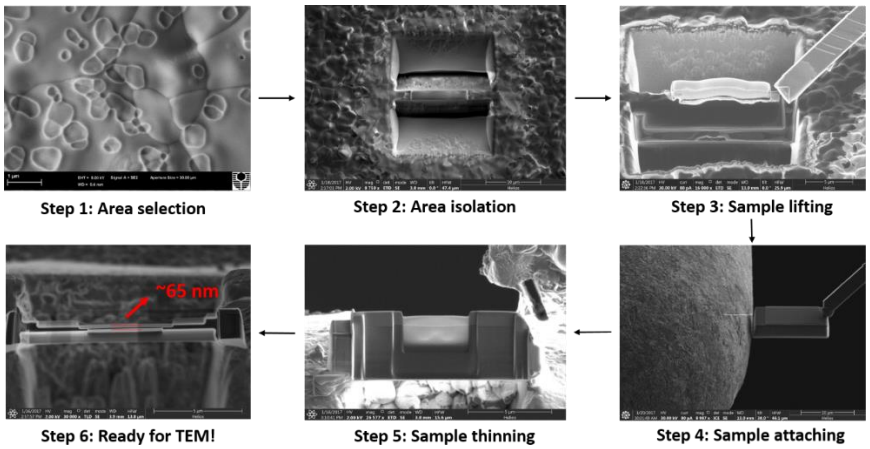

Figure 4.1 Scanning Electron or Ion Microscopy images of the flowchart of FIB operation procedures on the electrolytes in contact with LSM. LSM electrode coating was removed by acid treatment.

4.3 Results and Discussion

4.3.1. Thermal compatibility between LSM and YSZ and GDC electrolytes

Figure 4.2a shows XRD results of LSM-YSZ oxide couples sintered at different temperature. XRD pattern of LSM reveals strong reflection peaks of (110) and (024) planes, locating at 32.5^o and 47^o, respectively. Distinct reflection peaks appearing at 30^o and 51^o correspond to the (111) and (220) planes of YSZ. No additional peaks were detected for the LSM-YSZ oxide couples sintered at 800^{o}C and 1150^{o}C, and the lattice planes of (111) and (220) for YSZ as well as the (110) and (024) for LSM were easily observed. The XRD pattern for the oxide couples sintered at 1300^{o}C shows two additional peaks at 28.5^o and 48.5^o, corresponding to (222) and (440) lattice planes. The new phase is associated with the formation of insulating lanthanum zirconate phase[27]. The results indicate that LSM is thermally compatible with YSZ at sintering temperature of 1150 ^{o}C and formation of lanthanum zirconate occurs at a higher sintering temperature of 1300 ^{o}C.

LSM shows good thermal compatibility with GDC electrolyte (see Figure 4.2b). XRD pattern of pure GDC reveals strong peaks locating at 28.5^o, 47.4^o and 56.2^o with corresponding lattice planes of (111), (220) and (311), respectively. For LSM/GDC oxide couples sintered at 800, 1150 and 1300^{o}C, no additional or new peaks were detected except those for LSM and GDC phase, indicating no third phase formed. This

result confirms that no chemical reaction occurred between LSM and GDC at temperatures at high as 1300°C.

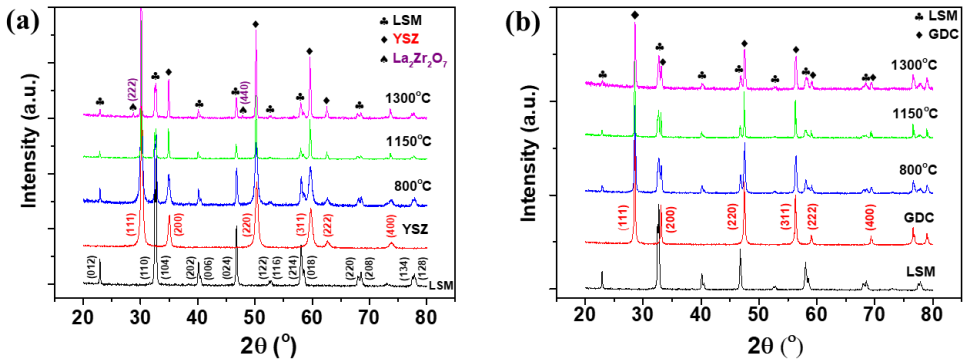

Figure 4.2 XRD patterns of (a) LSM-YSZ and (b)LSM-GDC powder mixture (1:1, w:w) calcined at 800, 1150 and 1300°C.

4.3.2 Electrochemical performance of LSM/YSZ and LSM/GDC

Figure 4.3 presents the electrochemical performance of LSM on YSZ and GDC electrolytes measured at 500 mA cm^{-2} and 800 °C. For the LSM/YSZ cell, initial R_Ω and R_p was 2.0 and 31.0 Ω cm^2, respectively. With the application of polarization current, the electrochemical impedance decreases significantly. After polarization for 3 h, R_p decreased to 2.6 Ω cm^2, substantially smaller than the initial value of 31.0 Ω cm^2 while the change in R_Ω is very small, 1.9 Ω cm^2, close to the value before the polarization (Figure 4.3a). The significant reduction in the electrode polarization impedance is also reflected by the rapid decrease in the polarization potential (see Figure 4.2c). In the case of LSM/GDC sample, the electrode impedance and polarization behave similarly. Initial R_Ω and R_p was 2.5 and 7.7 Ω cm^2 and decreased to 1.9 and 2.5 Ω cm^2, respectively after polarization for 20 h (Figure 4.3b and d). The rapid reduction in the electrode impedance and polarization potential is clearly due to the activation effect of cathodic polarization on the electrocatalytic activity of LSM electrodes for the O_2 reduction reaction [28, 29]. Early studies show that the enhanced activity of LSM electrode for the O_2 reduction reaction is most likely due to the increased three phase boundary [30] and the removal of passivating phases such as like SrO and MnO_x under the influence of cathodic polarization potentials[28, 31]. The oxygen vacancies generated under polarization during the O_2 reduction reaction could also contribute to the activation of LSM electrode[32]. In the present study, the negligible change in R_Ω with polarization indicates the relatively stable interface for

the LSM cathode on YSZ and GDC electrolytes formed under high temperature sintering.

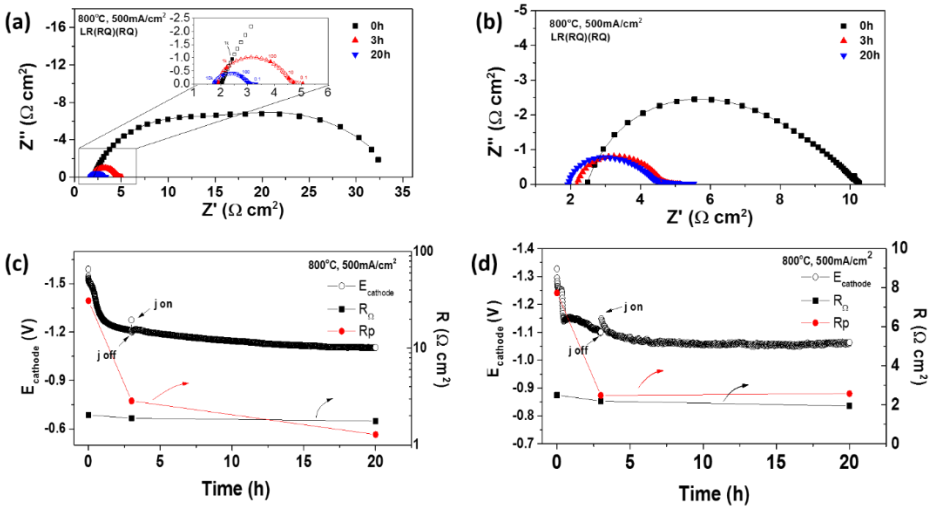

Figure 4.3 Electrochemical impedance and polarization curves of (a,c) LSM/YSZ and (b,d) LSM/GDC half-cells polarized at 500mA cm^{-2} and 800^{o}C for 3 and 20h.

4.3.3 Microstructure of contact rings

Figure 4.4 shows the SEM micrographs of the cross-section of LSM/YSZ and YSZ and GDC electrolyte surface in contact with LSM cathode after removal of LSM electrode coating by acid treatment. LSM particles form an intimate contact with YSZ and show the neck formation between LSM particles and YSZ electrolyte (indicated by circles in Figure 4.4b). The YSZ electrolyte surface after removal of LSM electrode by acid treatment is characterized by the formation of convex contact rings with sharp edges (Figure 4.4c), similar to that reported in the literature [16, 18-20, 22, 33, 34]. Similar to that on YSZ, GDC electrolyte surface is also characterized by the formation of convex contact rings with sharp edges (Figure 4.4d). The results indicate that the contact regions are formed between LSM electrode and YSZ electrolyte during the high temperature sintering as with no sintering steps, such contact rings were not observed[35].

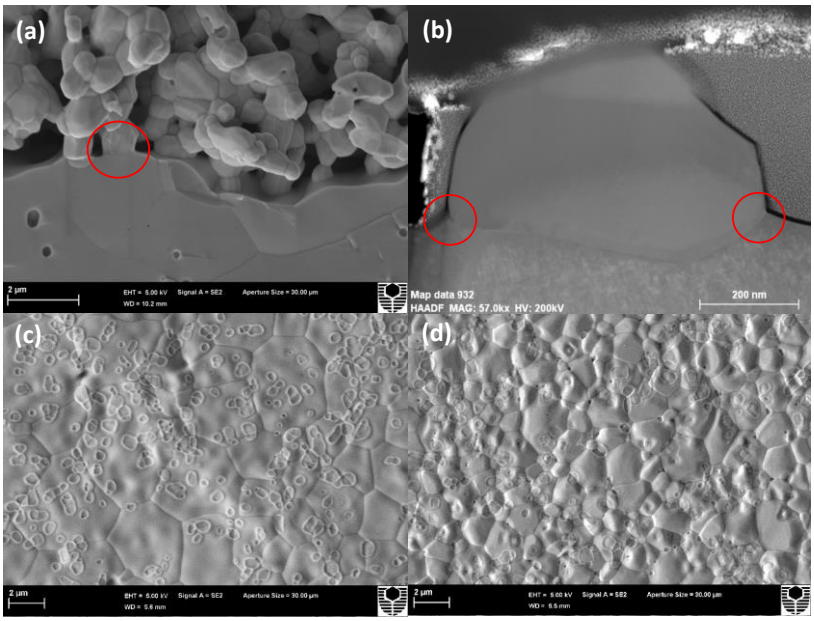

Figure 4.4 SEM micrographs of (a) cross-section of LSM/YSZ, (b) enlarged portion of LSM/electrolyte region, showing the formation of convex contact (indicated by circles), (c) YSZ and (d) GDC electrolyte surfaces in contact with LSM electrode after removal of LSM electrode by acid treatment.

The morphology of the convex contact ring was studied by AFM. The dimension of the rings on YSZ is approximately ~670±248 nm (by averaging the width of at least 50 contact rings). The height of the contact rings on the YSZ electrolyte surface is ~18.8±3.2 nm and the width of the ring edge is 150±13 nm (Figure 4.5c,d). In the case of GDC electrolyte in contact with LSM electrodes, the dimension of the rings on GDC is approximately ~600±170 nm (Figure 4.5b). The height of the contact rings on the GDC electrolyte surface is ~36±11 nm and the edge width is 176±40 nm (Figure 4.5e,f). The size of the contact rings is close to the size of LSM particles of the electrode, which is in the range of 0.5-1.6 μm, consistent to that reported in [34]. There is no significant difference in the morphology and microstructure of the convex contact rings on YSZ and GDC electrolyte surface.

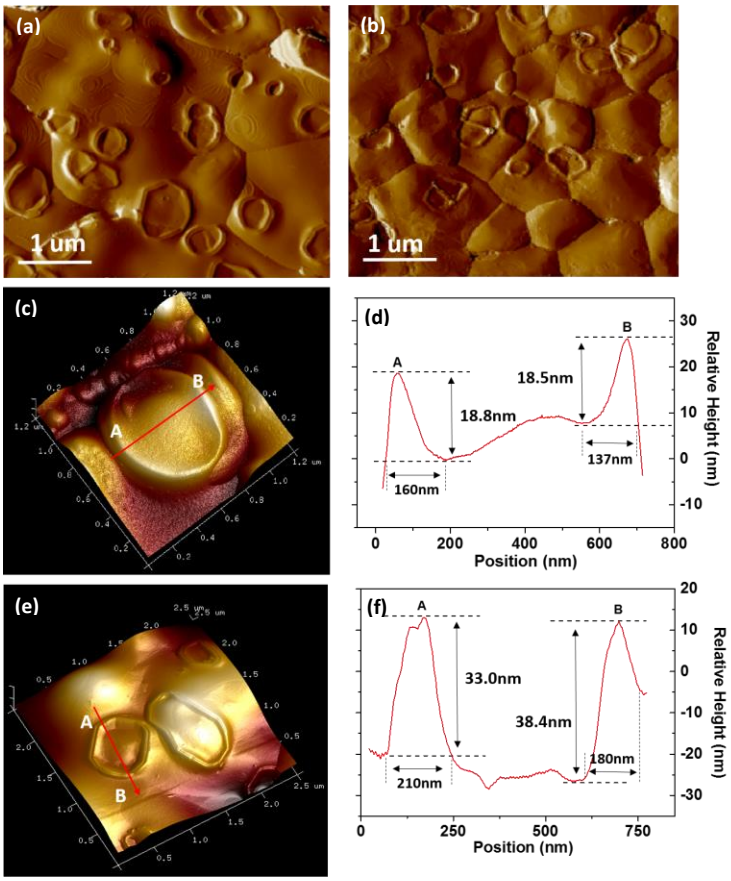

Figure 4.5 Atomic Force Microscopy micrographs of (a) YSZ and (b) GDC electrolyte surfaces and the corresponding line scan of (c,d) LSM/YSZ interface and (e,f) LSM/GDC interface before polarization. LSM cathode coating was removed by acid treatment.

4.3.4 LSM/YSZ interface

Figure 4.6 shows the HAADF image and element distribution of the contact ring region on YSZ electrolyte surface. The EDS mapping clearly indicates a significant accumulation of Mn and in less extend La in the edge region of the contact rings. In the same edge region of the contact rings, the intensity of Y signal is relatively lower as compared to that in the bulk of the YSZ electrolyte. This indicates that cation interdiffusion probably occurs via the replacement of Y by Mn within the YSZ cubic structure. There appears the presence of La in the edge region of the contact rings, but the amount of La is much smaller than Mn. Mn not only exists inside the contact ring region on YSZ electrolyte, but also diffuses along the surface of YSZ electrolyte. This is consistent with the high mobility of Mn species as observed by the extensive reaction between the diffused Mn species on the YSZ electrolyte surface and gaseous Cr in the

presence of Fe-Cr metallic interconnect[36] and by *in situ* XPS study of manganite based electrode on YSZ electrolyte [37]. There is also significant Mn and/or La diffusion along the grain boundary of YSZ (Figure 4.6a), consistent with that reported in the literature [26, 38-40].

The EDS spectrum of the edge of the contact ring (circled area, see Figure 4. 6b) indicates presence of Mn and La associated with the peaks at 5.9 eV and 4.6 eV, respectively. The intensity of Mn is much higher than that of La, consistent with the higher concentration of Mn inside the contact ring regions. The peak of Cu originates from the copper grid. The electron energy loss spectrum (EELS) measures the energy loss of the incident electron beam after interacting with the sample, and peaks observed in the spectrum suggest the ionization energy for each energy level in the atom. Thus, the L2, L3 regions shown in the Figure 4.6c represent the energy levels of two 2p-orbitals of manganese atoms. EELS experiment measured at the circled area shows the characteristics peak at 640.5 eV in region L3, which corresponds to the energy peaks of Mn^{2+} [41]. This indicates that Mn cations diffused in the YSZ contact ring areas exist in a valence of +2 under cathodic polarization conditions, after being reduced from its original state (between +3~+4)[8, 42] in LSM. The detection of Mn^{2+} within the YSZ electrolyte is in good agreement with that reported in the literature [25].

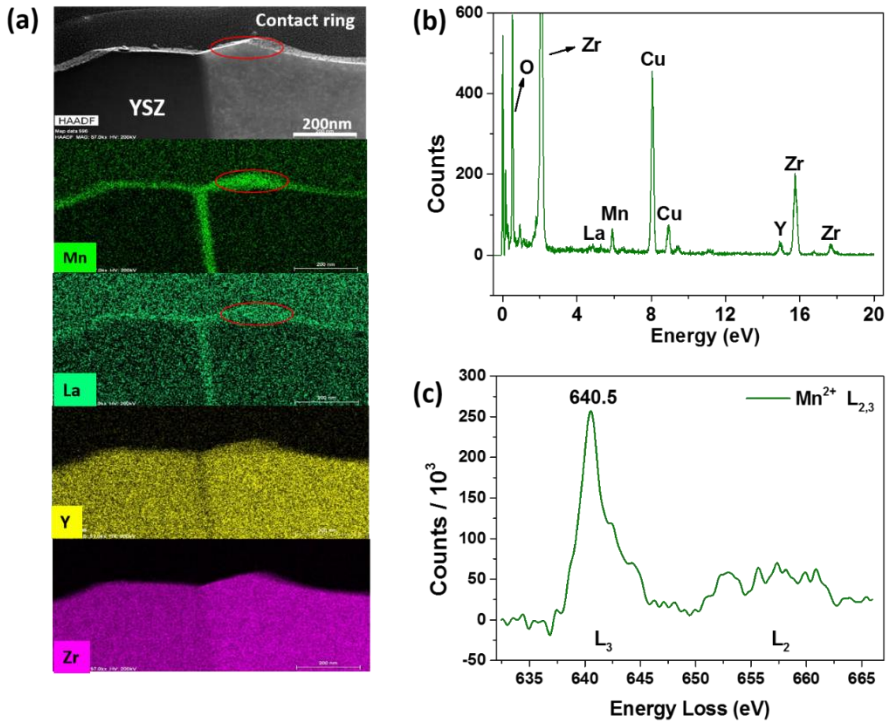

Figure 4.6 (a) High angle annular dark field image and corresponding EDS mapping of the contact ring region on YSZ electrolyte, (b) EDS pattern and (c) Electron Energy Loss spectrum obtained on the circled area of the edge of contact ring.

EDS line scan across the edge and the center of the convex ring was carried out, and the results are presented in Figure 4.7. In the edge of the convex contact ring, there is a clear accumulation and enrichment of manganese and the penetration depth of Mn is approximately ~100 nm in the YSZ substrate. The enrichment of Mn corresponds to the reduced intensity of Y, implying the replacement of lattice Y by Mn. The diffusion of Mn to YSZ is most likely due to the high solubility of Mn in YSZ (e.g., as high as 15 mol%[43]), forming a solid solution [44, 45]. On the other hand, the diffusion depth of La and Sr is very small probably due to the low solubility of La and Sr in YSZ. In the center of the convex contact ring, the penetration depth of Mn is ~30 nm, substantially smaller than that in the edge region of the contact ring. This indicates that Mn preferably diffuses into YSZ in the edge region of convex contact rings exposed to the oxygen environment.

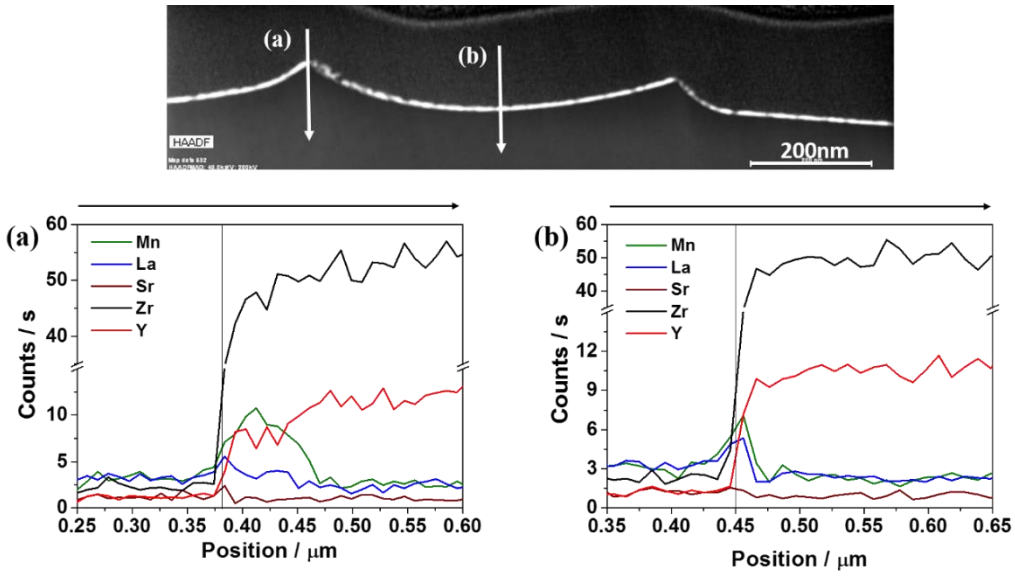

Figure 4.7 TEM micrograph of the cross-section of a convex contact ring on YSZ electrolyte surface and the corresponding line scan along (a) the edge and (b) the center of the convex contact ring.

Figure 4.8 shows the high resolution TEM (HRTEM) image of the edge of the convex contact ring. Mn signal was detected inside this edge region. YSZ cubic lattice presents a high symmetry of the atomistic configuration with periodicity and continuity. From the fast Fourier transform (FFT) image of the edge region, cubic crystallographic planes of 200 and 220 were identified with plane distances of 0.25 nm and 0.18 nm,

respectively. This is typically associated with YSZ crystalline structure. The FFT patterns taken within the bulk regions of YSZ show the planes of 200 and 220 with *d*-spacing of 0.25 nm and 0.18 nm, respectively, which are identical to that measured in the edge region of the contact ring on the YSZ. The calculated lattice constant (*a*) of the cubic YSZ phase measured in the edge and bulk regions of the substrate is exactly the same, *a* = 0.51 nm, indicating that the edge of the contact ring and bulk of the YSZ have identical crystallographic features. Therefore the diffusion of Mn cation into YSZ does not have any effect on the crystalline structure or lattice volume of the YSZ electrolyte at the TPB and interface regions.

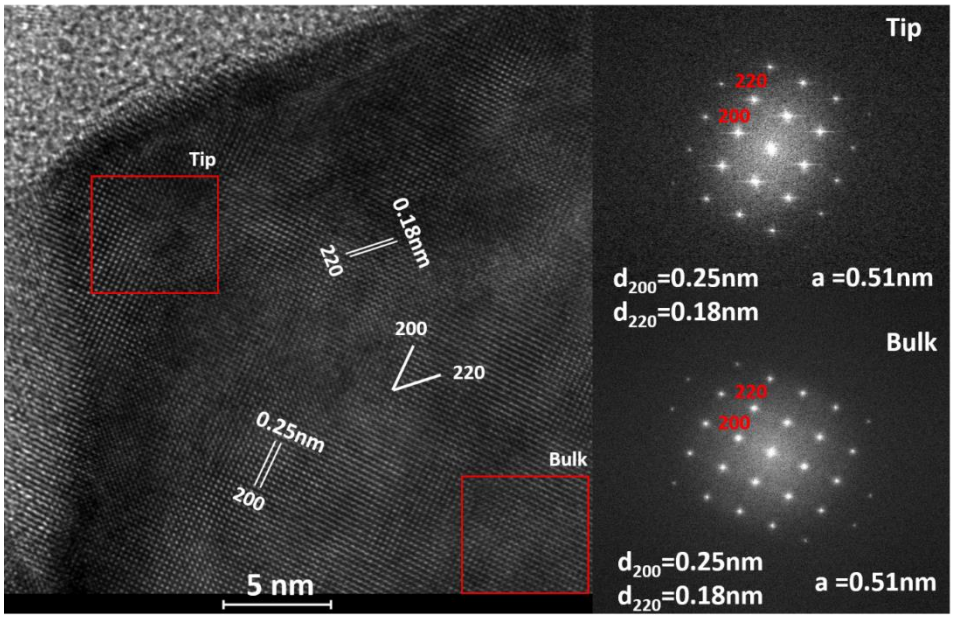

Figure 4.8 HRTEM of the convex contact ring and the corresponding FFT of the edge of the ring and the bulk of the YSZ. LSM electrode coating was removed by acid treatment.

Figure 4.9 presents the HRTEM analysis of the LSM/YSZ interface close to the TPB region. In this case, LSM electrode coating was removed by adhesive tape rather than by acid treatment in order to examine the crystalline structure along the interface between LSM and YSZ. Three interface regions were identified; Area1 is the edge region of the contact ring in the vicinity of TPB, Area2 is the contact region of LSM/YSZ on the YSZ electrolyte side and Area3 is the edge of contact ring on the LSM electrode side. FFT analysis of LSM region reveals the crystalline planes of 110 with planar spacing of 0.27 nm (Figure 4.9a), typical characteristics of perovskite structure of LSM[46, 47]. A slight distortion of LSM {110} planes was observed in

adjacent to the interface region. In the edge region of the contact ring (Area1), YSZ phase shows characteristic crystallographic {200} lattice planes with little dislocations upon the contact to air. In the boundary region between LSM and YSZ (Area2), a misplacement or disorientation of crystalline planes was observed parallel to the alignment of YSZ {200} planes. The inverse FFT (IFFT) of this boundary region reveals the misfit dislocation that formed in order to relax the strain accumulated during the sintering[48], and the distortion of YSZ {200} planes is a result of accommodating the lattice misfit between different LSM and YSZ crystallographic planes. In the case of interfaces between heterogeneous phases, mismatch of crystallographic planes would lead to the formation of either incoherent or semi-coherent interfaces in which locally coherent regions are disturbed by misfit dislocations that accommodate the lattice mismatch [49-51]. Area 1 and Area 2 are the regions close to TPB for the oxygen reduction reaction, and the good electrochemical performance of the LSM electrode (see Figure 4.3) indicates that the defects or disorientations at the interface would not impede the incorporation of O^{2-} from the cathode into the electrolyte, consistent with the observed oxygen transport through the tensile lattice distorted YSZ-CeO_2 heterointerface [52].

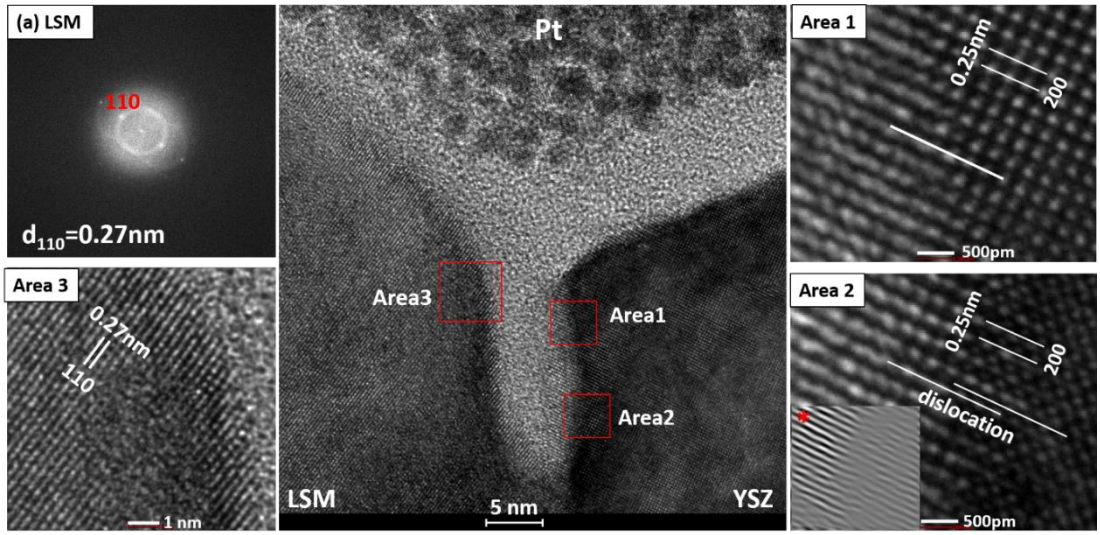

Figure 4.9 HRTEM of the convex contact ring region in the vicinity of TPB with three marked interface areas for examination. FFT of LSM phase is shown in (a) and the inset (*) in Area 2 is the IFFT of YSZ {200} planes. LSM electrode was removed by adhesive tape.

Figure 4.10 shows the HRTEM micrographs of two selected regions of LSM/YSZ interface. In one selected area, LSM phase is characterized by its LSM {110} lattice

planes with *d*-spacing of 0.27 nm, while YSZ is characterized by YSZ {200} planes with interplanar distance of 0.25 nm (Figure 4.10a). In the heterointerface region, lattice mismatch and distortion between LSM {110} and YSZ {200} crystallographic planes can be observed, yet no major defects are present by the interface. The appearance of misfit dislocation resulted from the lattice mismatch is favored thermodynamically, forming a semi-coherent interface [49, 50, 53]. The lattice planes of LSM {110} and YSZ {200} around the interface were reconstructed by IFFT, and distortion of the lattice planes in both phases at the interface region was observed, indicating the formation of heterointerface with disorientation and distortion during the high temperature sintering step. The width of the disorientation and distortion of the crystallographic lattice planes of the two phases at the interface was estimated to be ~0.10 nm. The significant activation effect of polarization on the enhancement of the activity of LSM electrode indicates that such disorientation at the heterointerface between LSM and YSZ would not inhibit the oxygen transport for the reaction, similar to the case as observed at the TPB (Figure 4.9). Moreover, another selected region of the LSM/YSZ interface is presented in Figure 4.10b. Within this interface area, the LSM phase is characterized by its lattice planes of LSM {110} with interplanar spacing of 0.27nm, while the YSZ {200} lattice planes are identified by its d-spacing of 0.25nm. Similar to the first region of LSM/YSZ interface, no major defects can be observed, and the lattice misfit dislocations can only be identified in adjacent to the interface, in a range of 1-5nm scale, without propagating into the bulk of the electrode and electrolyte. In addition, the IFFT reconstruction of LSM {110} and YSZ {200} planes clear indicates the enrichment of misfit dislocations around the interface. The misalignment of the LSM/YSZ planes accommodates the lattice mismatch of the two dissimilar phases, and the plane orientation at the interface is quite different to the first region of LSM/YSZ interface (Figure 4.10a). The different crystallographic orientation at the LSM/YSZ interface is clearly due to the nature of polycrystalline structure of both LSM electrode and YSZ electrolyte. The HRTEM results of LSM/YSZ interfaces apparently imply that semi-coherent electrode/electrolyte interface is formed after the high temperature sintering, and the absence of major defects explains the unaffected oxygen transport activities (see Figure 4.3), regardless of the small amount of lattice distortions observed in adjacent to the interface.

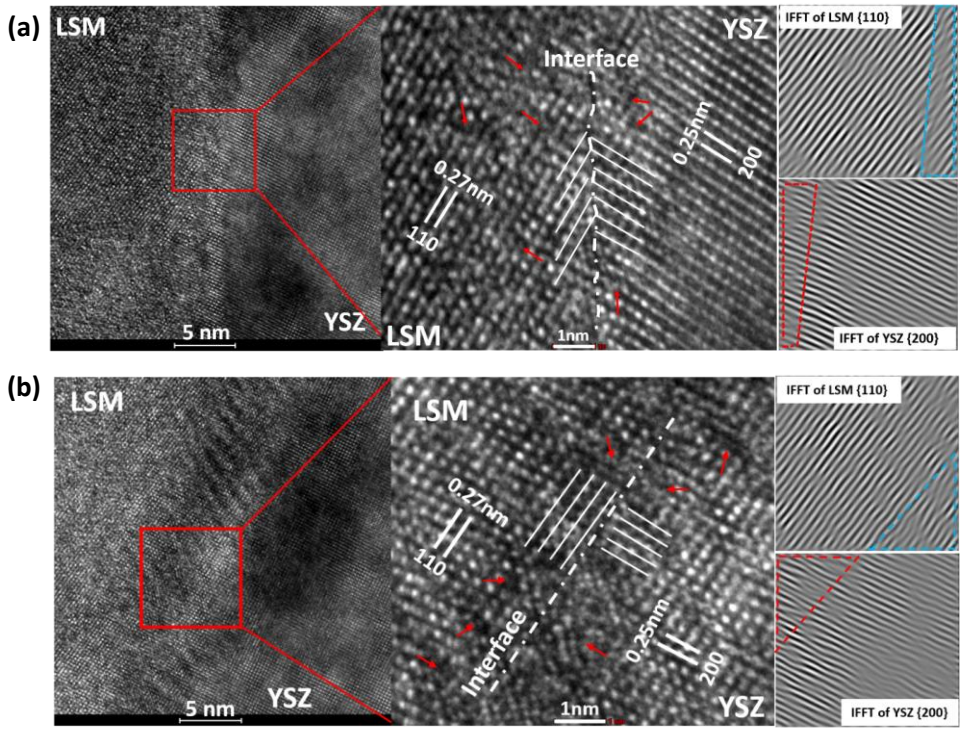

Figure 4.10 HRTEM micrographs of two selected regions of LSM/YSZ interface. The lattice planes of LSM {110} and YSZ {200} in adjacent to the interface are reconstructed by IFFT. LSM electrode was removed by adhesive tape. The dislocations are indicated by the red arrows.

4.3.5 LSM/GDC interface

Figure 4.11 shows the elemental distribution of the convex contact ring on the GDC electrolyte surface in contact with LSM electrode. LSM electrode was removed by acid treatment. Since the energy peaks of Gd, Ce, La and Mn are very close, the mapping results of La and Mn will overlap with signals of Gd and Ce, causing the overestimate of the intensity of Mn and La. Thus the Mn and La element maps were not presented. The EDS spectrum of the convex contact ring edge reveals the strong signals of cerium and gadolinium, whereas no manganese, lanthanum nor strontium can be detected. EDS line scan over the convex contact ring edge did not detect the presence of Mn and/or La cations within the convex contact ring region (Figure 4.11c). This clearly indicates no cation interdiffusion from the LSM towards LSM/GDC interface during the high temperature (~1150^{o}C) sintering process, very different to that observed at the LSM/YSZ interface under identical experimental conditions (Figure 4.6&4.7). Zhao et al [54] studied the solubility in CeO_2 using XRD and Raman

spectroscopy techniques and found out that the solubility limit of Mn in CeO_2 is less than 3 mol%, probably due to the much smaller ionic radius of Mn as compared to Ce. The much lower solubility of Mn in CeO_2 as compared to that in YSZ [43-45, 55], explains the no detection of cation interdiffusion in the LSM/GDC system as observed in this study.

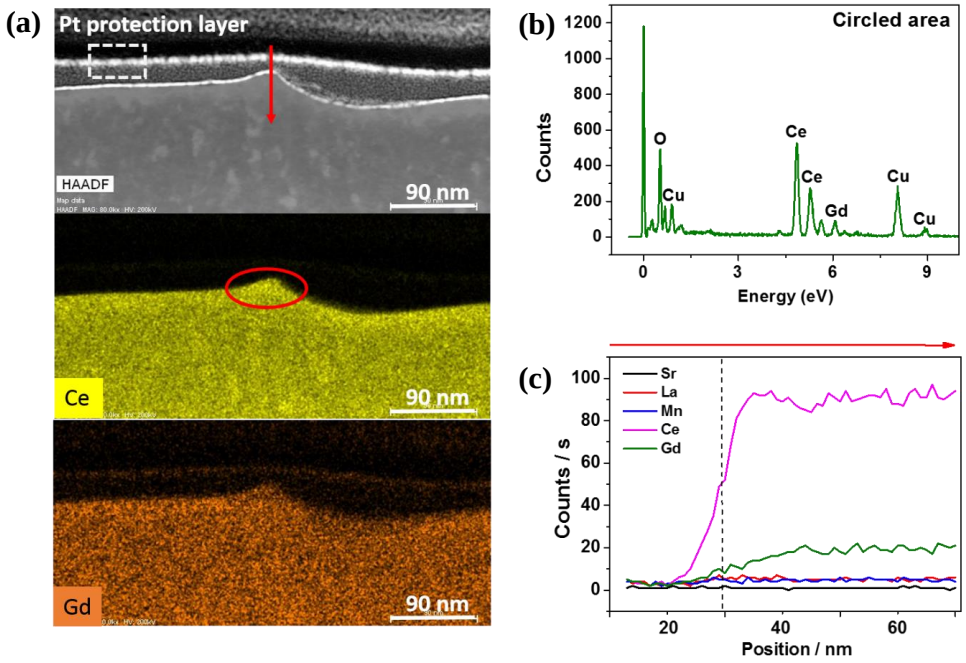

Figure 4.11 (a) High angle annular dark field image and corresponding EDS mapping of the contact ring region on GDC electrolyte, (b) EDS pattern and (c) line scan along the edge of the convex contact ring. LSM was removed by acid treatment.

Similar to LSM/YSZ cells, two selected regions of LSM/GDC interface were also examined by FIB-STEM and the results are shown in Figure 4.12. In this case, LSM electrode coating was removed by adhesive tape. In one selected area, LSM phase is characterized by a clear lattice alignment of 202 planes with an interplanar distance of 0.22 nm, whereas the symmetrical lattice structure of GDC {111} planes is identified with a *d*-spacing of 0.31 nm (Figure 4.12a). Within the interface region, accommodation of GDC {111} and LSM {202} crystallographic planes is accompanied with disorientation and dislocation within a narrow space of ~0.13 nm. The lattice mismatch between cubic GDC and LSM phases is mainly relieved by lattice dislocations (Figure 4.12), leading to the formation of a semi-coherent interface [49, 50, 53], similar to that observed in the case of LSM/YSZ interface. The appearance of

localized misfit dislocations results in the relaxation of strain and the subsequent reduction in interfacial Gibbs free energy, which is thermodynamically favorable[56, 57]. IFFT reconstruction of GDC {111} and LSM {202} in adjacent to the interface also shows the presence of lattice plane dislocations. The heterointerfaces with limited misfit dislocations would not inhibit the migration of oxygen from LSM cathode to GDC electrolyte, as shown by the significant enhanced electrochemical performance of LSM under the effect of polarization (Figure 4.3). In another selected region of LSM/GDC interface (Figure 4.12b), the clear lattice arrangement of LSM {012} can be identified with a planar distance of 0.38nm, while the periodic GDC {200} planes can also be characterized by its d-spacing of 0.27 nm. A sharp and abrupt interface is observed with a high level of semi-coherence, and likewise, no major crystal defects are found in the bulk of the materials, however, the lattice misfit dislocations only exists in adjacent to the LSM/GDC interface, in a narrow range of 1-3nm. The IFFT reconstruction of LSM {012} and GDC {200} planes also confirms the enrichment of lattice distortion around the interface area. The LSM/GDC interface in this area is characterized by the match and interaction of LSM {012} and GDC {200} lattice planes, very different to the first LSM/GDC interface area, which is identified by the accommodation of LSM {202} and GDC {111} planes. Similar to LSM/YSZ interfaces, the dissimilar crystallography of LSM/GDC interface structure is clearly a result of different orientation of LSM and GDC grains, which is the typical nature of polycrystalline materials. However, despite the small amount of misfit dislocations observed, the high level of semi-coherence of both LSM/GDC interfaces rationalizes the unaffected oxygen transport activities, regardless of the orientation of electrode and electrolyte crystals.

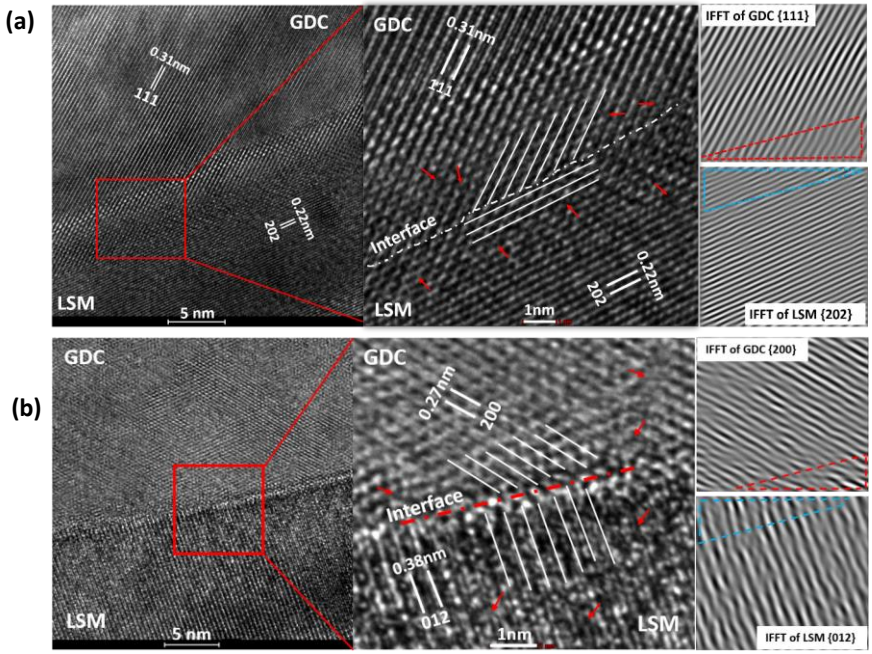

Figure 4.12. HRTEM micrographs of two selected regions of LSM/GDC interface and the corresponding IFFT reconstruction of (a) GDC {111} and LSM {202} and (b) GDC {200} and LSM {012} lattice planes in adjacent to the interface. LSM electrode was removed by adhesive tape. The dislocations are indicated by the red arrows.

The formation of LSM/YSZ and LSM/GDC interfaces during the high temperature sintering is illustrated schematically in Figure 4.13. Before the sintering, irregular shaped LSM particles are attached to the electrolyte surface with point contacts between LSM particles and electrolyte. After exposed to high temperatures, LSM particles gradually grow and sintering between LSM and YSZ occurs, indicated by the neck formation (Figure 4.4a). The grain growth and neck formation would diminish the curvature of the interface as well as the surface free energy [58, 59]. Cations such as manganese would segregate from the LSM perovskite structure and start to migrate along the YSZ electrolyte surface. In the case of YSZ electrolyte, Mn diffuses into YSZ, particularly at the contact ring edge region, replacing Y in YSZ lattice. On the other hand, Mn would diffuse along the GDC electrolyte surface but cation interdiffusion would not occur at the LSM/GDC interface, most likely due to the very low solubility of Mn in ceria [54]. The high temperature sintering leads to the formation of semi-coherent interface between LSM/YSZ and LSM/GDC crystallographic planes, despite the significant differences in orientation relationship and mismatch factors of two systems. The electrochemical performance of the LSM

electrode indicates that the presence of such crystallographic defects and lattice dislocations does not inhibit the O_2 reduction reaction at the interface.

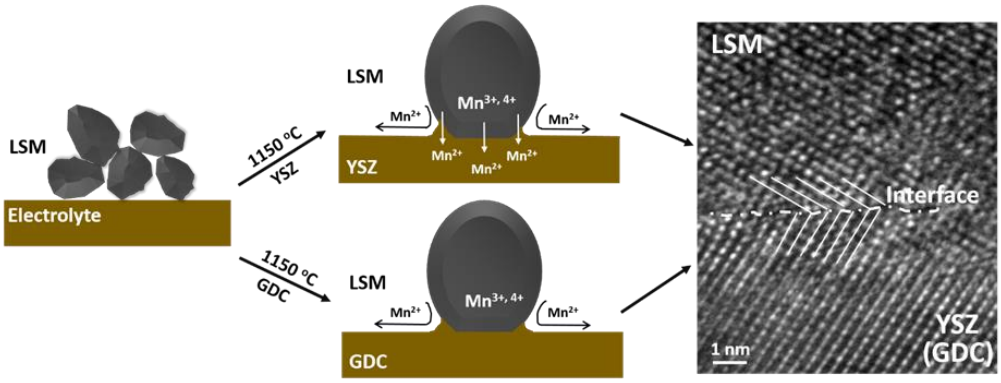

Figure 4.13 Schematic diagram showing the formation of electrode/electrolyte interfaces under the influence of high temperature sintering, *e.g.*, 1150°C.

4.4 Conclusion

LSM/YSZ and LSM/GDC heterointerfaces formed under high temperature sintering were studied using a combined FIB-STEM technique. The main outcomes of the study can be summarized as follows:

1. Electrochemically LSM electrode behaves similarly on YSZ and GDC electrolytes and shows a typical activation effect, *i.e.*, its electrocatalytic activity increases significantly with the cathodic polarization.
2. In both cases, electrode/electrolyte interface is characterized by the formation of convex contact rings on the YSZ and GDC electrolyte surface with dimension of 600-670 nm and depth of 20-38 nm. The negligible change in R_Ω with polarization indicates the stable LSM/YSZ and LSM/GDC interfaces formed under high temperature sintering.
3. In the case of LSM/YSZ interface, significant diffusion of Mn in the form of Mn^{2+} and in less extent La along the YSZ electrolyte surface and the edge of the convex contact rings was observed, replacing lattice Y. The replacement of Mn in YSZ does not affect the crystalline structure of YSZ phase. No cation interdiffusion was observed for LSM/GDC system. The results indicate that cation interdiffusion is not an essential requirement for the interface formation in the LSM electrodes.

4. Lattice disorientation and misfit dislocations of LSM electrode and YSZ or GDC electrolyte crystallographic planes occur to accommodate the lattice mismatch and surface energy at the interface. The results indicate the formation of semi-coherent interface in both LSM/YSZ and LSM/GDC, despite the fact that lattice mismatch factor between LSM and GDC crystallographic planes at the interface (f = ~29.0%) is significantly higher than 7.4% between LSM and YSZ. Disorientation and dislocation of crystallographic planes occur within a narrow region of 0.10-0.5 nm. The results indicate that such disorientation at the heterointerface between LSM electrode and YSZ or GDC electrolyte would not impede the oxygen transport for the O_2 reduction reaction.

4.5 References

[1] R.M. Ormerod, Solid oxide fuel cells, Chemical Society Reviews, 32 (2003) 17-28.

[2] S. Park, J.M. Vohs, R.J. Gorte, Direct oxidation of hydrocarbons in a solid-oxide fuel cell, Nature, 404 (2000) 265-267.

[3] A.B. Stambouli, E. Traversa, Solid oxide fuel cells (SOFCs): a review of an environmentally clean and efficient source of energy, Renewable and Sustainable Energy Reviews, 6 (2002) 433-455.

[4] T.M. Gür, Comprehensive review of methane conversion in solid oxide fuel cells: Prospects for efficient electricity generation from natural gas, Progress in Energy and Combustion Science, 54 (2016) 1-64.

[5] A. Choudhury, H. Chandra, A. Arora, Application of solid oxide fuel cell technology for power generation—A review, Renewable and Sustainable Energy Reviews, 20 (2013) 430-442.

[6] H. Moon, S. Kim, S. Hyun, H. Kim, Development of IT-SOFC unit cells with anode-supported thin electrolytes via tape casting and co-firing, International Journal of Hydrogen Energy, 33 (2008) 1758-1768.

[7] T. Fukui, S. Ohara, M. Naito, K. Nogi, Performance and stability of SOFC anode fabricated from NiO–YSZ composite particles, Journal of Power Sources, 110 (2002) 91-95.

[8] S.P. Jiang, Development of lanthanum strontium manganite perovskite cathode materials of solid oxide fuel cells: a review, Journal of Materials Science, 43 (2008) 6799-6833.

[9] Y.L. Liu, K. Thydén, M. Chen, A. Hagen, Microstructure degradation of LSM-YSZ cathode in SOFCs operated at various conditions, Solid State Ionics, 206 (2012) 97-103.

[10] T. Matsui, Y. Mikami, H. Muroyama, K. Eguchi, Influence of (La,Sr)MnO3+δ cathode composition on cathode/electrolyte interfacial structure during long-term operation of solid oxide fuel cells, Journal of Power Sources, 242 (2013) 790-796.

[11] A.L. Soldati, L. Baqué, H. Troiani, C. Cotaro, A. Schreiber, A. Caneiro, A. Serquis, High resolution FIB-TEM and FIB-SEM characterization of electrode/electrolyte interfaces in solid oxide fuel cells materials, International Journal of Hydrogen Energy, 36 (2011) 9180-9188.

[12] Z.-P. Li, T. Mori, G.J. Aucheterlonie, J. Zou, J. Drennan, M. Miyayama, Diffusion and segregation along grain boundary at the electrolyte–anode interface in IT-SOFC, Solid State Ionics, 191 (2011) 55-60.

[13] H. Fukunaga, M. Ihara, K. Sakaki, K. Yamada, The relationship between overpotential and the three phase boundary length, Solid State Ionics, 86-8 (1996) 1179-1185.

[14] M. Mukhopadhyay, J. Mukhopadhyay, A.D. Sharma, R.N. Basu, In-situ patterned intra-anode triple phase boundary in SOFC electroless anode: An enhancement of electrochemical performance, International Journal of Hydrogen Energy, 36 (2011) 7677-7682.

[15] S. Jiang, J.G. Love, L. Apateanu, Effect of contact between electrode and current collector on the performance of solid oxide fuel cells, Solid State Ionics, 160 (2003) 15-26.

[16] M. Kuznecov, P. Otschik, P. Obenaus, K. Eichler, W. Schaffrath, Diffusion controlled oxygen transport and stability at the perovskite/electrolyte interface, Solid State Ionics, 157 (2003) 371-378.

[17] S.P. Jiang, Activation, microstructure, and polarization of solid oxide fuel cell cathodes, Journal of Solid State Electrochemistry, 11 (2005) 93-102.

[18] S.P. Jiang, W. Wang, Effect of Polarization on the Interface Between (La,Sr)MnO[sub 3] Electrode and Y[sub 2]O[sub 3]-ZrO[sub 2] Electrolyte, Electrochemical and Solid-State Letters, 8 (2005) A115.

[19] Y.L. Liu, A. Hagen, R. Barfod, M. Chen, H.J. Wang, F.W. Poulsen, P.V. Hendriksen, Microstructural studies on degradation of interface between LSM–YSZ cathode and YSZ electrolyte in SOFCs, Solid State Ionics, 180 (2009) 1298-1304.

[20] T. Matsui, Y. Mikami, H. Muroyama, K. Eguchi, Quantitative Analysis of Microstructural Change at the Interface Between (La,Sr)MnO[sub 3] Cathode and YSZ Electrolyte upon Discharge Operation, Journal of The Electrochemical Society, 157 (2010) B1790.

[21] T. Matsui, M. Komoto, H. Muroyama, K. Eguchi, Interfacial Stability between Air Electrode and Ceria-Based Electrolyte under Cathodic Polarization in Solid Oxide Fuel Cells, Fuel Cells, 14 (2014) 1022-1027.

[22] T. Horita, T. Tsunoda, K. Yamaji, N. Sakai, T. Kato, a.H. Yokokawa, Microstructures and oxygen diffusion at the LaMnO3 film/yttria-stabilized zirconia interface, Solid State Ionics, 152-153 (2002) 439–446.

[23] A. Mitterdorfer, L.J. Gauckler, La2Zr2O7 formation and oxygen reduction kinetics of the La0.85Sr0.15MnyO3, O2(g)|YSZ system, Solid State Ionics, 111 (1998) 185-218.

[24] T. Horita, K. Yamaji, N. Sakai, Y. Xiong, T. Kato, H. Yokokawa, T. Kawada, Imaging of Oxygen Transport at SOFC cathode/electrolyte interfaces by a novel technique, Journal of Power Sources, 106 (2002) 224-230.

[25] M. Backhausricoult, Interface chemistry in LSM–YSZ composite SOFC cathodes, Solid State Ionics, 177 (2006) 2195-2200.

[26] C. Argirusis, M. Kilo, A. Müller, A. Weber, G. Borchardt, E. Ivers-Tiffée, Interdiffusion between electrode and electrolyte materials for cathode supported SOFCs with thin film electrolytes, 10th International IUPAC conference on high temperature materials chemistry (Jülich, Germany), 2000.

[27] J. Nair, P. Nair, E.B.M. Doesburg, J.G. Van Ommen, J.R.H. Ross, A.J. Burggraaf, J. Nair, Preparation and characterization of lanthanum zirconate, Journal of Materials Science, 33 (1998) 4517-4523.

[28] S.P. Jiang, J.G. Love, Origin of the initial polarization behavior of Sr-doped LaMnO3 for O-2 reduction in solid oxide fuel cells, Solid State Ionics, 138 (2001) 183-190.

[29] S.P. Jiang, Activation, microstructure, and polarization of solid oxide fuel cell cathodes, J. Solid State Electrochem., 11 (2007) 93-102.

[30] S.P. Jiang, W. Wang, Effect of polarization on the interface between (La,Sr) MnO3 electrode and Y2O3-ZrO2 electrolyte, Electrochem. Solid State Lett., 8 (2005) A115-A118.

[31] S. Jiang, J. Love, Origin of the initial polarization behavior of Sr-doped LaMnO3 for O2 reduction in solid oxide fuel cells, Solid State Ionics, 138 (2001) 183-190.

[32] Hee Y. Lee, Woo S. Cho, Seung M. Oh, H.-D. Wiemh6fer, W. Gopel, Active Reaction Sites for Oxygen Reduction in La0.gSr0.,MnO3/YSZ Electrodes, Journal of Electrochemical Society, 142 (1995) 2659-2664.

[33] S.P. Jiang, Thermally and Electrochemically Induced Electrode/Electrolyte Interfaces in Solid Oxide Fuel Cells: An AFM and EIS Study, Journal of The Electrochemical Society, 162 (2015) F1119-F1128.

[34] N. Li, N. Ai, K. Chen, Y. Cheng, S. He, M. Saunders, A. Dodd, A. Suvorova, S.P. Jiang, In situ assembled La0.8Sr0.2MnO3 cathodes on a Y2O3–ZrO2 electrolyte of solid oxide fuel cells – interface and electrochemical activity, RSC Adv., 6 (2016) 99211-99219.

[35] N. Li, N. Ai, K. Chen, Y. Cheng, S. He, M. Saunders, A. Dodd, A. Suvorova, S.P. Jiang, In situ assembled La0.8Sr0.2MnO3 cathodes on a Y2O3-ZrO2 electrolyte of solid oxide fuel cells - interface and electrochemical activity, RSC Advances, 6 (2016) 99211-99219.

[36] S.P. Jiang, J.P. Zhang, L. Apateanu, K. Foger, Deposition of chromium species at Sr-doped LaMnO3 electrodes in solid oxide fuel cells I. Mechanism and kinetics, J. Electrochem. Soc., 147 (2000) 4013-4022.

[37] M. Backhaus-Ricoult, K. Adib, T. St.Clair, B. Luerssen, L. Gregoratti, A. Barinov, In-situ study of operating SOFC LSM/YSZ cathodes under polarization by photoelectron microscopy, Solid State Ionics, 179 (2008) 891-895.

[38] M. Backhaus-Ricoult, M. Badding, Y. Thibault, Grain boundary segregation and conductivity in yttria-stabilized zirconia, Ceramic Transactions, 2006, pp. 173-191.

[39] H. Taimatsu, K. Wada, H. Kaneko, H. Yamamura, Mechanism of Reaction between Lanthanum Manganite and Yttria-Stabilized Zirconia, Journal of the American Ceramic Society, 75 (1992) 401-405.

[40] K. Kleveland, M.-A. Einarsrud, C.R. Schmidt, S. Shamsili, S. Faaland, K. Wiik, T. Grande, Reactions between Strontium-Substituted Lanthanum Manganite and Yttria-Stabilized Zirconia: II, Diffusion Couples, Journal of the American Ceramic Society, 82 (2004) 729-734.

[41] L.A.J. Garvie, A.J. Craven, R. Brydson, Use of Electron-Energy-Loss near-Edge Fine-Structure in the Study of Minerals, American Mineralogist, 79 (1994) 411-425.

[42] B.C. Tofield, W.R. Scott, Oxidative nonstoichiometry in perovskites, an experimental survey; the defect structure of an oxidized lanthanum manganite by powder neutron diffraction, Journal of Solid State Chemistry, 10 (1974) 183-194.

[43] Tatsuya Kawada, Natsuko Sakai, Harumi Yokokawa, M. Dokiya, Reaction between solid oxide fuel cell materials, Solid State Ionics, 50 (1992) 189-196.

[44] M. Mori, T. Abe, H. Itoh, O. Yamamoto, G.Q. Shen, Y. Takeda, N. Imanishi, Reaction mechanism between lanthanum manganite and yttria doped cubic zirconia, Solid State Ionics, 123 (1999) 113-119.

[45] S.P. Jiang, J.P. Zhang, K. Foger, Chemical interactions between 3 mol% yttria-zirconia and Sr-doped lanthanum manganite, J. Eur. Ceram. Soc., 23 (2003) 1865-1873.

[46] R. Moriche, D. Marrero-López, F.J. Gotor, M.J. Sayagués, Chemical and electrical properties of LSM cathodes prepared by mechanosynthesis, Journal of Power Sources, 252 (2014) 43-50.

[47] A. Hammouche, E. Siebert, A. Hammou, Crystallographic, thermal and electrochemical properties of the system La1−xSrxMnO3 for high temperature solid electrolyte fuel cells, Materials Research Bulletin, 24 (1989) 367-380.

[48] F.K. LeGoues, The Effect of Strain on the Formation of Dislocations at the SiGe/Si Interface, MRS Bulletin, 21 (1996) 38-44.

[49] F. Ernst, P. Pirouz, A.H. Heuer, HRTEM study of a Cu/Al2O3interface, Philosophical Magazine A, 63 (1991) 259-277.

[50] A. Trampert, F. Ernst, C.P. Flynn, H.F. Fischmeister, M. Ru¨hle, High resolution transmission electron microscopy studies of the Ag/MgO interface, Acta Metallurgica et Materialia, 40 (1992) S227-S236.

[51] O.I. Lebedev, G.V. Tendeloo, S. Amelinckx, H.L. Ju, K.M. Krishnan, High-resolution electron microscopy study of strained epitaxial La0.7Sr0.3MnO3thin films, Philosophical Magazine A, 80 (2000) 673-691.

[52] D. Pergolesi, E. Fabbri, S.N. Cook, V. Roddatis, E. Traversa, J.A. Kilner, Tensile lattice distortion does not affect oxygen transport in yttria-stabilized zirconia-CeO2 heterointerfaces, ACS Nano, 6 (2012) 10524-10534.

[53] S. Cazottes, Z.L. Zhang, R. Daniel, J.S. Chawla, D. Gall, G. Dehm, Structural characterization of a Cu/MgO(001) interface using CS-corrected HRTEM, Thin Solid Films, 519 (2010) 1662-1667.

[54] L. Zhao, J. Hyodo, T. Ishihara, K. Sasaki, S.R. Bishop, XRD and Raman Spectroscopy Study of Mn Solubility in Cerium Oxide, ECS Transactions, 57 (2013) 1607-1612.

[55] V.P. Dravid, V. Ravikumar, M.R. Notis, C.E. Lyman, G. Dhalenne, A. Revcolevschi, Stabilization of Cubic Zirconia with Manganese Oxide, Journal of the American Ceramic Society, 77 (1994) 2758-2762.

[56] S.B. Sinnott, E.C. Dickey, Ceramic/metal interface structures and their relationship to atomic- and meso-scale properties, Materials Science and Engineering: R: Reports, 43 (2003) 1-59.

[57] R. Schweinfest, S. Köstlmeier, F. Ernst, C. Elsäser, T. Wagner, M.W. Finnis, Atomistic and electronic structure of Al/MgAl2O4and Ag/MgAl2O4interfaces, Philosophical Magazine A, 81 (2001) 927-955.

[58] M. Cologna, R. Raj, Surface Diffusion-Controlled Neck Growth Kinetics in Early Stage Sintering of Zirconia, with and without Applied DC Electrical Field, Journal of the American Ceramic Society, 94 (2011) 391-395.

[59] W.D. Kingery, Introduction to ceramics / W. D. Kingery, H. K. Bowen, D. R. Uhlmann, 2d ed.. ed., New York : Wiley, New York, 1976.

Chapter 5: A FIB-STEM Study of Strontium Segregation and Interface Formation of Directly Assembled $La_{0.6}Sr_{0.4}Co_{0.2}Fe_{0.8}O_{3-\delta}$ Cathode on Y_2O_3-ZrO_2 Electrolyte of Solid Oxide Fuel Cells

Abstract

Electrode/electrolyte interface plays a critical role in the performance and stability of solid oxide fuel cells (SOFCs). Here, interface formation, Sr segregation and reaction of directly assembled $La_{0.6}Sr_{0.4}Co_{0.2}Fe_{0.8}O_{3-\delta}$ (LSCF) cathode on barrier-layer-free Y_2O_3-ZrO_2 (YSZ) electrolyte are studied in detail using focused ion beam and scanning transmission electron microscopy (FIB-STEM) techniques. The results indicate that polarization promotes the formation of LSCF/YSZ interface with plane orientation relationship of $\theta_{\{110\}LSCF/\{111\}YSZ}$ =48.8^o and low mismatch factor of $f_{\{110\}LSCF/\{111\}YSZ}$ = 6.9%. Further polarization induces the Sr segregation and diffusion towards the LSCF/YSZ interface, forming Sr rich layer (SRL, primarily SrO) at LSCF and YSZ interface. This is followed by the interaction between SRL and YSZ, forming $SrZrO_3$ insulating phase. The formation of $SrZrO_3$ phase at the interface is characterized by crater-shaped contact marks on YSZ electrolyte surface with crystallography lattice plane orientation affected by the YSZ electrolyte ($\theta_{\{022\}YSZ/\{040\}SrZrO3}$ = 7.5^o and $f_{\{022\}YSZ/\{040\}SrZrO3}$ = 0.0%). Further polarization increases the thickness of the $SrZrO_3$ reaction layer with the disintegration of LSCF structure at the interface. The results indicate that chemical reaction between LSCF and YSZ can occur at 750 ^{o}C under polarization conditions, which is kinetically induced by the segregated SrO and subsequent reaction with YSZ to form $SrZrO_3$ phase.

5.1 Introduction

In the previous chapter, $La_{0.8}Sr_{0.2}MnO_3$ electrode was pre-sintered on the electrolyte at high temperature to form intimate contact. However, some electrodes tend to react with electrolyte during the pre-sintering process. Thus in this chapter, we will discuss the possibility of applying the electrode without high temperature firing. Lanthanum strontium cobalt ferrite (LSCF) perovskite is one of the most popular and investigated mixed ionic and electronic conducting (MIEC) cathodes for intermediate temperature solid oxide fuel cells (IT-SOFCs) due to its superior electrical conductivity (~250 S cm^{-1} at 800^{o}C)[1], oxygen ion conductivity (~0.2 S cm^{-1} at 900^{o}C)[2, 3] and high electrocatalytic activity for O_2 reduction reaction[4-6]. However, LSCF electrode suffers from the performance degradation due to the Sr segregation, which is driven by the ionic radius mismatch of Sr and La, and the tendency to minimize surface

stress/strain[7-9]. A degradation rate of 0.08 to 0.17% per hour was reported for anode-supported LSCF cells under polarization conditions of 750^{o}C and 0.7V for 100 h[10]. The enrichment of Sr at the cathode surface de-activates the reaction sites for oxygen reduction reaction and thus increase the cathode resistance[11]. High temperature sintering can accelerate the Sr segregation at the surface of LSCF perovskite as well as at the cathode/electrolyte interface[12], greatly affecting the durability and electrocatalytic activity of the LSCF electrodes[8, 9, 11, 13]. LSCF is also chemically reactive with yttrium stabilized zirconia (YSZ), forming insulating products like $La_2Zr_2O_7$ and $SrZrO_3$ at temperatures as low as 800^{o}C[14, 15]. In order to prevent the detrimental reactions at the interface, a barrier layer of doped ceria such as Gd doped ceria (GDC) is required between LSCF and YSZ[16-22], which is currently proved to be an effective way to prevent the detrimental reactions at the interface. Shimura et al[21] adopted the samaria doped ceria interlayer for LSCF/YSZ symmetrical cell and then operated at 900^{o}C and a constant current density of 0.5A cm^{-2} for 5500 h, and they found very stable electrode IR-free overpotential during the tests, while the cathode ohmic resistance increased markedly. Nevertheless, the use of ceria-based barrier layer not only complicates the fabrication steps with increasing costs, but may also contribute to the degradation at the ceria/YSZ interface after long-term operation in some cases [17, 18, 23-25].

It has been known that electrochemical polarization has a significant effect on the Sr segregation on the surface of porous LSCF electrodes and the segregated Sr tends to migrate across the ceria barrier layer to react with the YSZ electrolyte, forming insulating $SrZrO_3$ phase[26-28]. Our early study also showed that cathodic polarization can induce the interface formation between directly assembled LSCF electrode and YSZ electrolyte and further polarization leads to the significant Sr segregation and diffusion at the electrode/electrolyte interface[29]. However, despite the importance of the Sr segregation and interface formation in SOFCs, there appears no systematic study on the effect of polarization on the interface formation, Sr segregation/diffusion and reaction at the LSCF/YSZ interface region.

Herein, the intrinsic relationship between polarization, Sr segregation and interface formation between LSCF cathode and YSZ electrolyte is investigated in detail using a combined focused ion beam - scanning transmission electron microscopy (FIB-STEM) technique. Direct assembly technique has been used to apply LSCF cathode on barrier-

layer-free YSZ electrolyte without subsequent high temperature sintering[29-33]. The results reveal that cathodic polarization induces the electrode/electrolyte interface with concomitant Sr segregation and diffusion. Sr segregation and diffusion at the interface region becomes significant with prolonged polarization, leading to the formation of $SrZrO_3$ phase and a gradual degradation in the electrochemical performance.

5.2 Experimental

5.2.1 Fabrication of electrolyte supported cells and directly assembled electrode

$La_{0.6}Sr_{0.4}Co_{0.2}Fe_{0.8}O_{3-\delta}$ (LSCF) powder was synthesised using a sol-gel method, using $La(NO_3)_3 \cdot 6H_2O$ (99.9%, Alfa-Aesar, UK), $Sr(NO_3)_2$ (99%, Sigma-Aldrich, US), $Co(NO_3)_2 \cdot 6H_2O$ (98.0−102.0%, Alfa-Aesar, UK), $Fe(NO_3)_3 \cdot 9H_2O$ (98%,Chem Supply, Australia), citric acid (99.5%, Chem Supply, Australia), ethylenediaminetetraacetic acid (EDTA, 99%, Acros Organics, Australia), and ammonia solution (28%, Ajax Finechem, Australia). In this method, citric acid and EDTA act as complexing agents with the molar ratio of 1:1.5:1 (metal ions: citric acid: EDTA). Stoichiometric metal nitrates were blended with deionized water, and the calculated amounts of citric acid and EDTA ammonia solution were subsequently added. The pH of the solution was adjusted to 7 and the solution was stirred on a hot plate until the dry gel was formed. The resultant dried gel powder was calcined at 900 ^oC for 2 h, forming LSCF powder.

Electrolyte pellets were prepared by die-pressing of 8 mol% Y_2O_3 stabilized zirconia powder (YSZ, Tosoh, Japan), followed by sintering at 1450 ^oC for 5 h. The thickness of the YSZ electrolyte pellets was ~1.0 mm. Pt paste (Gwent Electronic Materials Ltd., UK) was painted on the centre and edge of the YSZ electrolyte pellet and sintered at 1100^oC for 2h as the counter and reference electrodes. As-synthesized LSCF powder was dispersed in an ink vehicle (Fuel Cell Materials, US) with a weight ratio of 1:1 and subsequently the cathode paste was painted on the other side of the electrolyte symmetrically opposite to the Pt counter electrode. Au mesh was used as the current collector in order to eliminate the contamination and migration of Pt to the electrode/electrolyte interface during the polarization experiments [34-37]. In order to study the interaction between LSCF and YSZ, LSCF paste was also painted on the

polished single crystal YSZ [111] pellet (Hefei Kejing Materials Technology Co., LTD., China), and the electrode was subsequently sintered at 900ºC for 100 h.

5.2.2 Characterization

Electrochemical performance was measured on a Zahner Electrochemical Workstation. Directly assembled LSCF on YSZ cells were cathodically polarised at 750 ºC and 1000 $mAcm^{-2}$ for 1, 12 and 100 h, and electrochemical impedance was measured under open circuit conditions in a frequency range of 0.1 Hz to 100 kHz with a signal amplitude of 20 mV. The electrode ohmic resistance, R_Ω, was obtained from the high-frequency intercept and consisted of the ohmic resistance of the electrolyte, electrode and contact resistance at the electrode/electrolyte interface. The overall electrode polarization resistance, R_P, was estimated by the differences between the high- and low-frequency intercepts.

Thermal compatibility between LSCF cathode and YSZ electrolyte was investigated using LSCF/YSZ oxide couples in a weight ratio of 1:1. To prepare the oxide couple, the same amount of LSCF and YSZ powders were grinded in an agate mortar for 1h. The oxide couple was calcined at 750, 800 and 900 ºC for 2 h in air, and then was characterised by the Bruker D8 Advance X-ray diffractometer. The microstructure of the electrolyte surface in contact with LSCF cathode was examined by scanning electron microscopy (SEM, Neon 40EsB, Zesis, Germany). To examine the morphology of the YSZ electrolyte surface, LSCF electrode coating was removed by hydrochloric acid (32 wt%, Sigma-Aldrich, US) treatment, and in some cases, directly assembled LSCF electrode was partially peeled off by stick tape in order to study the electrode/electrolyte interface. The topographic features of the electrolyte surface were obtained by atomic force microscopy (AFM, Alpha 300 SAR, WITec GmbH, Ulm Germany) at intermittent contact mode. YSZ lamella was lifted out and milled to around 70 nm in thickness using Dual Beam Focused Ion Beam - Scanning Electron Microscope (FIB-SEM, Helios Nanolab G3 CX, FEI company, US) with Ga^+ ion source as described elsewhere[38]. The elemental mapping and microstructural micrographs were obtained on the FIB milled sample using a high angle annular dark field scanning transmission electron microscopy (HAADF-STEM, FEI Titan G2 80-200 TEM/STEM with ChemiSTEM Technology, FEI company, US) at 200 kV. The fast Fourier transform (FFT) images were extracted using TEM Imaging & Analysis software (TIA, FEI Company, US) to examine the diffraction behavior of selected area,

while inverse FFT (IFFT) simulations were performed on Gatan Digital Micrograph (Gatan Digital Microscopy Suite, Gatan Inc., US) to reconstruct the selected lattice planes using FFT images.

5.3 Results and Discussion

5.3.1 Thermal compatibility and electrochemical performance

Figure 5.1a shows the XRD result of the LSCF/YSZ oxide couple sintered at different temperatures. The oxide couple sintered at 750^{o}C only shows the presence of LSCF and YSZ phases. However, as the sintering temperature of the oxide couple increased to 800^{o}C or above, diffraction peaks at 30.8^{o}, 44.7^{o} and 54.9^{o} were observed, which can be associated with the $SrZrO_3$ (110), (200) and (211) planes, respectively [39, 40]. This indicates that LSCF is chemically stable with YSZ at 750^{o}C. Thus the test temperature of directly assembled LSCF electrodes on barrier-layer-free YSZ was chosen as 750 ^{o}C in this study to avoid the interaction between LSCF and YSZ. As shown in Figure 5.1b, initial R_Ω was 2.5 Ω cm^2 and decreased significantly to 1.5 Ω cm^2 after polarization at 1000 mAcm^{-2} for 12 h. The reduction in R_Ω indicates the formation of electrode/electrolyte interface under the influence of cathodic polarization[29, 32]. R_p was reduced slightly from 1.5 Ω cm^2 to 1.1 Ω cm^2 after 12 h polarization. With further cathodic polarization, the electrochemical activity of directly assembled LSCF electrodes starts to deteriorate. After polarization for 100 h, R_Ω and R_p increased to 2.0 and 1.3 Ω cm^2, respectively. The subsequent increase in R_P and in particular R_Ω after prolonged polarization may imply the formation of resistive phase at the interface. The change of cathode potential ($E_{cathode}$) as a function of polarization time can be clarified into three stages (Figure 5.1c). At the initial stage (stage I), $E_{cathode}$ drops quickly under the influence of cathodic polarization, indicating an improved electrochemical performance and consistent with the decrease in both R_Ω and R_p. At stage II, the cathode potential remains more or less the same with the polarization. After polarization at 750 ^{o}C and 1000 mAcm^{-2} for ~5 h (stage III), $E_{cathode}$ starts to increase gradually, reaching 1.8V at the end of test for 100 h. This indicates the deterioration in the electrocatalytic activity of directly assembled LSCF electrodes on barrier-layer-free YSZ electrolyte with prolonged cathodic polarization.

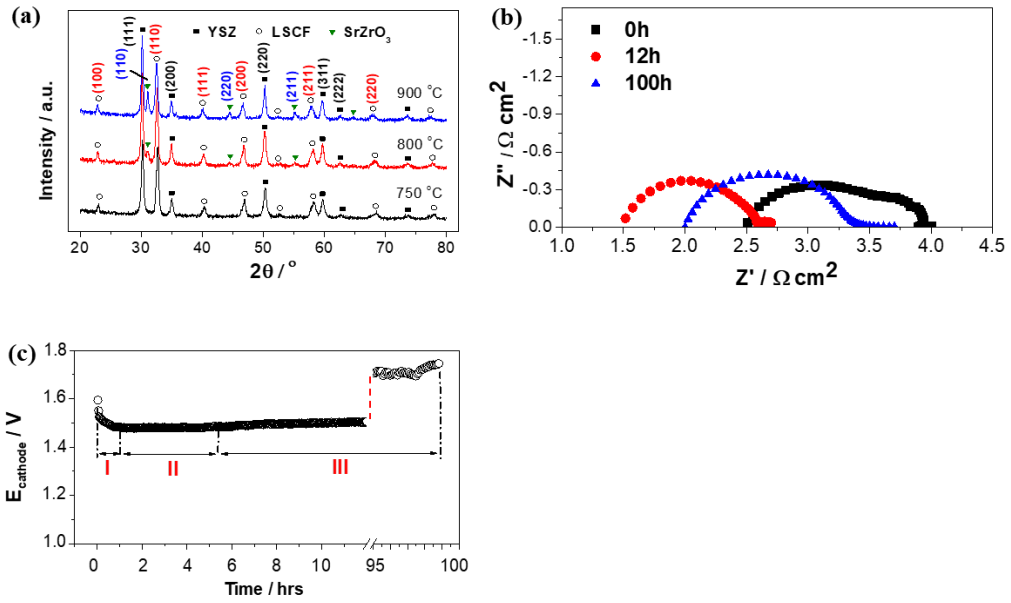

Figure 5.1 (a) XRD patterns of LSCF and YSZ oxide couples calcined at different temperatures, (b) electrochemical impedance curves of directly assembled LSCF on YSZ electrolyte, measured under open circuit after polarization at 750 ^{o}C and 1000 mAcm^{-2} for 0, 12 and 100 h, and (c) cathode potential ($E_{cathode}$) measured at 1000 mAcm^{-2} and 750 ^{o}C.

5.3.2 Microstructure of directly assembled LSCF/YSZ interfaces

Figure 5.2 shows the SEM micrographs of YSZ surface in contact with directly assembled LSCF after polarization at 750 ^{o}C and 1000 mAcm^{-2} for 1, 12 and 100 h. LSCF was removed by either adhesive tape or by acid treatment. In the case of the electrode after polarization for 1 h, YSZ surface is generally smooth and clean (Figure 5.2a), similar to that of pristine YSZ electrolyte surface (Figure 5.2g). Particles left on the YSZ electrolyte surface were quite small, 200±120 nm (Figure 5.2b). With the polarization time increased to 12 h, the electrolyte surface starts to have crater-shaped contact marks (Figure 5.2c) and size of particles left on the YSZ electrolyte surface also increases to 350±200 nm (Figure 5.2d). The crater-shaped contact marks continue to grow with prolonged polarization and the particles left on the YSZ electrolyte surface increased significantly to 520±200 nm after polarization for 100 h (Figure 5.2e and 5.2f). The YSZ surface in contact with LSCF electrode at OCP condition (750^{o}C for 12h) is also shown in Figure 5.2h. The electrode particles scatter on the electrolyte

surface, and there are no crater-shaped contact marks formed, i.e. no Sr segregation is observed under OCP condition at 750^{o}C.

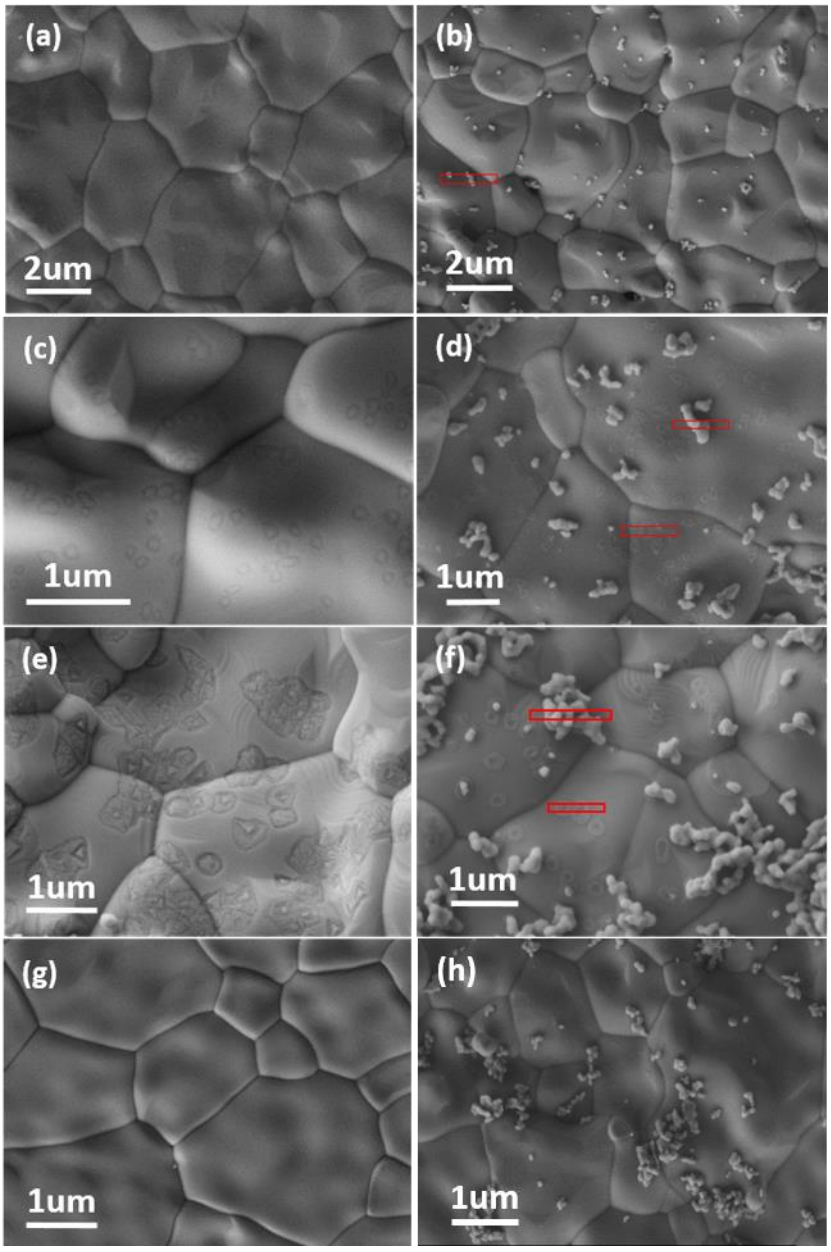

Figure 5.2 SEM micrographs of YSZ surface in contact with directly assembled LSCF electrodes after polarization at 750^{o}C and 1000 mA cm^{-2} for (h) 0 h, (a,b) 1 h, (c,d) 12 h and (e,f) 100 h. Pristine YSZ electrolyte surface with no contact with LSCF is given in (g). LSCF was removed by (a,c,e) acid treatment and by (b,d,f,h) adhesive tape. The red boxes indicate the locations of FIB milling.

Figure 5.3 presents the AFM micrographs of the YSZ surface in contact with directly assembled LSCF after polarization at 750^{o}C and 1000mA cm^{-2} for 1, 12 and 100 h. LSCF cathode was removed by acid treatment. There are no isolated contact marks on

the YSZ electrolyte surface after polarization for a short period of 1 h (Figure 5.3a). On the other hand, a large number of crater-shaped contact marks on the YSZ surface were clearly visible after polarization at 1000 mA cm^{-2} for 12 h and in a typical contact mark, the dimension of the crater is 150±30 nm in diameter and 1.3±1 nm in depth. The size of the crater contact marks corresponds to the size of the partilces left on YSZ surface as shown in Figure 5.2c. For the electrode polarized at 1000 mA cm^{-2} for 100 h, the size as well as the depth of the crater-shaped contact marks formed on the YSZ electrolyte surface increases dramatically, 300±100 nm in diameter and 3±2 nm in depth measured in a typical contact mark (Figure 5.3c). This clearly demonstrates the significant effect of polarization on the formation and microstructure of the interface between LSCF and YSZ.

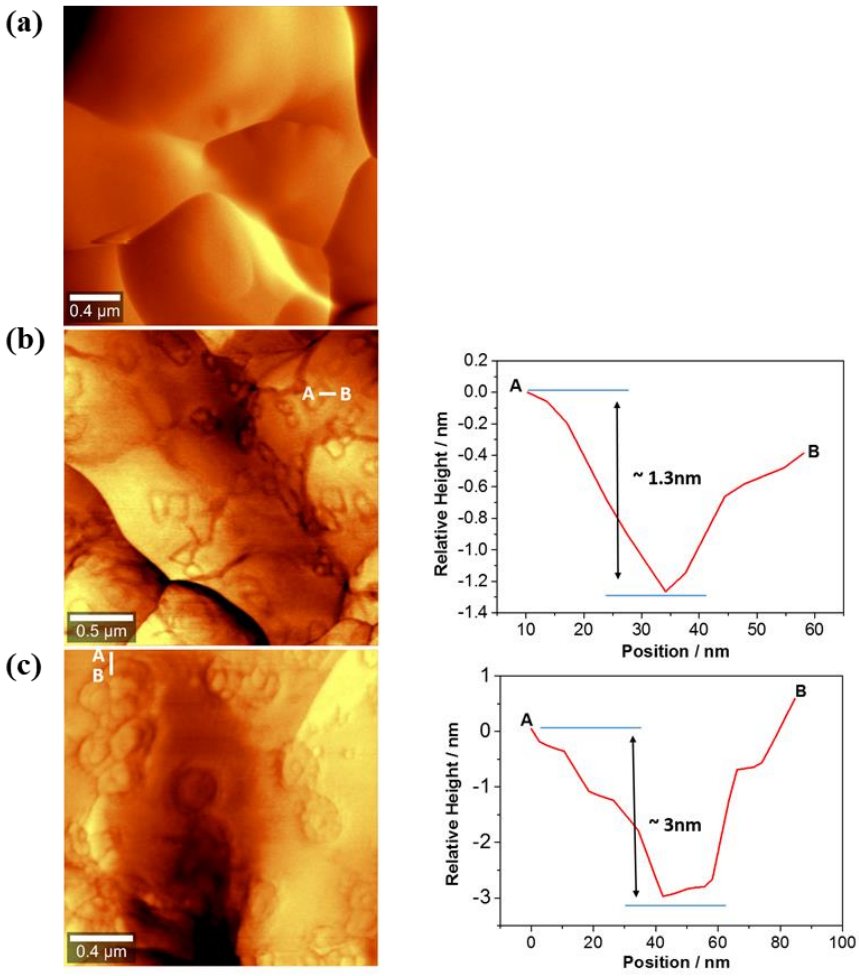

Figure 5.3 AFM micrographs of the YSZ electrolyte surface in contact with directly assembled LSCF electrode after polarization at 750 ^{o}C and 1000 mAcm^{-2} for (a) 1 h, (b) 12 h and (c) 100 h. LSCF electrode was removed by acid treatment.

Figure 5.4 shows the electrode/electrolyte interface lamella prepared by FIB corresponding to the regions of FIB milling as shown in Figure 5.2. After polarization for 1 h, a sharp and clean electrode/electrolyte interface was observed (Figure 5.4b), while a thin layer appears at the LSCF/YSZ interface after polarization for 12 h (Figure 5.4c). This layer can also be seen at the LSCF/YSZ interface after polarization for 100 h with significantly increased thickness. This indicates the change of the interface microstructure as a function of cathodic polarization time.

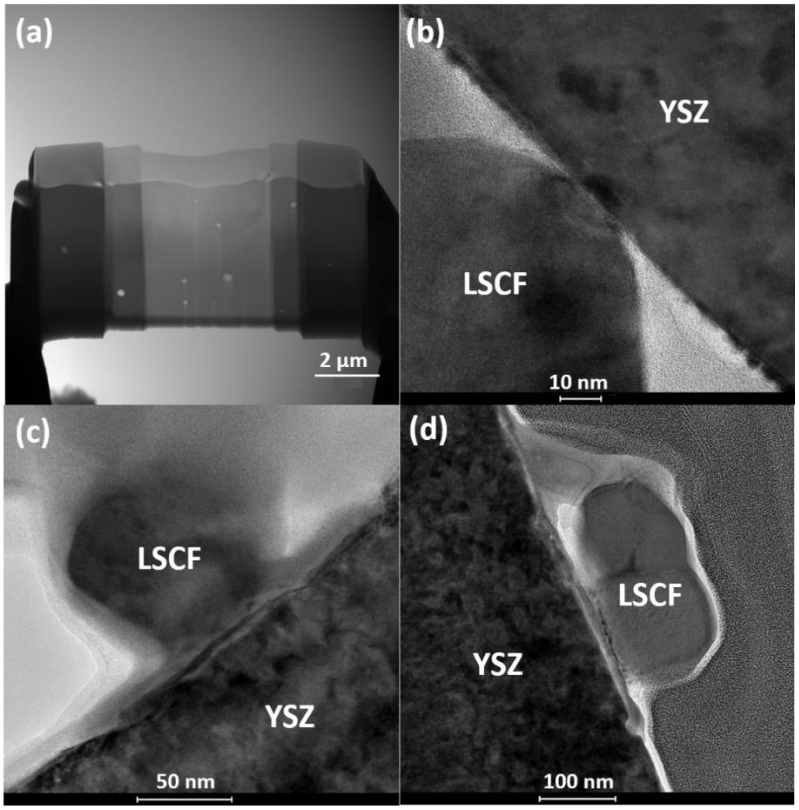

Figure 5.4 TEM micrographs of (a) typical FIB lamella prepared from LSCF/YSZ interface sample, and LSCF/YSZ interfaces after polarization at 750 ^{o}C and 1000 mA cm^{-2} for (b) 1 h, (c) 12 h and (d) 100 h.

5.3.3 LSCF/YSZ interfaces after polarization for 1 h

Figure 5.5 shows the STEM-EDS mapping of the LSCF/YSZ interface after polarization at 750 ^{o}C and 1000 mA cm^{-2} for 1 h. LSCF electrode particles are in good contact with the YSZ electrolyte surface with no voids or cracks at the interface. The EDS mapping analysis shows the clear interface between LSCF particles and YSZ electrolyte with no amorphous or additional interfacial layer. There is no Sr segregation or accumulation at the interface between LSCF and YSZ.

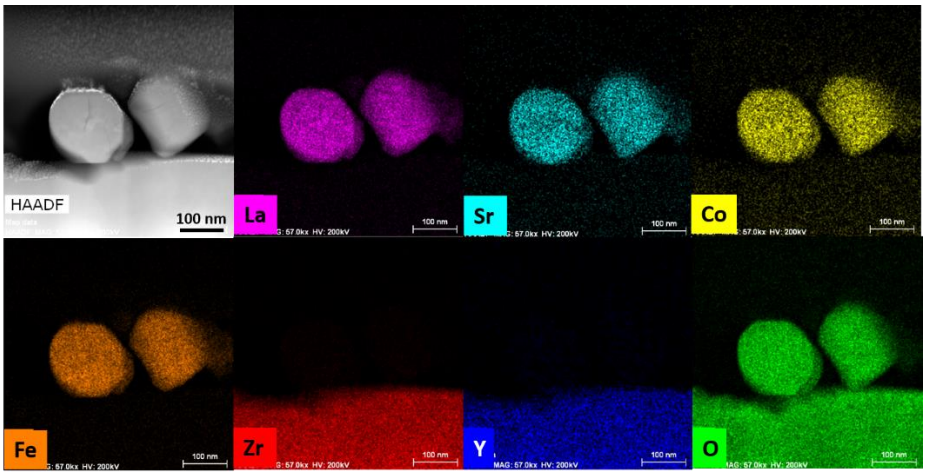

Figure 5.5 STEM-EDS mapping of directly assembled LSCF/YSZ interface after polarization at 750 ^{o}C and 1000 mA cm^{-2} for 1 h.

The directly assembled LSCF/YSZ interface after polarization at 750 ^{o}C and 1000 mA cm^{-2} for 1 h was examined by HRTEM and FFT, taken along $[011]_{LSCF}$ zone axis (Figure 5.6). The atomic geometry of the interface is characterised by a high level of periodicity and symmetry. The diffractogram of the interface is presented by the FFT micrograph, showing the overlapping of the cubic perovskite structure of LSCF[41] and the diffraction of $\{111\}_{YSZ}$ planes[42]. For example, $\{110\}_{LSCF}$ and $\{111\}_{YSZ}$ lattice planes can be identified with inter-planar spacing of 0.27 nm and 0.29 nm, respectively. As shown in the HRTEM micrograph, lattice planes of $\{110\}_{LSCF}$ and $\{111\}_{YSZ}$ meet at the interface with no amorphous or other solid solution phases. The orientation relationship between $\{110\}_{LSCF}$ and $\{111\}_{YSZ}$ planes can be identified as

$$\theta_{\{110\}LSCF/\{111\}YSZ} = 48.8\ ^{o} \quad (1)$$

where $\theta_{\{110\}LSCF/\{111\}YSZ}$ represents the angle between the two planes. It should be noted that the observed orientation relationship between $\{110\}_{LSCF}$ and $\{111\}_{YSZ}$ lattice planes may be different at other contact regions due to the polycrystalline nature of both phases, similar to that observed at LSM/YSZ and LSM/GDC interfaces[38]. The lattice mismatch factor (*f*) [43-45] between $\{110\}_{LSCF}$ and $\{111\}_{YSZ}$ planes can also be calculated:

$$f = \frac{d_{\{111\}YSZ} - d_{\{110\}LSCF}}{d_{\{111\}YSZ}} * 100\% = 6.9\% \quad (2)$$

Due to the crystallographic structure mismatch of the two heterogeneous phases, misfit dislocations occur (indicated by red arrows in Figure 5.6), in order to relax the

mismatch strain and to accommodate the lattice misfit at the interface[46-49]. Consequently, distorted and discontinuous lattice planes of the electrode and electrolyte were observed in adjacent to the interface. However, such misfit dislocations only exist within several nano-meters around the interface, without propagating into the electrode or electrolyte bulk. This indicates excellent interface formation between the LSCF cathode and YSZ electrolyte, consistent with the low mismatch factor (f=6.9%). However, it is also possible that the appearance of the observed dislocations in adjacent to the interface could be due to the overlapping of phases, or the local curvature of the FIB lamella [50-54]. For instance, Rentenberger et al.[50] analysed the HRTEM images of the nanostructured alloys, and found that the strong contrast variations on a small scale inside the grains could be caused by moiré effect arising from the overlapping of the grain boundaries instead of the dislocations, since moiré patterns and lattice misorientation occurring in the nanograins can dominate the image contrast. The formation of an excellent electrode/electrolyte interface under the influence of cathodic polarization is supported by the significantly reduced electrode ohmic resistance of the directly assembled LSCF electrode (see Figure 5.1). The results also indicate that distortion and misfit at the LSCF/YSZ heterointerface as shown in Figure 5.6 will not impede the oxygen transfer process of the O_2 reduction reaction, which is in good agreement with the previous studies on LSM/YSZ and LSM/GDC interface and on pulsed laser deposition (PLD) induced interface[38, 55].

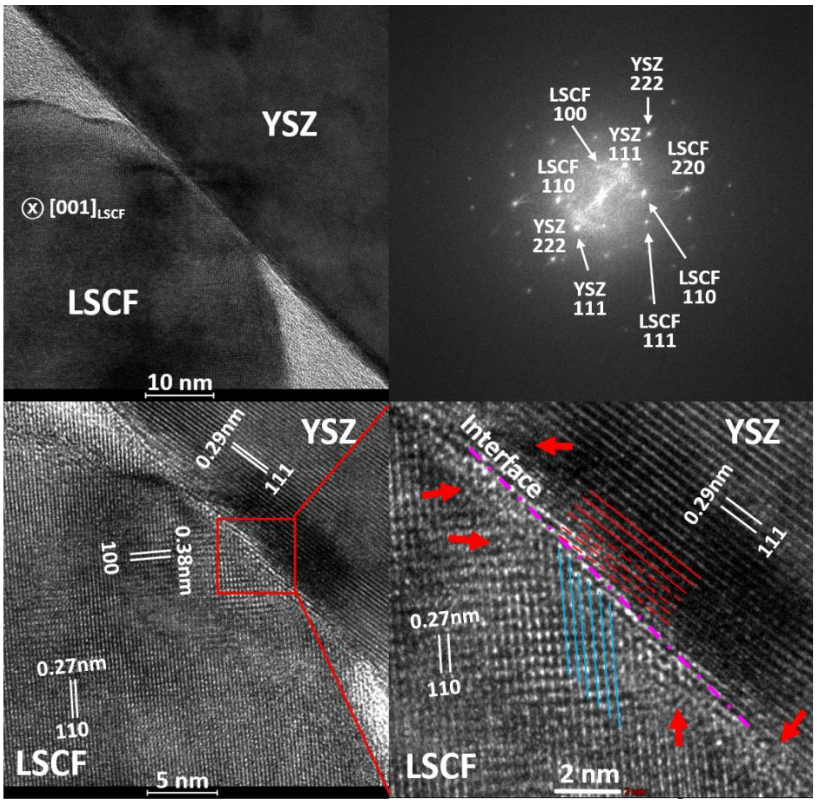

Figure 5.6 HRTEM and the corresponding FFT micrograph of directly assembled LSCF/YSZ interface after polarization at 750 ^{o}C and 1000 mA cm^{-2} for 1 h, observed along [001]$_{LSCF}$ zone axis. The lattice distortion is indicated by red arrows.

5.3.4 LSCF/YSZ interfaces after polarization for 12 h

After the LSCF/YSZ cell was polarized at 750 ^{o}C and 1000 mAcm^{-2} for 12 h, a thin layer at the electrode/electrolyte interface was observed, see Figure 5.4c. STEM-EDS mapping analysis shows that the thin layer primarily contains Sr and the content of La, Fe and Zr is much smaller (Figure 5.7), indicating the formation of SrO. The formation of Sr-rich layer (SRL) at the interface indicates the significant Sr segregation and diffusion under the influence of cathodic polarization [9, 11, 29, 56, 57].

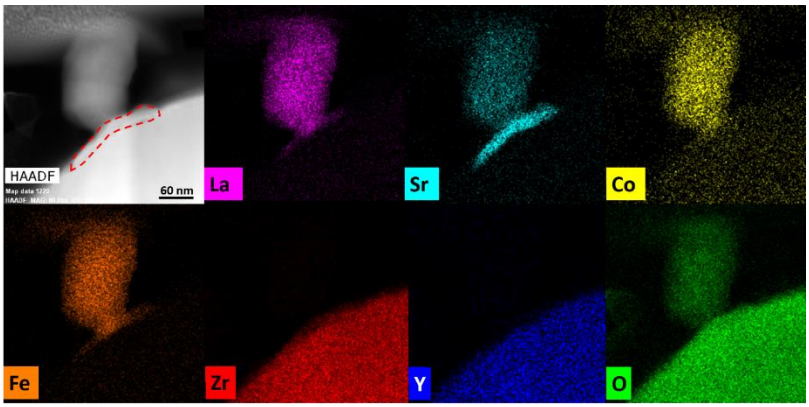

Figure 5.7 STEM-EDS mapping of directly assembled LSCF/YSZ interface after polarization at 750 ºC and 1000 mA cm^{-2} for 12 h.

Figure 5.8 shows the corresponding HRTEM micrographs of the LSCF/YSZ interface after polarization at 750 ºC and 1000 mA cm^{-2} for 12 h, observed along $[1\bar{1}\bar{2}]_{YSZ}$ zone axis. The thickness of the SRL is 15±5 nm and sandwiched between LSCF and YSZ, forming distinct LSCF/SRL and SRL/YSZ interfaces. The abrupt change at the interface regions is most likely due to the orientation change at the interfaces during the deposition of the SRL[46, 50, 58, 59] and the strain effect resulted from the lattice mismatch of the heterogeneous phases[49, 60], i.e. LSCF/SRL and SRL/YSZ. SRL exhibits the symmetry and crystallography similar with the YSZ electrolyte, characterised by the $\{111\}_{SRL}$ lattice planes with inter-planar spacing of 0.29 nm. This is supported by the diffractogram at the SRL/YSZ interface, showing a single YSZ cubic phase pattern, along $[1\bar{1}\bar{2}]_{YSZ}$ zone axis[61] (see the inset in Figure 5.8). This indicates that the SRL grows along the crystallography orientation of YSZ electrolyte, supported by the observed $\theta_{\{111\}SRL/\{111\}YSZ}$ =0 º. In the case of SRL/LSCF interface, the $\theta_{\{111\}SRL/\{210\}LSCF}$ =44.3º, with a mismatch factor of *f*=41.3%. Similar to the LSCF/YSZ interface after polarization for 1h, the orientation relationship between SRL and LSCF or SRL and YSZ observed in this case, only represents the local examined interface, and cannot be generalized to all other locations.

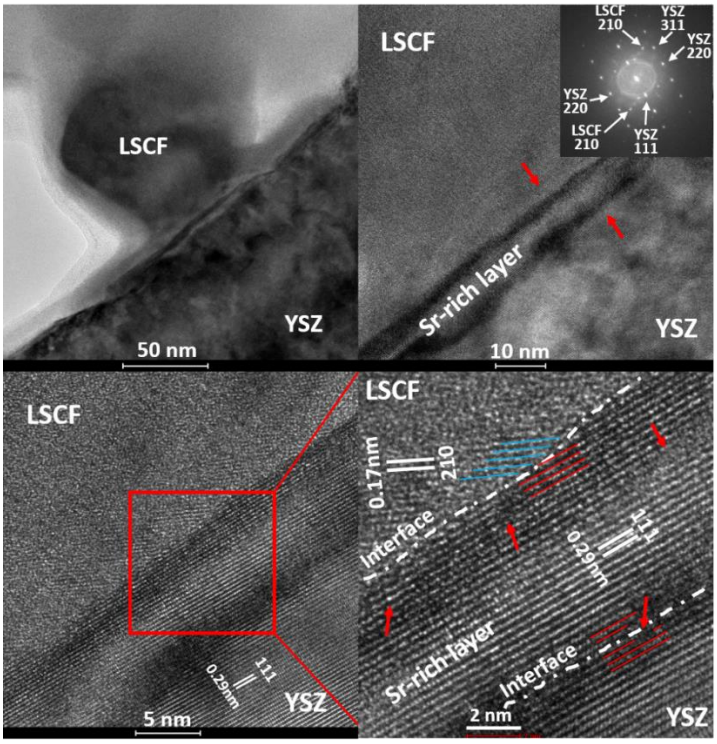

Figure 5.8 HRTEM micrographs of LSCF/SRL/YSZ interfaces after polarization at 750 ºC and 1000 mA cm^{-2} for 12 h. The inset presents the FFT diffractogram over the three-phase interface. The lattice distortion is indicated by red arrows.

The composition of the SRL was further examined by STEM-EDS analysis and the results are shown in Figure 5.9. In a thinner region of SRL (Region I), a significant accumulation of Sr and Zr is detected with almost no detection of Fe and La. Within the depth of ~10 nm, the intensities of Sr and Zr atoms are almost identical, indicating the formation of $SrZrO_3$. In the thick region of the SRL, i.e., Region II, the depth of Sr is ~20 nm, distributed across the entire layer. In addition to the significant presence of Sr and Zr, there is also a presence of Fe and La with a thickness of ~10 nm, half of that of Sr depth. The close match between Sr and Zr indicates the formation of $SrZrO_3$, while the presence of La and Fe in thick SRL indicates disintegration of LSCF due to the excess segregation of Sr at the A-site of LSCF.

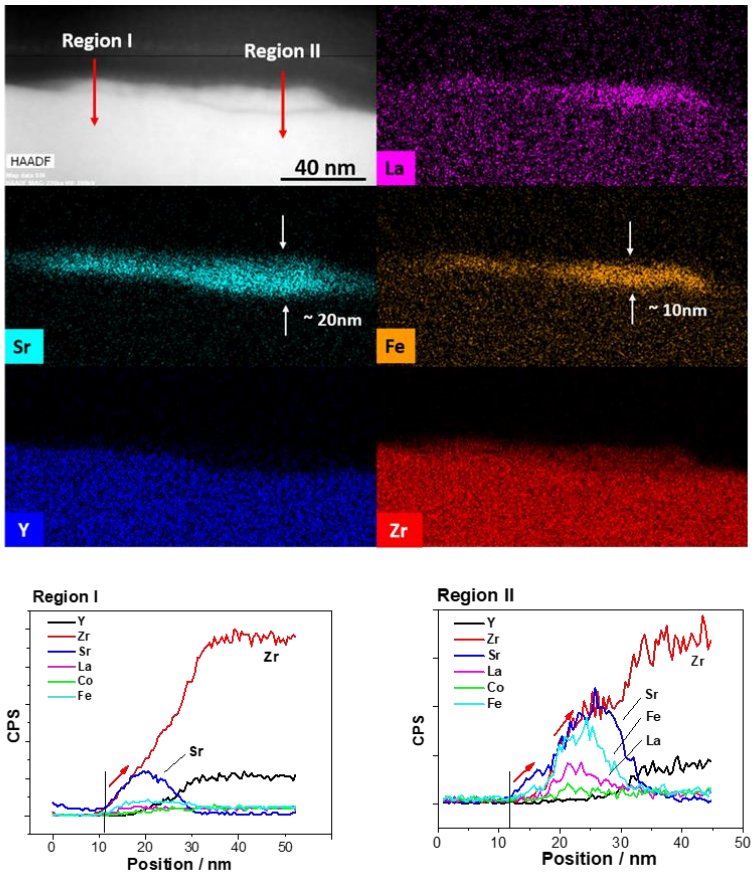

Figure 5.9 Element mapping and line scan results across a Sr-rich layer on YSZ electrolyte in contact with directly assembled LSCF after polarization at 750 ^{o}C and 1000 mAcm^{-2} for 12 h. LSCF was removed by adhesive tape.

Figure 5.10 shows the HRTEM micrographs of the Region I of SRL, observed along the $[011]_{YSZ}$ zone axis. From the micrograph, two different arrays of atoms aligned with identical geometry can be identified, showing almost the same symmetry and periodicity. SRL grows epitaxially to the electrolyte, supported by the STEM-EDS analysis (Figure 5.9). The cubic structure of the YSZ as well as the SRL is further confirmed by the FFT pattern shown as the inset in Area 2. The YSZ phase is characterized by its $\{111\}_{YSZ}$ and $\{200\}_{YSZ}$ planes with inter-planar spacing of 0.29 nm and 0.25 nm, respectively, in good accordance with that reported in the literature [62]. While the epitaxial SRL can also be identified by its $\{111\}_{SRL}$ and $\{200\}_{SRL}$ lattice planes with inter-planar spacing of 0.29 nm and 0.25 nm, respectively, corresponding to the typical SrO cubic structure [63]. The orientation relationship between the YSZ and the SRL reveals the parallel planes of $\{111\}_{YSZ}//\{111\}_{SRL}$ and $\{200\}_{YSZ}//\{200\}_{SRL}$, and the parallel axis of $[011]_{YSZ}//[011]_{SRL}$ with a low mismatch factor (f = 0.0%) between YSZ and SRL phase at the interface. During the epitaxial

growth of the SRL, slight deviation and/or distortion of the lattice planes at the YSZ/SRL interface also occurs. As shown in the Area 1 (see Figure 5.10), the slight misorientation of the $\{200\}_{YSZ}$ planes was observed, highlighted by the dotted line, and the IFFT image of the $\{200\}_{YSZ}$ planes also confirms the localised misalignment of the lattice plane structure near the interface region. This phenomenon in turn implies that during the growth of the first few lattice planes, the SRL film is slightly distorted in order to establish a coherent interface, i.e. atom-by atom match, with the YSZ electrolyte, which is also commonly observed in the field of epitaxial film growth areas [42, 46, 49, 64-67]. As the SRL, most likely SrO, has similar cubic structure to YSZ electrolyte with space group symmetry of Fm-3m for both phases and lattice constants (*a*) of 5.14 Å and 5.13 Å, respectively [40, 62, 63, 68], the initial growth of SRL appears to be coherent and atomically continuous, with negligible plane distortion at the interface.

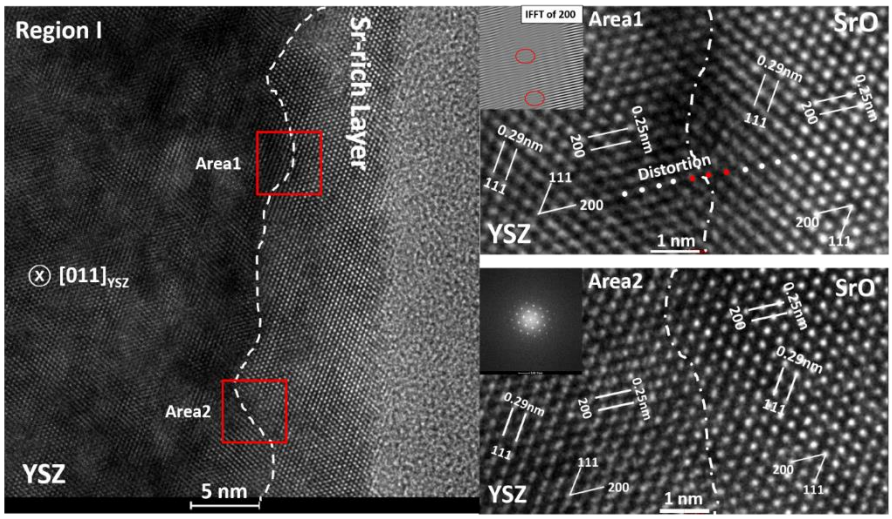

Figure 5.10 HRTEM micrographs of the SRL (Region I), observed along $[011]_{YSZ}$ zone axis. The insets are inverse fast Fourier transform in Area1 and fast Fourier transform of 200 planes in Area2.

In the case of thick SRL (Region II), the SRL shows an evidently different crystallography to the YSZ electrolyte, which is also supported by their different diffractogram, i.e. the FFT patterns (Figure 5.11). For example, YSZ is identified by its $\{111\}_{YSZ}$ planes with an inter-planar spacing of 0.29 nm, while SRL is characterised by its $\{040\}_{SRL}$ and $\{002\}_{SRL}$ planes, with inter-planar spacing of 0.20 nm and 0.29 nm, respectively. The lattice parameters of the SRL closely corresponds to that of orthorhombic $SrZrO_3$, which is characterized by the space group symmetry of Pnma

and the lattice constants of *a*=5.81 Å, *b*=8.22 Å and *c*=5.81 Å [40], while the lattice inter-planar spacing of $\{040\}_{SrZrO_3}$ and $\{002\}_{SrZrO_3}$ are also 0.20 nm and 0.29 nm, respectively[69]. The YSZ/SRL interface (magnified image, Figure 5.11) is characterized by an orientation relationship of $\theta_{\{111\}YSZ/\{040\}SRL}$ = 65.8° between $\{111\}_{YSZ}$ and $\{040\}_{SRL}$ planes, and parallel planes of $\{111\}_{YSZ}$ and $\{002\}_{SRL}$ can also be identified with a low lattice mismatch factor of 0.7%. Nevertheless, similar to Region I, lattice plane distortion can also be identified at the interface during the continued growth of SRL (see red arrows in Figure 5.11), consistent with the IFFT filtering images showing the misalignment of $\{111\}_{YSZ}$ and $\{040\}_{SRL}$ planes.

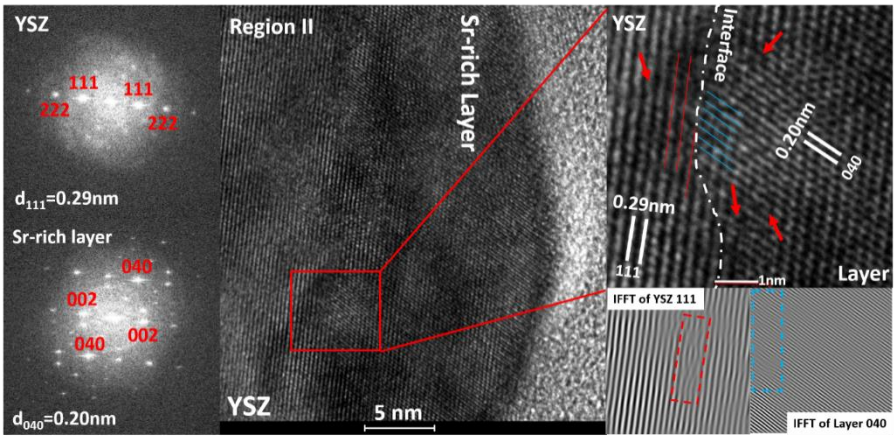

Figure 5.11 HRTEM micrographs of the SRL (Region II). The insets are inverse fast Fourier transform of YSZ [111] plane. The lattice distortion is indicated by red arrows. The directly assembled LSCF electrode was polarized at 750 °C and 1000 mA cm^{-2} for 12 h.

5.3.5 LSCF/YSZ interfaces polarised for 100 h

The directly assembled LSCF/YSZ cells after polarization at 750 °C and 1000 $mAcm^{-2}$ for 100 h were also studied. Figure 5.12 presents the STEM-EDS element distribution for YSZ electrolyte in contact with directly assembled LSCF particle. Similar to the LSCF electrode polarized for 12 h, a thick layer was formed at the interface. From the EDS analysis, there is predominant presence of Sr and Zr and to a less extent, Fe, La and Y in the SRL, consistent with that observed for the SRL of the LSCF electrode after polarization for 12h (see Figure 5.9). The Cu peaks observed in the EDS spectrum comes from the copper grid used for TEM test.

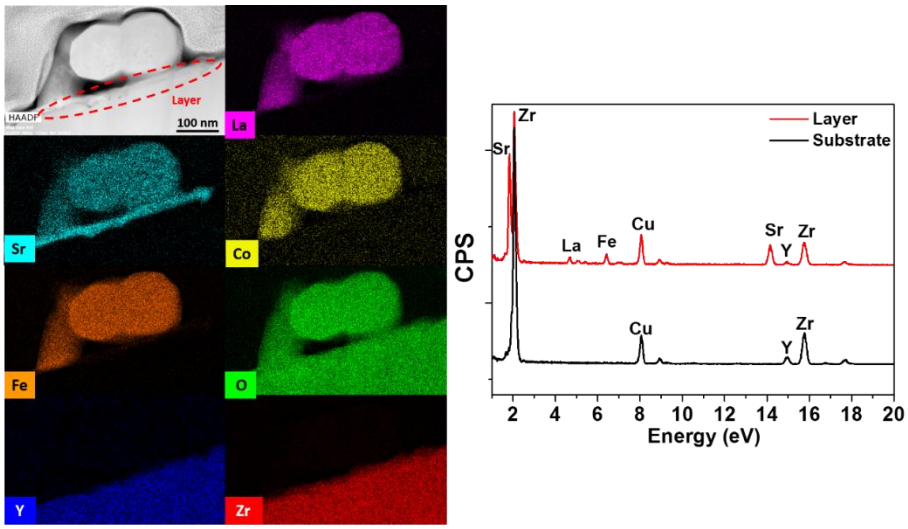

Figure 5.12 STEM-EDS mapping of the YSZ electrolyte in contact with LSCF electrode after polarization at 750^{o}C and 1000 mA cm^{-2} for 100h.

Figure 5.13a shows the HRTEM micrographs of the YSZ/SRL/LSCF three-phase region. Within the LSCF phase, the $\{110\}_{LSCF}$ plane with inter-planar spacing of 0.27 nm was identified by the FFT diffractogram. From the HRTEM image of LSCF/SRL interface, the SRL shows a different lattice geometry to the LSCF, indicating the change of crystalline structure after deposition of Sr, Fe and La. In addition, the HRTEM and FFT analysis of the SRL/YSZ interface, observed along $[011]_{YSZ}$ zone axis indicate that the SRL and the YSZ electrolyte show different crystallography (Figure 5.13b), different from that observed after polarization for a short period of 12 h. For example, the YSZ electrolyte phase is characterised by $\{111\}_{YSZ}$ and $\{022\}_{YSZ}$ planes with inter-planar spacings of 0.29 nm and 0.18 nm, respectively, while the $\{040\}_{SRL}$ inter-planar spacing of 0.20 nm is identified. As shown by the magnified SRL/YSZ interface area, the atomic geometry of the interface is exposed with high symmetries for each phases. The orientation realtionship of $\theta_{\{022\}YSZ/\{040\}SRL} = 7.5^{o}$ between $\{022\}_{YSZ}$ and $\{040\}_{SRL}$ lattice planes is identified, with a lattice mismatch factor of 10.0%. Nevertheless, at the SRL/YSZ interface, the planes are slightly misaligned and bended. The IFFT images of the lattice planes around the interface confirm the existence of plane distortion, similar to the misaligned interface structure after polarisation for 12 h (Figure 5.11). Therefore, prolonged polarization further facilitates the segregation and accumulation of Sr and its subsequent reaction with Zr, forming crater-shaped contact marks on the YSZ electrolyte (Figure 5.2 and 5.3).

Excess Sr segregation or Sr depression would lead to the localized disintegration of LSCF structure, indicated by the presence of Fe, La and Y at the interface region.

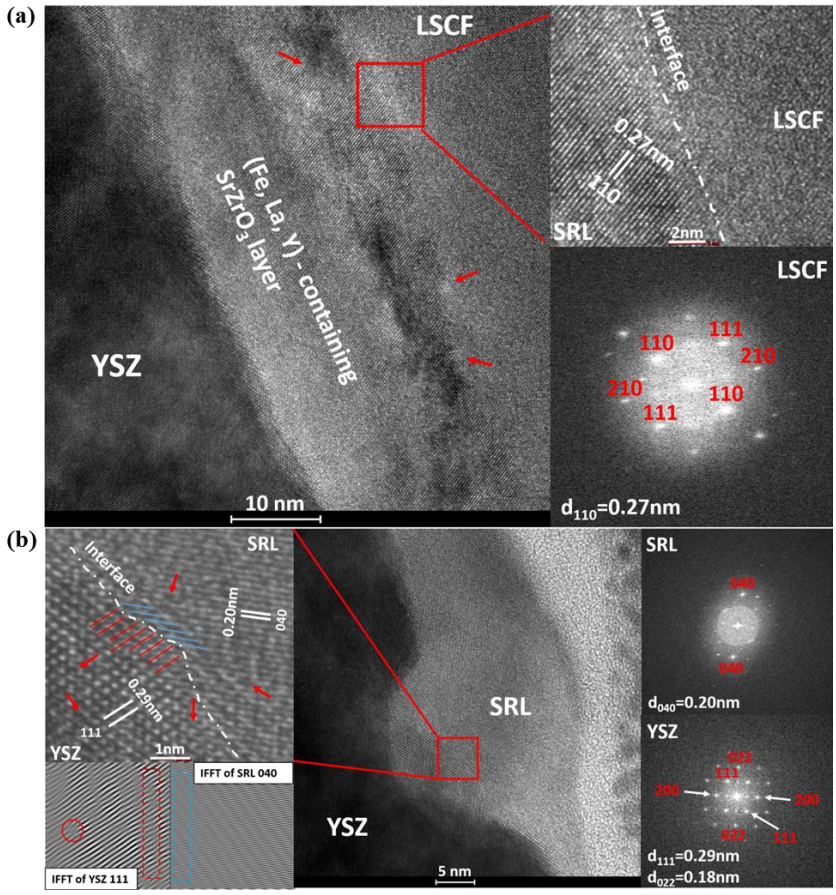

Figure 5.13 (a) HRTEM micrographs of the LSCF/(Fe, La, Y)-containing $SrZrO_3$ reaction layer/YSZ interfaces and the corresponding FFT micrograph of LSCF and (b) HRTEM and the corresponding FFT micrograph of the (Fe, La, Y)-containing $SrZrO_3$ reaction layer and the IFFT of the interface. LSCF/YSZ was polarized at 750^{o}C and 1000 mA cm^{-2} for 100h. The lattice distortion is indicated by red arrows.

Directly assembled LSCF electrode on polished YSZ pellet was sintered at 900^{o}C for 100 h in order to further study the chemical interactions between LSCF and YSZ as a comparison to that of polarization induced interface and the results are shown in Figure 5.14. Before sintering, the polished YSZ surface is flat and sharp (see the inset in Figure 5.14a). After the heat treatment at 900^{o}C for 100h, a continuous and thick reaction layer with thickness of 159.6±88.1 nm was formed at the LSCF/YSZ interface (Figure 5.14b). The reaction product is most likely $SrZrO_3$, as shown by X-ray diffraction pattern of the LSCF/YSZ oxide couples sintered at 900 ^{o}C (see Figure 5. 1a). This is supported by the STEM-EDS element mapping, showing the main

composition of the reaction layer is Sr and Zr (Figure 5.14c). The presence of Fe and La in the reaction layer is most likely due to the disintegration of LSCF perovskite structure at the interface. In addition, the originally flat YSZ surface becomes rough and curved after the thermal treatment, similar to that on YSZ electrolyte surface induced by cathodic polarization at 750^{o}C for 100 h (Figure 5.13). Zhang et al. studied the chemical interactions between $Pr_{0.8}Sr_{0.2}MnO_3$ (PSM) and YSZ at 1400^{o}C for 24 h, and also found the roughened YSZ surface after the formation of a pyrochlore phase, $Pr_2Zr_2O_7$ at the PSM/YSZ interface[70]. The similarities in the interface morphology as well as the element distribution for the thermally and electrochemically induced reaction layer imply that the polarization can induce chemical reactions between LSCF electrode and YSZ electrolyte at low temperature of 750 ^{o}C in this case. This is consistent with a previous study of a cathodic polarization induced reaction between $Ba_{0.5}Sr_{0.5}Co_{0.8}Fe_{0.2}O_3$ (BSCF) cathode and $Ce_{0.9}Gd_{0.1}O_{1.95}$ (GDC) and $Ce_{0.8}Sm_{0.2}O_{1.95}$ (SDC) electrolytes at 700^{o}C, forming Ba-containing particles at the electrode/electrolyte interface[71]. Without polarization, such reaction only occurs at 900 ^{o}C. This has been ascribed the reactions to the Ba segregation induced by cathodic polarization[71]. The effect of the polarization on Sr and Zr diffusion is also investigated by Wang et al [24]. Despite the use of GDC barrier interlayer, the formation of $SrZrO_3$ is observed at the GDC/YSZ interface at 1000^{o}C after polarization for 400h, using LSCF as electrode. Chen et al. [72] studied the boron deposition and poisoning of $La_{0.8}Sr_{0.2}MnO_3$ cathode under cathodic polarization conditions, and observed the preferential boron deposition at the electrode/electrolyte interface, which accelerates the reactions between LSM cathode and boron, forming $LaBO_3$.

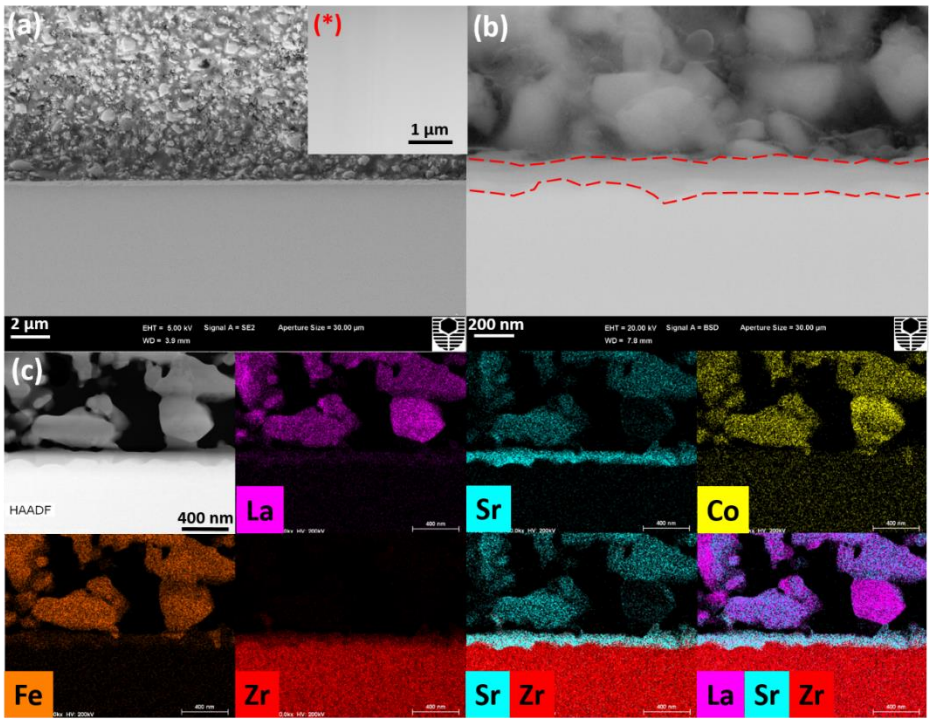

Figure 5.14 (a,b) SEM micrographs and (c) STEM-EDS element mapping of the cross-section of LSCF in contact with the polished YSZ pellet. The cell was sintered at 900 ºC for 100 h. The inset (*) in (a) shows the surface of the polished YSZ pellet before applying the LSCF coating.

Figure 5.15 shows the HRTEM micrographs of two selected $SrZrO_3$/YSZ interface areas. According to Figure 5.15a, a thick reaction layer of $SrZrO_3$ with a depth of 100±50nm was observed, separating the LSCF and YSZ phases. The curved or roughened YSZ electrolyte surface is clearly the result of the reaction between LSCF and YSZ. Similar to that observed in polarization induced interface, a distinct dark line resulting from the orientation change appears at the $SrZrO_3$/YSZ interface. The atomic geometry of the interface is characterized by the high level of symmetry of $\{002\}_{SrZrO3}$ and $\{111\}_{YSZ}$ lattice planes. For example, from the interface area, the $SrZrO_3$ phase is identified by its $\{002\}_{SrZrO3}$ planes with inter-planar spacing of 0.29 nm, while YSZ is characterized by its $\{111\}_{YSZ}$ planes with inter-planar spacing of 0.29 nm. The FFT diffractogram shown for the two phases indicate the different crystallography of orthorhombic $SrZrO_3$ [40] and cubic YSZ [62]. It is worth mentioning that the $\{002\}_{SrZrO3}$ and $\{111\}_{YSZ}$ lattice planes are almost parallel, i.e. $\{002\}_{SrZrO3}//\{111\}_{YSZ}$, with a lattice mismatch factor of 0.7%, exactly the same to that revealed in SRL/YSZ interface after polarization for 12h. In a different region of the LSCF/$SrZrO_3$/YSZ

interface, similar lattice plane arrangement and the plane orientation relationship were observed (Figure 5.15b). The lattice plane distortion occurs in adjacent to the interface region, as indicated by the red arrows in the figure.

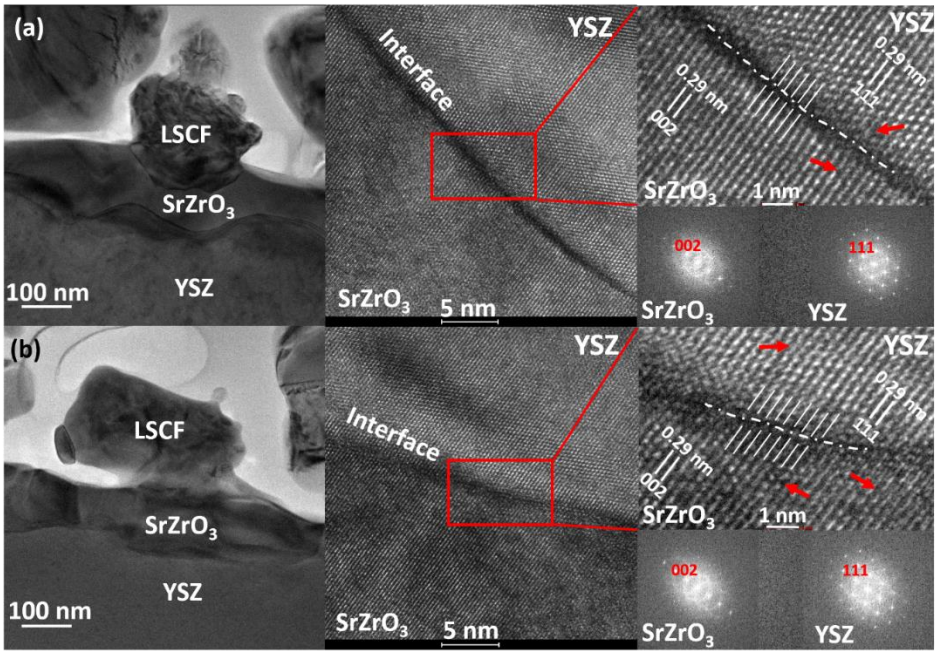

Figure 5.15 HRTEM micrographs of two selected areas of LSCF/$SrZrO_3$/YSZ interfaces and the corresponding FFT diffractograms for $SrZrO_3$ and YSZ. The LSCF/YSZ cell was sintered at 900 ^oC for 100 h.

5.3.6 Effect of polarization on Sr segregation and LSCF/YSZ interface formation

The results of current study clearly demonstrate that cathodic polarization induces the interface formation and accelerates the Sr segregation and diffusion, leading to the reaction between the segregated Sr and YSZ to form $SrZrO_3$ phase at the LSCF/YSZ interface. The observation of Sr segregation and change of directly assembled LSCF/YSZ interface microstructure under polarization can be summarized as follows:

In the initial stage of cathodic polarization, LSCF cathode/YSZ electrolyte interface forms with substantially reduced electrode ohmic resistance. The polarization induced LSCF/YSZ interface is clean and free of voids and amorphous phase, and is characterised by a high level of symmetry and periodicity. The heterointerface has been identified by the lattice plane matching of $\{110\}_{LSCF}$ and $\{111\}_{YSZ}$ with $\theta_{\{110\}LSCF/\{111\}YSZ}$ =48.8^o and f=6.9%. Lattice plane distortion for both phases has been observed in the vicinity of the LSCF/YSZ interface, however, electrochemical performance of the directly assembled LSCF electrode shows that such

crystallography distortion would not retard the oxygen ionic migration process at the interface for the O_2 reduction reaction.

Sr starts to segregate from the surface of LSCF perovskite electrode and diffuses towards the LSCF/YSZ interface region with further polarization, consistent with the reported accelerated Sr segregation and migration under cathodic polarization[73, 74], forming a thin Sr-rich layer (SRL) on electrolyte surface. EDS mapping and diffraction analysis indicate that the main component of SRL is SrO, which grows epitaxially on the surface of YSZ electrolyte with identical crystalline plane orientation. This is most likely due to their similar intrinsic cubic structure with space group symmetry of Fm-3m and lattice constants of 5.14 Å and 5.13 Å, respectively[63, 68]. The SrO/YSZ interface is coherent and continuous with negligible lattice plane distortion.

The reaction between segregated Sr and YSZ is kinetically favourable, forming $SrZrO_3$ layer. $SrZrO_3$ has an orthorhombic structure at room temperature[40], different to the cubic structure of YSZ electrolyte. The $SrZrO_3$/YSZ interface is characterized by the matching of $\{111\}_{YSZ}$ and $\{002\}_{SrZrO3}$ planes with low lattice distortion, showing a parallel orientation relationship with f=0.7%. The formation of $SrZrO_3$ phase results in a significant microstructural change on YSZ surface, indicated by the formation of crater-shaped contact marks on the YSZ electrolyte surface.

Prolonged polarization promotes the Sr segregation and subsequent reaction with YSZ, forming thick $SrZrO_3$ layer at the interface. The excess Sr segregation leads to the disintegration of LSCF perovskite structure, forming a Fe, La, Y-containing $SrZrO_3$ solid solution layer at the interface.

The phenomenon of polarization promoted Sr segregation and subsequent reaction with YSZ electrolyte is comparable to that of the LSCF/YSZ interface after heat treatment at a higher temperature of 900 ^oC for 100 h. This is supported by the observation of formation of a (Fe, La, Y)-containing $SrZrO_3$ reaction layer at LSCF/YSZ interface and lattice matching between $\{111\}_{YSZ}$ and $\{002\}_{SrZrO3}$ lattice planes with f=0.7%, similar to that observed in LSCF/YSZ interface induced by polarization. However, different from the thermodynamic interface chemistry which generally would occur at high temperatures[75, 76], the interface reaction under polarization can occur at a much lower temperature (e.g., 750 ^oC for LSCF/YSZ) and is kinetically induced by the segregated Sr as shown below:

Cathodic polarization, $i_{Cathodic}$, induced Sr segregation:

$$La_{0.6}Sr_{0.4}Co_{0.2}Fe_{0.8}O_{3-\delta} \xrightarrow{i_{Cathodic},\,750^{o}} La_{0.6}Sr_{0.4-x}Co_{0.2}Fe_{0.8}O_{3-\delta} + xSrO_s \quad (3)$$

Diffusion of segregated Sr from surface of LSCF to LSCF/YSZ interface:

$$xSrO_s \xrightarrow{diffusion} xSrO_i \quad (4)$$

Reaction between segregated Sr and YSZ, forming $SrZrO_3$:

$$xSrO_i + Y_{0.08}Zr_{0.92}O_2 \xrightarrow{750^{o}} SrZrO_3 + Y_2O_3 \quad (5)$$

Excess segregation and reaction leads to the disintegration of LSCF perovskite structure:

$$La_{0.6}Sr_{0.4}Co_{0.2}Fe_{0.8}O_{3-\delta} \xrightarrow{i_{Cathodic},\,750^{o}} SrO + La_2O_3 + Co_3O_4 + FeO \quad (6)$$

Figure 5.16 shows the scheme of the formation of LSCF/YSZ interface, Sr segregation and subsequent reaction between segregated Sr and YSZ at the interface region, forming $SrZrO_3$ phase with disintegration of LSCF perovskite structure in contact with YSZ electrolyte as a function of polarization time at 1000 mA cm^{-2} and 750 ºC. However, Sr cation at the A-site of cobaltite based perovskites such as LSCF, $SrCoO_{3-\delta}$ and BSCF can be stabilized by doping in the B-site with high valence cations such as Nb[77, 78], Sb[79], Mo[80], Ta[81] and Y[82, 83]. Our recent results show that co-doping of Nb and Pd substantially reduces the Sr segregation and enhances the stability of directly assembled LSCF electrodes on barrier-layer-free YSZ electrolyte[84].

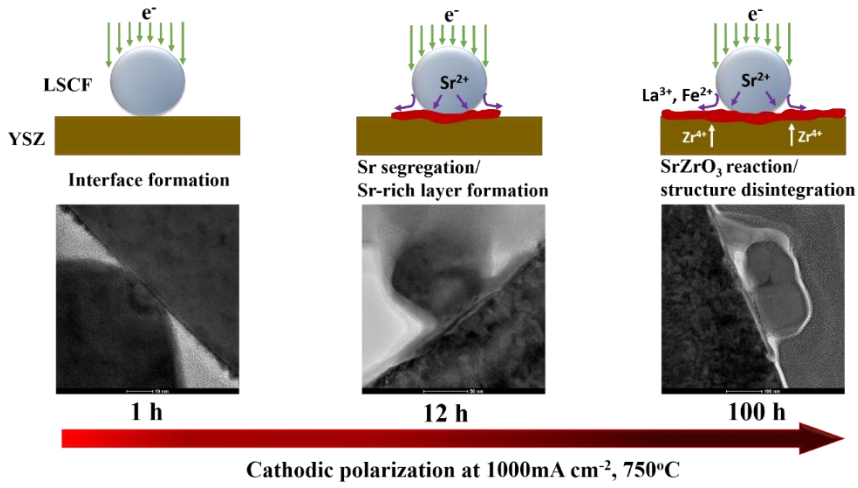

Figure 5.16 Scheme of the effect of polarization time at 1000 mA cm^{-2} and 750 ^{o}C on the interface formation, Sr segregation and diffusion, formation of Sr-rich layer and (Fe, La, Y)-containing $SrZrO_3$ reaction layer at LSCF/YSZ interface region.

5.4 Conclusion

The interface formation, Sr segregation and diffusion and subsequent chemical reaction between segregated Sr and YSZ at the directly assembled LSCF cathode/YSZ electrolyte interface was thoroughly investigated by FIB-STEM technique in the present study. The results shows evidently that cathodic current passage induces the formation of clean electrode/electrolyte interface free of voids and amorphous phases or solid solutions, leading to an increase of the electrochemical performances of the directly assembled LSCF electrode on YSZ electrolyte. However, prolonged polarization promotes the Sr segregation and diffusion to the interface, reacting with YSZ and forming $SrZrO_3$ phase with significantly modified microstructure of the electrolyte surface. The results indicate that chemical reaction between LSCF and YSZ at low temperature of 750 ^{o}C is essentially induced by the segregated Sr under cathodic polarization conditions. The lattice matching and crystallography orientation of LSCF/YSZ interface as a function of polarization have been presented and discussed for the first time in great detail. The information obtained from the directly assembled LSCF electrode on barrier-layer-free YSZ will have significant implications in the fundamental understanding of the interface evolution and cation segregation in SOFCs under polarization conditions in general.

5.5 References

[1] A. Mineshige, J. Izutsu, M. Nakamura, K. Nigaki, J. Abe, M. Kobune, S. Fujii, T. Yazawa, Introduction of A-site deficiency into La0.6Sr0.4Co0.2Fe0.8O3–δ and its effect on structure and conductivity, Solid State Ionics, 176 (2005) 1145-1149.

[2] S. Carter, A. Selcuk, R.J. Chater, J. Kajda, J.A. Kilner, a.B.C.H. Steele, Oxygen transport in selected nonstoichiometric perovskite-structure oxides, Solid State Ionics, 53-56 (1992) 597-605.

[3] Y. Teraoka, T. Nobunaga, K. Okamoto, N. Miura, N. Yamazoe, Influence of constituent metal cations in substituted LaCoO3 on mixed conductivity and oxygen permeability, Solid State Ionics, 48 (1991) 207-212.

[4] C. Sun, R. Hui, J. Roller, Cathode materials for solid oxide fuel cells: a review, Journal of Solid State Electrochemistry, 14 (2009) 1125-1144.

[5] N.A. Baharuddin, H.A. Rahman, A. Muchtar, A.B. Sulong, H. Abdullah, Development of lanthanum strontium cobalt ferrite composite cathodes for intermediate- to low-temperature solid oxide fuel cells, Journal of Zhejiang University SCIENCE A, 14 (2013) 11-24.

[6] S.P. Jiang, A comparison of O-2 reduction reactions on porous (La,Sr)MnO3 and (La,Sr)(Co,Fe)O-3 electrodes, Solid State Ionics, 146 (2002) 1-22.

[7] W. Lee, J.W. Han, Y. Chen, Z. Cai, B. Yildiz, Cation size mismatch and charge interactions drive dopant segregation at the surfaces of manganite perovskites, J Am Chem Soc, 135 (2013) 7909-7925.

[8] Z. Pan, Q. Liu, L. Zhang, X. Zhang, S.H. Chan, Effect of Sr Surface Segregation of La0.6Sr0.4Co0.2Fe0.8O3 − δElectrode on Its Electrochemical Performance in SOC, Journal of The Electrochemical Society, 162 (2015) F1316-F1323.

[9] D. Oh, D. Gostovic, E.D. Wachsman, Mechanism of La0.6Sr0.4Co0.2Fe0.8O3 cathode degradation, Journal of Materials Research, 27 (2012) 1992-1999.

[10] J.Y. Kim, V.L. Sprenkle, N.L. Canfield, K.D. Meinhardt, L.A. Chick, Effects of chrome contamination on the performance of La0.6Sr0.4Co0.2Fe0.8O3 cathode used in solid oxide fuel cells, J. Electrochem. Soc., 153 (2006) A880-A886.

[11] S.P. Simner, M.D. Anderson, M.H. Engelhard, J.W. Stevenson, Degradation Mechanisms of La–Sr–Co–Fe–O[sub 3] SOFC Cathodes, Electrochemical and Solid-State Letters, 9 (2006) A478.

[12] L. Zhao, J. Drennan, C. Kong, S. Amarasinghe, S.P. Jiang, Insight into surface segregation and chromium deposition on La0.6Sr0.4Co0.2Fe0.8O3−δ cathodes of solid oxide fuel cells, Journal of Materials Chemistry A, 2 (2014) 11114.

[13] H. Ding, A.V. Virkar, M. Liu, F. Liu, Suppression of Sr surface segregation in La(1-x)Sr(x)Co(1-y)Fe(y)O(3-delta): a first principles study, Phys Chem Chem Phys, 15 (2013) 489-496.

[14] A. Mai, M. Becker, W. Assenmacher, F. Tietz, D. Hathiramani, E. Iverstiffee, D. Stover, W. Mader, Time-dependent performance of mixed-conducting SOFC cathodes, Solid State Ionics, 177 (2006) 1965-1968.

[15] H. Yokokawa, Understanding Materials Compatibility, Annual Review of Materials Research, 33 (2003) 581-610.

[16] C. Rossignola, G. Constantina, P. Brioisb, A. Billardb, E. Djuradoa, L. Dessemonda, Interfaces and Durability for Different LSCF-CGO-YSZ Systems for IT-SOFC, ECS Transactions, 66 (2015) 109-114.

[17] S.J. Kim, G.M. Choi, Stability of LSCF electrode with GDC interlayer in YSZ-based solid oxide electrolysis cell, Solid State Ionics, 262 (2014) 303-306.

[18] R. Kiebach, W.-W. Zhang, W. Zhang, M. Chen, K. Norrman, H.-J. Wang, J.R. Bowen, R. Barfod, P.V. Hendriksen, Stability of La0.6Sr0.4Co0.2Fe0.8O3/Ce0.9Gd0.1O2 cathodes during sintering and solid oxide fuel cell operation, Journal of Power Sources, 283 (2015) 151-161.

[19] P. Puengjinda, H. Nishino, K. Kakinuma, M.E. Brito, H. Uchida, Effect of Microstructure on Performance of Double-Layer Hydrogen Electrodes for Reversible SOEC/SOFC, Journal of The Electrochemical Society, 164 (2017) F889-F894.

[20] K. Shimura, H. Nishino, K. Kakinuma, M.E. Brito, H. Uchida, Effect of samaria-doped ceria (SDC) interlayer on the performance of La 0.6 Sr 0.4 Co 0.2 Fe 0.8 O 3-δ /SDC composite oxygen electrode for reversible solid oxide fuel cells, Electrochimica Acta, 225 (2017) 114-120.

[21] K. Shimura, H. Nishino, K. Kakinuma, M.E. Brito, H. Uchida, High durability of La0.6Sr0.4Co0.2Fe0.8O3/samaria-doped ceria (SDC) composite oxygen electrode with SDC interlayer for reversible solid oxide fuel cell/solid oxide electrolysis cell, Journal of the Ceramic Society of Japan, 125 (2017) 218-222.

[22] H. Uchida, P. Puengjinda, K. Shimura, H. Nishino, K. Kakinuma, M.E. Brito, Important Roles of Ceria-Based Materials on Durability of Hydrogen and Oxygen Electrodes for Reversible SOEC/SOFC, ECS Transactions, 78 (2017) 3189-3195.

[23] M. Izuki, M.E. Brito, K. Yamaji, H. Kishimoto, D.-H. Cho, T. Shimonosono, T. Horita, H. Yokokawa, Interfacial stability and cation diffusion across the LSCF/GDC interface, Journal of Power Sources, 196 (2011) 7232-7236.

[24] F. Wang, M.E. Brito, K. Yamaji, D.-H. Cho, M. Nishi, H. Kishimoto, T. Horita, H. Yokokawa, Effect of polarization on Sr and Zr diffusion behavior in LSCF/GDC/YSZ system, Solid State Ionics, 262 (2014) 454-459.

[25] H. Fan, M. Keane, P. Singh, M. Han, Electrochemical performance and stability of lanthanum strontium cobalt ferrite oxygen electrode with gadolinia doped ceria barrier layer for reversible solid oxide fuel cell, Journal of Power Sources, 268 (2014) 634-639.

[26] S.P. Simner, M.D. Anderson, M.H. Engelhard, J.W. Stevenson, Degradation mechanisms of La-Sr-Co-Fe-O3SOFC cathodes, Electrochem. Solid State Lett., 9 (2006) A478-A481.

[27] F. Wang, M. Nishi, M.E. Brito, H. Kishimoto, K. Yamaji, H. Yokokawa, T. Horita, Sr and Zr diffusion in LSCF/10GDC/8YSZ triplets for solid oxide fuel cells (SOFCs), Journal of Power Sources, 258 (2014) 281-289.

[28] G. Vovk, X. Chen, C.A. Mims, In Situ XPS Studies of Perovskite Oxide Surfaces under Electrochemical Polarization†, The Journal of Physical Chemistry B, 109 (2004) 2445-2454.

[29] K. Chen, N. Li, N. Ai, Y. Cheng, W.D. Rickard, S.P. Jiang, Polarization-Induced Interface and Sr Segregation of in Situ Assembled La0.6Sr0.4Co0.2Fe0.8O3-delta Electrodes on Y2O3-ZrO2 Electrolyte of Solid Oxide Fuel Cells, ACS Appl Mater Interfaces, 8 (2016) 31729-31737.

[30] N. Ai, N. Li, W.D. Rickard, Y. Cheng, K. Chen, S.P. Jiang, Highly Stable Sr-Free Cobaltite-Based Perovskite Cathodes Directly Assembled on a Barrier-Layer-Free Y2 O3 -ZrO2 Electrolyte of Solid Oxide Fuel Cells, ChemSusChem, 10 (2017) 993-1003.

[31] S.P. Jiang, Thermally and Electrochemically Induced Electrode/Electrolyte Interfaces in Solid Oxide Fuel Cells: An AFM and EIS Study, Journal of The Electrochemical Society, 162 (2015) F1119-F1128.

[32] N. Li, N. Ai, K. Chen, Y. Cheng, S. He, M. Saunders, A. Dodd, A. Suvorova, S.P. Jiang, In situ assembled La0.8Sr0.2MnO3 cathodes on a Y2O3–ZrO2 electrolyte of solid oxide fuel cells – interface and electrochemical activity, RSC Adv., 6 (2016) 99211-99219.

[33] K. Chen, N. Li, N. Ai, M. Li, Y. Cheng, W.D.A. Rickard, J. Li, S.P. Jiang, Direct application of cobaltite-based perovskite cathodes on the yttria-stabilized zirconia electrolyte for intermediate temperature solid oxide fuel cells, Journal of Materials Chemistry A, 4 (2016) 17678-17685.

[34] S.P. Simner, M.D. Anderson, L.R. Pederson, J.W. Stevenson, Performance Variability of La(Sr)FeO[sub 3] SOFC Cathode with Pt, Ag, and Au Current Collectors, Journal of The Electrochemical Society, 152 (2005) A1851.

[35] Y. Xiong, K. Yamaji, H. Kishimoto, M.E. Brito, T. Horita, H. Yokokawa, Deposition of Platinum Particles at LSM/ScSZ/Air Three-Phase Boundaries Using a Platinum Current Collector, Electrochemical and Solid-State Letters, 12 (2009) B31.

[36] K. Yamaji, T. Shimonosono, H. Kishimoto, M.E. Brito, T. Horita, D.-H. Cho, M. Izuki, F. Wang, H. Yokokawa, Effect of Polarization on Platinum Deposition at LSM/YSZ Interfaces, ECS Transactions, 35 (2011) 2213-2216.

[37] S.M. Shin, B.Y. Yoon, J.H. Kim, J.M. Bae, Performance improvement by metal deposition at the cathode active site in solid oxide fuel cells, International Journal of Hydrogen Energy, 38 (2013) 8954-8964.

[38] S. He, K. Chen, M. Saunders, J. Li, C.Q. Cui, S.P. Jiang, A FIB-STEM Study of La0.8Sr0.2MnO3 Cathode and Y2O3-ZrO2/Gd2O3-CeO2 Electrolyte Interfaces of Solid Oxide Fuel Cells, Journal of The Electrochemical Society, 164 (2017) F1437-F1447.

[39] K. Yang, J.-H. Shen, K.-Y. Yang, I.M. Hung, K.-Z. Fung, M.-C. Wang, Formation of La2Zr2O7 or SrZrO3 on cathode-supported solid oxide fuel cells, Journal of Power Sources, 159 (2006) 63-67.

[40] T. Matsuda, S. Yamanaka, K. Kurosaki, S.-i. Kobayashi, High temperature phase transitions of SrZrO3, Journal of Alloys and Compounds, 351 (2003) 43-46.

[41] M. Li, Z. Sun, W. Yang, T. Hong, Z. Zhu, Y. Zhang, X. Wu, C. Xia, Mechanism for the enhanced oxygen reduction reaction of La0.6Sr0.4Co0.2Fe0.8O3-delta by strontium carbonate, Phys Chem Chem Phys, 19 (2016) 503-509.

[42] C.M. Wang, S. Azad, V. Shutthanandan, D.E. McCready, C.H.F. Peden, L. Saraf, S. Thevuthasan, Microstructure of ZrO2–CeO2 hetero-multi-layer films grown on YSZ substrate, Acta Materialia, 53 (2005) 1921-1929.

[43] D. Wolf, S. Yip, Materials Interfaces: Atomic-level Structure and Properties, Springer Netherlands1993.

[44] S. Cazottes, Z.L. Zhang, R. Daniel, J.S. Chawla, D. Gall, G. Dehm, Structural characterization of a Cu/MgO(001) interface using CS-corrected HRTEM, Thin Solid Films, 519 (2010) 1662-1667.

[45] Y. Ikuhara, Grain Boundary and Interface Structures in Ceramics, Journal of the Ceramic Society of Japan, 109 (2001) S110-S120.

[46] F.K. LeGoues, The Effect of Strain on the Formation of Dislocations at the SiGe/Si Interface, MRS Bulletin, 21 (1996) 38-44.

[47] F. Ernst, P. Pirouz, A.H. Heuer, HRTEM study of a Cu/Al2O3interface, Philosophical Magazine A, 63 (1991) 259-277.

[48] A. Trampert, F. Ernst, C.P. Flynn, H.F. Fischmeister, M. Ru¨hle, High resolution transmission electron microscopy studies of the Ag/MgO interface, Acta Metallurgica et Materialia, 40 (1992) S227-S236.

[49] O.I. Lebedev, G.V. Tendeloo, S. Amelinckx, H.L. Ju, K.M. Krishnan, High-resolution electron microscopy study of strained epitaxial La0.7Sr0.3MnO3thin films, Philosophical Magazine A, 80 (2000) 673-691.

[50] C. Rentenberger, T. Waitz, H.P. Karnthaler, HRTEM analysis of nanostructured alloys processed by severe plastic deformation, Scripta Materialia, 51 (2004) 789-794.

[51] S. Auzary, F. Pailloux, M.F. Denanot, R.J. Gaboriaud, Microstructure imaging of the YBCO thin film/MgO substrate interface: HRTEM and Fourier analysis of the Moiré fringe pattern, Thin Solid Films, 319 (1998) 163-167.

[52] F. Morales, SiC voids, mosaic microstructure and dislocations distribution in Si carbonized layers, Diamond and Related Materials, 12 (2003) 1227-1230.

[53] J.H. Warner, M.H. Rummeli, T. Gemming, B. Buchner, G.A. Briggs, Direct imaging of rotational stacking faults in few layer graphene, Nano Lett, 9 (2009) 102-106.

[54] H. Rösner, J. Weissmüller, G. Wilde, HRTEM observation of interfacial dislocations at faceted Al–Pb interfaces, Philosophical Magazine Letters, 84 (2004) 673-683.

[55] D. Pergolesi, E. Fabbri, S.N. Cook, V. Roddatis, E. Traversa, J.A. Kilner, Tensile lattice distortion does not affect oxygen transport in yttria-stabilized zirconia-CeO2 heterointerfaces, ACS Nano, 6 (2012) 10524-10534.

[56] G.J. la O', R.F. Savinell, Y. Shao-Horn, Activity Enhancement of Dense Strontium-Doped Lanthanum Manganite Thin Films under Cathodic Polarization: A Combined AES and XPS Study, Journal of The Electrochemical Society, 156 (2009) B771-B781.

[57] H. Kishimoto, N. Sakai, T. Horita, K. Yamaji, M. Brito, H. Yokokawa, Cation transport behavior in SOFC cathode materials of La0.8Sr0.2CoO3 and La0.8Sr0.2FeO3 with perovskite structure, Solid State Ionics, 178 (2007) 1317-1325.

[58] C. Rentenberger, C. Mangler, S. Scheriau, R. Pippan, H.P. Karnthaler, TEM Study of Local Disordering: A Structural Phase Change Induced by High-Pressure Torsion, Materials Science Forum, 584-586 (2008) 422-427.

[59] X.L. Wu, E. Ma, Accommodation of large plastic strains and defect accumulation in nanocrystalline Ni grains, Journal of Materials Research, 22 (2011) 2241-2253.

[60] M. Sillassen, P. Eklund, N. Pryds, E. Johnson, U. Helmersson, J. Bøttiger, Low-Temperature Superionic Conductivity in Strained Yttria-Stabilized Zirconia, Advanced Functional Materials, 20 (2010) 2071-2076.

[61] R.H. Piva, D.H. Piva, M.R. Morelli, Thermal stability and phase transformation in fully indium oxide (InO 1.5) stabilized zirconia, Materials Characterization, 123 (2017) 58-66.

[62] U. Martin, H. Boysen, F. Frey, Neutron powder investigation of tetragonal and cubic stabilized zirconia, TZP and CSZ, at temperatures up to 1400 K, Acta Crystallographica Section B Structural Science, 49 (1993) 403-413.

[63] W. Primak, H. Kaufman, R. Ward, X-Ray Diffraction Studies of Systems Involved in the Preparation of Alkaline Earth Sulfide and Selenide Phosphors1, Journal of the American Chemical Society, 70 (1948) 2043-2046.

[64] H.J. Gao, C.L. Chen, B. Rafferty, S.J. Pennycook, G.P. Luo, C.W. Chu, Atomic structure of Ba0.5Sr0.5TiO3 thin films on LaAlO3, Applied Physics Letters, 75 (1999) 2542-2544.

[65] J.H. Chen, C.L. Lia, K. Urban, C.L. Chen, Unusual lattice distortion in a Ba0.5Sr0.5TiO3 thin film on a LaAlO3 substrate, Applied Physics Letters, 81 (2002) 1291-1293.

[66] C.-M. Wang, S. Thevuthasan, C.H.F. Peden, Interface Structure of an Epitaxial Cubic Ceria Film on cubic Zirconia, Journal of the American Ceramic Society, 86 (2003) 363-365.

[67] C. Ma, M. Liu, C. Chen, Y. Lin, Y. Li, J.S. Horwitz, J. Jiang, E.I. Meletis, Q. Zhang, The origin of local strain in highly epitaxial oxide thin films, Sci Rep, 3 (2013) 3092.

[68] C.C. Appel, Zirconia stabilized by Y and Mn: A microstructural characterization, Ionics, 1 (1995) 406-413.

[69] S. Hasegawa, T. Sugimoto, T. Hashimoto, Investigation of structural phase transition behavior of SrZrO3 by thermal analyses and high-temperature X-ray diffraction, Solid State Ionics, 181 (2010) 1091-1097.

[70] J.P. Zhang, S.P. Jiang, J.G. Love, K. Foger, S.P.S. Badwal, Chemical interactions between strontium-doped praseodymium manganite and 3 mol% yttria-zirconia, J. Mater. Chem., 8 (1998) 2787-2794.

[71] H. Yung, L. Jian, S.P. Jiang, Polarization Promoted Chemical Reaction between Ba0.5Sr0.5Co0.8Fe0.2O3- Cathode and Ceria Based Electrolytes of Solid Oxide Fuel Cells, Journal of the Electrochemical Society, 159 (2012) F794-F798.

[72] K. Chen, S.-S. Liu, P. Guagliardo, M.R. Kilburn, M. Koyama, S.P. Jiang, A Fundamental Study of Boron Deposition and Poisoning of La0.8Sr0.2MnO3Cathode of Solid Oxide Fuel Cells under Accelerated Conditions, Journal of The Electrochemical Society, 162 (2015) F1282-F1291.

[73] E. Mutoro, E.J. Crumlin, H. Pöpke, B. Luerssen, M. Amati, M.K. Abyaneh, M.D. Biegalski, H.M. Christen, L. Gregoratti, J. Janek, Y. Shao-Horn, Reversible Compositional Control of Oxide Surfaces by Electrochemical Potentials, The Journal of Physical Chemistry Letters, 3 (2012) 40-44.

[74] G. Vovk, X. Chen, C.A. Mims, In situ XPS studies of perovskite oxide surfaces under electrochemical polarization, J Phys Chem B, 109 (2005) 2445-2454.

[75] H. Yokokawa, N. Sakai, T. Kawada, M. Dokiya, Chemical thermodynamic stabilities of the interface, Science and Technology of Zirconia V, Technomic Publishing Company, Inc., Melbourne, Australia, 1993, pp. 752-763.

[76] H. Yokokawa, Materials development in solid oxide fuel cells, Denki Kagaku, 66 (1998) 134-140.

[77] T. Nagai, W. Ito, T. Sakon, Relationship between cation substitution and stability of perovskite structure in SrCoO3–δ-based mixed conductors, Solid State Ionics, 177 (2007) 3433-3444.

[78] X.B. Chen, S.P. Jiang, Highly active and stable (La0.24Sr0.16Ba0.6)(Co0.5Fe0.44Nb0.06)O3-delta (LSBCFN) cathodes for solid oxide fuel cells prepared by a novel mixing synthesis method, Journal of Materials Chemistry A, 1 (2013) 4871-4878.

[79] A. Aguadero, D. Perez-Coll, C. de la Calle, J.A. Alonso, M.J. Escudero, L. Daza, SrCo1-xSbxO3-δ perovskite oxides as cathode materials in solid oxide fuel cells, Journal of Power Sources, 192 (2009) 132-137.

[80] A. Aguadero, D. Pérez-Coll, J.A. Alonso, S.J. Skinner, J. Kilner, A New Family of Mo-Doped SrCoO3−δ Perovskites for Application in Reversible Solid State Electrochemical Cells, Chemistry of Materials, 24 (2012) 2655-2663.

[81] M. Li, M. Zhao, F. Li, W. Zhou, V.K. Peterson, X. Xu, Z. Shao, I. Gentle, Z. Zhu, A niobium and tantalum co-doped perovskite cathode for solid oxide fuel cells operating below 500 degrees C, Nat Commun, 8 (2017) 13990.

[82] M. Meffert, L.-S. Unger, L. Grünewald, H. Störmer, S.F. Wagner, E. Ivers-Tiffée, D. Gerthsen, The impact of grain size, A/B-cation ratio, and Y-doping on secondary phase formation in (Ba0.5Sr0.5)(Co0.8Fe0.2) O3−δ, Journal of Materials Science, 52 (2017) 2705-2719.

[83] W. He, X. Wu, G. Yang, H. Shi, F. Dong, M. Ni, BaCo0.7Fe0.22Y0.08O3−δ as an Active Oxygen Reduction Electrocatalyst for Low-Temperature Solid Oxide Fuel Cells below 600° C, ACS Energy Letters, 2 (2017) 301-305.

[84] K. Chen, S. He, N. Li, Y. Cheng, N. Ai, M. Chen, W.D.A. Rickard, T. Zhang, S.P. Jiang, Nb and Pd co-doped La 0.57 Sr 0.38 Co 0.19 Fe 0.665 Nb 0.095 Pd 0.05 O 3-δ as a stable, high performance electrode for barrier-layer-free Y 2 O 3 -ZrO 2 electrolyte of solid oxide fuel cells, Journal of Power Sources, 378 (2018) 433-442.

Chapter 6: Interface Formation and Mn Segregation of Directly Assembled $La_{0.8}Sr_{0.2}MnO_3$ Cathode on Y_2O_3-ZrO_2 and Gd_2O_3-CeO_2 Electrolytes of Solid Oxide Fuel Cells

Abstract

The establishment of intimate electrode/electrolyte interface is critical in solid oxide fuel cells (SOFCs), as it plays an essential role in the overall cell performance and durability. In this study, Mn segregation and interface formation between directly assembled $La_{0.8}Sr_{0.2}MnO_3$ (LSM) and yttrium-stabilized zirconia (YSZ) or gadolinium-doped ceria (GDC) are studied using combined focused ion beam and scanning transmission electron microscopy (FIB-STEM). In the case of LSM/YSZ and LSM/GDC electrodes, a significant reduction in the electrode ohmic resistance is observed after cathodic polarization at 900^{o}C and 500 $mAcm^{-2}$, indicating the formation of an intimate interface. However, LSM particles start to disintegrate at the electrode/electrolyte interface with the increase of polarization time in the case of LSM/YSZ electrode. On the other hand, the LSM/GDC interface is very stable with negligible microstructure change at the interface. Mn segregation from the LSM perovskite structure is identified under the influence of polarization in both LSM/YSZ and LSM/GDC electrodes. The results demonstrate that nature of the electrolyte plays a critical role in the microstructure, morphology and stability of LSM/electrolyte interface under SOFC operation conditions.

6.1 Introduction

Solid oxide fuel cells (SOFCs) are energy conversion devices to efficiently produce electricity from chemical energy of a wide variety of fuels, such as hydrogen, natural gas and hydrocarbons[1-4]. SOFCs are considered as environmentally friendly technologies with significantly less greenhouse gas emission as compared to the coal combustion plants[5, 6]. Typical SOFC cells consist of Ni-yttria-stabilized zirconia (Ni-YSZ) cermet anodes, YSZ electrolyte and lanthanum strontium manganite (LSM) perovskite cathode. Generally, the ceramic components of the SOFC devices are pre-sintered at high temperature, e.g., ~1400^{o}C for Ni-YSZ cermet anode and ~1150^{o}C for

LSM cathodes[7-9] to establish an intimate electrode/electrolyte interface. The performance of SOFCs not only depends on the electrocatalytic activity of electrode materials, but also the microstructure of the electrode/electrolyte interface[10-13]. In Chapter 4, we discussed the pre-sintered LSM/YSZ and LSM/GDC interfaces. Here we will further study the *in situ* formed LSM/YSZ and LSM/GDC interfaces under the influence of cathodic polarisation.

LSM perovskite is one of the most commonly and widely investigated cathode materials due to its high electronic conductivity and excellent electrocatalytic activity for oxygen reduction reaction (ORR) at high temperatures[9, 14, 15]. As LSM is predominantly an electronic conductor with negligible ionic conductivity, the ORR mainly occur at the triple phase boundary (TPB) where the oxygen, electrode and electrolyte meet. The formation of an intimate electrode/electrolyte interface is thus critical in determining the performance and durability of SOFC cells. This is because the interface provides a direct pathway for oxygen species migration from electrode to electrolyte. In the case of LSM cathode pre-sintered at high temperatures, the interface is characterized by the formation of convex contact rings on YSZ and GDC electrolyte surface[13, 16-21]. On the other hand, it has been known that cathodic polarization has a significant effect on the electrode/electrolyte interface under the fuel cell operation conditions. This is reflected from the formation of micro-pores and dense layers at the interface[18, 22-24], increase in TPB length[25] and change in electrolyte morphology[20, 26]. Early studies show that polarization can broaden and flatten the edges of the contact rings[17]. The distinct topography changes of the convex rings is most likely due to the incorporation of oxygen and/or interdiffusion between LSM and YSZ electrolyte at the interface. The microstructural change at the electrode/electrolyte interface during long-term cathodic polarization can also lead to a significant cell performance degradation. Appel et al.[23] reported that after polarization at 300 $mAcm^{-2}$ and 1000^{o}C for 2000 h, the overvoltage a LSM-YSZ composite cathode based cell exceeds by 100% of the initial value. The morphology changes at the interface due to pore formation and densification of the electrode layer were considered as the main reasons for the increase in the polarization resistance during the stability test.

Recently, we have shown the feasibility of applying directly assembled electrode on electrolyte without requiring further high temperature sintering, and the *in situ*

formation of electrode/electrolyte interface induced by cathodic polarization[27-36]. In the case of LSM electrode and YSZ electrolyte, the initial results indicate that the electrochemical performance of cathodic polarization induced interface is comparable to that of the conventional pre-sintered electrodes, though the topography of the interface is very different, i.e. the formation of convex contact rings for the thermally induced interface and contact clusters for the electrochemically induced interface[27]. The formation of the electrochemically induced LSM/YSZ interface is accompanied by the pronounced decrease of ohmic resistance, particularly at the initial stage of polarization[30]. Studies show that LSM is thermally compatible with YSZ and GDC electrolytes and the formation of lanthanum zirconate only occurs at a higher temperature of 1300 ^{o}C in the case of LSM/YSZ but in the case of LSM/GDC, no reaction was observed [21]. However, the evolution of the electrode/electrolyte interface under the influence of cathodic polarization as well as the fundamental understanding of the crystallographic and compositional changes of the polarization induced interface in the case of directly assembled LSM electrodes are still unclear at this stage.

In this chapter, a comparative study was carried out on the electrochemical activity, interface formation and Mn segregation of the directly assembled LSM electrode on YSZ or GDC electrolytes using combined FIB-STEM technique. The results indicate that the electrochemical performance of directly assembled LSM/YSZ and LSM/GDC electrodes is greatly enhanced by the cathodic polarization. The electrode/electrolyte hetero-interface formed is characterized by the periodic lattice plane matching, accompanied by the presence of lattice mismatch and distortion. The nature of the electrolyte shows a significant effect on the stability of the interface formed between LSM and YSZ or GDC electrolyte.

6.2 Experimental

6.2.1. Fabrication of direct assembled LSM electrode on YSZ or GDC electrolyte

$La_{0.8}Sr_{0.2}MnO_3$ (LSM) cathode powder was synthesized via sol-gel method, using $La(NO_3)_3{\cdot}6H_2O$ (99.9%, A.R., Alfa Aesar, UK), $Sr(NO_3)_2$ (99%, A.R., Sigma-Aldrich, US), $Mn(NO_3)_2$ (50 wt% solution, A.R., Alfa Aesar, UK) as raw materials, and anhydrous citric acid (99.5%, A.R., Chem Supply, Australia),

ethylenediaminetetraacetic acid (EDTA, 99%, Acros Organics, Australia) and ammonia solution (28%w.w., Sigma-Aldrich, US) as complexing agents with a molar ratio of 1:1.5:1 (metal ions/citric acid/EDTA). Stoichiometric metal nitrates were blended with deionized water, and the calculated amounts of citric acid, EDTA and ammonia solution were subsequently added. The pH of the solution was adjusted to 7 and the solution was stirred on a hot plate until the dry gel was formed. The resultant gel powder was calcined at 1000^{o}C for 2 h.

Electrolyte pellets were fabricated by die-pressing powders of 8 mol% Y_2O_3 doped ZrO_2 (YSZ, Tosoh, Japan) and $Gd_{0.1}Ce_{0.9}O_{1.95}$ (GDC, AGC Seimi Chemical Co Ltd), followed by sintering at 1450^{o}C for 5 h. The pellets were approximately 1 mm in thickness and 18 mm in diameter. Pt paste (Gwent Electronic Materials Ltd., UK) was painted on the centre and ring of the electrolyte, and sintered at 1100^{o}C for 2 h as the counter and reference electrodes. LSM powder was thoroughly mixed with an ink vehicle (Fuel Cell Materials, US) at a weight ratio of 5:5 in an agate mortar to form a uniform electrode paste. The paste was subsequently screen-printed on the other side of the electrolyte pellet symmetrically opposite to the Pt counter electrode and then dried at 100^{o}C for 2h to form the directly assembled cathode/electrolyte electrodes without further high temperature pre-sintering[37].

6.2.2. Characterization

Electrochemical performance of directly assembled LSM/YSZ and LSM/GDC electrodes was measured using a Zahner Electrochemical Workstation. The electrodes were cathodically polarized at 750 ^{o}C and 500 mAcm^{-2} for 1 or 12 h, and electrochemical impedance was measured under open circuit conditions in a frequency range of 0.1 Hz to 100 kHz with a signal amplitude of 20 mV. Air was supplied to the cathode side at a flow rate of 100 mL min^{-1}. Electrode ohmic resistance (R_Ω) was obtained from the high frequency intercept, and electrode polarization resistance (R_p) was obtained from the differences between the low- and high-frequency intercepts of the impedance curves.

The microstructure of the electrolyte surface in contact with LSM was examined by scanning electron microscopy (SEM, Zeiss Neon 40EsB, Germany). In order to examine the morphology of the electrolyte surface, the LSM coating was completely removed by HCl (32 wt%, Sigma-Aldrich, US) treatment, and in some cases, the

electrode was partly peeled off to study the electrode/electrolyte interface. The topographic features of the acid cleaned electrolyte surface were examined by atomic force microscopy (AFM, Alpha 300 SAR, WITec GmbH, Ulm Germany) at intermittent contact mode. Electrolyte lamella in contact with LSM particle was lifted out and milled to around 70 nm in thickness using FEI Helios Nanolab G3 CX Dual Beam Focused Ion Beam - Scanning Electron Microscope (FIB-SEM, Helios Nanolab G3 CX, FEI company, US) with Ga^+ ion source. The elemental mapping and microstructural micrographs were obtained on the FIB milled sample using a high angle annular dark field scanning transmission electron microscopy (HAADF-STEM, FEI Titan G2 80-200 TEM/STEM with ChemiSTEM Technology, US) at 200 kV. The fast Fourier transform (FFT) images were extracted using TEM Imaging & Analysis software (TIA, FEI Company, US) to examine the diffraction behavior of selected areas, and inverse FFT (IFFT) simulations were performed on Gatan Digital Micrograph (Gatan Digital Microscopy Suite, Gatan Inc., US) to reconstruct the selected lattice planes using FFT images.

6.3 Results and Discussion

6.3.1 Electrochemical performance of directly assembled LSM/YSZ and LSM/GDC electrodes

Figure 6.1 shows the electrochemical performance of the directly assembled LSM cathode on YSZ and GDC electrolytes after polarization at 900^{o}C and 500 mAcm^{-2} for 12 h. The electrochemical activity of the LSM/YSZ electrode for ORR improves significantly with the cathodic polarization. R_p was remarkably reduced from 60.0 Ω cm^2 to 0.8 Ω cm^2 and R_Ω decreased from 2.1 Ω cm^2 to 0.9 Ω cm^2 after polarization (Figure 6.1a). The cathode potential measured between LSM electrode and Pt reference electrode ($E_{cathode}$) also dropped quickly from its initial value of 1.3 V to ~0.9 V under the influence of cathodic polarization. For the LSM/GDC electrode, the electrochemical performance also experiences a significant improvement (see Figure 6.1b). The initial R_Ω and R_p were 1.1 Ω cm^2 and 1.0 Ω cm^2, respectively, and decreased to 0.6 Ω cm^2 and 0.3 Ω cm^2 after polarization for 12 h. The $E_{cathode}$ also decreases gradually from 0.55V to 0.45V. The significantly enhanced activity is due to the well-known activation behaviour of LSM-based cathode [9, 13, 38-42]. The significant

decrease in the R_Ω for both LSM/YSZ and LSM/GDC electrodes implies the establishment of cathode/electrolyte interface under the influence of cathodic polarization, as in the case of pre-sintered LSM/YSZ and LSM/GDC electrodes, there is no change in R_Ω under similar cathodic polarization conditions [21, 30].

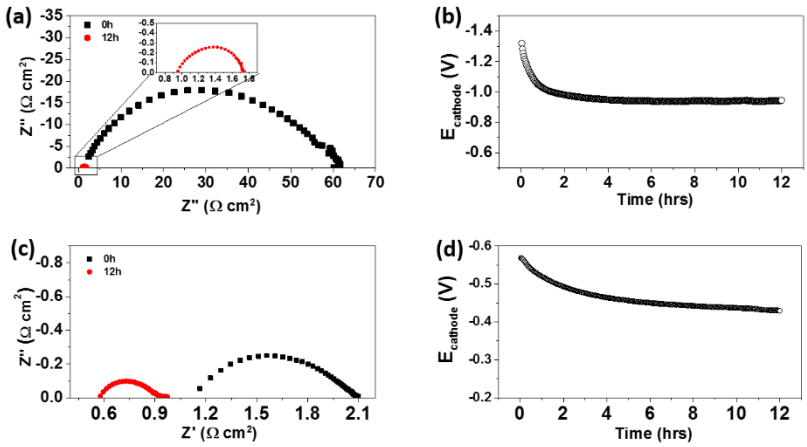

Figure 6.1 Electrochemical performance of directly assembled LSM cathode on (a,b) YSZ and (c,d) GDC electrolytes before and after polarization at 900°C and 500 $mAcm^{-2}$ for 12 h.

6.3.2 Microstructure of the polarization induced interface

The microstructure of the YSZ and GDC electrolytes surface in contact with LSM cathode before and after polarization is presented in Figure 6.2 and Figure 6.3, respectively. For LSM/YSZ electrode, the morphology of the electrolyte surface is greatly changed after polarization at 900°C and 500 $mAcm^{-2}$ for just 1 h (Figure 6.2). The formation of ring-shaped contact marks was observed and the diameter of the contact rings is in the range of 0.57-1.1 µm (Figure 6.2b). The dimension of the contact rings is close to that of the LSM particles of the directly assembled LSM, 1.27 ± 0.54 µm (Figure 6.2a). Within the contact rings, a considerable number of particles with a dimension of 28.8 ± 8.4 nm were found, indicating the possible disintegration of the LSM particles under the influence of polarization. After the polarization for 12 h, the ring-shaped contact marks continue to grow and merge together, forming contact craters with dimension as large as 2 µm on the YSZ electrolyte (Figure 6.2c and 6.2d). An intrinsic YSZ electrolyte surface without LSM coating is also presented (Figure 6.2e), and it is characterized to be smooth and flat, with a grain size of 3.77 ± 3.12 µm. The YSZ surface in contact with LSM electrode under OCP condition is also shown

in Figure 6.2f. The electrolyte surface is clean and smooth, comparable to that of pristine YSZ. This may indicate that there is no reaction between LSM and YSZ at 900^{o}C without polarisation, i.e. under OCP condition. Matsui *et al*. also observed the significant microstructural change at the interface between pre-sintered LSM electrode and YSZ electrolyte and the increase of roughness of YSZ surface both in and out of contact with LSM particles with the increase of the polarization time at 1000 ^{o}C [13]. An increase in the length of three phase boundary was observed after polarization at 200 mA cm^{-2} for 5 h.

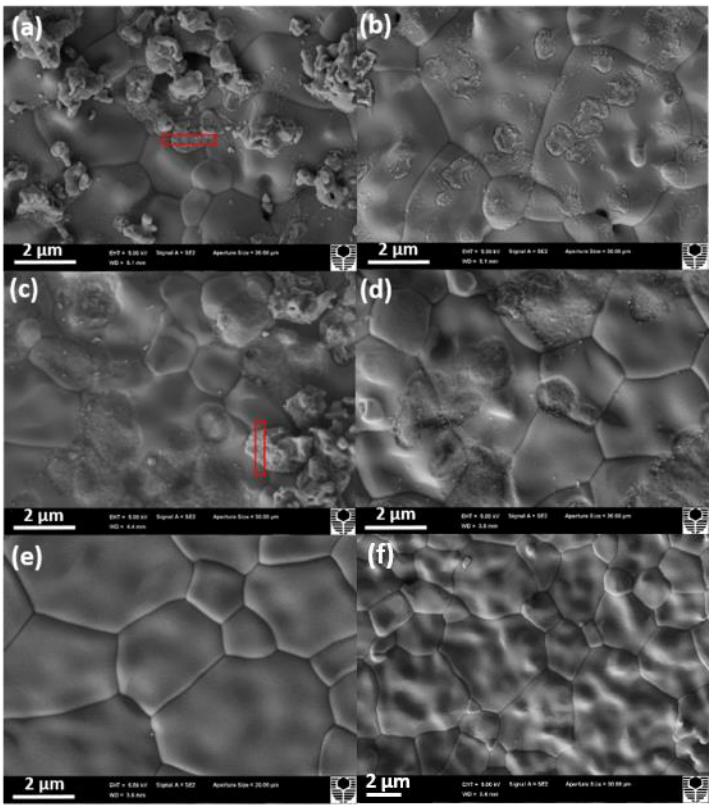

Figure 6.2 SEM micrographs of YSZ electrolyte surface after polarization at 900^{o}C and 500 mAcm^{-2} for (a,b) 1 h, (c,d) 12 h or (f) 0 h. The LSM electrodes were removed (a,c) by stick tape and (b,d,f) by HCl treatment. The original YSZ electrolyte surface without LSM coating is given in (e). The red boxes indicate the locations of FIB milling.

In the case of LSM/GDC electrodes, the change in the morphology of GDC electrolyte is much smaller during the cathodic polarization as compared to that on YSZ electrolyte (see Figure 6.3). For instance, after polarization for 1 h, the morphology of the GDC electrolyte surface is still smooth with a formation of small and shallow ring-shaped contact marks, as shown in Figure 6.3a and b. After polarization for 12 h, the

contact marks also grow (Figure 6.3d), but no ring-shaped craters were found as in the case of LSM/YSZ electrode (Figure 6.2d). The changes in the microstructure of GDC electrolyte in contact with LSM under the influence of polarization are much less significant as compared to that of YSZ electrolyte. An intrinsic GDC electrolyte surface without LSM coating is also presented in Figure 6.3e. The grain size of the GDC is identified to be 1.19 ± 1.04 μm. The GDC electrolyte in contact with LSM under OCP condition is also shown in Figure 6.3f. The electrolyte surface is smooth and flat, indicating stable electrode/electrolyte interface under OCP condition at 900ºC.

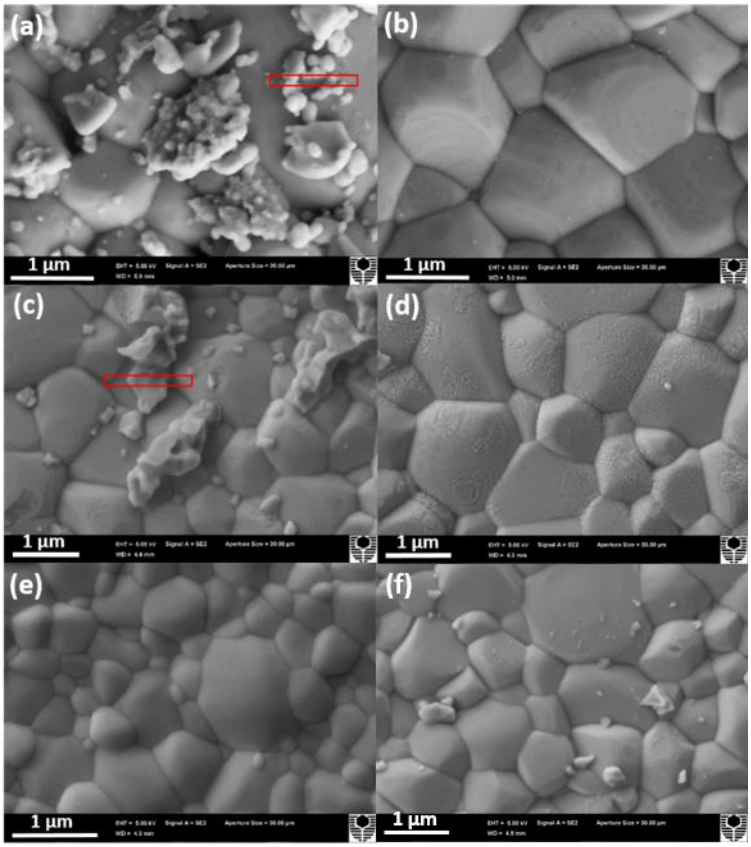

Figure 6.3 SEM micrographs of GDC electrolyte surface after polarization at 900ºC and 500 $mAcm^{-2}$ for (a,b) 1 h, (c,d) 12 h and (f) 0 h. The LSM electrodes were removed (a,c,f) by stick tape and (b,d) by HCl treatment. The original GDC electrolyte surface without LSM coating is given in (e). The red boxes indicate the locations of FIB milling.

Figure 6.4 shows the AFM topography of the YSZ and GDC electrolyte surfaces in contact with LSM cathode. LSM electrodes were removed by acid treatment. In the case of LSM/YSZ electrode, convex contact rings with a dimension of 1.14 ± 0.54 μm was formed on the YSZ surface after the cathodic polarization for 1 h (Figure 6.4a).

After polarization for 12 h, the contact rings grow significantly, and the dimension of the rings increases to 1.80±0.71 μm (Figure 6.4b). The AFM line scan across the edge of the contact rings reveals the ring depth profile of 0.14±0.06 μm (Figure 6.4c), showing the significant roughening of the YSZ electrolyte surface. For the LSM/GDC electrode, the change in the electrolyte morphology is almost negligible after polarization for 1 h (Figure 6.4d). After polarization for 12 h, the formation of contact clusters or marks on GDC electrolyte surface becomes clearly visible (Figure 6.4e). The average dimension of these clusters is 0.22±0.09 μm with the depth profile of 5.2±0.7 nm (Figure 6.4f), substantially smaller than that on YSZ electrolyte. The relatively small microstructure change of the GDC electrolyte at the interface implies that the LSM cathode is more stable with GDC as compared to that with YSZ under the influence of polarization, consistent with the thermal compatibility studies[21].

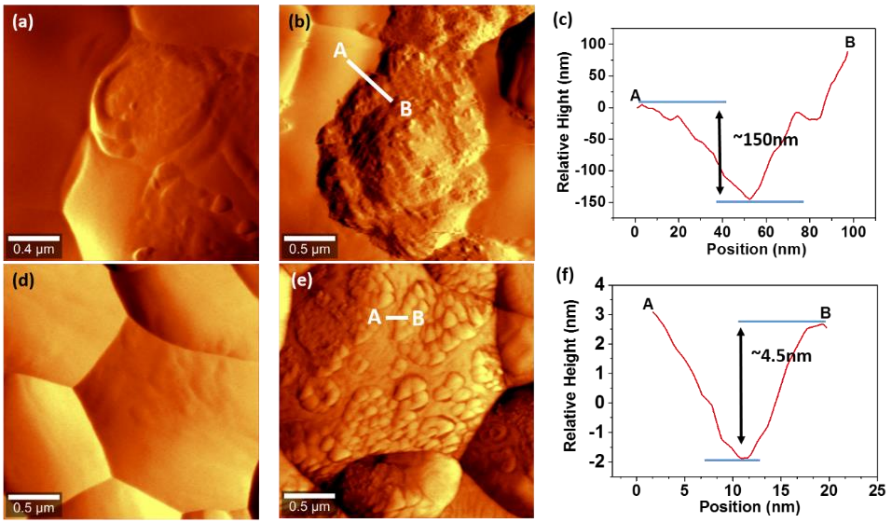

Figure 6.4 AFM micrographs and line scan of (a,b,c) YSZ and (d,e,f) GDC electrolyte surfaces in contact with LSM electrode after polarization at 900°C and 500 $mAcm^{-2}$ for (a,d) 1 h and (b,e) 12 h. The LSM cathode was removed by HCl treatment.

Figure 6.5 presents the LSM/YSZ and LSM/GDC interface lamella prepared by FIB, taking in the interface regions as shown in Figs. 2 and 3. The TEM images of the electrode/electrolyte interfaces clearly demonstrate the interface evolution under the influence of cathodic polarization. For example, in the case of LSM/YSZ electrode, it appears that the LSM particle starts to disintegrate at the electrode/electrolyte interface after the polarization for 1 h, forming discrete contact areas with the electrolyte. With further polarization for 12 h, the disintegration of the LSM cathode particle at the

interface becomes clearly visible (Figure 6.5b). In the case of LSM/GDC electrode, no visible disintegration of the LSM cathode particle was observed. After polarization for 1 h, an intimate and void-free contact between LSM and GDC electrolyte is established (Figure 6.5c). The interface appears stable after polarization for 12 h (Figure 6.5d), very different to the LSM/YSZ interface.

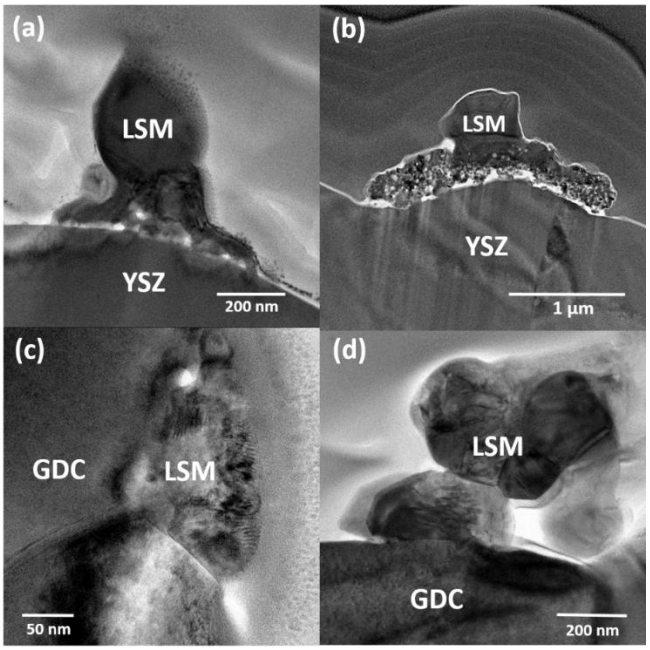

Figure 6.5 TEM micrographs of (a,b) LSM/YSZ interface and (c,d) LSM/GDC interface after polarization at 900^{o}C and 500 mAcm^{-2} for (a,c) 1 h and (b,d) 12 h.

6.3.3 LSM/YSZ interface

Figure 6.6 shows the STEM-EDS and HRTEM results of a directly assembled LSM cathode on YSZ electrolyte after polarization at 900^{o}C and 500 mAcm^{-2} for 1 h. There is a disintegration at the interface and a clear presence of La, Sr and Mn was observed in the disintegrated nanoparticles (Figure 6.6a). A strong accumulation of Mn was also observed on the surface of one of the LSM particles, indicating the Mn segregation under the influence of cathodic polarization. Nevertheless, the segregated Mn is not located at the electrode/electrolyte interface, indicating that segregation of Mn species from LSM perovskite structure may not be necessarily driven by the ORR at the interface. The HRTEM analysis shows an intimate contact between the cathode particle and electrolyte with lattice planes meeting and matching at the interface. For example, the particle can be identified by the periodic lattice arrangement of $\{202\}_{LSM}$ planes with a plane spacing of 0.22 nm[43, 44], indicating that disintegrated particles

exist as LSM perovskite phase. The YSZ electrolyte is characterized by the $\{111\}_{YSZ}$ lattice planes with plane spacing of 0.29 nm[45]. In this instance the orientation relationship, *i.e.*, the angle between the $\{202\}_{LSM}$ and $\{111\}_{YSZ}$ lattice planes at the interface, was found to be $\theta_{\{202\}LSM/\{111\}YSZ} = 46.9^{o}$, and the mismatch factor (*f*) [46-49] for these two planes can also be calculated:

$$f = \frac{d_{\{111\}YSZ} - d_{\{202\}LSM}}{d_{\{111\}YSZ}} * 100\% = 24.1\% \quad [1]$$

However, it should be noted that the current examined interface and the orientation relationship between $\{202\}_{LSM}$ and $\{111\}_{YSZ}$ lattice planes may be different at different locations, as a result of the polycrystalline nature of both phases. The establishment of the interface between disintegrated LSM particles and YSZ electrolyte is supported by the significant decrease in R_{Ω}.

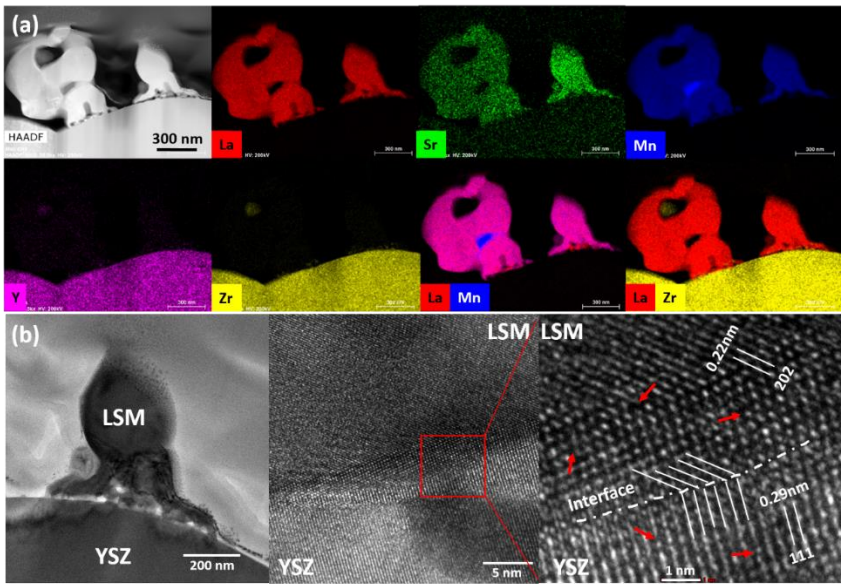

Figure 6.6 (a) STEM-EDS element mapping and (b) HRTEM micrographs of directly assembled LSM cathode on YSZ electrolyte after polarization at 900°C and 500 $mAcm^{-2}$ for 1 h. The red arrows indicate the locations of lattice distortion.

The disintegration of LSM cathode particle at the electrode/electrolyte interface becomes quite pronounced after polarization at 900°C and 500 $mAcm^{-2}$ for 12 h, as shown in Figure 6.7. The portion of the LSM particle in contact with YSZ electrolyte decomposed into a large number of small particles with the formation of voids in the bulk, and Mn segregation was also observed. In the disintegrated LSM particles, there is presence of Zr and Y in addition to La, Sr and Mn, implying the interaction and

formation of La-Mn-Zr solid solution[50-53]. Although the formation of $La_2Zr_2O_7$ cannot be ruled out at this stage, the continuous decrease of R_Ω during the polarization may indicate that the presence of such solid solutions between LSM and YSZ on the ORR is negligible and insignificant[54]. The atomic geometry of the hetero-interface between the YSZ electrolyte and the disintegrated LSM particles shows the lattice plane matching of the LSM and YSZ phases at the interface, *i.e.*, YSZ phase with $\{220\}_{YSZ}$ planes and plane spacing of 0.18 nm and LSM with $\{202\}_{LSM}$ planes and plane spacing of 0.22 nm (Figure 6.7b). The orientation relationship between the two examined planes was found to be $\theta_{\{202\}LSM/\{220\}YSZ} = 50.0^o$ with a lattice mismatch factor of f =18.2%. The FFT diffractogram of the electrolyte shows a typical cubic YSZ structure[45, 55], while for the LSM phase, it appears to be an overlap of two sets of same patterns at different orientation. This clearly indicates the overlap of two disintegrated LSM particles. Also, the abrupt image contrast change at the LSM/YSZ interface is obvious, most likely due to the strain effect resulted from the lattice mismatch of the heterogeneous phases[56-59]. The mismatch strain and the lattice misfit are usually relaxed and accommodated by the occurrence of misfit dislocations [60-62], e.g. lattice plane distortion and bending at the interface, as indicated in Figure 6.7.

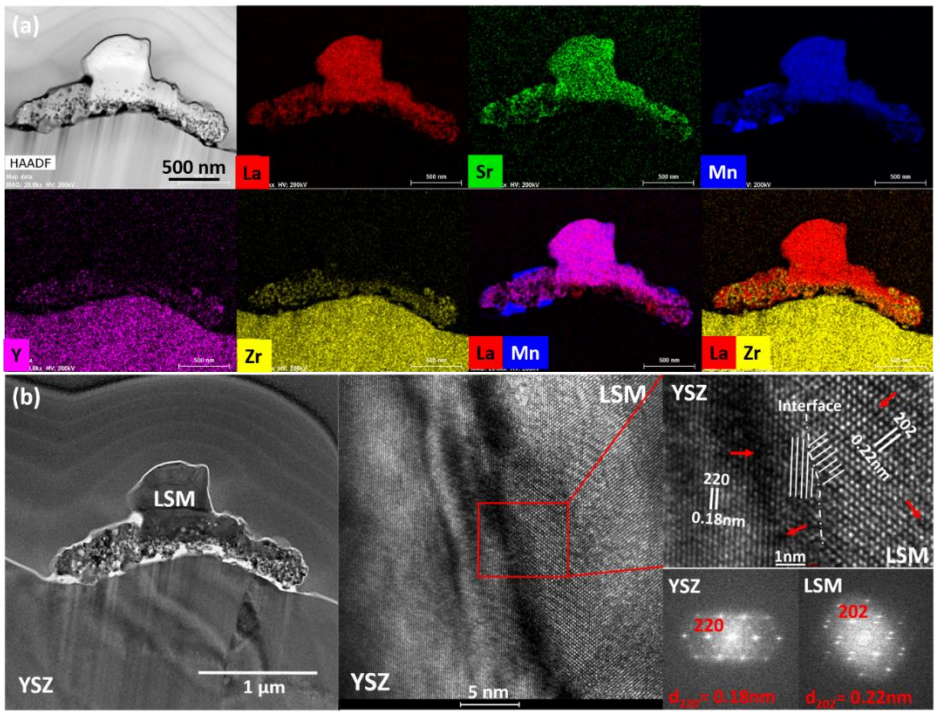

Figure 6.7 (a) STEM-EDS element mapping and (b) HRTEM micrographs of directly assembled LSM cathode on YSZ electrolyte after polarization at 900°C and 500

mAcm^{-2} for 12 h. The FFT shows the diffractograms of the YSZ and LSM phases. The red arrows indicate the locations of lattice distortion.

6.3.4 LSM/GDC interface

The influence of cathodic polarization on the interface of directly assembled LSM/GDC electrodes was also investigated and the results are shown in Figure 6.8. Different to that observed on the LSM/YSZ electrode, no Mn segregation was observed after polarization at 900^{o}C and 500 mAcm^{-2} for 1 h (Figure 6.8a). An intimate LSM/GDC interface was established with a high level of periodicity and symmetry, free of voids and amorphous phases (Figure 6.8b). The GDC electrolyte is characterized by $\{111\}_{GDC}$ planes with plane spacing of 0.31 nm, while LSM cathode can be identified by $\{110\}_{LSM}$ lattice planes with plane spacing of 0.27 nm. The orientation relationship of these two planes was $\theta_{\{111\}GDC/\{110\}LSM} = 11.0^{o}$ with f = 12.9%. Similar to the LSM/YSZ interface, the lattice plane distortion was also observed (indicated by the red arrows in Figure 6.8b). Nevertheless, the observed lattice distortion only exists locally at the interface region without propagating into the electrode or electrolyte bulk.

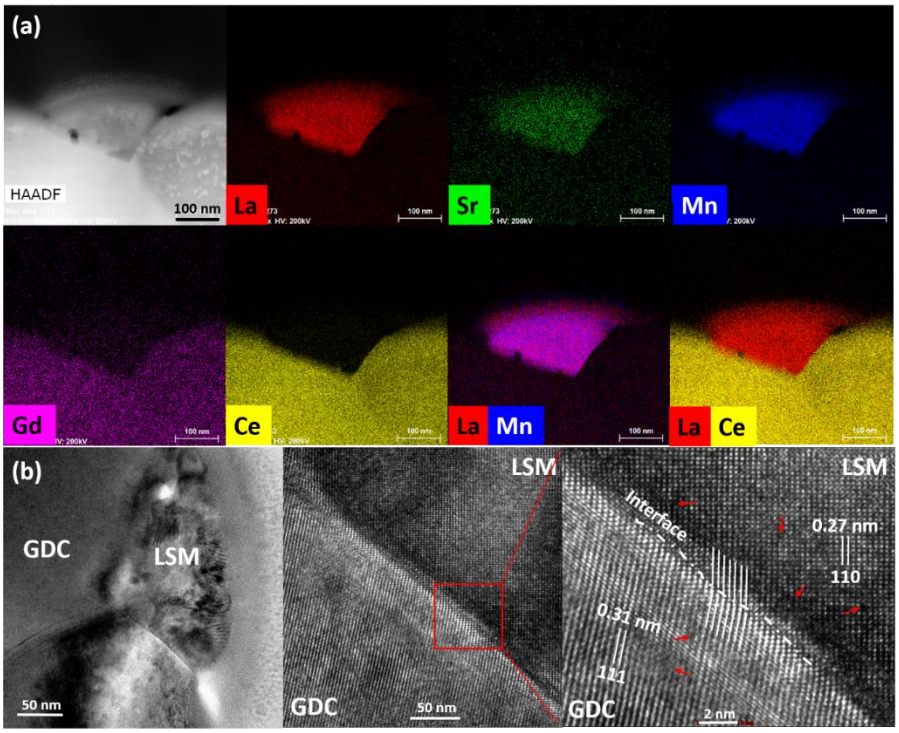

Figure 6.8 (a) STEM-EDS element mapping and (b) HRTEM micrographs of directly assembled LSM cathode on GDC electrolyte after polarization at 900^{o}C and 500 mAcm^{-2} for 1 h. The red arrows indicate the locations of lattice distortion.

The directly assembled LSM on GDC electrolyte was also polarized at 900°C and 500 $mAcm^{-2}$ for 12 h. LSM particles were in good contact with GDC electrolyte and there is no disintegration of LSM phase at the interface (Figure 6.9a), very different to that of LSM/YSZ electrode under the identical polarization conditions (Figure 6.7). However, similar to that observed on LSM/YSZ electrodes, Mn segregation from the LSM perovskite was observed. The polarization induced LSM/GDC interface is sharp and abrupt, characterized by a high symmetry of lattice plane structure for both LSM and GDC phases (see Figure 6.9b). From the FFT diffractogram images, the GDC electrolyte phase can be identified by its $\{220\}_{GDC}$ lattice planes with plane spacing of 0.19 nm, while LSM phase by the $\{012\}_{LSM}$ and $\{024\}_{LSM}$ planes with plane spacing of 0.39 nm and 0.19 nm, respectively. The orientation relationship of $\{220\}_{GDC}$ and $\{024\}_{LSM}$ was found to be 14.7° with lattice mismatch factor of 13%. The much stable LSM/GDC interface may indicate that the solubility of La^{3+} and Mn^{2+} in GDC is much lower than that in YSZ[51, 53, 63, 64].

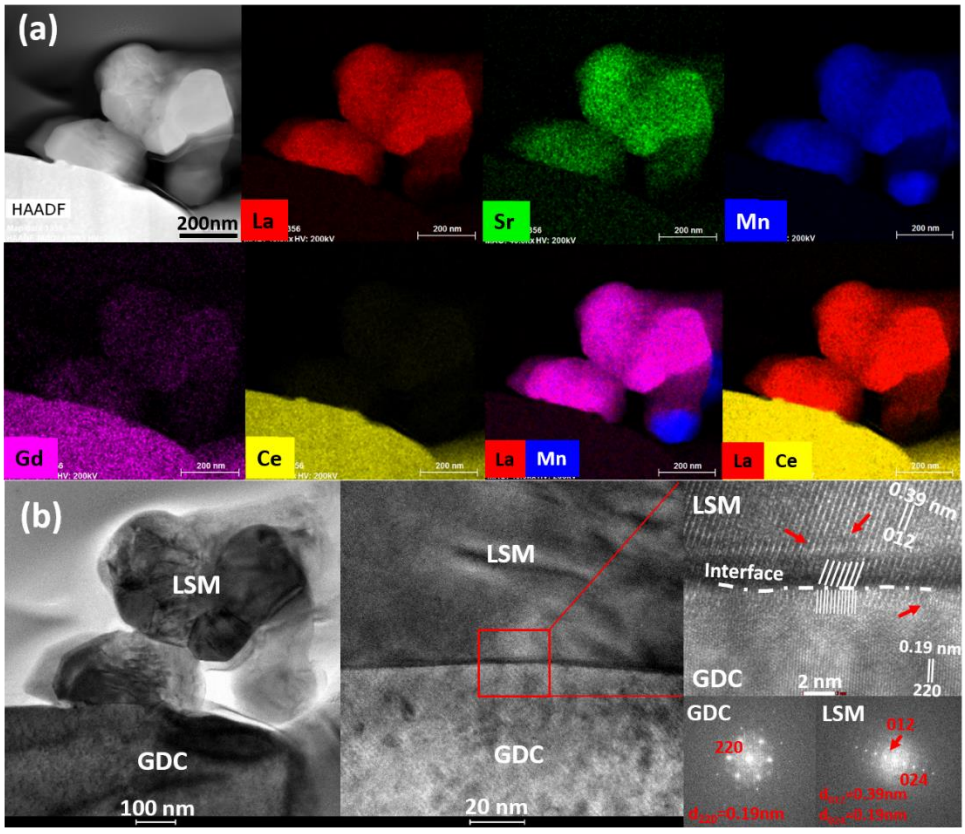

Figure 6.9 (a) STEM-EDS element mapping and (b) HRTEM micrographs of directly assembled LSM cathode on GDC electrolyte after polarization at 900°C and 500 $mAcm^{-2}$ for 12 h. The red arrows indicate the locations of lattice distortion.

Mn segregation from the LSM perovskite structure occurs in both LSM/YSZ and LSM/GDC electrodes under SOFC polarization conditions. Figure 6.10 presents typical STEM-EDS element mapping and HRTEM analysis of the interface between segregated manganese oxide (MnO_x) and LSM electrode on GDC electrolyte after polarization at 900ºC and 500 $mAcm^{-2}$ for 12 h. The segregation of MnO_x can be identified by the $\{013\}_{MnOx}$ and $\{111\}_{MnOx}$ planes with corresponding lattice plane spacing of 0.29 nm and 0.25 nm, respectively (Figure 6.10b). The MnO_x particle is in an intimate contact with LSM electrode, free of voids or other phases, characterized by a high level of symmetry and periodicity in lattice plane arrangement at the interface. The interface geometry of MnO_x/LSM is revealed as the matching of $\{111\}_{MnOx}$ and $\{110\}_{LSM}$ lattice planes with an orientation relationship of $\theta_{\{111\}MnOx/\{110\}LSM} = 40.7^o$ and a mismatch factor of 7.4%. The influence of Mn segregation on the performance degradation of the LSM/YSZ and LSM/GDC cells is not clear at this stage. However, MnO_x has a low electronic conductivity. The segregated MnO_x, if diffuses at the TPB, would partially block the transfer of electrons thus the increase of contact resistance might be expected, leading to the degradation of LSM electrode.

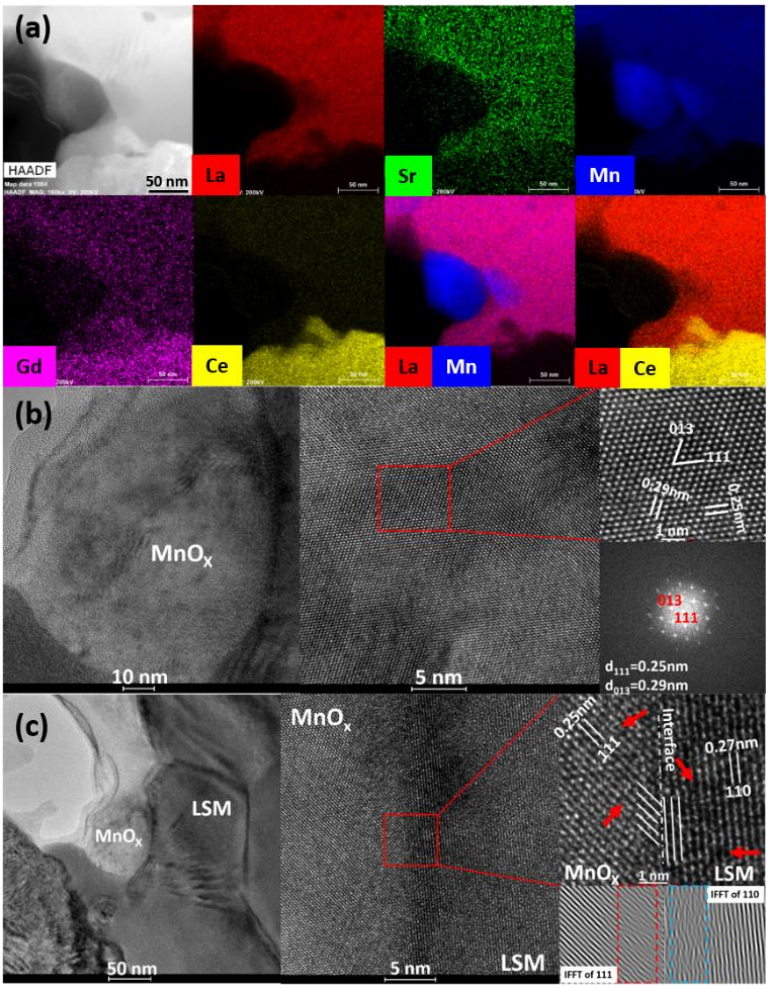

Figure 6.10 (a) STEM-EDS element mapping and HRTEM micrographs of (b) segregated MnO_x particle and (c) MnO_x/LSM interface after polarization at 900°C and 500 $mAcm^{-2}$ for 12 h on LSM/GDC electrode. The red arrows indicate the locations of lattice distortion.

6.3.5 Effect of polarization on the interface formation and Mn segregation

The results shown in the present study clearly indicate the significant effect of cathodic polarization on the interface formation and Mn segregation of directly assembled LSM/YSZ and LSM/GDC electrodes. The findings on the cathode/electrolyte interface microstructure and Mn segregation is summarized below:

1. For directly assembled LSM/YSZ electrode, there is a significant change in the microstructure and morphology of the YSZ electrolyte surface in contact with LSM electrode, indicated by the disintegration of LSM particles and formation of ring-shaped craters. With the increase of the polarization time, the contact rings continue to grow in size, and the disintegration of the LSM particle

becomes much more obvious at the interface, resulting in the formation of La-Mn-Zr solid solution. The results indicate the establishment of an intimate interface and the atomic geometry of the LSM/YSZ interface is characterized by the matching of $\{202\}_{LSM}$ and $\{111\}_{YSZ}$ or $\{220\}_{YSZ}$ lattice planes with a mismatch factor of 18.2-24.1%. The significantly enhanced electrochemical performance with the cathodic polarization demonstrates that the disintegrated LSM particles at the LSM/YSZ interface do not significantly impede the oxygen reduction process.

2. In the case of directly assembled LSM/GDC electrode, the change in the microstructure and morphology of GDC electrolyte is much smaller, very different from the substantial microstructure changes observed for the LSM/YSZ electrodes under the identical polarization conditions. Disintegration of LSM particles at the interface was not observed. The polarization induced LSM/GDC interface is indicated by the formation of small and shallow contact marks, and characterized by the matching of $\{024\}_{LSM}$ and $\{220\}_{GDC}$ or $\{110\}_{LSM}$ and $\{111\}_{GDC}$ lattice planes with a mismatch factor in the range of 1.3% to 12.9%. As compared to the LSM/YSZ electrode, the LSM/GDC interface is quite stable under polarization conditions, which is in good agreement with that reported in the literature[63]. Electrochemically, LSM/GDC electrode behaves similarly to that of LSM/YSZ electrode, showing the significantly reduced polarization and ohmic resistance with the polarization, though the magnitude in the change of the resistances is relatively smaller (see Figure 6.1).
3. The significantly enhanced electrochemical performance of LSM electrodes during the cathodic polarization indicates that the presence of misfit dislocations and distortions at the interface does not impede the migration and incorporation of O^{2-} from the LSM cathode into the electrolyte at the three phase boundary region. This is consistent with that reported in the literature [21, 36, 65]. For example, Pergolesi *et al*.[65] fabricated CeO_2 and YSZ biaxially textured epitaxial thin film using pulsed laser deposition method, and found that the hetero-interfaces are not uniform but significantly strained, yet no detectable contribution to the oxygen transport properties is found.
4. For both LSM/YSZ and LSM/GDC electrodes, Mn segregation from the cathode has been observed under the influence of the cathodic polarization. The segregated Mn particle most likely exists as MnO_x, and does not show

preferential deposition at the interface, indicating that Mn segregation is not driven to the cathode/electrolyte interface by the oxygen reduction process. The observed MnO_x/LSM interface is sharp and clean without any noticeable voids or amorphous phase. The atomic geometry of the examined interface can be identified by the matching of $\{111\}_{MnOx}$ and $\{110\}_{LSM}$ lattice planes with a mismatch factor of 7.4%.

Mn segregation has been commonly observed on the LSM electrodes under SOFC operation conditions. Chen *et al*.[66] studied the interface reactions between LSM cathode and YSZ electrolyte in different atmospheres at 1000ºC and found that Mn segregation is more pronounced at low oxygen partial pressure. This is consistent with that reported by Nishiyama [67], in which the oxygen potential gradient developed in the manganite was considered to give rise to the similar gradients in chemical potential of manganese, providing a driving force for manganese oxide segregation at the surface. Liu *et al*.[68] studied the influence of water vapour on the degradation behaviour of LSM based cells and observed an enrichment of Mn_2O_3 and Mn_3O_4 nano-particles (~100 nm in size) on the electrode surface by STEM-EDS mapping after the cell was exposed to 20 vol.% humidified air and operated at 800ºC for 200 h. We also observed a clear formation of Mn-rich phase, possibly Mn_3O_4 in the LSM electrode after the LSM-YSZ based cell was subject to a current load of 500 $mAcm^{-2}$ at 1000ºC for 2543 h[69].

Liu *et al*.[70] reported that Mn segregation occurs for the LSM-YSZ composite cathode and YSZ electrolyte after polarization at 850ºC and 1.76 Acm^{-2} for 1500 h, and proposed that the Mn migration cannot be simply attributed to the element diffusion. For perovskite-type LSM, the electrical neutrality due to substitution of La^{3+} by Sr^{2+} at the A site is maintained by a change in Mn valence. Lee *et al.* investigated active sites for O_2 reduction in the LSM electrode under various cathodic polarization potentials using *in situ* X-ray photoelectron spectroscopy (XPS) and observed a shifting of the Mn2p peaks to the lower binding energy side as the applied potential became more cathodic[71]. A recent study by Traulsen *et al*.[72] using operando X-ray absorption spectroscopy techniques showed that cathodic polarizations induces a shift in the Mn K edge energy towards lower energies due to a decrease in the average Mn oxidation state. This suggests the valence change of Mn ions in the lattice and interstitial sites under cathodic polarization. The valence change of Mn ions in the

perovskite can cause the structural change and segregation of Mn species to the electrode and electrolyte surface[73, 74]. The segregation of Mn species under cathodic polarization conditions has also been suggested as the main nucleation agents for the deposition of Cr on LSM electrodes under SOFC operation conditions[75, 76].

The current study also demonstrates that nature of electrolyte has a significant effect on the stability of the LSM/electrolyte interface. LSM on GDC electrolyte shows a more stable interface than that of LSM on YSZ electrolyte under identical polarization conditions. Due to the fact that the directly assembled electrodes do not go through the high temperature sintering, the initial physical contact between LSM electrode with YSZ or GDC electrolyte is very weak. Consequently, the low contact area would result in the initial high contact resistance (*i.e.*, R_Ω), 2.1 Ω cm^2 in the case of LSM/YSZ electrode and 1.0 Ω cm^2 in the case of LSM/GDC electrode. The high ohmic resistance will result in a much higher local current density at the interface, leading to the localized sintering due to the Joule heating. The heat generated will sinter the interface and thus enhance the contacts at the interface. This explains the significant reductions in R_Ω after polarization at 900ºC and 500 mAcm^{-2} for 12 h from 2.1 to 0.9 Ω cm^2 on LSM/YSZ electrode and from 1.0 Ω cm^2 to 0.3 Ω cm^2 on LSM/GDC electrode (Figure 6.1). However, the observed disintegration of LSM particles at the LSM/YSZ interface indicates that the heat generated at the LSM/YSZ interface would be significantly higher than that at the LSM/GDC interface. The underlying reason for the differences in the localized heating at the interface is most likely related to the significant differences in the ionic and electronic conducting properties of YSZ and GDC materials. YSZ is a pure oxygen ion conductor with the ionic conductivity in 0.08-0.11 S/cm range at 1000 ºC [77, 78], while the doped ceria, such as GDC, is a mixed ionic and electronic conductor with significantly higher conductivities (0.20-0.25 S/cm at 1000 ºC) [79, 80]. The high ionic conductivity and mixed ionic and electronic conducting properties of GDC could reduce the electrode ohmic resistance and at the same time accelerate the oxygen migration and diffusion at the interface between LSM and GDC. This is in fact supported by the much lower R_Ω and R_p values of the LSM/GDC electrode, as compared to that measured on LSM/YSZ electrodes before polarization (see Figure 6.1). However, it should be mentioned that the electronic conductivity of GDC becomes distinctively higher at low oxygen partial pressure and

high operating temperature (>800ºC) [81, 82], therefore the electronic current in GDC could be expected and may also influence the LSM/GDC interface structure.

Figure 6.11 shows a schematic diagram to compare the Mn diffusion and interface formation in pre-sintered[21] and directly assembled LSM/YSZ and LSM/GDC electrodes in this study. For the pre-sintered LSM/YSZ cell, the interface establishment after high temperature sintering is characterised by the formation of convex contact rings on the electrolyte, and the atomic geometry of the intimate electrode/electrolyte interface can be identified by a high level of symmetry, free of voids and amorphous phases (Figure 6.11a). In addition, Mn^{2+} and La^{3+} cation diffuse towards the YSZ electrolyte and cation accumulation in the convex contact rings were observed, indicating a strong solubility of La^{3+} and in particular Mn^{2+} species in YSZ. Similar to the LSM/YSZ electrodes, the pre-sintered LSM/GDC interface is also characterised by the formation of convex contact rings on the GDC electrolyte surface. No cation diffusion is detected due to their low solubility in doped ceria. This is in good accordance to the phase diagram data reported in the literature [83], in which the estimated solubility of Mn cation in ZrO_2-MnO-$MnO_{1.5}$-MnO_2 system is up to 5.1 % at 1000 ºC, and under the cathodic polarization condition, the solubility might be promoted. In contrast, no solid solution was observed in MnO-Mn_2O_3-CeO_2 system above 800 ºC. As the Mn segregation is most likely caused by the valence change of Mn ions in the perovskite structure under cathodic polarization conditions[71, 72], this also explains the observation that no MnO_x segregation occurs on pre-sintered LSM/YSZ and LSM/GDC electrodes (see Figure 6.11a)[21]. In the case of the directly assembled LSM/YSZ and LSM/GDC electrodes, the formation of an intimate electrode/electrolyte interface is also observed under the cathodic polarization conditions (Figure 6.11b). The significant differences in the microstructure and morphology of the electrode/electrolyte interface can be attributed to the significant differences in the nature of YSZ and GDC electrolyte materials as discussed above.

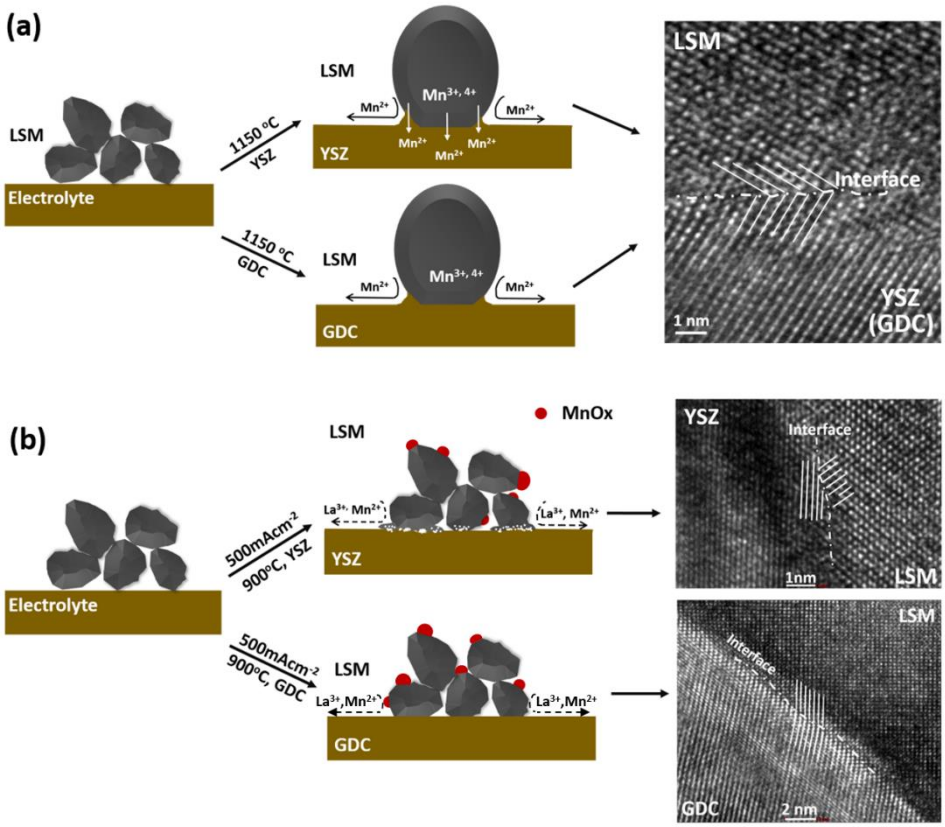

Figure 6.11 Schematic diagram showing the Mn diffusion and interface formation of (a) pre-sintered and (b) directly assembled LSM/YSZ and LSM/GDC electrodes.

6.4 Conclusion

The interface formation and Mn segregation and diffusion of directly assembled LSM/YSZ and LSM/GDC electrodes were studied under cathodic polarization conditions at 900 ^{o}C using combined FIB-STEM techniques. The results indicate that in the case of both LSM/YSZ and LSM/GDC electrodes, the cathodic current passage induces the formation of intimate electrode/electrolyte interface, indicated by the significant reduction in both R_p and R_Ω. However, the change in the YSZ electrolyte surface in contact with LSM electrode is substantial, as compared to that on GDC electrolyte, characterized by the disintegration of LSM phase at the electrode/electrolyte interface and the formation of ring-shaped contact craters at the interface. The main reason for the disintegration of LSM phase at the interface is due to the much higher localized heat generated at the interface due to the low ionic conductivity of YSZ electrolyte material in comparison to that of GDC electrolyte. In

addition, Mn segregation was observed for both LSM/YSZ and LSM/GDC electrodes under the effect of cathodic polarization, and the segregated MnO_x does not show preferential deposition at the interface. This may be the main reason for the negligible detrimental effect of segregated MnO_x on the electrochemical activity of LSM electrode studied in this work. This study provides an insight in the fundamental understanding of electrode/electrolyte interface formation and Mn segregation in relation to the nature of electrolyte of SOFCs and has significant implications in the development of active and stable cathodes of SOFCs in general.

6.5 References

[1] T.M. Gür, Comprehensive review of methane conversion in solid oxide fuel cells: Prospects for efficient electricity generation from natural gas, Progress in Energy and Combustion Science, 54 (2016) 1-64.

[2] A. Choudhury, H. Chandra, A. Arora, Application of solid oxide fuel cell technology for power generation—A review, Renewable and Sustainable Energy Reviews, 20 (2013) 430-442.

[3] K. Chen, L. Zhang, N. Ai, S. Zhang, Y. Song, Y. Song, Q. Yi, C.-Z. Li, S.P. Jiang, Feasibility of Direct Utilization of Biomass Gasification Product Gas Fuels in Tubular Solid Oxide Fuel Cells for On-Site Electricity Generation, Energy & Fuels, (2015).

[4] D. Papurello, R. Borchiellini, P. Bareschino, V. Chiodo, S. Freni, A. Lanzini, F. Pepe, G.A. Ortigoza, M. Santarelli, Performance of a Solid Oxide Fuel Cell short-stack with biogas feeding, Applied Energy, 125 (2014) 254-263.

[5] N. Mahato, A. Banerjee, A. Gupta, S. Omar, K. Balani, Progress in material selection for solid oxide fuel cell technology: A review, Progress in Materials Science, 72 (2015) 141-337.

[6] S.C. Singhal, Solid oxide fuel cells for power generation, Wiley Interdisciplinary Reviews: Energy and Environment, 3 (2014) 179-194.

[7] H. Moon, S. Kim, S. Hyun, H. Kim, Development of IT-SOFC unit cells with anode-supported thin electrolytes via tape casting and co-firing, International Journal of Hydrogen Energy, 33 (2008) 1758-1768.

[8] T. Fukui, S. Ohara, M. Naito, K. Nogi, Performance and stability of SOFC anode fabricated from NiO–YSZ composite particles, Journal of Power Sources, 110 (2002) 91-95.

[9] S.P. Jiang, Development of lanthanum strontium manganite perovskite cathode materials of solid oxide fuel cells: a review, Journal of Materials Science, 43 (2008) 6799-6833.
[10] M. Backhausricoult, Interface chemistry in LSM–YSZ composite SOFC cathodes, Solid State Ionics, 177 (2006) 2195-2200.
[11] Y.L. Liu, A. Hagen, R. Barfod, M. Chen, H.J. Wang, F.W. Poulsen, P.V. Hendriksen, Microstructural studies on degradation of interface between LSM–YSZ cathode and YSZ electrolyte in SOFCs, Solid State Ionics, 180 (2009) 1298-1304.
[12] J.T.S. Irvine, D. Neagu, M.C. Verbraeken, C. Chatzichristodoulou, C. Graves, M.B. Mogensen, Evolution of the electrochemical interface in high-temperature fuel cells and electrolysers, Nature Energy, 1 (2016) 15014.
[13] T. Matsui, Y. Mikami, H. Muroyama, K. Eguchi, Quantitative Analysis of Microstructural Change at the Interface Between, (La, Sr)MnO3 Cathode and YSZ Electrolyte upon Discharge Operation, J. Electrochem. Soc., 157 (2010) B1790-B1794.
[14] S. Jiang, J.G. Love, L. Apateanu, Effect of contact between electrode and current collector on the performance of solid oxide fuel cells, Solid State Ionics, 160 (2003) 15-26.
[15] A. Belzner, T. Gur, R. Huggins, Oxygen chemical diffusion in strontium doped lanthanum manganites, Solid State Ionics, 57 (1992) 327-337.
[16] T. Horita, T. Tsunoda, K. Yamaji, N. Sakai, T. Kato, a.H. Yokokawa, Microstructures and oxygen diffusion at the LaMnO3 film/yttria-stabilized zirconia interface, Solid State Ionics, 152-153 (2002) 439–446.
[17] S.P. Jiang, W. Wang, Effect of Polarization on the Interface Between (La,Sr)MnO[sub 3] Electrode and Y[sub 2]O[sub 3]-ZrO[sub 2] Electrolyte, Electrochemical and Solid-State Letters, 8 (2005) A115.
[18] T. Matsui, Y. Mikami, H. Muroyama, K. Eguchi, Influence of (La,Sr)MnO3+δ cathode composition on cathode/electrolyte interfacial structure during long-term operation of solid oxide fuel cells, Journal of Power Sources, 242 (2013) 790-796.
[19] B. Hu, M. Keane, M.K. Mahapatra, P. Singh, Stability of strontium-doped lanthanum manganite cathode in humidified air, Journal of Power Sources, 248 (2014) 196-204.
[20] T. Matsui, M. Komoto, H. Muroyama, K. Eguchi, Interfacial Stability between Air Electrode and Ceria-Based Electrolyte under Cathodic Polarization in Solid Oxide Fuel Cells, Fuel Cells, 14 (2014) 1022-1027.

[21] S. He, K.F. Chen, M. Saunders, J. Li, C.Q. Cui, S.P. Jiang, A FIB-STEM Study of La0.8Sr0.2MnO3 Cathode and Y2O3-ZrO2/Gd2O3-CeO2 Electrolyte Interfaces of Solid Oxide Fuel Cells, J. Electrochem. Soc., 164 (2017) F1437-F1447.
[22] J. Yang, H. Muroyama, T. Matsui, K. Eguchi, The influence of discharge operation on the microstructure of strontium-doped lanthanum manganite cathode for solid oxide fuel cells, Journal of Power Sources, 204 (2012) 25-33.
[23] M.J. Jørgensen, P. Holtappels, C.C. Appel, Durability test of SOFC cathodes, Journal of Applied Electrochemistry, 30 (2000) 411-418.
[24] M.A. Haider, S. McIntosh, Evidence for Two Activation Mechanisms in LSM SOFC Cathodes, Journal of The Electrochemical Society, 156 (2009).
[25] T. Matsui, Y. Mikami, H. Muroyama, K. Eguchi, Quantitative Analysis of Microstructural Change at the Interface Between (La,Sr)MnO[sub 3] Cathode and YSZ Electrolyte upon Discharge Operation, Journal of The Electrochemical Society, 157 (2010) B1790.
[26] K. Chen, S.S. Liu, N. Ai, M. Koyama, S.P. Jiang, Why solid oxide cells can be reversibly operated in solid oxide electrolysis cell and fuel cell modes?, Phys Chem Chem Phys, 17 (2015) 31308-31315.
[27] S.P. Jiang, Thermally and Electrochemically Induced Electrode/Electrolyte Interfaces in Solid Oxide Fuel Cells: An AFM and EIS Study, Journal of The Electrochemical Society, 162 (2015) F1119-F1128.
[28] K. Chen, N. Li, N. Ai, Y. Cheng, W.D. Rickard, S.P. Jiang, Polarization-Induced Interface and Sr Segregation of in Situ Assembled La0.6Sr0.4Co0.2Fe0.8O3-delta Electrodes on Y2O3-ZrO2 Electrolyte of Solid Oxide Fuel Cells, ACS Appl Mater Interfaces, 8 (2016) 31729-31737.
[29] M. Li, K. Chen, B. Hua, J.-l. Luo, W.D.A. Rickard, J. Li, J.T.S. Irvine, S.P. Jiang, Smart utilization of cobaltite-based double perovskite cathodes on barrier-layer-free zirconia electrolyte of solid oxide fuel cells, Journal of Materials Chemistry A, 4 (2016) 19019-19025.
[30] N. Li, N. Ai, K. Chen, Y. Cheng, S. He, M. Saunders, A. Dodd, A. Suvorova, S.P. Jiang, In situ assembled La0.8Sr0.2MnO3 cathodes on a Y2O3–ZrO2 electrolyte of solid oxide fuel cells – interface and electrochemical activity, RSC Adv., 6 (2016) 99211-99219.
[31] N. Ai, N. Li, S. He, Y. Cheng, M. Saunders, K. Chen, T. Zhang, S.P. Jiang, Highly active and stable Er0.4Bi1.6O3 decorated La0.76Sr0.19MnO3+δ nanostructured

oxygen electrodes for reversible solid oxide cells, J. Mater. Chem. A, 5 (2017) 12149-12157.
[32] N. Ai, N. Li, W.D. Rickard, Y. Cheng, K. Chen, S.P. Jiang, Highly Stable Sr-Free Cobaltite-Based Perovskite Cathodes Directly Assembled on a Barrier-Layer-Free Y2 O3 -ZrO2 Electrolyte of Solid Oxide Fuel Cells, ChemSusChem, 10 (2017) 993-1003.
[33] N. Ai, S. He, N. Li, Q. Zhang, W.D.A. Rickard, K. Chen, T. Zhang, S.P. Jiang, Suppressed Sr segregation and performance of directly assembled La 0.6 Sr 0.4 Co 0.2 Fe 0.8 O 3-δ oxygen electrode on Y 2 O 3 -ZrO 2 electrolyte of solid oxide electrolysis cells, Journal of Power Sources, 384 (2018) 125-135.
[34] N. Li, N. Ai, S. He, Y. Cheng, W.D.A. Rickard, K. Chen, T. Zhang, S.P. Jiang, Effect of Pd doping on the activity and stability of directly assembled La 0.95 Co 0.19 Fe 0.76 Pd 0.05 O 3-δ cathodes of solid oxide fuel cells, Solid State Ionics, 316 (2018) 38-46.
[35] K. Chen, S. He, N. Li, Y. Cheng, N. Ai, M. Chen, W.D.A. Rickard, T. Zhang, S.P. Jiang, Nb and Pd co-doped La 0.57 Sr 0.38 Co 0.19 Fe 0.665 Nb 0.095 Pd 0.05 O 3-δ as a stable, high performance electrode for barrier-layer-free Y 2 O 3 -ZrO 2 electrolyte of solid oxide fuel cells, Journal of Power Sources, 378 (2018) 433-442.
[36] S. He, M. Saunders, K. Chen, H. Gao, A. Suvorova, W.D.A. Rickard, Z. Quadir, C.Q. Cui, S.P. Jiang, A FIB-STEM Study of Strontium Segregation and Interface Formation of Directly Assembled La0.6Sr0.4Co0.2Fe0.8O3-δCathode on Y2O3-ZrO2 Electrolyte of Solid Oxide Fuel Cells, Journal of The Electrochemical Society, 165 (2018) F417-F429.
[37] K. Chen, N. Li, N. Ai, M. Li, Y. Cheng, W.D.A. Rickard, J. Li, S.P. Jiang, Direct application of cobaltite-based perovskite cathodes on the yttria-stabilized zirconia electrolyte for intermediate temperature solid oxide fuel cells, Journal of Materials Chemistry A, 4 (2016) 17678-17685.
[38] S.P. Jiang, Activation, microstructure, and polarization of solid oxide fuel cell cathodes, Journal of Solid State Electrochemistry, 11 (2005) 93-102.
[39] S. Jiang, J. Love, Origin of the initial polarization behavior of Sr-doped LaMnO3 for O2 reduction in solid oxide fuel cells, Solid State Ionics, 138 (2001) 183-190.
[40] W. Wang, S.P. Jiang, A mechanistic study on the activation process of (La, Sr)MnO3 electrodes of solid oxide fuel cells, Solid State Ionics, 177 (2006) 1361-1369.
[41] M.A. Haider, S. McIntosh, Evidence for Two Activation Mechanisms in LSM SOFC Cathodes, J. Electrochem. Soc., 156 (2009) B1369-B1375.

[42] A.A. Vance, S. McIntosh, Performance and activation behavior of surface-doped thin-film La0.8Sr0.2MnO3-delta cathodes, J. Electrochem. Soc., 155 (2008) B1-B7.
[43] R. Moriche, D. Marrero-López, F.J. Gotor, M.J. Sayagués, Chemical and electrical properties of LSM cathodes prepared by mechanosynthesis, Journal of Power Sources, 252 (2014) 43-50.
[44] A. Hammouche, E. Siebert, A. Hammou, Crystallographic, thermal and electrochemical properties of the system La1−xSrxMnO3 for high temperature solid electrolyte fuel cells, Materials Research Bulletin, 24 (1989) 367-380.
[45] C.M. Wang, S. Azad, V. Shutthanandan, D.E. McCready, C.H.F. Peden, L. Saraf, S. Thevuthasan, Microstructure of ZrO2–CeO2 hetero-multi-layer films grown on YSZ substrate, Acta Materialia, 53 (2005) 1921-1929.
[46] D. Wolf, S. Yip, Materials Interfaces: Atomic-level Structure and Properties, Springer Netherlands1993.
[47] S. Cazottes, Z.L. Zhang, R. Daniel, J.S. Chawla, D. Gall, G. Dehm, Structural characterization of a Cu/MgO(001) interface using CS-corrected HRTEM, Thin Solid Films, 519 (2010) 1662-1667.
[48] Y. Ikuhara, Grain Boundary and Interface Structures in Ceramics, Journal of the Ceramic Society of Japan, 109 (2001) S110-S120.
[49] J.P. Locquet, D. Neerinck, L. Stockman, Y. Bruynseraede, I.K. Schuller, Long-range order and lattice mismatch in metallic superlattices, Physical Review B, 38 (1988) 3572-3575.
[50] Tatsuya Kawada, Natsuko Sakai, Harumi Yokokawa, M. Dokiya, Reaction between solid oxide fuel cell materials, Solid State Ionics, 50 (1992) 189-196.
[51] M. Mori, T. Abe, H. Itoh, O. Yamamoto, G.Q. Shen, Y. Takeda, N. Imanishi, Reaction mechanism between lanthanum manganite and yttria doped cubic zirconia, Solid State Ionics, 123 (1999) 113-119.
[52] S.P. Simner, J.P. Shelton, M.D. Anderson, J.W. Stevenson, Interaction between La(Sr)FeO3 SOFC cathode and YSZ electrolyte, Solid State Ionics, 161 (2003) 11-18.
[53] S.P. Jiang, J.P. Zhang, K. Foger, Chemical interactions between 3 mol% yttria-zirconia and Sr-doped lanthanum manganite, J. Eur. Ceram. Soc., 23 (2003) 1865-1873.
[54] A. Mitterdorfer, L.J. Gauckler, La2Zr2O7 formation and oxygen reduction kinetics of the La0.85Sr0.15MnyO3, O2(g)|YSZ system, Solid State Ionics, 111 (1998) 185-218.

[55] U. Martin, H. Boysen, F. Frey, Neutron powder investigation of tetragonal and cubic stabilized zirconia, TZP and CSZ, at temperatures up to 1400 K, Acta Crystallographica Section B Structural Science, 49 (1993) 403-413.
[56] O.I. Lebedev, G.V. Tendeloo, S. Amelinckx, H.L. Ju, K.M. Krishnan, High-resolution electron microscopy study of strained epitaxial La0.7Sr0.3MnO3thin films, Philosophical Magazine A, 80 (2000) 673-691.
[57] C. Rentenberger, C. Mangler, S. Scheriau, R. Pippan, H.P. Karnthaler, TEM Study of Local Disordering: A Structural Phase Change Induced by High-Pressure Torsion, Materials Science Forum, 584-586 (2008) 422-427.
[58] X.L. Wu, E. Ma, Accommodation of large plastic strains and defect accumulation in nanocrystalline Ni grains, Journal of Materials Research, 22 (2011) 2241-2253.
[59] M. Sillassen, P. Eklund, N. Pryds, E. Johnson, U. Helmersson, J. Bøttiger, Low-Temperature Superionic Conductivity in Strained Yttria-Stabilized Zirconia, Advanced Functional Materials, 20 (2010) 2071-2076.
[60] F.K. LeGoues, The Effect of Strain on the Formation of Dislocations at the SiGe/Si Interface, MRS Bulletin, 21 (1996) 38-44.
[61] F. Ernst, P. Pirouz, A.H. Heuer, HRTEM study of a Cu/Al2O3interface, Philosophical Magazine A, 63 (1991) 259-277.
[62] A. Trampert, F. Ernst, C.P. Flynn, H.F. Fischmeister, M. Ru¨hle, High resolution transmission electron microscopy studies of the Ag/MgO interface, Acta Metallurgica et Materialia, 40 (1992) S227-S236.
[63] L. Zhao, J. Hyodo, T. Ishihara, K. Sasaki, S.R. Bishop, XRD and Raman Spectroscopy Study of Mn Solubility in Cerium Oxide, ECS Transactions, 57 (2013) 1607-1612.
[64] V.P. Dravid, V. Ravikumar, M.R. Notis, C.E. Lyman, G. Dhalenne, A. Revcolevschi, Stabilization of Cubic Zirconia with Manganese Oxide, Journal of the American Ceramic Society, 77 (1994) 2758-2762.
[65] D. Pergolesi, E. Fabbri, S.N. Cook, V. Roddatis, E. Traversa, J.A. Kilner, Tensile lattice distortion does not affect oxygen transport in yttria-stabilized zirconia-CeO2 heterointerfaces, ACS Nano, 6 (2012) 10524-10534.
[66] M. Chen, Y.L. Liu, A. Hagen, P.V. Hendriksen, F.W. Poulsen, LSM-YSZ Reactions in Different Atmospheres, Fuel Cells, 9 (2009) 833-840.

[67] H. Nishiyama, Stability of Lanthanum Calcium Chromite-Lanthanum Strontium Manganite Interfaces in Solid Oxide Fuel Cells, Journal of The Electrochemical Society, 143 (1996).
[68] R.R. Liu, S.H. Kim, S. Taniguchi, T. Oshima, Y. Shiratori, K. Ito, K. Sasaki, Influence of water vapor on long-term performance and accelerated degradation of solid oxide fuel cell cathodes, Journal of Power Sources, 196 (2011) 7090-7096.
[69] S. Jiang, W. Wang, Sintering and grain growth of (La,Sr)MnO3 electrodes of solid oxide fuel cells under polarization, Solid State Ionics, 176 (2005) 1185-1191.
[70] Y.L. Liu, K. Thydén, M. Chen, A. Hagen, Microstructure degradation of LSM-YSZ cathode in SOFCs operated at various conditions, Solid State Ionics, 206 (2012) 97-103.
[71] H.Y. Lee, W.S. Cho, S.M. Oh, H.D. Wiemhofer, W. Gopel, Active Reaction Sites for Oxygen Reduction in La0.9sr0.1mno3/Ysz Electrodes, J. Electrochem. Soc., 142 (1995) 2659-2664.
[72] M.L. Traulsen, H.W.P. de Carvalho, P. Zielke, J.D. Grunwaldt, The Effect of Electrical Polarization on Electronic Structure in LSM Electrodes: An Operando XAS, RIXS and XES Study, J. Electrochem. Soc., 164 (2017) F3064-F3072.
[73] S.P. Jiang, J.G. Love, Observation of structural change induced by cathodic polarization on (La,Sr)MnO3 electrodes of solid oxide fuel cells, Solid State Ionics, 158 (2003) 45-53.
[74] M. Backhaus-Ricoult, K. Adib, T.S. Clair, B. Luerssen, L. Gregoratti, A. Barinov, In-situ study of operating SOFC LSM/YSZ cathodes under polarization by photoelectron microscopy, Solid State Ionics, 179 (2008) 891-895.
[75] S.P. Jiang, J.P. Zhang, L. Apateanu, K. Foger, Deposition of chromium species at Sr-doped LaMnO3 electrodes in solid oxide fuel cells I. Mechanism and kinetics, J. Electrochem. Soc., 147 (2000) 4013-4022.
[76] S.P. Jiang, S. Zhang, Y.D. Zhen, Early interaction between Fe-Cr alloy metallic interconnect and Sr-doped LaMnO3 cathodes of solid oxide fuel cells, J. Mater. Res., 20 (2005) 747-758.
[77] X.J. Chen, K.A. Khor, S.H. Chan, L.G. Yu, Influence of microstructure on the ionic conductivity of yttria-stabilized zirconia electrolyte, Materials Science and Engineering: A, 335 (2002) 246-252.

[78] S.P.S. Badwal, ZIRCONIA-BASED SOLID ELECTROLYTES - MICROSTRUCTURE, STABILITY AND IONIC-CONDUCTIVITY, Solid State Ionics, 52 (1992) 23-32.
[79] K. Eguchi, T. Setoguchi, T. Inoue, H. Arai, Electrical properties of ceria-based oxides and their application to solid oxide fuel cells, Solid State Ionics, 52 (1992) 165-172.
[80] H. Inaba, Ceria-based solid electrolytes, Solid State Ionics, 83 (1996) 1-16.
[81] S. Lübke, H.D. Wiemhöfer, Electronic conductivity of gadolinia doped ceria, Berichte der Bunsengesellschaft für physikalische Chemie, 102 (1998) 642-649.
[82] S. Wang, T. Kobayashi, M. Dokiya, T. Hashimoto, Electrical and Ionic Conductivity of Gd-Doped Ceria, Journal of The Electrochemical Society, 147 (2000).
[83] Rober S. Roth, T.A. Vanderah, Phase Equilibria Diagrams - Volume XIV: Oxides, American Ceramic Society, U.S., 2005.

Chapter 7: In situ Formation of $Er_{0.4}Bi_{1.6}O_3$ Protective Layer at Cobaltite Cathode/Y_2O_3-ZrO_2 Electrolyte Interface under Solid Oxide Fuel Cells Operation Conditions

Abstract

Bismuth based oxides exhibit outstanding oxygen ionic conductivity and fast oxygen surface kinetics and have shown great potential as a highly active component for

electrode materials in solid oxide fuel cells (SOFC). Herein, a Nb-doped $La_{0.6}Sr_{0.4}Co_{0.2}Fe_{0.7}Nb_{0.1}O_{3-\delta}$ (LSCFNb) electrode with 40% $Er_{0.4}Bi_{1.6}O_3$ (ESB) composite electrode was successfully fabricated by decoration method and directly assembled on barrier-layer-free yttrium stabilized zirconia (YSZ) electrolyte cells, achieving a peak power density of 1.32 W cm^{-2} and excellent stability at 750^oC and 250 $mAcm^{-2}$ for 100 hrs. ESB decoration also significantly reduces the activation energy from 214 kJ mol^{-1} for the O_2 reduction on pristine LSCFNb electrode to 98 kJ mol^{-1}. Further microstructural analysis reveals that there is a redistribution and migration of the ESB phase in the ESB-LSCFNb composite towards the YSZ electrolyte under the influence of cathodic polarization, forming a thin ESB layer at the cathode/YSZ electrolyte interface. The *in situ* formed ESB layer not only prevents the direct contact and subsequent reaction between segregated SrO and YSZ electrolyte, but also remarkably promotes the oxygen migration/diffusion at the interface for O_2 reduction reaction, resulting in a remarkable increase in power output and decrease in activation energy. The present study clearly demonstrated the in situ formation of a highly functional and active ESB protective layer at LSCFNb cobaltite cathode and YSZ electrolyte interface via ESB decorated LSCFNb composite cathode under SOFC operation conditions.

7.1 Introduction

In previous chapters, *in situ* formed electrode/electrolyte interfaces were studied and compared with the conventional high temperature formed interfaces. In this chapter, the direct assembly method will be further adopted to anode-supported fuel cell, and the evolution of electrode/electrolyte interface under the influence of polarisation will be discussed and correlated with its overall electrochemical performance.

Solid oxide fuel cells (SOFCs) are the most efficient energy conversion devices to electrochemically convert the chemical energy of fuels such as hydrogen and natural gas to electricity with intrinsically high efficiency, low pollutant emissions and flexible fuel options [1-4]. However, the development of conventional SOFCs operated at high temperatures of ~1000^oC has been retarded by problems of high manufacturing and maintenance cost and high performance degradation due to microstructure degradation,[5-7] cation inter-diffusion,[8, 9] contamination[10, 11] and chemical

reactions at the electrode/electrolyte interface.[12-14] Thus, significant effort has been made to reduce the operating temperature to intermediate and low temperatures of 500-800^{o}C to increase the durability, thermal compatibility and thermal cycle capability and to reduce the fabrication and materials costs of SOFCs.[4, 15, 16] With the reduction in operating temperature, the cell performance is increasingly dominated by the polarization losses of electrode reactions, especially at the cathode side due to the slow oxygen reduction reaction (ORR).[17] Mixed ionic and electronic conducting (MIEC) material such as $La_{0.6}Sr_{0.4}Co_{0.2}Fe_{0.8}O_{3-\delta}$ (LSCF) is probably the most popular and studied cathode for intermediate and low temperature SOFCs because of its superior mixed electronic conductivity (~250 S cm^{-1} at 800^{o}C) [18] and oxygen ionic conductivity (~0.2 S cm^{-1} at 900^{o}C),[19, 20] excellent oxygen surface exchange rate and high electrocatalytic activity for ORR.[21-26] Unfortunately, the activation energy of LSCF based cathode for ORR is in the range of 130-160 kJ mol^{-1}.[26-28] The high activation energy implies the significant increase of polarization resistance with the decrease of operating temperature for the reaction on LSCF based cathodes.

Doped bismuth oxides such as erbium stabilized bismuth oxide (ESB) have been reported to possess excellent oxygen surface exchange kinetics and one to two orders of magnitude larger ionic conductivities as compared to conventional yttria stabilized zirconia (YSZ) at intermediate and low temperatures (0.023 S cm^{-1} at 500 ^{o}C and 0.37 S cm^{-1} at 700 ^{o}C).[29-31] Doped bismuth oxides have been applied as electrolyte,[32] an interfacial layer between the electrolyte and cathode,[33, 34] as well as an active component for $La_{0.8}Sr_{0.2}MnO_{3-\delta}$ (LSM),[35, 36] $Pr_{0.5}Ba_{0.5}MnO_3$ [37] and composite cathodes.[38-40] However, due to its low melting temperature, high reactivity and phase instability in reducing atmosphere, the adoption of doped bismuth oxide is way less popular than other oxygen ion conductors. There is also a concern in the incorporation of bismuth oxide into cobaltite perovskite electrodes due to its high reactivity with cobaltite materials.[41-43] For instance, Lee *et al*. investigated the compatibility between ESB and LSCF after been heated at 850 ^{o}C for 1h and observed significant new phase formation.[41] ESB reacted with LSCF, forming a $La(Sr,Bi)CoO_{3-\delta}$ phase at the LSCF/ESB interface.[42] It was reported that LSCF started to react with yttria stabilized bismuth oxide (YSB) at 650^{o}C, but by infiltrating YSB into LSCF scaffold followed by 600^{o}C sintering, the performance of the YSB-

LSCF cell with proton conducting electrolyte was significantly enhanced, reaching a peak power density of 167 mW cm^{-2} at 550 ^{o}C.[43]

Most recently, we have shown that the incorporation of ESB with LSM and $Sm_{0.95}Co_{0.95}Pd_{0.05}O_{3-\delta}$ (SmCPd) composite electrodes via a decoration technique without pre-sintering process at high temperature significantly enhances the performance of the cathode.[44, 45] For example, an anode supported YSZ electrolyte cell with directly assembled ESB decorated LSM cathode exhibited a peak power density of 1.62 W cm^{-2} at 750 ^{o}C, and excellent operation stability in reversible solid oxide cell (SOC) modes for more than 200 h.[44] The decoration method has significant advantages over the conventional composite by mechanical mixing or infiltration techniques. Bismuth oxide based composite electrodes prepared by mechanical mixing require a high temperature pre-sintering step,[35, 41, 46] which can be detrimental to the phase and structural stability of bismuth oxide phase. The infiltration technique avoids the high temperature sintering step, but the process is time consuming and the loading of the infiltrated phase is limited.[47] Excess infiltration also reduces the porosity and increases the diffusion resistance for the reaction.[48] Decoration methods used in this study not only avoid the high temperature sintering but also are highly flexible in the component composition without detrimental effect on the microstructure.

In this work, ESB decoration is applied to cobaltite based perovskite cathode such as Nb-doped LSCF (LSCFNb) to form an ESB decorated LSCFNb composite cathode directly assembled on YSZ electrolyte. The use of B-site doping with high valence cations like niobium is to reduce the Sr segregation and therefore increase the structural stability of LSCF.[49, 50] The results indicate that there is a redistribution of ESB phase in the ESB-LSCFNb composite under polarization conditions, forming an ESB interlayer at the cathode/YSZ interface. Such formed interlayer prevents the direct contact between the segregated SrO and YSZ, resulting in the significant enhancement of the performance of LSCFNb cathode.

7.2 Experimental

7.2.1 Synthesis and fabrication of ESB decorated LSCFNb cathode and anode-supported cell

$La_{0.6}Sr_{0.4}Co_{0.2}Fe_{0.7}Nb_{0.1}O_{3-\delta}$ (LSCFNb) powder was synthesized by sol-gel method. The starting chemicals were $La(NO_3)_3 \cdot 6H_2O$ (99.9%, A.R., Alfa-Aesar), $Sr(NO_3)_2$ (99%, A.R., Sigma-Aldrich), $Co(NO_3)_2 \cdot 6H_2O$ (98-102%, A.R., Alfa-Aesar), $Fe(NO_3)_3 \cdot 9H_2O$ (98%, Sigma-Aldrich), ammonium niobate oxalate hydrate ($C_4H_4NNbO_9 \cdot xH_2O$, 99.99%, Sigma-Aldrich), anhydrous citric acid (99.5%, A.R., Chem Supply), ethylenediaminetetraacetic acid (EDTA, 99%, Acros Organics), and ammonia solution (28%w.w., Sigma-Aldrich) with a molar ratio of 1:1.5:1(metal ions/citric acid/EDTA). The resultant gel powders were calcined at 900 °C in air for 2 h. $Er_{0.4}Bi_{1.6}O_3$ (ESB) decorated LSCFNb electrode powder with a weight percentage of 40 wt.% ESB and 60 wt.% LSCFNb was synthesized by sol-gel method. The use of 40wt% ESB is based on the percolation limit of conductive phase in the composite.[51] ESB aqueous precursor solution consisting of $Er(NO_3)_3 \cdot 5H_2O$ (99.9%, A.R., Sigma-Aldrich), $Bi(NO_3)_3 \cdot 5H_2O$ (98%, A.R., Sigma-Aldrich), EDTA, anhydrous citric acid and ammonia was constantly stirred on a heating stage (the precursor solution will produce 4 grams of ESB powder after calcination). Then 6 grams of LSCFNb powder was added to the ESB precursor solution and stirred until the gelation starts. The resultant gel was further dried in the oven at 150^{o}C overnight and then calcined at 600^{o}C in air for 2h, forming ESB decorated LSCFNb powder (ESB-LSCFNb). The ESB-LSCFNb powder was mechanically blended with the ink vehicle (Fuel Cell Materials, US) with a weight ratio of 7:3 using a mortar and pestle to obtain cathode ink. LSCFNb-YSZ oxide couples with a weight ratio of 5:5 were also made and heat treated at 750, 800, 850 and 900 ^{o}C in air for 2 h.

Ni-YSZ anode-supported YSZ electrolyte cells (φ 15 mm × 0.8 mm) were prepared by spin coating method followed by co-sintering at 1450^{o}C for 5h.[52] For the anode support, NiO (J.T. Baker), 8 mol% Y_2O_3-doped ZrO_2 (YSZ, Tosoh) powder and tapioca were blended with a weight ratio of 5:5:2.5. The anode functional layer (AFL) was fabricated by mixing YSZ and NiO with a weight ratio of 5:5. The thickness of the NiO-YSZ support, AFL and YSZ film was 800, 9 and 11 μm, respectively. The LSCFNb and ESB-LSCFNb cathode pastes were directly screen-printed onto the YSZ electrolyte and then dried at 100 ^{o}C for 2 h to obtain the directly assembled

LSCFNb/YSZ and ESB-LSCFNb/YSZ cells. Gold paste (Gwent Electronic Materials Ltd, UK) was painted on the electrode surface and dried at 150 ^{o}C, serving as the current collector. The cathode has a geometric area of 0.2 cm^2 with a thickness of ~19 μm. Stability test was performed at 750 ^{o}C and 250 mA cm^{-2} for 100 hrs. In order to study the influence of cathodic polarization on the electrode/electrolyte interface, an anode supported cell with directly assembled electrode was dwelled at 750 ^{o}C for 100 hrs without polarization treatment, *i.e.*, under open circuit condition.

YSZ electrolyte-supported cells were also prepared to study the electrochemical impedance behaviour of LSCFNb and ESB-LSCFNb electrodes for the oxygen reduction reaction via a three-electrode configuration.[53] YSZ electrolyte discs were fabricated by die pressing YSZ powder, followed by sintering at 1450^{o}C for 5 h. The thickness and diameter of the YSZ electrolyte pellet were 1.0 mm 20 mm, respectively. Platinum ink (Gwent Electronic Materials Ltd., UK) was printed at the centre and edge of the YSZ pellet as the counter and reference electrodes, followed by sintering at 1100 ^{o}C for 2 h. Cathode paste was painted on the other side of the YSZ electrolyte, symmetrically opposite to the platinum counter electrode.

7.2.2 Characterization

The anode supported YSZ electrolyte cells were sealed onto Al_2O_3 tubes using a ceramic sealant (Ceramabond 552, Aremco Products Inc.). H_2 at a flow rate of 50 mL min^{-1} was supplied to the NiO-YSZ anode and the cathode was exposed to the ambient air. The NiO-YSZ anode was reduced in H_2 at 750 ^{o}C for 1 h before the electrochemical tests. The electrochemical impedance, polarization curves and stability curves were recorded using a electrochemical workstation (Gamry Reference 3000 Potentiostat) at a temperature range of 600 -750 ^{o}C. The electrochemical impedance was recorded in a frequency range of 100 mHz to 100 kHz with a signal amplitude of 10 mV under open circuit conditions. Electrode ohmic resistance (R_Ω) was obtained from the high frequency intercept, and electrode polarization resistance (R_p) was calculated from the differences between the high and low frequency intercepts of the impedance curves.[54] The operation stability of the cell was recorded under a constant current of 250 mA cm^{-2} at 750 ^{o}C. In order to ensure the reproducibility, the measurements were repeated at least on two different cells. Activation energy of LSCFNb and ESB-LSCFNb cathodes for the oxygen reduction reaction was obtained from the slope of the

Arrhenius plots of R_p by the impedance measurements in the temperature range of 600-800 ^oC on YSZ electrolyte-supported cells.

The phases of the prepared cathode powders and the LSCFNb-YSZ oxide couple calcined at different temperatures were identified by a Bruker D8 Advance X-ray diffractometer (XRD) equipped with a copper Kα source. The microstructure of the YSZ electrolyte surface in contact with LSCFNb and ESB-LSCFNb cathodes was studied by scanning electron microscopy (SEM, Zeiss Neon 40EsB). To examine the morphology of the YSZ electrolyte surface, the electrode coating was completely removed by hydrochloric acid (HCl, 32 wt%, Sigma-Aldrich) treatment, and in some occasions, the electrode was partly peeled off to investigate the electrode/electrolyte interface. YSZ electrolyte lamella in contact with the cathode particles was prepared with a thickness of around 60 nm using a Dual Beam Focused Ion Beam - Scanning Electron Microscope (FIB-SEM, Helios Nanolab G3 CX, FEI company) with Ga^+ ion source at 30 kV. The FIB milled lamellae were examined using a high angle annular dark field scanning transmission electron microscopy (HAADF-STEM, FEI Titan G2 80-200 TEM/STEM with ChemiSTEM Technology) at 200 kV to obtain the EDS elemental mapping results and microstructural micrographs. TEM Imaging & Analysis software (TIA, FEI Company) was used to extract the fast Fourier transform (FFT) images from the TEM micrographs, in order to study the diffraction behavior of selected regions.

7.3 Results and Discussion

7.3.1. Thermal compatibility and microstructure of cathode powder and cell

Figure 7.1a presents the XRD pattern of the LSCFNb-YSZ oxide couples after heat treatment at 750, 800, 850 and 900^{o}C. XRD peaks for the pure perovskite and cubic phases were identified for the LSCFNb and YSZ oxides after the calcination at 750, 800 and 850^{o}C. The oxide couple started to react at 900^{o}C, forming $SrZrO_3$ phase. The $SrZrO_3$ (002), (040) and (042) planes were identified at 30.8 ^{o}, 44.7 ^{o} and 54.9 ^{o}.[55, 56] However, in the case of LSCF-YSZ oxide couple, the reaction starts at a temperature as low as 800^{o}C.[57, 58] This implies that the Nb doping evidently improves the chemical compatibility between LSCFNb and YSZ. However, bismuth oxide may not be stable at temperatures of ~850 ^{o}C. Therefore, to avoid the possible

decomposition and instability of ESB in the ESB-LSCFNb composite electrodes, test has been carried out at a low temperature of 750 ^{o}C in this study. The cross-section of the anode-supported YSZ electrolyte cell with ESB-LSCFNb cathode after the electrochemical tests is also shown in Figure 7.1b. A good contact between the porous cathode and the dense YSZ electrolyte was observed. The thickness of the electrolyte was ~10 µm. The STEM-EDS mapping showed the uniformly distributed LSCFNb nano-particles with a dimension of 154 ± 43 nm, encapsulated in the ESB network. The results indicate the successful fabrication of ESB decorated LSCFNb electrodes and directly assembled on barrier-layer-free YSZ electrolyte cell.

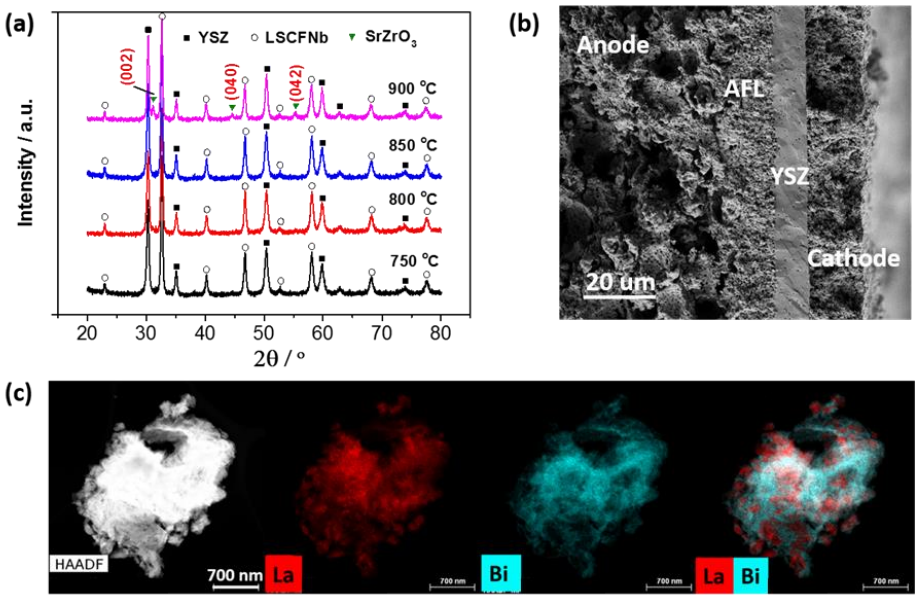

Figure 7.1 (a) XRD results of LSCFNb-YSZ oxide couples (1:1, w:w) sintered at 750, 800, 850, 900 ^{o}C for 2 h in air, (b) SEM image of the cross-section of an anode-supported YSZ electrolyte cell with a directly assembled ESB-LSCFNb cathode after the test. (c) STEM-EDS element mapping of as prepared ESB-LSCFNb cathode powder.

7.3.2. Electrochemical performance and microstructure of electrode/electrolyte interface

Figure 7.2 presents the electrochemical performance results of anode-supported YSZ electrolyte cells with directly assembled LSCFNb and ESB-LSCFNb cathodes polarized at 250 mAcm^{-2} and 750^{o}C. For the cell with ESB-LSCFNb cathode, the peak power density (PPD) is 1.32, 0.78, 0.45 and 0.24 W cm^{-2} at 750, 700, 650 and 600 ^{o}C, respectively (Figure 7.2a). R_{Ω} of the cell is 0.07, 0.10, 0.16 and 0.27 Ω cm^{2} at 750,

700, 650 and 600 ºC, respectively, and R_p of the cell is 0.40, 0.68, 1.33 and 3.00 Ω cm^2 at 750, 700, 650 and 600 ºC, respectively (Figure 7.2b). As a comparison, the cell with directly assembled LSCFNb cathode was also tested. The PPD of the LSCFNb cell is 0.53 W cm^{-2} at 750ºC, which is much lower as compared to 1.32 W cm^{-2} acquired on the ESB-LSCFNb cell (Figure 7.2c). The impedance of the LSCFNb cell is also much higher than that of ESB-LSCFNb cell. For example, R_Ω and R_p of the LSCFNb cell are 0.29 and 0.50 Ω cm^2 at 750ºC, respectively, significantly larger than 0.07 and 0.32 Ω cm^2 obtained on ESB-LSCFNb cells under identical test conditions. R_p of LSCFNb cell is also larger than 0.27 Ω cm^2 for the cell with directly assembled LSCF cathode under similar test conditions.[50] This indicates that Nb doping reduces the electrocatalytic activity of LSCF electrode for ORR, in good agreement with that reported on Nb-doped $Ba_{0.5}Sr_{0.5}Co_{0.8}Fe_{0.2}O_{3-\delta}$ (BSCF) membranes.[59]

The low polarization resistance of the cell with ESB-LSCFNb cathode is clearly due to the much higher electrocatalytic activity of the ESB-LSCFNb electrode for ORR. As shown in Figure 7.2e, R_p of the ESB-LSCFNb composite cathode on YSZ electrolyte supported cell is 7.2 Ω cm^2 at 600 ºC, which is significantly smaller than 55.2 Ω cm^2 obtained on LSCFNb cathode. Most importantly, activation energy of R_p for the ORR on the ESB-LSCFNb composite electrode is 98 kJ mol^{-1}, substantially lower than 214 kJ mol^{-1} acquired on LSCFNb electrode (Figure 7.2f). The results indicate that the ESB decoration significantly reduces the activation energy and improves the electrocatalytic activity of the electrode for ORR. This implies that decorated ESB is most effective to enhance the electrocatalytic activity of LSCF-based cathode at reduced temperatures. The ESB-LSCFNb cell was stable with negligible change in the cell voltage after polarization at 750 ºC and 250 mAcm^{-2} for 100 hrs (Figure 7.2g). The initial cell voltage was 0.96 V and slightly decreased to 0.90 V after cathodic polarization for 100 hrs. However, different from that of ESB-LSCFNb cell, the cell with LSCFNb cathode was not stable and the cell voltage decreased rather significantly from 0.87 V to 0.72 V under similar testing conditions (Figure 7.2h).

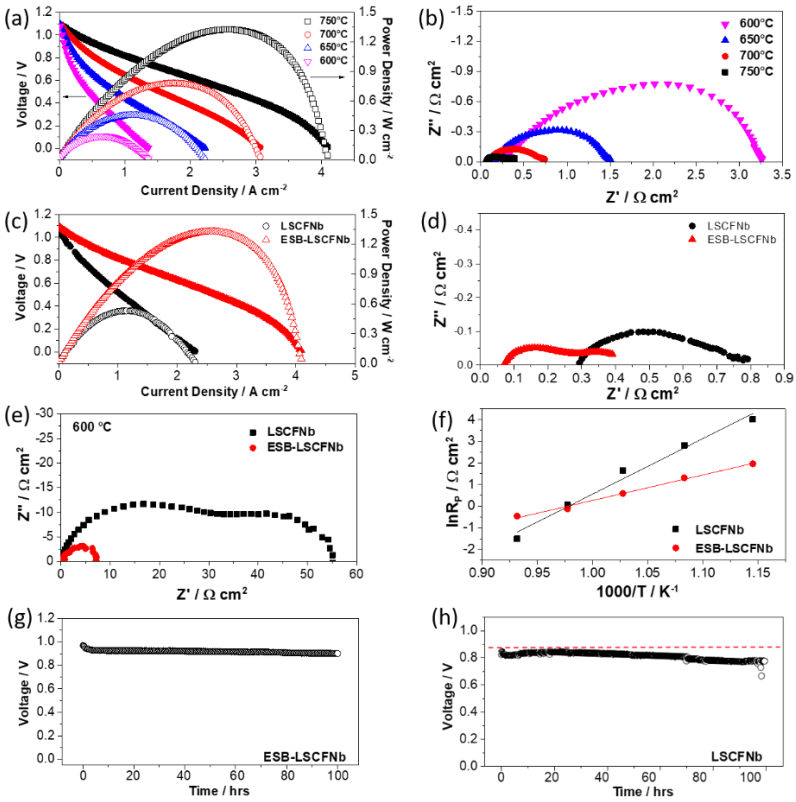

Figure 7.2 Electrochemical performance of anode support cell with directly assembled LSCFNb and ESB decorated LSCFNb (ESB-LSCFNb) cathodes as a function of polarization time at 750°C and 250mA cm^{-2}. (a) Polarization curves and (b) impedance spectra of the cell with ESB-LSCFNb cathode as a function of temperature. (c,d) Polarization curves and impedance curves of the cells with LSCFNb and ESB-LSCFNb cathodes at 750°C. (e) Impedance curves of the LSCFNb and ESB-LSCFNb cathodes on YSZ electrolyte supported cells measured at 600 °C. (f) Activation energy plots of R_p of LSCFNb and ESB-LSCFNb cathodes. Stability of the anode-supported cell with directly assembled (g) ESB-LSCFNb and (h) LSCFNb cathodes at 750°C and 250 mA cm^{-2}.

The morphology of YSZ electrolyte surface in contact with directly assembled LSCFNb and ESB-LSCFNb cathodes is shown in Figure 7.3. The cathodes were either peeled off using adhesive tape (Figure 7.3b,d,f) or removed by acid treatment (Figure 7.3a,c,e). The YSZ surface in contact with LSCFNb cathode was characterized by the formation of large number of ring-shaped contact craters with a dimension of 0.34 ± 0.15 μm (inset in Figure 7.3a). As shown in Figure 7.3b, a large number of island structure were observed after the LSCFNb cathode was peeled off using sticky tape.

These islands have a dimension of 0.53 ± 0.25 μm, which is close to that of the ring-shaped craters observed on the electrolyte. The change in the surface morphology of the YSZ electrolyte clearly indicates the significant interaction between LSCFNb cathode and YSZ electrolyte during the cathodic polarization. In contrast, in the case of the ESB-LSCFNb cell, the YSZ electrolyte surface was reasonably smooth and flat after the cathodic polarization at 750 ºC and 250 mA cm^{-2} for 100 hrs, and the size of ring-shaped contact craters was much smaller (0.17 ± 0.15 μm) (Figure 7.3c), as compared to that on YSZ surface in contact with LSCFNb cathode (Figure 7.3a). There was also formation of island structures on the YSZ surface but different to that observed on the YSZ electrolyte surface of the LSCFNb cell, the islands appear to consist of small particles deposited on a plate-like layer with size in the range of 0.77 ± 0.44 μm (Figure 7.3d), substantially larger than that of the ring-shaped contact craters. Without cathodic polarization, the YSZ surface in contact with ESB-LSCFNb cathode was smooth and no contact marks were observed (Figure 7.3e), indicating that no reactions occurred between ESB-LSCFNb cathode and YSZ electrolyte at 750 ºC under open circuit conditions. The particles left on the YSZ electrolyte surface after the cathode coating was removed by adhesive tape were ESB-LSCFNb cathode particles (Figure 7.3f). The morphology of the ESB-LSCFNb composite cathode particles is similar to the as-synthesized ESB-LSCFNb powder as shown in Figure 7.1c. This indicates again that the ring-shaped contact craters observed on YSZ electrolyte surface in contact with LSCFNb and ESB-LSCFNb cathode are induced by the cathodic polarization treatment.

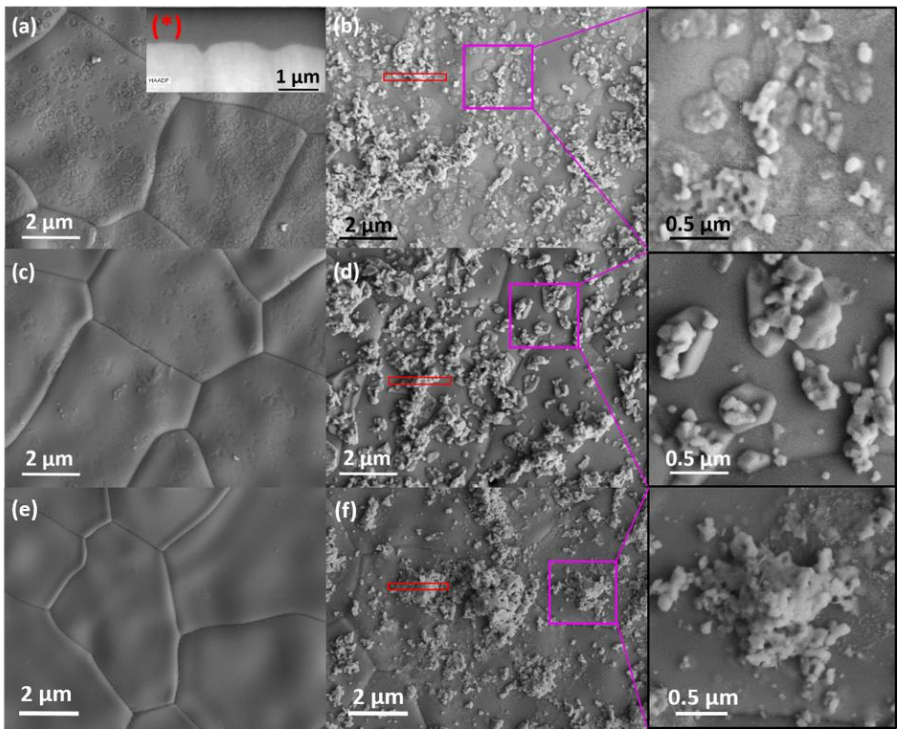

Figure 7.3 SEM micrographs of YSZ electrolyte surface in contact with directly assembled (a,b) LSCFNb, and (c,d) ESB decorated LSCFNb cathodes after polarization at 750ºC and 250 $mAcm^{-2}$ for 100 hrs. The YSZ surface with directly assembled ESB decorated LSCFNb electrode before polarization is also shown in (e,f). The cathodes were removed by (a,c,e) acid treatment or by (b,d,f) adhesive tape. The inset (*) in (a) is the cross-section of the convex-shaped rings and red boxes in (b,d,f) indicate the typical locations for FIB milling.

7.3.3. LSCFNb/YSZ interface

Figure 7.4 presents the HAADF micrograph and STEM-EDS element mapping of the LSCFNb/YSZ interface region of a directly assembled LSCFNb cell after cathodic polarization at 250 mA cm^{-2} and 750ºC for 100 hrs. A thick layer (~100 nm) with different contrast to that of dense YSZ electrolyte and porous LSCFNb cathode was observed between the cathode and electrolyte. The size of this reaction phase was 0.54 µm, similar to the size of island structures (0.53 ± 0.25 µm) observed in Figure 7.3b. The originally flat YSZ surface became curved (indicated by arrow in Figure 7.4a), corresponding to the ring-shaped convex contact craters (see Figure 7.3a). The mapping results clearly identified the LSCFNb cathode and YSZ electrolyte. For the reaction layer at the cathode/electrolyte interface, a strong accumulation of Sr and Zr was detected. This implies the possible formation of $SrZrO_3$ layer under the influence

of cathodic polarization, similar to that observed for the directly assembled LSCF cathode on YSZ electrolyte.[58] The accumulation of Sr at the interface region implies the substantial Sr segregation and diffusion under cathodic polarization conditions, in good agreement with that reported in the literature.[60-62] Different to the conventional chemical reaction between two phases, such surface segregation induced chemical reaction can occur at a much lower temperature. Yung *et al*. observed the chemical reaction between BSCF cathode and $Ce_{0.8}Sm_{0.2}O_{1.95}$ and $Ce_{0.9}Gd_{0.1}O_{1.95}$ electrolytes at 700 ^{o}C under the influence of cathodic polarization.[63] Without the influence of polarization, such reaction only occurs at 900 ^{o}C. The reaction has been attributed to the Ba segregation induced by cathodic polarization.

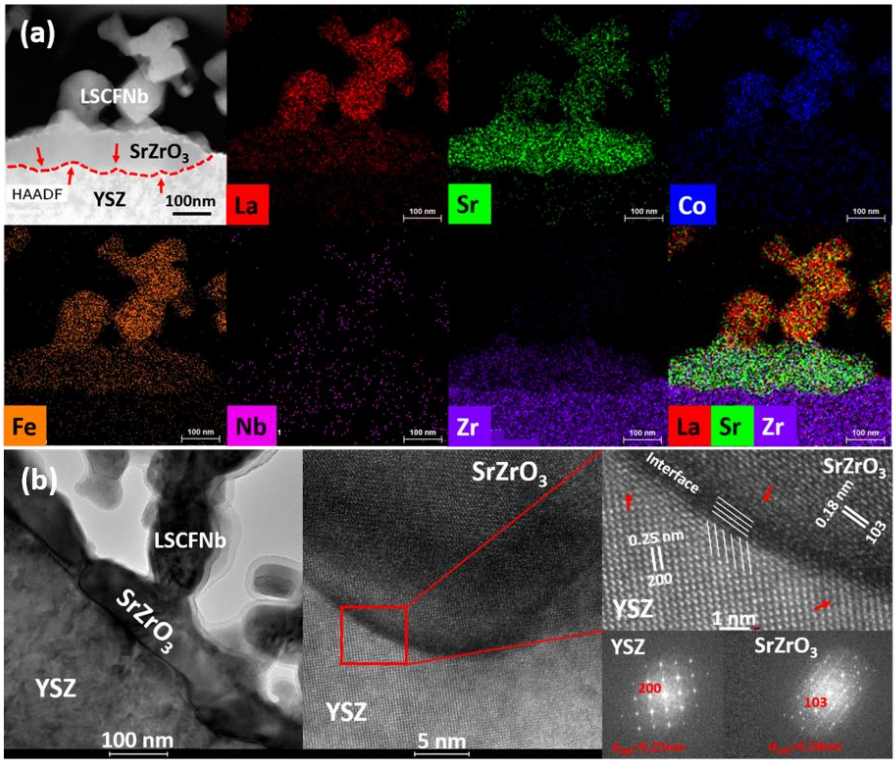

Figure 7.4 (a) STEM-EDS element mapping and (b) HRTEM and FFT images of the LSCFNb/YSZ interface of an anode supported YSZ electrolyte cell with a directly assembled LSCFNb electrode after polarization at 250 mAcm^{-2} and 750^{o}C for 100 hrs. The red arrows in (b) indicate the lattice distortion.

The reaction layer at the electrode/electrolyte interface of the directly assembled LSCFNb cell was examined by FIB-STEM (Figure 7.4b). The reaction layer has an intimate contact with the electrolyte. The $\{103\}_{SrZrO3}$ lattice planes with a plane spacing of 0.18 nm indicate the formation of $SrZrO_3$ phase in the reaction layer, while

the YSZ phase was identified by the $\{200\}_{YSZ}$ planes with plane spacing of 0.25 nm. The FFT image of YSZ phase shows a typical cubic structure, taken along $[001]_{YSZ}$ zone axis.[64] In this case, the $\{200\}_{YSZ}$ and $\{103\}_{SrZrO3}$ lattice planes meet at the interface with the corresponding orientation relationship, $\theta_{\{103\}SrZrO3/\{200\}YSZ}$ of 44.7^o and a mismatch factor (*f*) of 28.0%. The occurrence of the lattice plane distortion was observed in the interface region. The lattice distortion is widely observed for hetero-interfaces, in order to accommodate the lattice mismatch between two different phases.[65-67] This study indicates the substantial Sr segregation of Nb doped LSCF (LSCFNb), different from the suppressed Sr segregation reported on Nb-doped cobaltite perovskite cathode on GDC electrolyte.[49, 68] The reason may be related to the direct contact between the SrO and YSZ electrolyte, which leads to the formation of $SrZrO_3$ and in turn accelerates the Sr segregation.

7.3.4. ESB-LSCFNb/YSZ interface

Figure 7.5 shows the HAADF micrograph and STEM-EDS mapping of the cathode/electrolyte interface of a directly assembled ESB-LSCFNb cell after cathodic polarization at 250 $mAcm^{-2}$ and 750^{o}C for 100 hrs. Very different from that observed on the LSCFNb cell, the YSZ surface was flat and no curvature on the electrolyte surface in contact with ESB-LSCFNb electrode was observed, indicating a very stable interface between ESB-LSCFNb cathode and YSZ electrolyte even after the cathodic polarization at 250 $mAcm^{-2}$ and 750 ^{o}C for 100 hrs. Except individual and isolated Sr-rich areas/particles with size in the range of 10-40 nm, La and other elements of LSCFNb (not shown for clarity of the data) were uniformly distributed, indicating that Sr segregation and diffusion of LSCFNb electrode under polarization conditions are significantly suppressed by the ESB decoration. In contrast to the uniform distribution and network of bismuth in the original ESB decorated LSCFNb powders (see Figure 7.1c), there was almost no bismuth present in the LSCFNb particles at the cathode/electrolyte interface. Instead, there was a clear accumulation and enrichment of Bi on the electrolyte surface between YSZ and LSCFNb particles. The Bi layer is not uniform and appears to fill the open space on the electrolyte surface between the LSCFNb particles. The thickness of this bismuth oxide layer varies significantly between a few nm to 100-200 nm. The remarkable change in the distribution of Bi and its migration at the interface region in the ESB-LSCFNb cell evidently occurred under the influence of the cathodic polarization. The clear boundary between bismuth oxide

and LSCFNb phase also indicates no chemical reaction between LSCFNb and ESB. No Zr was observed in the ESB-LSCFNb cathode, indicating that there is no cation interdiffusion between YSZ electrolyte and ESB-LSCFNb electrode. The diffusion and accumulation of bismuth at the interface was also observed on the bismuth oxide decorated $Sm_{0.96}Co_{0.95}Pd_{0.05}O_{3-\delta}$ oxygen electrodes of reversible solid oxide cells after polarization at 500 mA cm^{-2} and 750 ^{o}C for 500 hrs.[45]

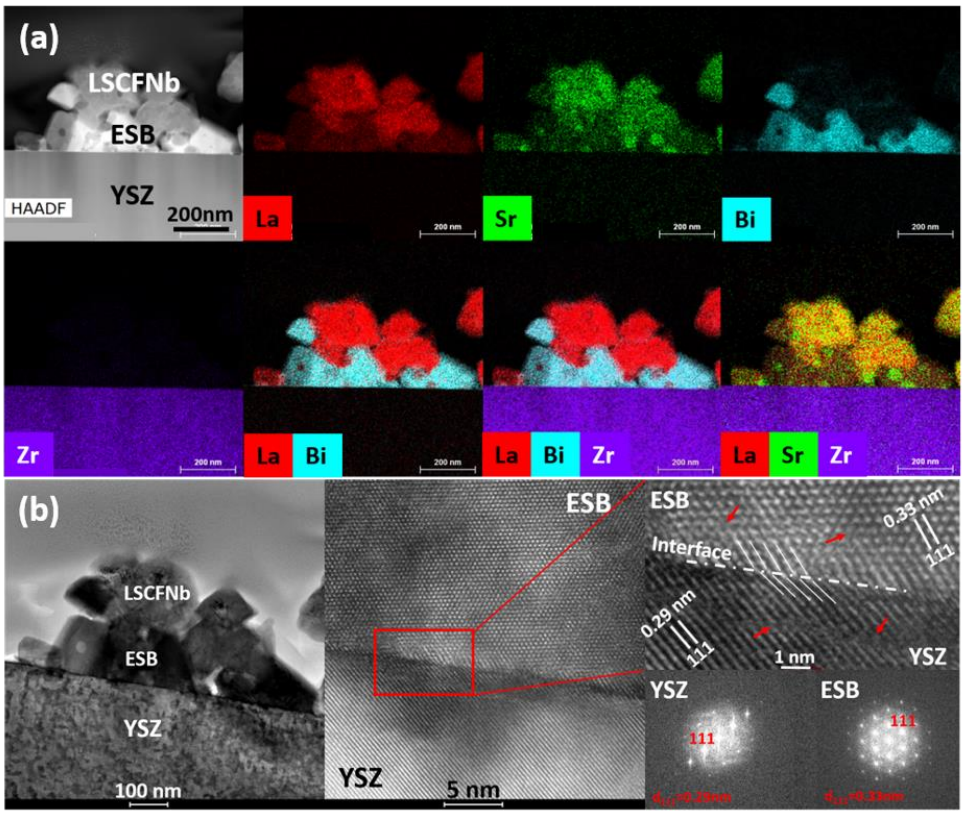

Figure 7.5 (a) STEM-EDS element mapping and (b) HRTEM and FFT images of the ESB-LSCFNb/YSZ interface of an anode supported YSZ electrolyte cell with a directly assembled ESB-LSCFNb electrode after polarization at 250 $mAcm^{-2}$ and 750^{o}C for 100 hrs. The red arrows indicate the lattice distortion.

The microstructure of the accumulated bismuth layer on the electrolyte surface was examined by HRTEM, taken along $[011]_{ESB}$ zone axis (Figure 7.5b). The migrated ESB phase has established an intimate contact with the YSZ electrolyte, and the ESB/YSZ interface was very sharp and abrupt as a result of their similar intrinsic cubic structure with space group symmetry of Fm-3m and lattice constants of 5.48 Å and 5.13 Å, respectively.[69, 70] From the interface region, the $\{111\}_{YSZ}$ lattice planes with a plane spacing of 0.29 nm and the $\{111\}_{ESB}$ lattice planes with a plane spacing

of 0.33 nm are associated with YSZ and ESB phases, respectively. The $\{111\}_{YSZ}$ and $\{111\}_{ESB}$ planes meet and match at the interface, with orientation relationship of 9.4^{o} and mismatch factor of 12.1%. Lattice distortion for the two phases was also observed around the interface, but no additional or amorphous phases were found at the ESB/YSZ interface. The formation of an ESB layer at the interface would act as a barrier layer, preventing the direct contact and subsequent reactions between the segregated SrO and YSZ electrolyte. This explains the high performance and stability of the ESB-LSCFNb cells tested at 750 ^{o}C and 250 mAcm^{-2} for 100 hrs (Figure 7.2).

In order to confirm the *in situ* formation of ESB interlayer on YSZ electrolyte induced under the influence of cathodic polarization, an anode supported cell with directly assembled ESB-LSCFNb electrode was prepared. Figure 7.6 presents the HAADF micrograph and STEM-EDS element mapping results for the cathode/electrolyte interface of the as-prepared ESB-LSCFNb cell after dwell at 750 ^{o}C for 100 hrs with no polarization. LSCFNb particles were identified with size of 129 ± 72 nm. ESB phase was characterized by fine and needle-like particles, probably due to dwell at 750 ^{o}C for 100 hrs, and uniformly distributed between LSCFNb particles, similar to the as-synthesized ESB-LSCFNb composite powder (Figure 7.1c). No specific accumulation or diffusion of bismuth toward the YSZ electrolyte surface was observed. This evidently indicates that the re-distribution and migration of ESB phase toward YSZ electrolyte does not occur at 750 ^{o}C under open circuit conditions. This in turn demonstrates that decorated ESB phase comes out of the ESB-LSCFNb composite and is driven to the YSZ electrolyte under the influence of cathodic polarization conditions, forming a bismuth interlayer at the LSCFNb cathode/YSZ electrolyte interface region (see Figure 7.5).

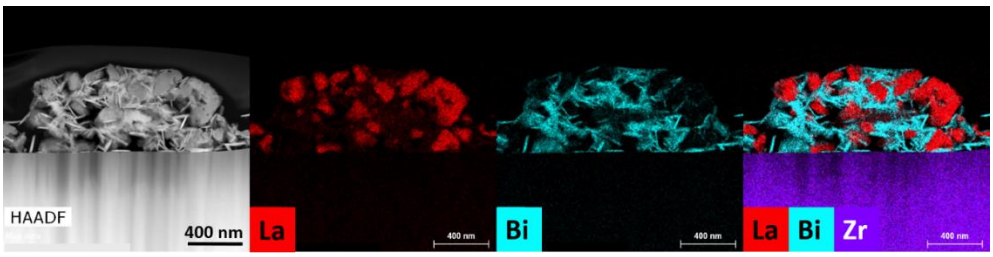

Figure 7.6 STEM-EDS element mapping of the ESB-LSCFNb/YSZ interface of an anode supported YSZ electrolyte cell with a directly assembled ESB-LSCFNb electrode after dwell at 750 ^{o}C for 100 hrs without polarization.

7.3.5. Effects of polarization on Sr segregation and ESB-LSCFNb/YSZ interface formation

The results of the present study clearly demonstrate the influence of cathodic polarization on the Sr segregation and electrode/electrolyte interface formation for LSCFNb/YSZ and ESB-LSCFNb/YSZ cells. In the case of LSCFNb/YSZ cell, a significant Sr segregation and diffusion was observed on the electrolyte surface, leading to the formation of ring-shaped contact craters on the electrolyte surface. The segregated SrO is highly mobile [5, 71, 72] and reacts with YSZ, forming a thick layer of $SrZrO_3$, similar to that observed in LSCF/YSZ cell.[62] This in turn indicates that the direct contact between segregated SrO and YSZ accelerates the Sr segregation despite the Nb doping at the B-site of LSCF.

In the case of ESB-LSCFNb/YSZ cell, ESB decoration significantly improves the electrocatalytic activity and stability of the LSCFNb cathode. The anode supported YSZ electrolyte cell with ESB-LSCFNb cathode exhibits a much higher PPD (1.32 W cm^{-2}) than that of LSCFNb cell (0.53 W cm^{-2}) at 750^oC. In contrast to the LSCFNb cell, the YSZ surface in contact with ESB-LSCFNb electrode is very stable. The stable interface is clearly due to the redistribution and diffusion of the ESB phase, forming a bismuth oxide layer at the cathode/electrolyte interface under the influence of cathodic polarization, as shown in Figure 7.5. The migration of bismuth oxide phase was also reported by others.[73, 74] Lee *et al*.[73] prepared the ESB-LSM composite cathode by a conjugated reverse-strike co-precipitation and glycine-nitrate combustion method and observed the formation of a continuous nano-scale ESB layer (~50 nm) at the electrode/YSZ electrolyte interface after polarization test. The formation of thin ESB layer was attributed to its high wettability and mobility due to the low melting temperature of bismuth oxide (~827^oC). Fan *et al*.[74] also observed a dense Bi_2O_3-LSCF film at the electrode/electrolyte interface on 1 mol% Bi_2O_3-LSCF composite electrode after polarization and proposed that the addition of Bi_2O_3 into LSCF promoted the formation of eutectic liquid, which flows down to the electrolyte surface to form a dense layer. In the present study, the HAADF and STEM-EDS element mapping of the cathode/electrolyte interface of anode supported YSZ electrolyte cells with ESB-LSCFNb cathodes before and after polarization evidently demonstrates that ESB is separated from the mixed ESB-LSCFNb phase and migrates to the electrolyte surface, forming an interlayer at the electrode/YSZ electrolyte interface. The formed

interlayer is irregular in shape and much thicker than that observed by Lee et al on ESB/LSM cathode/YSZ electrolyte interface.[73] This indicates the high mobility of the decorated ESB phase under the SOFC operating conditions. The possible formation of eutectic phase with LSCFNb can be ruled out as no LSCFNb elements were observed in the ESB layer at the interface (see Figure 7.5a). The presence of the highly oxygen ionic conducting ESB layer at the interface not only improves the electrocatalytic activity of the LSCFNb cathode, but also promotes the rapid ion migration at the electrode/electrolyte interface.[44, 73] The *in situ* formed ESB layer acts as a barrier layer to prevent the reaction between the segregated SrO and YSZ, inhibiting the formation of $SrZrO_3$ at the cathode/electrolyte interface and thus preventing the further segregation of Sr (Figure 7.5a). Figure 7.7 shows the schematic diagram of the fabrication of ESB-LSCFNb electrode via decoration method and the *in situ* formation of ESB layer at the cathode/electrolyte interface region under the influence of cathodic polarization.

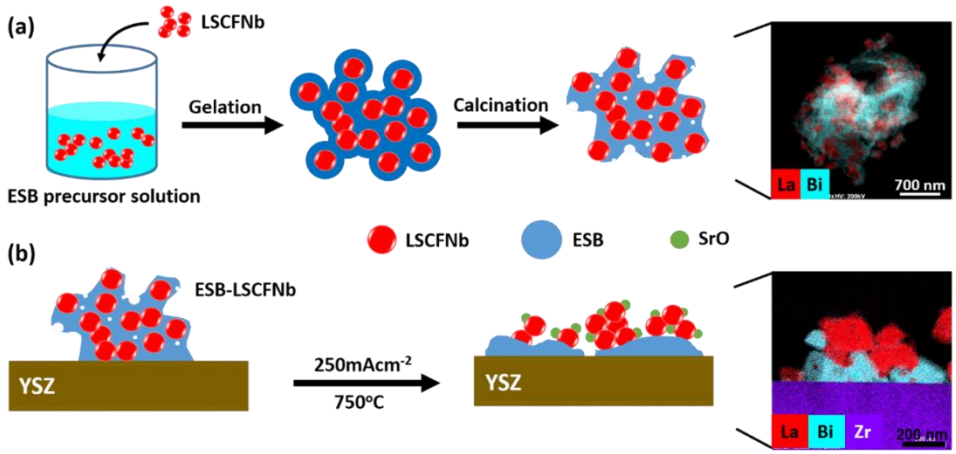

Figure 7.7 Schematic diagram of (a) the synthesis of ESB-LSCFNb composite cathode by decoration method and (b) the ESB-LSCFNb/YSZ interface formation under the influence of cathodic polarization at 750°C.

In general, direct addition of ESB interlayer between electrolyte and cathode would require high temperature sintering to form the strong adhesion between the ESB interface and electrolyte before the application of the cathode. However, due to the low decomposition temperature, pre-sintering of ESB interlayer may not be feasible. As shown in this study, ESB functional layer is formed *in situ* under the influence of polarization at operation temperatures of 750°C, which is below the decomposition temperature of bismuth oxide. The *in situ* formation of the ESB functional layer occurs

under normal operation conditions and does not require additional cell fabrication procedures. This also greatly simplifies the manufacturing process and thus reduces the cost of SOFCs.

7.4 Conclusions

The ESB decorated LSCFNb nanostructured cathode powder was successfully fabricated in the present study and the influence of ESB decoration on the electrochemical performance, electrode/electrolyte interface formation and Sr segregation of the LSCFNb/YSZ cell was investigated in detail via combined FIB-STEM technique. The results show evidently that the cell with the directly assembled ESB-LSCFNb electrode exhibits a much higher peak power density, 1.32 W cm^{-2} at 750 ^{o}C as compared to the 0.53 W cm^{-2} for the cell with LSCFNb electrode. The ESB-LSCFNb/YSZ cell also shows excellent stability under the cathodic polarization at 750 ^{o}C and 250 mA cm^{-2} for 100 hrs. In the case of the directly assembled LSCFNb/YSZ cell, there is significant reaction between the segregated SrO and YSZ electrolyte, forming a thick $SrZrO_3$ layer between LSCFNb electrode and YSZ electrolyte and characterized by the formation of ring-shaped convex craters on the electrolyte surface. On the other hand, in the ESB-LSCFNb/YSZ cell, the decorated nano-scaled ESB comes out of the ESB-LSCFNb composite and deposits at the cathode/electrolyte interface. The fundamental reason for its high wettability and mobility is most likely due to the low melting temperature of bismuth oxide (~827^{o}C).

The *in situ* formed ESB layer functions as barrier layer to prevent the direct contact and interaction between the segregated SrO and YSZ and promotes the ORR of the LSCFNb electrode. The significantly reduced activation energy for the ORR on ESB-LSCFNb cathode implies that ESB decoration is most effective for the enhancement of the electrocatalytic activity at reduced temperatures. The present study clearly demonstrates the dynamic relationship between interface, segregation, and performance of bismuth oxide decorated electrode materials for fuel cells. The *in situ* formation of highly active and functional ESB interlayer demonstrated the promising potential of the approach for the development in intermediate temperature SOFCs.

7.5 References

[1] T.M. Gür, Comprehensive review of methane conversion in solid oxide fuel cells: Prospects for efficient electricity generation from natural gas, Progress in Energy and Combustion Science, 54 (2016) 1-64.

[2] A. Choudhury, H. Chandra, A. Arora, Application of solid oxide fuel cell technology for power generation—A review, Renewable and Sustainable Energy Reviews, 20 (2013) 430-442.

[3] S. Wang, S.P. Jiang, Prospects of Fuel Cell Technologies, National Science Review, 4 (2017) 163-166.

[4] E.D. Wachsman, K.T. Lee, Lowering the Temperature of Solid Oxide Fuel Cells, Science, 334 (2011) 935-939.

[5] R. Kiebach, W.-W. Zhang, W. Zhang, M. Chen, K. Norrman, H.-J. Wang, J.R. Bowen, R. Barfod, P.V. Hendriksen, Stability of La0.6Sr0.4Co0.2Fe0.8O3/Ce0.9Gd0.1O2 cathodes during sintering and solid oxide fuel cell operation, Journal of Power Sources, 283 (2015) 151-161.

[6] S.P. Jiang, Sintering behavior of Ni/Y2O3-ZrO2 cermet electrodes of solid oxide fuel cells, J. Mater. Sci., 38 (2003) 3775-3782.

[7] S.P. Jiang, S.H. Chan, A review of anode materials development in solid oxide fuel cells, J. Mater. Sci., 39 (2004) 4405-4439.

[8] Y.L. Liu, A. Hagen, R. Barfod, M. Chen, H.J. Wang, F.W. Poulsen, P.V. Hendriksen, Microstructural studies on degradation of interface between LSM–YSZ cathode and YSZ electrolyte in SOFCs, Solid State Ionics, 180 (2009) 1298-1304.

[9] S.P. Jiang, J.P. Zhang, K. Foger, Chemical interactions between 3 mol% yttria-zirconia and Sr-doped lanthanum manganite, J. Eur. Ceram. Soc., 23 (2003) 1865-1873.

[10] S.P. Jiang, X.B. Chen, Chromium deposition and poisoning of cathodes of solid oxide fuel cells - A review, Int. J. Hydrog. Energy, 39 (2014) 505-531.

[11] J.C. De Vero, K. Develos-Bagarinao, S.S. Liu, H. Kishimoto, T. Ishiyama, K. Yamaji, T. Horita, H. Yokokawa, Sulfur poisoning behavior of La1-xSrxCo1-yFeyO3-delta thin films with different compositions, J. Alloy. Compd., 748 (2018) 608-619.

[12] H.Y. Lee, S.M. Oh, Origin of cathodic degradation and new phase formation at the La0.9Sr0.1MnO3/YSZ interface, Solid State Ionics, 90 (1996) 133-140.

[13] A. Mitterdorfer, L.J. Gauckler, La2Zr2O7 formation and oxygen reduction kinetics of the La0.85Sr0.15MnyO3, O2(g)|YSZ system, Solid State Ionics, 111 (1998) 185-218.
[14] H. Yokokawa, Understanding materials compatibility, Ann. Rev. Mater. Res., 33 (2003) 581-610.
[15] N.H. Menzler, F. Tietz, S. Uhlenbruck, H.P. Buchkremer, D. Stover, Materials and manufacturing technologies for solid oxide fuel cells, J. Mater. Sci., 45 (2010) 3109-3135.
[16] D.J.L. Brett, A. Atkinson, N.P. Brandon, S.J. Skinner, Intermediate temperature solid oxide fuel cells, Chem. Soc. Rev., 37 (2008) 1568-1578.
[17] S.B. Adler, Factors governing oxygen reduction in solid oxide fuel cell cathodes, Chem. Rev., 104 (2004) 4791-4843.
[18] A. Mineshige, J. Izutsu, M. Nakamura, K. Nigaki, J. Abe, M. Kobune, S. Fujii, T. Yazawa, Introduction of A-site deficiency into La0.6Sr0.4Co0.2Fe0.8O3–δ and its effect on structure and conductivity, Solid State Ionics, 176 (2005) 1145-1149.
[19] S. Carter, A. Selcuk, R.J. Chater, J. Kajda, J.A. Kilner, a.B.C.H. Steele, Oxygen transport in selected nonstoichiometric perovskite-structure oxides, Solid State Ionics, 53-56 (1992) 597-605.
[20] Y. Teraoka, T. Nobunaga, K. Okamoto, N. Miura, N. Yamazoe, Influence of constituent metal cations in substituted LaCoO3 on mixed conductivity and oxygen permeability, Solid State Ionics, 48 (1991) 207-212.
[21] E. Perry Murray, Electrochemical performance of (La,Sr)(Co,Fe)O3–(Ce,Gd)O3 composite cathodes, Solid State Ionics, 148 (2002) 27-34.
[22] M.A. Haider, S. McIntosh, The Influence of Grain Size on La0.6Sr0.4Co0.2Fe0.8O3-δ Thin Film Electrode Impedance, Journal of The Electrochemical Society, 158 (2011) B1128-B1136.
[23] C. Sun, R. Hui, J. Roller, Cathode materials for solid oxide fuel cells: a review, Journal of Solid State Electrochemistry, 14 (2009) 1125-1144.
[24] N.A. Baharuddin, H.A. Rahman, A. Muchtar, A.B. Sulong, H. Abdullah, Development of lanthanum strontium cobalt ferrite composite cathodes for intermediate- to low-temperature solid oxide fuel cells, Journal of Zhejiang University SCIENCE A, 14 (2013) 11-24.

[25] E. Bucher, W. Sitte, Long-term stability of the oxygen exchange properties of (La,Sr)1−z(Co,Fe)O3−δ in dry and wet atmospheres, Solid State Ionics, 192 (2011) 480-482.

[26] A. Esquirol, N.P. Brandon, J.A. Kilner, M. Mogensen, Electrochemical characterization of La0.6Sr0.4Co0.2Fe0.8O3 cathodes for intermediate-temperature SOFCs, J. Electrochem. Soc., 151 (2004) A1847-A1855.

[27] J. Chen, F.L. Liang, B. Chi, J. Pu, S.P. Jiang, L. Jian, Palladium and ceria infiltrated La0.8Sr0.2Co0.5Fe0.5O3-delta cathodes of solid oxide fuel cells, J. Power Sources, 194 (2009) 275-280.

[28] S.P. Jiang, A comparison of O-2 reduction reactions on porous (La,Sr)MnO3 and (La,Sr)(Co,Fe)O-3 electrodes, Solid State Ionics, 146 (2002) 1-22.

[29] C.-Y. Yoo, B.A. Boukamp, H.J.M. Bouwmeester, Oxygen surface exchange kinetics of erbia-stabilized bismuth oxide, Journal of Solid State Electrochemistry, 15 (2010) 231-236.

[30] N. M. Sammes, G. A. Tompsett, H. Nafe, F. Aldinger, Bismuth Based Oxide Electrolytes - Structure and Ionic Conductivity, Journal of European Ceramic Society, 19 (1999) 1801-1826.

[31] D.W. Jung, K.L. Duncan, E.D. Wachsman, Effect of total dopant concentration and dopant ratio on conductivity of (DyO1.5)(x)-(WO3)(y)-(BiO1.5)1-x-y, Acta Mater., 58 (2010) 355-363.

[32] D.W. Jung, J.C. Nino, K.L. Duncan, S.R. Bishop, E.D. Wachsman, Enhanced long-term stability of bismuth oxide-based electrolytes for operation at 500 A degrees C, Ionics, 16 (2010) 97-103.

[33] D.W. Joh, J.H. Park, D. Kim, E.D. Wachsman, K.T. Lee, Functionally Graded Bismuth Oxide/Zirconia Bilayer Electrolytes for High-Performance Intermediate-Temperature Solid Oxide Fuel Cells (IT-SOFCs), ACS Appl Mater Interfaces, 9 (2017) 8443-8449.

[34] J.S. Ahn, M.A. Camaratta, D. Pergolesi, K.T. Lee, H. Yoon, B.W. Lee, D.W. Jung, E. Traversa, E.D. Wachsman, Development of High Performance Ceria/Bismuth Oxide Bilayered Electrolyte SOFCs for Lower Temperature Operation, Journal of The Electrochemical Society, 157 (2010) B376-B382.

[35] A.S. Painter, Y.-L. Huang, E.D. Wachsman, Durability of (La 0.8 Sr 0.2) 0.95 MnO 3-δ -(Er 0.2 Bi 0.8) 2 O 3 composite cathodes for low temperature SOFCs, Journal of Power Sources, 360 (2017) 391-398.

[36] Z.Y. Jiang, Z.W. Lei, B. Ding, C.R. Xia, F. Zhao, F.L. Chen, Electrochemical characteristics of solid oxide fuel cell cathodes prepared by infiltrating (La,Sr)MnO3 nanoparticles into yttria-stabilized bismuth oxide backbones, Int. J. Hydrog. Energy, 35 (2010) 8322-8330.
[37] J. Hou, L. Bi, J. Qian, Z. Gong, Z. Zhu, W. Liu, A novel composite cathode Er 0.4 Bi 1.6 O 3 –Pr 0.5 Ba 0.5 MnO 3−δ for ceria-bismuth bilayer electrolyte high performance low temperature solid oxide fuel cells, Journal of Power Sources, 301 (2016) 306-311.
[38] S. Huang, G. Zhou, Y. Xie, Electrochemical performances of Ag–(Bi2O3)0.75(Y2O3)0.25 composite cathodes, Journal of Alloys and Compounds, 464 (2008) 322-326.
[39] M. Camaratta, a.E.D. Wachsman, Ag-Bi1. 6Er0. 4O3 as a Potential Cathode Material for IT-SOFCs, ECS Transactions, 1 (2006) 279-292.
[40] A. Jaiswal, C.T. Hu, E.D. Wachsman, Bismuth ruthenate-stabilized bismuth oxide composite cathodes for IT-SOFC, J. Electrochem. Soc., 154 (2007) B1088-B1094.
[41] K.T. Lee, D.W. Jung, H.S. Yoon, A.A. Lidie, M.A. Camaratta, E.D. Wachsman, Interfacial modification of La0.80Sr0.20MnO3−δ–Er0.4Bi0.6O3 cathodes for high performance lower temperature solid oxide fuel cells, Journal of Power Sources, 220 (2012) 324-330.
[42] V. Kharton, E. Naumovich, V. Samokhval, Formation and properties of reaction layers of cobaltite electrodes on bismuth oxide electrolytes, Solid State Ionics, 99 (1997) 269-280.
[43] G. Li, B. He, Y. Ling, J. Xu, L. Zhao, Highly active YSB infiltrated LSCF cathode for proton conducting solid oxide fuel cells, International Journal of Hydrogen Energy, 40 (2015) 13576-13582.
[44] N. Ai, N. Li, S. He, Y. Cheng, M. Saunders, K. Chen, T. Zhang, S.P. Jiang, Highly active and stable Er0.4Bi1.6O3 decorated La0.76Sr0.19MnO3+δ nanostructured oxygen electrodes for reversible solid oxide cells, J. Mater. Chem. A, 5 (2017) 12149-12157.
[45] N. Ai, M. Chen, S. He, K. Chen, T. Zhang, S.P. Jiang, High performance nanostructured bismuth oxide–cobaltite as a durable oxygen electrode for reversible solid oxide cells, Journal of Materials Chemistry A, 6 (2018) 6510-6520.

[46] J. Li, S. Wang, X. Sun, R. Liu, X. Ye, Z. Wen, Improvement of (La0.74Bi0.10Sr0.16)MnO3–Bi1.4Er0.6O3 composite cathodes for intermediate-temperature solid oxide fuel cells, Journal of Power Sources, 185 (2008) 649-655.
[47] S.P. Jiang, Nanoscale and nano-structured electrodes of solid oxide fuel cells by infiltration: Advances and challenges, Int. J. Hydrog. Energy, 37 (2012) 449-470.
[48] S.P. Jiang, Y.Y. Duan, J.G. Love, Fabrication of high-performance NiOY2O3-ZrO2 cermet anodes of solid oxide fuel cells by ion impregnation, J. Electrochem. Soc., 149 (2002) A1175-A1183.
[49] X.B. Chen, S.P. Jiang, Highly active and stable (La0.24Sr0.16Ba0.6)(Co0.5Fe0.44Nb0.06)O3-delta (LSBCFN) cathodes for solid oxide fuel cells prepared by a novel mixing synthesis method, Journal of Materials Chemistry A, 1 (2013) 4871-4878.
[50] K.F. Chen, S. He, N. Li, Y. Cheng, N. Ai, M.L. Chen, W.D.A. Rickard, T. Zhang, S.P. Jiang, Nb and Pd co-doped La0.57Sr0.38Co0.19Fe0.665Nb0.095Pd0.05O3-delta as a stable, high performance electrode for barrier-layer-free Y2O3-ZrO2 electrolyte of solid oxide fuel cells, J. Power Sources, 378 (2018) 433-442.
[51] Y.D. Zhen, S.P. Jiang, Transition behavior for O-2 reduction reaction on (La,Sr)MnO3/YSZ composite cathodes of solid oxide fuel cells, J. Electrochem. Soc., 153 (2006) A2245-A2254.
[52] K. Chen, X. Chen, Z. Lü, N. Ai, X. Huang, W. Su, Performance of an anode-supported SOFC with anode functional layers, Electrochimica Acta, 53 (2008) 7825-7830.
[53] S.P. Jiang, Placement of Reference Electrode, Electrolyte Thickness and Three-Electrode Cell Configuration in Solid Oxide Fuel Cells: A Brief Review and Update on Experimental Approach, J. Electrochem. Soc., 164 (2017) F834-F844.
[54] N. Li, N. Ai, K. Chen, Y. Cheng, S. He, M. Saunders, A. Dodd, A. Suvorova, S.P. Jiang, In situ assembled La0.8Sr0.2MnO3 cathodes on a Y2O3–ZrO2 electrolyte of solid oxide fuel cells – interface and electrochemical activity, RSC Adv., 6 (2016) 99211-99219.
[55] S. Hasegawa, T. Sugimoto, T. Hashimoto, Investigation of structural phase transition behavior of SrZrO3 by thermal analyses and high-temperature X-ray diffraction, Solid State Ionics, 181 (2010) 1091-1097.
[56] T. Matsuda, S. Yamanaka, K. Kurosaki, S. Kobayashi, High temperature phase transitions of SrZrO3, J. Alloy. Compd., 351 (2003) 43-46.

[57] A. Mai, M. Becker, W. Assenmacher, F. Tietz, D. Hathiramani, E. Iverstiffee, D. Stover, W. Mader, Time-dependent performance of mixed-conducting SOFC cathodes, Solid State Ionics, 177 (2006) 1965-1968.

[58] K. Chen, N. Li, N. Ai, Y. Cheng, W.D. Rickard, S.P. Jiang, Polarization-Induced Interface and Sr Segregation of in Situ Assembled La0.6Sr0.4Co0.2Fe0.8O3-delta Electrodes on Y2O3-ZrO2 Electrolyte of Solid Oxide Fuel Cells, ACS Appl Mater Interfaces, 8 (2016) 31729-31737.

[59] S.M. Fang, C.Y. Yoo, H.J.M. Bouwmeester, Performance and stability of niobium-substituted Ba0.5Sr0.5Co0.8Fe0.2O3-delta membranes, Solid State Ionics, 195 (2011) 1-6.

[60] G. Vovk, X. Chen, C.A. Mims, In situ XPS studies of perovskite oxide surfaces under electrochemical polarization, J Phys Chem B, 109 (2005) 2445-2454.

[61] E. Mutoro, E.J. Crumlin, H. Pöpke, B. Luerssen, M. Amati, M.K. Abyaneh, M.D. Biegalski, H.M. Christen, L. Gregoratti, J. Janek, Y. Shao-Horn, Reversible Compositional Control of Oxide Surfaces by Electrochemical Potentials, The Journal of Physical Chemistry Letters, 3 (2012) 40-44.

[62] S. He, M. Saunders, K. Chen, H. Gao, A. Suvorova, W.D.A. Rickard, Z. Quadir, C.Q. Cui, S.P. Jiang, A FIB-STEM Study of Strontium Segregation and Interface Formation of Directly Assembled La0.6Sr0.4Co0.2Fe0.8O3-δ Cathode on Y2O3-ZrO2 Electrolyte of Solid Oxide Fuel Cells, J. Electrochem. Soc., 165 (2018) F417-F429.

[63] H. Yung, L. Jian, S.P. Jiang, Polarization Promoted Chemical Reaction between Ba0.5Sr0.5Co0.8Fe0.2O3- Cathode and Ceria Based Electrolytes of Solid Oxide Fuel Cells, Journal of the Electrochemical Society, 159 (2012) F794-F798.

[64] C.M. Wang, S. Azad, V. Shutthanandan, D.E. McCready, C.H.F. Peden, L. Saraf, S. Thevuthasan, Microstructure of ZrO2–CeO2 hetero-multi-layer films grown on YSZ substrate, Acta Materialia, 53 (2005) 1921-1929.

[65] F. Ernst, P. Pirouz, A.H. Heuer, HRTEM study of a Cu/Al2O3interface, Philosophical Magazine A, 63 (1991) 259-277.

[66] A. Trampert, F. Ernst, C.P. Flynn, H.F. Fischmeister, M. Ru¨hle, High resolution transmission electron microscopy studies of the Ag/MgO interface, Acta Metallurgica et Materialia, 40 (1992) S227-S236.

[67] O.I. Lebedev, G.V. Tendeloo, S. Amelinckx, H.L. Ju, K.M. Krishnan, High-resolution electron microscopy study of strained epitaxial La0.7Sr0.3MnO3thin films, Philosophical Magazine A, 80 (2000) 673-691.
[68] L. Zhao, Y. Cheng, S.P. Jiang, A new, high electrochemical activity and chromium tolerant cathode for solid oxide fuel cells, Int. J. Hydrog. Energy, 40 (2015) 15622-15631.
[69] C.C. Appel, Zirconia stabilized by Y and Mn: A microstructural characterization, Ionics, 1 (1995) 406-413.
[70] N. Jiang, E.D. Wachsman, Structural Stability and Conductivity of Phase-Stabilized Cubic Bismuth Oxides, Journal of the American Ceramic Society, 82 (2004) 3057-3064.
[71] F. Wang, M.E. Brito, K. Yamaji, D.-H. Cho, M. Nishi, H. Kishimoto, T. Horita, H. Yokokawa, Effect of polarization on Sr and Zr diffusion behavior in LSCF/GDC/YSZ system, Solid State Ionics, 262 (2014) 454-459.
[72] F. Wang, M. Nishi, M.E. Brito, H. Kishimoto, K. Yamaji, H. Yokokawa, T. Horita, Sr and Zr diffusion in LSCF/10GDC/8YSZ triplets for solid oxide fuel cells (SOFCs), Journal of Power Sources, 258 (2014) 281-289.
[73] K.T. Lee, A.A. Lidie, H.S. Yoon, E.D. Wachsman, Rational Design of Lower-Temperature Solid Oxide Fuel Cell Cathodes via Nanotailoring of Co-Assembled Composite Structures, Angew. Chem.-Int. Edit., 53 (2014) 13463-13467.
[74] B. Fan, J. Yan, W. Shi, A high performance solid oxide fuel cells operating at intermediate temperature with a modified interface between cathode and electrolyte, Journal of the European Ceramic Society, 30 (2010) 1803-1808.

Chapter 8: Conclusions and Recommendations

8.1 Conclusions

Solid oxide fuel cells (SOFCs) are considered one of the most promising technologies to tackle the energy crisis in the not far future. SOFCs stand out due to its high energy conversion efficiency, low pollutant emission, excellent fuel flexibility and minimal requirement for precious metal catalysts. However, the durability and degradation of SOFC devices are some of the most concerned issues that limit their further application and development. The degradation and failure of a cell normally originate from the change in the electrochemically active region at the electrode/electrolyte interface, extending a few microns into the electrode bulk, and thus it is critical to understand the fundamental mechanism that governs the evolution of the interface during the cell operation. In this thesis, by using the state-of-the-art characterisation techniques, the conventional high temperature pre-sintered electrode/electrolyte interface was investigated regarding its microstructure, composition and crystallography, and as a comparison, the polarisation induced interface and its evolution were also studied. A general idea was presented to better understand the degrading interface under the influence of polarisation. The concept of polarisation induced electrode/electrolyte interface was further applied to an anode supported cell, with excellent electrochemical performance and stability achieved. According to these studies, the following conclusions can be drawn.

8.1.1 A FIB-STEM Study of $La_{0.8}Sr_{0.2}MnO_3$ Cathode and Y_2O_3-ZrO_2/Gd_2O_3-CeO_2 Electrolyte Interfaces of Solid Oxide Fuel Cells

- High temperature pre-sintered LSM/YSZ and LSM/GDC interfaces were studied in terms of their microstructure, composition and crystallography.
- In both cases, electrode/electrolyte interface is characterized by the formation of convex contact rings on the YSZ and GDC electrolyte surface. The negligible change in ohmic resistance (R_Ω) with polarization indicates the stable LSM/YSZ and LSM/GDC interfaces formed under high temperature sintering.

- In the case of LSM/YSZ interface, significant diffusion of Mn in the form of Mn^{2+} and in less extent La along the YSZ electrolyte surface and the edge of the convex contact rings was observed. No cation interdiffusion was observed for LSM/GDC system. The results indicate that cation interdiffusion is not an essential requirement for the interface formation in the LSM electrodes.
- Lattice disorientation and misfit dislocations of LSM electrode and YSZ or GDC electrolyte crystallographic planes occur to accommodate the lattice mismatch and surface energy at the interface. The results indicate that such disorientation at the heterointerface between LSM electrode and YSZ or GDC electrolyte would not impede the oxygen transport for the O_2 reduction reaction.

8.1.2 A FIB-STEM Study of Strontium Segregation and Interface Formation of Directly Assembled $La_{0.6}Sr_{0.4}Co_{0.2}Fe_{0.8}O_{3-\delta}$ Cathode on Y_2O_3-ZrO_2 Electrolyte of Solid Oxide Fuel Cells

- Directly assembled LSCF/YSZ interface was thoroughly studied as a function of cathodic polarisation time. The interface formation, Sr segregation and subsequent chemical reaction between segregated Sr and YSZ were investigated using FIB-STEM technique.
- The cathodic current passage induces the formation of clean electrode/electrolyte interface, free of voids and amorphous phases or solid solutions, leading to an increase of the electrochemical performance of the cell.
- Prolonged cathodic polarisation promotes the Sr segregation and diffusion to the interface, reacting with YSZ electrolyte and forming $SrZrO_3$ phase with significantly modified microstructure of the electrolyte surface. The chemical reaction between LSCF and YSZ at a low temperature of 750 ^oC is essentially induced by the segregated Sr under cathodic polarisation conditions.
- The phenomenon of polarisation promoted Sr segregation and subsequent reaction with YSZ electrolyte is comparable to that of the LSCF/YSZ interface after heat treatment at a higher temperature of 900 ^oC. Different from the thermodynamic interface chemistry which generally would occur at high

temperatures, the interface reaction under polarisation can occur at a much lower temperature and is kinetically induced by the segregated Sr.

8.1.3 Interface Formation and Mn Segregation of Directly Assembled $La_{0.8}Sr_{0.2}MnO_3$ Cathode on Y_2O_3-ZrO_2 and Gd_2O_3-CeO_2 Electrolytes of Solid Oxide Fuel Cells

- Directly assembled LSM/YSZ and LSM/GDC interfaces formation and Mn segregation were studied under the influence of cathodic polarization using combined FIB-STEM techniques.
- In the case of both LSM/YSZ and LSM/GDC cells, the cathodic current passage induces the formation of intimate electrode/electrolyte interface, with significant reduction in cell impedance observed.
- The change in YSZ electrolyte surface morphology is substantial, characterized by the disintegration of LSM at the interface and the formation of ring-shaped contact craters. Whereas the GDC electrolyte appears to be much more stable, with negligible change in surface microstructure.
- Mn segregation was observed for both LSM/YSZ and LSM/GDC cells under the effect of cathodic polarization, and the segregated MnO_x does not show preferential deposition at the interface. The Mn segregation shows negligible detrimental effect on the electrochemical activity of LSM electrode in the studied conditions.

8.1.4 In situ Formation of $Er_{0.4}Bi_{1.6}O_3$ Protective Layer at Cobaltite Cathode/Y_2O_3-ZrO_2 Electrolyte Interface under Solid Oxide Fuel Cells Operation Conditions

- The influence of ESB decoration on the electrochemical performance, electrode/electrolyte interface formation and Sr segregation of the anode supported LSCFNb/YSZ cell were studied in detail.
- The cell with directly assembled ESB-LSCFNb electrode shows a much higher peak power density, 1.32 W cm^{-2} at 750 ^oC as compared to the 0.53 W cm^{-2} for the cell with LSCFNb electrode. The ESB-LSCFNb/YSZ cell also exhibits excellent operation stability under the cathodic polarization.
- In the case of the LSCFNb/YSZ cell, there is significant reaction between the segregated SrO and YSZ electrolyte, forming a thick $SrZrO_3$ layer between LSCFNb electrode and YSZ electrolyte and characterized by the formation of ring-shaped convex craters on the electrolyte surface.

- For the ESB-LSCFNb/YSZ cell, the decorated nano-scaled ESB comes out of the composite electrode and deposits at the cathode/electrolyte interface under the influence of cathodic polarisation. The change in the electrolyte surface morphology is negligible after operation. The *in situ* formed ESB layer functions as barrier layer to prevent the direct contact and interaction between the segregated SrO and YSZ. The significantly reduced activation energy for the ORR on ESB-LSCFNb cathode indicates that ESB decoration is most effective for the enhancement of the electrocatalytic activity at reduced temperatures.

8.2 Recommendations

In this thesis, the thermally and electrochemically promoted cathode/electrolyte interfaces were investigated in detail using combined FIB-STEM technique. The evolution of electrode/electrolyte interface under the influence of cathodic polarization was examined and it implies that cathodic polarization can not only promote the formation of intimate interface, but also facilitate the element diffusion and chemical reactions in some cases. Despite the great effort put in these studies, further work is suggested to complete the entire picture of interface evolution, and to explore the feasibility of adopting direct assembly method to a wider range of electrode materials.

1. Although the pre-sintered LSM/YSZ and LSM/GDC interfaces were examined, it is of great interests to study their evolution under the influence of cathodic polarization, particularly from the microstructure, composition and crystallography points of view.
2. The evolution of directly assembled LSCF/YSZ interface was studied in this thesis. However, it is also worth investigating the evolution of directly assembled LSCF/GDC interface under the influence of cathodic polarization, since the segregation of SrO from LSCF electrode could be related to the nature of electrolyte materials.
3. The cathode/electrolyte interfaces studied in this thesis were all tested in SOFC mode, thus it is of interest to investigate the evolution of electrode/electrolyte interface in electrolysis (SOEC) mode.

4. The ESB migration under the influence of cathodic polarization has shown great potential in the development of stable and active intermediate temperature SOFCs (ITSOFCs). As shown in Chapter 7, the *in situ* formed ESB layer can prevent the reaction between segregated SrO and YSZ electrolyte, significantly improving the stability of the cell. Therefore, the ESB decoration method can be adopted to anode supported GDC electrolyte cell, in order to find out if the ESB migration is effective to block the electronic current leakage issue of GDC electrolyte.
5. The electrode/electrolyte interfaces examined in this thesis were all based on the oxygen electrode materials, therefore investigations on the hydrogen electrode/electrolyte interface can be equally important to better understand the fundamental failure mechanism of the SOFCs.

Appendix: Permission of Reproduction from the Copyright Owner

Copyright Clearance Center RightsLink®

Home | Account Info | Help

Title: In-situ study of operating SOFC LSM/YSZ cathodes under polarization by photoelectron microscopy

Author: M. Backhaus-Ricoult,K. Adib,T. St.Clair,B. Luerssen,L. Gregoratti,A. Barinov

Publication: Solid State Ionics

Publisher: Elsevier

Date: 15 September 2008

Logged in as:
Shuai He
Account #:
3001366142
LOGOUT

Order Completed

Thank you for your order.

This Agreement between Shuai He ("You") and Elsevier ("Elsevier") consists of your license details and the terms and conditions provided by Elsevier and Copyright Clearance Center.

Your confirmation email will contain your order number for future reference.

printable details

License Number	4470521015941
License date	Nov 15, 2018
Licensed Content Publisher	Elsevier
Licensed Content Publication	Solid State Ionics
Licensed Content Title	In-situ study of operating SOFC LSM/YSZ cathodes under polarization by photoelectron microscopy
Licensed Content Author	M. Backhaus-Ricoult,K. Adib,T. St.Clair,B. Luerssen,L. Gregoratti,A. Barinov
Licensed Content Date	Sep 15, 2008
Licensed Content Volume	179
Licensed Content Issue	21-26
Licensed Content Pages	5
Type of Use	reuse in a thesis/dissertation
Portion	figures/tables/illustrations
Number of figures/tables/illustrations	1
Format	both print and electronic
Are you the author of this Elsevier article?	No
Will you be translating?	No
Original figure numbers	Figure 6
Title of your thesis/dissertation	Thermally and Electrochemically Induced Cathode/Electrolyte Interfaces in Solid Oxide Fuel Cells
Expected completion date	Dec 2018
Estimated size (number of pages)	205
Requestor Location	Shuai He Building 614 5 De Laeter Way Bentley, W.A. 6102 Australia Attn: Shuai He
Publisher Tax ID	GB 494 6272 12
Total	0.00 AUD

ORDER MORE | CLOSE WINDOW

Order Completed

Thank you for your order.

This Agreement between Shuai He ("You") and Elsevier ("Elsevier") consists of your license details and the terms and conditions provided by Elsevier and Copyright Clearance Center.

Your confirmation email will contain your order number for future reference.

printable details

License Number	4467961091793
License date	Nov 14, 2018
Licensed Content Publisher	Elsevier
Licensed Content Publication	Solid State Ionics
Licensed Content Title	Microstructures and oxygen diffusion at the LaMnO3 film/yttria-stabilized zirconia interface
Licensed Content Author	Teruhisa Horita,Tatsuro Tsunoda,Katsuhiko Yamaji,Natsuko Sakai,Tohru Kato,Harumi Yokokawa
Licensed Content Date	Dec 1, 2002
Licensed Content Volume	152
Licensed Content Issue	n/a
Licensed Content Pages	8
Type of Use	reuse in a thesis/dissertation
Portion	figures/tables/illustrations
Number of figures/tables/illustrations	2
Format	both print and electronic
Are you the author of this Elsevier article?	No
Will you be translating?	No
Original figure numbers	Figure 2a, Figure 6
Title of your thesis/dissertation	Thermally and Electrochemically Induced Cathode/Electrolyte Interfaces in Solid Oxide Fuel Cells
Expected completion date	Dec 2018
Estimated size (number of pages)	205
Requestor Location	Shuai He Building 614 5 De Laeter Way Bentley, W.A. 6102 Australia Attn: Shuai He
Publisher Tax ID	GB 494 6272 12
Total	0.00 AUD

ORDER MORE | CLOSE WINDOW

Order Completed

Thank you for your order.

This Agreement between Shuai He ("You") and Elsevier ("Elsevier") consists of your license details and the terms and conditions provided by Elsevier and Copyright Clearance Center.

Your confirmation email will contain your order number for future reference.

printable details

License Number	4467970493219
License date	Nov 14, 2018
Licensed Content Publisher	Elsevier
Licensed Content Publication	Solid State Ionics
Licensed Content Title	La2Zr2O7 formation and oxygen reduction kinetics of the La0.85Sr0.15Mn y O3, O2(g)|YSZ system
Licensed Content Author	A. Mitterdorfer,L.J. Gauckler
Licensed Content Date	Sep 1, 1998
Licensed Content Volume	111
Licensed Content Issue	3-4
Licensed Content Pages	34
Type of Use	reuse in a thesis/dissertation
Portion	figures/tables/illustrations
Number of figures/tables/illustrations	2
Format	both print and electronic
Are you the author of this Elsevier article?	No
Will you be translating?	No
Original figure numbers	Figure 10a, Figure 13
Title of your thesis/dissertation	Thermally and Electrochemically Induced Cathode/Electrolyte Interfaces in Solid Oxide Fuel Cells
Expected completion date	Dec 2018
Estimated size (number of pages)	205
Requestor Location	Shuai He Building 614 5 De Laeter Way Bentley, W.A. 6102 Australia Attn: Shuai He
Publisher Tax ID	GB 494 6272 12
Total	0.00 USD

ORDER MORE | CLOSE WINDOW

Copyright Clearance Center

Print this page

Confirmation Number: 11765245
Order Date: 11/14/2018

Customer Information

Customer: Shuai He
Account Number: 3001366142
Organization: Shuai He
Email: imheshuai508@gmail.com
Phone: +61 (4)20460509
Payment Method: Invoice

This is not an invoice

Order Details

Electrochemical and solid-state letters

Billing Status: **N/A**

Order detail ID:	71662915
ISSN:	1099-0062
Publication Type:	Journal
Volume:	
Issue:	
Start page:	
Publisher:	ELECTROCHEMICAL SOCIETY, INC.
Author/Editor:	Institute of Electrical and Electronics Engineers ; Electrochemical Society

Permission Status: Granted

Permission type: Republish or display content
Type of use: Republish in a thesis/dissertation
Order License Id: 4467971462816

Requestor type	Academic institution
Format	Print, Electronic
Portion	chart/graph/table/figure
Number of charts/graphs/tables/figures	1
The requesting person/organization	Shuai He/Curtin University
Title or numeric reference of the portion(s)	Figure 4
Title of the article or chapter the portion is from	Effect of Polarization on the Interface Between (La,Sr)MnO3 Electrode and Y2O3-ZrO2 Electrolyte
Editor of portion(s)	N/A
Author of portion(s)	S. P. Jiang, W. Wang
Volume of serial or monograph	8
Page range of portion	A115-A118
Publication date of portion	2005
Rights for	Main product
Duration of use	Life of current edition
Creation of copies for the disabled	no
With minor editing privileges	no
For distribution to	Worldwide
In the following language(s)	Original language of publication
With incidental promotional use	no
Lifetime unit quantity of new product	Up to 499
Title	Thermally and Electrochemically Induced Cathode/Electrolyte Interfaces in Solid Oxide Fuel Cells
Institution name	n/a
Expected presentation date	Dec 2018

Note: This item was invoiced separately through our **RightsLink service.** More info **$ 0.00**

Total order items: 1 **Order Total: $0.00**

Clearance Center

Print this page

Confirmation Number: 11765246
Order Date: 11/14/2018

Customer Information

Customer: Shuai He
Account Number: 3001366142
Organization: Shuai He
Email: imheshuai508@gmail.com
Phone: +61 (4)20460509
Payment Method: Invoice

This is not an invoice

Order Details

Journal of the Electrochemical Society

Billing Status: **N/A**

Order detail ID:	71662916
ISSN:	1945-7111
Publication Type:	e-Journal
Volume:	
Issue:	
Start page:	
Publisher:	Electrochemical Society
Author/Editor:	Electrochemical Society

Permission Status: Granted
Permission type: Republish or display content
Type of use: Republish in a thesis/dissertation
Order License Id: 4467990148232

Requestor type	Academic institution
Format	Print, Electronic
Portion	chart/graph/table/figure
Number of charts/graphs/tables/figures	1
The requesting person/organization	Shuai He/Curtin University
Title or numeric reference of the portion(s)	Figure 3
Title of the article or chapter the portion is from	Polarization Promoted Chemical Reaction between Ba0.5Sr0.5Co0.8Fe0.2O3-Cathode and Ceria Based Electrolytes of Solid Oxide Fuel Cells
Editor of portion(s)	N/A
Author of portion(s)	H. Yung, L. Jian, S.P. Jiang
Volume of serial or monograph	159
Page range of portion	F794-F798
Publication date of portion	2012
Rights for	Main product
Duration of use	Life of current edition
Creation of copies for the disabled	no
With minor editing privileges	no
For distribution to	Worldwide
In the following language(s)	Original language of publication
With incidental promotional use	no
Lifetime unit quantity of new product	Up to 499
Title	Thermally and Electrochemically Induced Cathode/Electrolyte Interfaces in Solid Oxide Fuel Cells
Institution name	n/a
Expected presentation date	Dec 2018

Note: This item was invoiced separately through our **RightsLink service.** More info

$ 0.00

Journal of the Electrochemical Society

Billing Status: **N/A**

Order detail ID:	71662917
ISSN:	0013-4651
Publication Type:	Journal
Volume:	
Issue:	
Start page:	
Publisher:	ELECTROCHEMICAL SOCIETY,
Author/Editor:	ELECTROCHEMICAL SOCIETY

Permission Status: Granted

Permission type: Republish or display content

Type of use: Republish in a thesis/dissertation

Order License Id: 4467990149732

Requestor type	Academic institution
Format	Print, Electronic
Portion	chart/graph/table/figure
Number of charts/graphs/tables/figures	3
The requesting person/organization	Shuai He/Curtin University
Title or numeric reference of the portion(s)	Figure 8, Figure 11 and Figure 16
Title of the article or chapter the portion is from	Performance Variability of La(Sr)FeO3 SOFC Cathode with Pt, Ag, and Au Current Collectors
Editor of portion(s)	N/A
Author of portion(s)	S.P. Simner, M.D. Anderson, L.R. Pederson, J.W. Stevenson
Volume of serial or monograph	152
Page range of portion	A1851
Publication date of portion	2005
Rights for	Main product
Duration of use	Life of current edition
Creation of copies for the disabled	no
With minor editing privileges	no
For distribution to	Worldwide
In the following language(s)	Original language of publication
With incidental promotional use	no
Lifetime unit quantity of new product	Up to 499
Title	Thermally and Electrochemically Induced Cathode/Electrolyte Interfaces in Solid Oxide Fuel Cells
Institution name	n/a
Expected presentation date	Dec 2018

Note: This item was invoiced separately through our **RightsLink service.** More info

$ 0.00

Electrochemical and solid-state letters

Billing Status: **N/A**

Order detail ID:	71662918
ISSN:	1099-0062
Publication Type:	Journal
Volume:	
Issue:	
Start page:	
Publisher:	ELECTROCHEMICAL SOCIETY, INC.
Author/Editor:	Institute of Electrical and Electronics Engineers ; Electrochemical Society

Permission Status: Granted

Permission type: Republish or display content

Type of use: Republish in a thesis/dissertation

Order License Id: 4467990151021

Requestor type	Academic institution
Format	Print, Electronic
Portion	chart/graph/table/figure
Number of charts/graphs/tables/figures	2
The requesting person/organization	Shuai He/Curtin University
Title or numeric reference of the portion(s)	Figure 2, Figure 4
Title of the article or chapter the portion is from	Deposition of Platinum Particles at LSM/ScSZ/Air Three-Phase Boundaries Using a Platinum Current Collector
Editor of portion(s)	N/A
Author of portion(s)	Y. Xiong, K. Yamaji, H. Kishimoto, M.E. Brito, T. Horita, H. Yokokawa
Volume of serial or monograph	12
Page range of portion	B31
Publication date of portion	2009
Rights for	Main product
Duration of use	Life of current edition
Creation of copies for the disabled	no
With minor editing privileges	no
For distribution to	Worldwide
In the following language(s)	Original language of publication
With incidental promotional use	no
Lifetime unit quantity of new product	Up to 499
Title	Thermally and Electrochemically Induced Cathode/Electrolyte Interfaces in Solid Oxide Fuel Cells
Institution name	n/a
Expected presentation date	Dec 2018

Note: This item was invoiced separately through our **RightsLink service.** More info **$ 0.00**

Journal of the Electrochemical Society

Billing Status: **N/A**

Order detail ID:	71662919
ISSN:	0013-4651
Publication Type:	Journal
Volume:	
Issue:	
Start page:	
Publisher:	ELECTROCHEMICAL SOCIETY,
Author/Editor:	ELECTROCHEMICAL SOCIETY

Permission Status: Granted

Permission type: Republish or display content

Type of use: Republish in a thesis/dissertation

Order License Id: 4467990152340

Requestor type	Academic institution
Format	Print, Electronic
Portion	chart/graph/table/figure
Number of charts/graphs/tables/figures	4
The requesting person/organization	Shuai He/Curtin University
Title or numeric reference of the portion(s)	Figure 1a, Figure 2c, Figure 4c and Figure 5d
Title of the article or chapter the portion is from	Thermally and Electrochemically Induced Electrode/Electrolyte Interfaces in Solid Oxide Fuel Cells: An AFM and EIS Study
Editor of portion(s)	N/A
Author of portion(s)	S. P. Jiang
Volume of serial or monograph	162
Page range of portion	F1119-F1128
Publication date of portion	2015
Rights for	Main product
Duration of use	Life of current edition
Creation of copies for the disabled	no
With minor editing privileges	no
For distribution to	Worldwide
In the following language(s)	Original language of publication
With incidental promotional use	no
Lifetime unit quantity of new product	Up to 499
Title	Thermally and Electrochemically Induced Cathode/Electrolyte Interfaces in Solid Oxide Fuel Cells
Institution name	n/a
Expected presentation date	Dec 2018

Note: This item was invoiced separately through our **RightsLink service.** More info **$ 0.00**

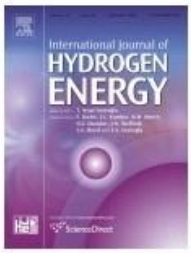

Title: Failure mechanism of (La,Sr)MnO3 oxygen electrodes of solid oxide electrolysis cells
Author: Kongfa Chen,San Ping Jiang
Publication: International Journal of Hydrogen Energy
Publisher: Elsevier
Date: August 2011

Order Completed

Thank you for your order.

This Agreement between Shuai He ("You") and Elsevier ("Elsevier") consists of your license details and the terms and conditions provided by Elsevier and Copyright Clearance Center.

Your confirmation email will contain your order number for future reference.

printable details

License Number	4470491207880
License date	Nov 15, 2018
Licensed Content Publisher	Elsevier
Licensed Content Publication	International Journal of Hydrogen Energy
Licensed Content Title	Failure mechanism of (La,Sr)MnO3 oxygen electrodes of solid oxide electrolysis cells
Licensed Content Author	Kongfa Chen,San Ping Jiang
Licensed Content Date	Aug 1, 2011
Licensed Content Volume	36
Licensed Content Issue	17
Licensed Content Pages	9
Type of Use	reuse in a thesis/dissertation
Portion	figures/tables/illustrations
Number of figures/tables/illustrations	4
Format	both print and electronic
Are you the author of this Elsevier article?	No
Will you be translating?	No
Original figure numbers	Figure 1a, Figure 3a, Figure 3b, Figure 4b
Title of your thesis/dissertation	Thermally and Electrochemically Induced Cathode/Electrolyte Interfaces in Solid Oxide Fuel Cells
Expected completion date	Dec 2018
Estimated size (number of pages)	205
Requestor Location	Shuai He Building 614 5 De Laeter Way Bentley, W.A. 6102 Australia Attn: Shuai He
Publisher Tax ID	GB 494 6272 12
Total	0.00 AUD

ORDER MORE | CLOSE WINDOW

Copyright Clearance Center

Welcome, Shuai Not you? | Log out | Cart (0) | Manage Account | Feedback | Help | Live Help

Get Permission / Find Title

1463-9084 Go

Advanced Search Options

Note: Copyright.com supplies permissions but not the copyrighted content itself.

1 PAYMENT — 2 REVIEW — 3 CONFIRMATION

Step 3: Order Confirmation

Start new search › | View your Order History ›

Print order information: includes order confirmation, terms and conditions, and citation information (What's this?)

Thank you for your order! A confirmation for your order will be sent to your account email address. If you have questions about your order, you can call us 24 hrs/day, M-F at +1.855.239.3415 Toll Free, or write to us at info@copyright.com. This is not an invoice.

Confirmation Number: 11765617
Order Date: 11/15/2018

If you paid by credit card, your order will be finalized and your card will be charged within 24 hours. If you choose to be invoiced, you can change or cancel your order until the invoice is generated.

Payment Information

Shuai He
imheshuai508@gmail.com
+61 (4)20460509
Payment Method: n/a

Order Details

Physical chemistry chemical physics

Order detail ID:	71664132
Order License Id:	4470500760749
ISSN:	1463-9084
Publication Type:	e-Journal
Volume:	
Issue:	
Start page:	
Publisher:	ROYAL SOCIETY OF CHEMISTRY
Author/Editor:	Royal Society of Chemistry (Great Britain)

Permission Status: Granted

Permission type: Republish or display content
Type of use: Thesis/Dissertation

Hide details

Requestor type	Academic institution
Format	Print, Electronic
Portion	chart/graph/table/figure
Number of charts/graphs/tables/figures	2
The requesting person/organization	Shuai He/Curtin University
Title or numeric reference of the portion(s)	Figure 3b, Figure 11
Title of the article or chapter the portion is from	Why solid oxide cells can be reversibly operated in solid oxide electrolysis cell and fuel cell modes?
Editor of portion(s)	N/A
Author of portion(s)	K. Chen, S.S. Liu, N. Ai, M. Koyama, S.P. Jiang
Volume of serial or monograph	17
Page range of portion	31308-31315
Publication date of portion	2015
Rights for	Main product
Duration of use	Life of current edition
Creation of copies for the disabled	no
With minor editing privileges	no
For distribution to	Worldwide
In the following language(s)	Original language of publication
With incidental promotional use	no
Lifetime unit quantity of new product	Up to 499
Title	Thermally and Electrochemically Induced Cathode/Electrolyte Interfaces in Solid Oxide Fuel Cells
Institution name	n/a
Expected presentation date	Dec 2018

Note: This item will be invoiced or charged separately through CCC's **RightsLink** service. More info **$ 0.00**

Total order items: 1

This is not an invoice.

Order Total: 0.00 USD

Order Completed

Thank you for your order.

This Agreement between Shuai He ("You") and John Wiley and Sons ("John Wiley and Sons") consists of your license details and the terms and conditions provided by John Wiley and Sons and Copyright Clearance Center.

Your confirmation email will contain your order number for future reference.

printable details

License Number	4470501032952
License date	Nov 15, 2018
Licensed Content Publisher	John Wiley and Sons
Licensed Content Publication	Journal of the American Ceramic Society
Licensed Content Title	Reactions between Strontium|Substituted Lanthanum Manganite and Yttria|Stabilized Zirconia: II, Diffusion Couples
Licensed Content Author	Kjersti Kleveland, Mari|Ann Einarsrud, Christian R. Schmidt, et al
Licensed Content Date	Dec 22, 2004
Licensed Content Volume	82
Licensed Content Issue	3
Licensed Content Pages	6
Type of use	Dissertation/Thesis
Requestor type	University/Academic
Format	Print and electronic
Portion	Figure/table
Number of figures/tables	1
Original Wiley figure/table number(s)	Figure 3
Will you be translating?	No
Title of your thesis / dissertation	Thermally and Electrochemically Induced Cathode/Electrolyte Interfaces in Solid Oxide Fuel Cells
Expected completion date	Dec 2018
Expected size (number of pages)	205
Requestor Location	Shuai He Building 614 5 De Laeter Way Bentley, W.A. 6102 Australia Attn: Shuai He
Publisher Tax ID	EU826007151
Total	0.00 AUD

Would you like to purchase the full text of this article? If so, please continue on to the content ordering system located here: Purchase PDF

If you click on the buttons below or close this window, you will not be able to return to the content ordering system.

ORDER MORE | CLOSE WINDOW

Title: Sr and Zr diffusion in LSCF/10GDC/8YSZ triplets for solid oxide fuel cells (SOFCs)

Author: Fangfang Wang,Mina Nishi,Manuel E. Brito,Haruo Kishimoto,Katsuhiko Yamaji,Harumi Yokokawa,Teruhisa Horita

Publication: Journal of Power Sources

Publisher: Elsevier

Date: 15 July 2014

Order Completed

Thank you for your order.

This Agreement between Shuai He ("You") and Elsevier ("Elsevier") consists of your license details and the terms and conditions provided by Elsevier and Copyright Clearance Center.

Your confirmation email will contain your order number for future reference.

printable details

License Number	4470510311445
License date	Nov 15, 2018
Licensed Content Publisher	Elsevier
Licensed Content Publication	Journal of Power Sources
Licensed Content Title	Sr and Zr diffusion in LSCF/10GDC/8YSZ triplets for solid oxide fuel cells (SOFCs)
Licensed Content Author	Fangfang Wang,Mina Nishi,Manuel E. Brito,Haruo Kishimoto,Katsuhiko Yamaji,Harumi Yokokawa,Teruhisa Horita
Licensed Content Date	Jul 15, 2014
Licensed Content Volume	258
Licensed Content Issue	n/a
Licensed Content Pages	9
Type of Use	reuse in a thesis/dissertation
Portion	figures/tables/illustrations
Number of figures/tables/illustrations	1
Format	both print and electronic
Are you the author of this Elsevier article?	No
Will you be translating?	No
Original figure numbers	Figure 4
Title of your thesis/dissertation	Thermally and Electrochemically Induced Cathode/Electrolyte Interfaces in Solid Oxide Fuel Cells
Expected completion date	Dec 2018
Estimated size (number of pages)	205
Requestor Location	Shuai He Building 614 5 De Laeter Way Bentley, W.A. 6102 Australia Attn: Shuai He
Publisher Tax ID	GB 494 6272 12
Total	0.00 AUD

ORDER MORE | CLOSE WINDOW

Copyright Clearance Center

Welcome, Shuai Not you? | Log out | Cart (0) | Manage Account | Feedback | Help | Live Help

Get Permission / Find Title

2050-7488 Go

Advanced Search Options

Note: Copyright.com supplies permissions but not the copyrighted content itself.

1 PAYMENT — 2 REVIEW — 3 CONFIRMATION

Step 3: Order Confirmation

Start new search › | View your Order History ›

Print order information: includes order confirmation, terms and conditions, and citation information (What's this?)

Thank you for your order! A confirmation for your order will be sent to your account email address. If you have questions about your order, you can call us 24 hrs/day, M-F at +1.855.239.3415 Toll Free, or write to us at info@copyright.com. This is not an invoice.

Confirmation Number: 11765622
Order Date: 11/15/2018

If you paid by credit card, your order will be finalized and your card will be charged within 24 hours. If you choose to be invoiced, you can change or cancel your order until the invoice is generated.

Payment Information

Shuai He
imheshuai508@gmail.com
+61 (4)20460509
Payment Method: n/a

Order Details

Journal of materials chemistry. A, Materials for energy and sustainability

Order detail ID:	71664136
Order License Id:	4470510738172
ISSN:	2050-7488
Publication Type:	Journal
Volume:	
Issue:	
Start page:	
Publisher:	Royal Society of Chemistry
Author/Editor:	Royal Society of Chemistry (Great Britain)

Permission Status: Granted

Permission type: Republish or display content
Type of use: Thesis/Dissertation

Hide details

Requestor type	Academic institution
Format	Print, Electronic
Portion	chart/graph/table/figure
Number of charts/graphs/tables/figures	1
The requesting person/organization	Shuai He/Curtin University
Title or numeric reference of the portion(s)	Figure 7
Title of the article or chapter the portion is from	Smart utilization of cobaltite-based double perovskite cathodes on barrier-layer-free zirconia electrolyte of solid oxide fuel cells
Editor of portion(s)	N/A
Author of portion(s)	M. Li, K. Chen, B. Hua, J.-l. Luo, W.D.A. Rickard, J. Li, J.T.S. Irvine, S.P. Jiang
Volume of serial or monograph	4
Page range of portion	19019-19025
Publication date of portion	2016
Rights for	Main product
Duration of use	Life of current edition
Creation of copies for the disabled	no
With minor editing privileges	no
For distribution to	Worldwide
In the following language(s)	Original language of publication
With incidental promotional use	no
Lifetime unit quantity of new product	Up to 499
Title	Thermally and Electrochemically Induced Cathode/Electrolyte Interfaces in Solid Oxide Fuel Cells
Institution name	n/a
Expected presentation date	Dec 2018

Note: This item will be invoiced or charged separately through CCC's **RightsLink** service. More info **$ 0.00**

Total order items: 1

This is not an invoice.

Order Total: 0.00 USD

Order Completed

Thank you for your order.

This Agreement between Shuai He ("You") and Elsevier ("Elsevier") consists of your license details and the terms and conditions provided by Elsevier and Copyright Clearance Center.

Your confirmation email will contain your order number for future reference.

printable details

License Number	4470510986623
License date	Nov 15, 2018
Licensed Content Publisher	Elsevier
Licensed Content Publication	Solid State Ionics
Licensed Content Title	Microstructure degradation of an anode/electrolyte interface in SOFC studied by transmission electron microscopy
Licensed Content Author	Y.L. Liu,Chengge Jiao
Licensed Content Date	Feb 14, 2005
Licensed Content Volume	176
Licensed Content Issue	5-6
Licensed Content Pages	8
Type of Use	reuse in a thesis/dissertation
Portion	figures/tables/illustrations
Number of figures/tables/illustrations	5
Format	both print and electronic
Are you the author of this Elsevier article?	No
Will you be translating?	No
Original figure numbers	Figure 1, Figure 2, Figure 3, Figure 4a, Figure 6
Title of your thesis/dissertation	Thermally and Electrochemically Induced Cathode/Electrolyte Interfaces in Solid Oxide Fuel Cells
Expected completion date	Dec 2018
Estimated size (number of pages)	205
Requestor Location	Shuai He Building 614 5 De Laeter Way Bentley, W.A. 6102 Australia Attn: Shuai He
Publisher Tax ID	GB 494 6272 12
Total	0.00 AUD

ORDER MORE | CLOSE WINDOW

Copyright Clearance Center

Welcome, Shuai
Not you?

Log out | Cart (0) | Manage Account | Feedback | Help | Live Help

Get Permission / Find Title

Go

Advanced Search Options

Note: Copyright.com supplies permissions but not the copyrighted content itself.

1 PAYMENT — 2 REVIEW — 3 CONFIRMATION

Step 3: Order Confirmation

Start new search › | View your Order History ›

Print order information: includes order confirmation, terms and conditions, and citation information (What's this?)

Thank you for your order! A confirmation for your order will be sent to your account email address. If you have questions about your order, you can call us 24 hrs/day, M-F at +1.855.239.3415 Toll Free, or write to us at info@copyright.com. This is not an invoice.

Confirmation Number: 11765623
Order Date: 11/15/2018

If you paid by credit card, your order will be finalized and your card will be charged within 24 hours. If you choose to be invoiced, you can change or cancel your order until the invoice is generated.

Payment Information

Shuai He
imheshuai508@gmail.com
+61 (4)20460509
Payment Method: n/a

Order Details

Journal of the Electrochemical Society

Order detail ID:	71664137
Order License Id:	4470511328342
ISSN:	1945-7111
Publication Type:	e-Journal
Volume:	
Issue:	
Start page:	
Publisher:	Electrochemical Society
Author/Editor:	Electrochemical Society

Permission Status: Granted
Permission type: Republish or display content
Type of use: Republish in a thesis/dissertation

Hide details

Requestor type	Academic institution
Format	Print, Electronic
Portion	chart/graph/table/figure
Number of charts/graphs/tables/figures	1
The requesting person/organization	Shuai He/Curtin University
Title or numeric reference of the portion(s)	Figure 5
Title of the article or chapter the portion is from	Performance Enhancement of SOFC Anode Through Electrochemically Induced Ni/YSZ Nanostructures
Editor of portion(s)	N/A
Author of portion(s)	D. Klotz, B. Butz, A. Leonide, J. Hayd, D. Gerthsen, E. Ivers-Tiffée
Volume of serial or monograph	158
Page range of portion	B587-B595
Publication date of portion	2011
Rights for	Main product
Duration of use	Life of current edition
Creation of copies for the disabled	no
With minor editing privileges	no
For distribution to	Worldwide
In the following language(s)	Original language of publication
With incidental promotional use	no
Lifetime unit quantity of new product	Up to 499
Title	Thermally and Electrochemically Induced Cathode/Electrolyte Interfaces in Solid Oxide Fuel Cells
Institution name	n/a
Expected presentation date	Dec 2018

Note: This item will be invoiced or charged separately through CCC's **RightsLink** service. More info **$ 0.00**

Total order items: 1

This is not an invoice.

Order Total: 0.00 USD

Title: Mesoscale-structure control at anode/electrolyte interface in solid oxide fuel cell

Author: Akio Konno,Hiroshi Iwai,Kenji Inuyama,Atsushi Kuroyanagi,Motohiro Saito,Hideo Yoshida,Kazufumi Kodani,Kuniaki Yoshikata

Publication: Journal of Power Sources

Publisher: Elsevier

Date: 1 January 2011

Order Completed

Thank you for your order.

This Agreement between Shuai He ("You") and Elsevier ("Elsevier") consists of your license details and the terms and conditions provided by Elsevier and Copyright Clearance Center.

Your confirmation email will contain your order number for future reference.

printable details

License Number	4470511462445
License date	Nov 15, 2018
Licensed Content Publisher	Elsevier
Licensed Content Publication	Journal of Power Sources
Licensed Content Title	Mesoscale-structure control at anode/electrolyte interface in solid oxide fuel cell
Licensed Content Author	Akio Konno,Hiroshi Iwai,Kenji Inuyama,Atsushi Kuroyanagi,Motohiro Saito,Hideo Yoshida,Kazufumi Kodani,Kuniaki Yoshikata
Licensed Content Date	Jan 1, 2011
Licensed Content Volume	196
Licensed Content Issue	1
Licensed Content Pages	12
Type of Use	reuse in a thesis/dissertation
Portion	figures/tables/illustrations
Number of figures/tables/illustrations	3
Format	both print and electronic
Are you the author of this Elsevier article?	No
Will you be translating?	No
Original figure numbers	Figure 6b, Figure 7, Figure 17
Title of your thesis/dissertation	Thermally and Electrochemically Induced Cathode/Electrolyte Interfaces in Solid Oxide Fuel Cells
Expected completion date	Dec 2018
Estimated size (number of pages)	205
Requestor Location	Shuai He Building 614 5 De Laeter Way Bentley, W.A. 6102 Australia Attn: Shuai He
Publisher Tax ID	GB 494 6272 12
Total	0.00 AUD

ORDER MORE | CLOSE WINDOW

Copyright Clearance Center

Welcome, Shuai Not you? | Log out | Cart (0) | Manage Account | Feedback | Help | Live Help

Get Permission / Find Title Go

Advanced Search Options

Note: Copyright.com supplies permissions but not the copyrighted content itself.

1 PAYMENT — 2 REVIEW — 3 CONFIRMATION

Step 3: Order Confirmation

Start new search › | View your Order History ›

Print order information: includes order confirmation, terms and conditions, and citation information (What's this?)

Thank you for your order! A confirmation for your order will be sent to your account email address. If you have questions about your order, you can call us 24 hrs/day, M-F at +1.855.239.3415 Toll Free, or write to us at info@copyright.com. This is not an invoice.

Confirmation Number: 11765625
Order Date: 11/15/2018

If you paid by credit card, your order will be finalized and your card will be charged within 24 hours. If you choose to be invoiced, you can change or cancel your order until the invoice is generated.

Payment Information

Shuai He
imheshuai508@gmail.com
+61 (4)20460509
Payment Method: n/a

Order Details

Journal of the Electrochemical Society

Order detail ID:	71664139
Order License Id:	4470520748352
ISSN:	1945-7111
Publication Type:	e-Journal
Volume:	
Issue:	
Start page:	
Publisher:	Electrochemical Society
Author/Editor:	Electrochemical Society

Permission Status: Granted
Permission type: Republish or display content
Type of use: Republish in a thesis/dissertation

Hide details

Requestor type	Academic institution
Format	Print, Electronic
Portion	chart/graph/table/figure
Number of charts/graphs/tables/figures	2
The requesting person/organization	Shuai He/Curtin University
Title or numeric reference of the portion(s)	Figure 4, Figure 6
Title of the article or chapter the portion is from	Observation of the Ni/YSZ Interface in a Conventional SOFC
Editor of portion(s)	N/A
Author of portion(s)	S.S. Liu, Z. Jiao, N. Shikazono, S. Matsumura, M. Koyama
Volume of serial or monograph	162
Page range of portion	F750-F754
Publication date of portion	2015
Rights for	Main product
Duration of use	Life of current edition
Creation of copies for the disabled	no
With minor editing privileges	no
For distribution to	Worldwide
In the following language(s)	Original language of publication
With incidental promotional use	no
Lifetime unit quantity of new product	Up to 499
Title	Thermally and Electrochemically Induced Cathode/Electrolyte Interfaces in Solid Oxide Fuel Cells
Institution name	n/a
Expected presentation date	Dec 2018

Note: This item will be invoiced or charged separately through CCC's **RightsLink** service. More info **$ 0.00**

Total order items: 1

This is not an invoice.

Order Total: 0.00 USD

Order Completed

Thank you for your order.

This Agreement between Shuai He ("You") and Springer Nature ("Springer Nature") consists of your license details and the terms and conditions provided by Springer Nature and Copyright Clearance Center.

Your confirmation email will contain your order number for future reference.

printable details

License Number	4470520559874
License date	Nov 15, 2018
Licensed Content Publisher	Springer Nature
Licensed Content Publication	Nature Materials
Licensed Content Title	Three-dimensional reconstruction of a solid-oxide fuel-cell anode
Licensed Content Author	James R. Wilson, Worawarit Kobsiriphat, Roberto Mendoza, Hsun-Yi Chen, Jon M. Hiller et al.
Licensed Content Date	Jun 11, 2006
Licensed Content Volume	5
Licensed Content Issue	7
Type of Use	Thesis/Dissertation
Requestor type	academic/university or research institute
Format	print and electronic
Portion	figures/tables/illustrations
Number of figures/tables/illustrations	2
High-res required	no
Will you be translating?	no
Circulation/distribution	<501
Author of this Springer Nature content	no
Title	Thermally and Electrochemically Induced Cathode/Electrolyte Interfaces in Solid Oxide Fuel Cells
Institution name	n/a
Expected presentation date	Dec 2018
Portions	Figure 2, Figure 3
Requestor Location	Shuai He Building 614 5 De Laeter Way Bentley, W.A. 6102 Australia Attn: Shuai He
Billing Type	Invoice
Billing address	Shuai He Building 614 5 De Laeter Way Bentley, Australia 6102 Attn: Shuai He
Total	0.00 AUD

ORDER MORE | CLOSE WINDOW

Appendix - Co-author attribution statement

1. Chapter 4. Paper "A FIB-STEM Study of $La_{0.8}Sr_{0.2}MnO_3$ Cathode and Y_2O_3-ZrO_2/Gd_2O_3-CeO_2 Electrolyte Interfaces of Solid Oxide Fuel Cells", Journal of The Electrochemical Society, 164 (13), F1437-F1447.

	Conception and design	Acquisition of data & method	Data conditioning & manipulation	Analysis & statistical method	Interpretation & discussion	Final Approval
Dr Kongfa Chen				×	×	×
I acknowledge that these represent my contribution to the above research output. Signed.						
Dr Martin Saunders		×		×	×	×
I acknowledge that these represent my contribution to the above research output. Signed.						
Dr Jian Li					×	×
I acknowledge that these represent my contribution to the above research output. Signed.						
Dr C.Q. Cui					×	×
I acknowledge that these represent my contribution to the above research output. Signed.						
Dr San Ping Jiang	×			×	×	×
I acknowledge that these represent my contribution to the above research output. Signed.						

2. Chapter 5. Paper "A FIB-STEM Study of Strontium Segregation and Interface Formation of Directly Assembled $La_{0.6}Sr_{0.4}Co_{0.2}Fe_{0.8}O_{3-\delta}$ Cathodeon Y_2O_3-ZrO_2 Electrolyte of Solid Oxide Fuel Cells", Journal of The Electrochemical Society, 165 (7), F417-F429.

	Conception and design	Acquisition of data & method	Data conditioning & manipulation	Analysis & statistical method	Interpretation & discussion	Final Approval
Dr Martin Saunders		×		×	×	×
I acknowledge that these represent my contribution to the above research output. Signed. M. Saunders						
Dr Kongfa Chen				×	×	×
I acknowledge that these represent my contribution to the above research output. Signed. 陈. 32.4						
Dr Alexandra Suvorova		×			×	×
I acknowledge that these represent my contribution to the above research output. Signed. Suvorova						
Dr William D.A. Rickard		×			×	×
I acknowledge that these represent my contribution to the above research output. Signed. W. Rickard						
Dr Zakaria Quadir					×	×
I acknowledge that these represent my contribution to the above research output. Signed.						
Dr C.Q. Cui					×	×
I acknowledge that these represent my contribution to the above research output. Signed.						
Dr San Ping Jiang	×			×	×	×
I acknowledge that these represent my contribution to the above research output. Signed.						

3. **Chapter 6.** Paper "Interface formation and Mn segregation of directly assembled $La_{0.8}Sr_{0.2}MnO_3$ cathode on Y_2O_3-ZrO_2 and Gd_2O_3-CeO_2 electrolytes of solid oxide fuel cells", Solid State Ionics, 325, 176-188.

	Conception and design	Acquisition of data & method	Data conditioning & manipulation	Analysis & statistical method	Interpretation & discussion	Final Approval
Dr Kongfa Chen				×	×	×
I acknowledge that these represent my contribution to the above research output. Signed.						
Dr Martin Saunders		×			×	×
I acknowledge that these represent my contribution to the above research output. Signed.						
Dr Zakaria Quadir					×	×
I acknowledge that these represent my contribution to the above research output. Signed.						
Dr Shanwen Tao					×	×
I acknowledge that these represent my contribution to the above research output. Signed.						
Dr C.Q. Cui					×	×
I acknowledge that these represent my contribution to the above research output. Signed.						
Dr San Ping Jiang	×			×	×	×
I acknowledge that these represent my contribution to the above research output. Signed.						

4. **Chapter 7.** Paper "In Situ Formation of $Er_{0.4}Bi_{1.6}O_3$ Protective Layer at Cobaltite Cathode/Y_2O_3-ZrO_2 Electrolyte Interface under Solid Oxide Fuel Cell Operation Conditions", ACS Applied Materials & Interfaces, 10(47), 40549-40559.

	Conception and design	Acquisition of data & method	Data conditioning & manipulation	Analysis & statistical method	Interpretation & discussion	Final Approval
Dr Qi Zhang		×		×	×	×
I acknowledge that these represent my contribution to the above research output. Signed.						
Dr Giulio Maurizio				×	×	×
I acknowledge that these represent my contribution to the above research output. Signed.						
Dr Lorenzo Catellani				×	×	×
I acknowledge that these represent my contribution to the above research output. Signed.						
Dr Kongfa Chen				×	×	×
I acknowledge that these represent my contribution to the above research output. Signed.						
Dr Qibing Chang					×	×
I acknowledge that these represent my contribution to the above research output. Signed.						
Dr Massimo Santarelli					×	×
I acknowledge that these represent my contribution to the above research output. Signed.						
Dr San Ping Jinag	×			×	×	×
I acknowledge that these represent my contribution to the above research output. Signed.						